An analysis of variability and predictability of organised deep convection and its divergent upper tropospheric outflow

Dissertation submitted for the award of the title
"Doctor of Natural Sciences"
to the Faculty of Physics, Mathematics and Computer Science of
Johannes Gutenberg University in Mainz

Edward Groot
Born 15 November 1995 in Schiedam, The Netherlands

JG|U

Mainz,

February 24, 2023

Cover picture: cumulonimbus cloud over Southern Hesse, taken from Bodenheim directly south of Mainz on March 14th, 2021 by the author.

"*The condensation is building tension*" (Gary Lightbody, Snow Patrol, in *Fallen Empires*, 2011)

Summary

The consequences of convective organisation, aggregation and convective momentum transport for upper tropospheric divergent outflows from deep convection are explored. Furthermore, the variability and predictability of these outflows is thereby connected to other aspects of dynamics and predictability of the convective systems. Different approaches to the simulation of convection are investigated, in which the conditional dependence of divergent outflow, on net latent heating rate, differs as a consequence of different methods to represent convective systems.

The theoretical understanding of the convective outflows is addressed first, by investigating a comprehensive set of idealised Large Eddy Simulations. The experiments, with four prototypes of convective systems, reveal that convective organisation and net latent heat release (convertible to precipitation rate) shape the patterns in magnitude of the divergent outflows. Dimensionality of convective outflows (2D convection versus 3D convection, or a mixed/intermediate regime) bounds an envelope of divergent outflow variability. This outcome is mostly consistent with convective outflows, if represented in older linear gravity wave models.

Investigating these convective outflows in the NWP model ICON for an event on 10^{th}-11^{th} of June 2019 over Central Europe, the divergent outflows in a parameterised and an explicit representations of deep convective systems are intercompared. Near-linear response of deep convective outflows to net latent heating is found in parameterised convection, while coherent patterns in variability are found in convection-permitting simulations, at 1 km horizontal grid spacing. Convective organisation and aggregation induce a non-linear increase in the magnitude deep convective outflows, with increasing net latent heating. This non-linearity is demonstrated by the confidence interval of the best fit, between power transformed net latent heating and detected magnitude of outflows. Other statistical patterns also support the representation of that pattern in the studied case. However, mixed and weaker than expected signals are found, in an attempt to detect the representation of dimensionality of the convection and its consequences for the divergent outflows. To detect the representation, an ellipse fitting algorithm that describes the elongation of the intense (convective) precipitation systems is used. These signals are understandable and suggest the need of further investigation. Convective momentum transport is suggested to slightly increase the magnitude of divergent outflows, in the studied case.

In a subset of the Large Eddy Simulations, in which a so-called squall line is triggered, error or difference growth is investigated in relation to dynamics and precipitation variability, amongst others. During the two hour simulations, the first stage of convective initiation is associated with crucial gravity wave activity, which induces de-correlation between ensemble members. After an initial trigger of convection (about 20 minutes into the simulations), a second phase of convective initiation (at 30 minutes) determines much of the structure in the ensemble spread, for the next hour or so. Directly after that second phase of convective initiation, spread in cold pool acceleration is found, while cold pool propagation velocity is maintained afterwards ($t = 45$ to $t = 100$ minutes). Coherent flow anomalies, initiated directly after the second phase of convective initiation, are also maintained on the time scale of an hour. They dissipate after about 80 to 100 minutes simulation time. When flow is evaluated in a frame relative to cold pool edge, it is shown that error or difference growth in terms of zonal wind, within the ensemble, is substantially smaller than in the Eulerian perspective. Furthermore, feedbacks acting within the squall line are not dominating this difference growth: much of the difference is directly explained by differences in cold pool propagation. Much of the ensemble spread still maintained in the cold pool-relative framework, such as in precipitation and downdrafts, is also strongly related to the decisive second phase of convective triggering.

Looking at convective variability from a (Bayesian) perspective, conditional on precipitation rate, the often subtle threshold behaviour in convective initiation is bypassed. However, the approach demonstrates that a conditional view can shed important light on convective variability and how it is represented in NWP. Here, it shows contrasts in between idealised Large Eddy Simulations, convection-permitting NWP and deep convection parameterising NWP, where implicit assumptions on divergent convective outflows are identified. Strong coupling between dynamics, predictability and precipitation is accentuated. In representativity studies of other aspects in an NWP (e.g. microphysics, turbulence, radiation) and predictability studies, the applied conditional approach may be fruitful.

Zusammenfassung

Im Folgenden wird untersucht, wie die Organisation von Konvektion und der konvektive Impulstransport die divergente Ausströmung von hochreichender Konvektion in der oberen Troposphäre beeinflussen. Die Variabilität und Vorhersagbarkeit dieses Ausströmens wird mit anderen Aspekten der atmosphärischen Dynamik und Vorhersagbarkeit von konvektiven Systemen in Verbindung gebracht. Dazu werden verschiedene Ansätze zur Repräsentation von Konvektion untersucht, die ein unterschiedliches Verhalten der divergenten Ausströmung für gegebene latente Wärmefreisetzung aufweisen.
Zunächst wird das theoretische Verständnis über konvektive Ausströmungen durch Untersuchung einer umfassenden Reihe an idealisierten *Large Eddy Simulationen* behandelt. Die Simulationen zeigen anhand von vier Prototypen von konvektiven Systemen, dass die Organisation der Konvektion und die netto freigesetzte latente Wärme die Stärke der divergenten Ausströmung bestimmen. Zudem wird deutlich, dass die Variabilität der divergenten Ausströmung durch die Dimensionalität der Konvektion (2D versus 3D) eingeschränkt wird. Dies ist konsistent mit früheren Ergebnissen basierend auf Simulationen mit linearisierten Schwerewellenmodellen.
Ergänzend zu den *Large Eddy Simulationen* wird eine Fallstudie mit dem Wettervorhersagemodell ICON durchgeführt. In der Fallstudie werden Modellsimulationen mit parametrisierter Darstellung hochreichender Konvektion und mit expliziter Darstellung hochreichender Konvektion durchgeführt und deren Ergebnisse zur divergenten Ausströmung miteinander verglichen. Bei der parametrisierten Konvektion wird ein nahezu linearer Zusammenhang der divergenten Ausströmung mit der netto freigesetzten latenten Wärme gefunden, wohingegen die Simulationen mit expliziter Darstellung der Konvektion einen komplexeren Zusammenhang aufweisen. Hier wird festgestellt, dass mit zunehmender freigesetzter latenter Wärme die Zunahme an divergenter Ausströmung immer geringer wird. Ein Versuch, die Dimensionalität der Konvektion in explizit aufgelösten Simulationen zu bestimmen, lieferte verschiedene, uneindeutige Ergebnisse. Weiterhin wurde in dieser Fallstudie gefunden, dass der konvektive Impulstransport die divergente Ausströmung verstärkt.
Fehlerwachstum und Ensemblestreuung werden anhand von *Large Eddy Simulationen*, in denen eine sogenannte *Squall Line* ausgelöst wird, unter anderem hinsichtlich der Dynamik und der Niederschlagsvariabilität untersucht. Während der Simulationszeit von zwei Stunden ist die erste Phase der konvektiven Auslösung (nach etwa 20 Minuten Simulationszeit) mit Schwerewellenaktivität assoziiert, die essentiell dazu beiträgt, eine Dekorrelation innerhalb des Ensembles herbeizuführen. Nach 30 Minuten setzt eine zweite Phase konvektiver Auslösung ein, die in der nächsten Stunde einen Großteil der Struktur in der Ensemblevariabilität bestimmt. Unmittelbar nach Einsetzen dieser konvektiven Auslösung wird eine variable Beschleunigung des *Cold Pools* festgestellt, auf die eine Phase konstanter Fortbewegungsgeschwindigkeit des *Cold Pools* folgt (zwischen 45 und 100 Minuten Simulationszeit). Kohärente Strömungsanomalien, die direkt nach der zweiten Phase der konvektiven Auslösung auftreten, bleiben ebenfalls auf der Zeitskala von einer Stunde erhalten, lösen sich aber nach etwa 80 bis 100 Minuten auf. Wenn die Strömung relativ zum Rand des *Cold Pools* untersucht wird, zeigt sich, dass das Fehler- oder Differenzwachstum innerhalb des Ensembles bezüglich Windgeschwindigkeiten wesentlich geringer ist als von der eulerischen Perspektive aus betrachtet. Ferner sind Rückkopplungen, die innerhalb der *Squall Line* auftreten, nicht ausschlaggebend für das Wachstum von Winddifferenzen: ein Großteil dieser kann direkt durch Unterschiede in der Cold Pool Bewegung erklärt werden. Die Ensemblevariabilität (z. B. bei Niederschlagmengen und Downdrafts), die der Transformation in das *Cold Pool* bezogene Referenzsystem standgehalten hat, ist entscheidend mit der zweiten Phase der konvektiven Auslösung verbunden.
Wird die konvektive Variabilität aus einer von der Niederschlagsrate abhängigen Perspektive betrachtet, wird das quasi-zufällige Verhalten bei der konvektiven Auslösung umgangen. Der Ansatz in dieser Arbeit zeigt jedoch, dass eine bedingte Betrachtung wichtige Erkenntnisse über die konvektive Variabilität und deren Darstellung in Wettervorhersagemodellen bringen kann. In diesem Fall zeigt es Unterschiede zwischen hochreichender Konvektion in idealisierten *Large Eddy Simulationen*, konvektionszulassenden und konvektionsparametrisierenden Wettervorhersagemodellen auf, indem implizite Annahmen zu divergenten konvektiven Ausströmungen identifiziert werden. Die starke Kopplung zwischen Dynamik, Vorhersagbarkeit und Niederschlag wird dabei herausgestellt. Um die Darstellung von weiteren Aspekten in Wettervorhersagemodellen (z.B. Mikrophysik, Turbulenz) zu untersuchen sowie um Vorhersagbarkeitsstudien durchzuführen, kann der angewandte Ansatz vielversprechend sein.

Contents

List of publications

The following publications are included as part of dissertation, in the respective chapters and appendices.

- **Evolution of squall line variability and error growth in an ensemble of large eddy simulations, Groot, Edward and Tost, Holger. 2023. Atmospheric Physics and Chemistry. Copernicus. Published: 13-01-2023**
  The research for this manuscript was fully designed and conducted by me. I would like to thank Holger Tost for his advices/supervision on the way and for his useful help, especially when creating the first revised version of the manuscript (after peer review).

- **Divergent convective outflow in large eddy simulations, Groot, Edward and Tost, Holger. 2022 (preprint). Atmospheric Physics and Chemistry. Copernicus. In review (as of December 2022)**
  The research for this manuscript was partly based on the proposal for Waves to Weather (W2W) Phase 2, Project A1, and informal gatherings at the Kick-off Annual Meeting of Phase 2 of W2W. However, under the supervision of Holger Tost, I worked out the details of the experimental design, including subsequent improvements. These were first documented in another manuscript (listed as the next item), but got rejected for publication during the peer reviewing process. Only after much additional experimentation, detailed analysis of those experiments and a literature study that I subsequently did, it got more favourable for publication and subsequently I analysed and wrote the manuscript for publication under the supervision of and being advised by Holger Tost.

- **Analysis of variability in divergence and turn-over induced by three idealized convective systems with a 3D cloud resolving model, Groot, Edward and Tost, Holger, 2020. Atmospheric Physics and Chemistry Discussions. Copernicus. Rejected for ACP, after peer reviews.**
  From this publication, material of the main content and the appendix is included in the appendices of this thesis and some of the experimental design is inherited into the publication listed (directly) above, as previous list item. Therefore, the statement about the publication as given with the item above applies here.

- **Divergent convective outflow in ICON deep convection permitting and parameterised deep convection simulations, Groot, Edward, Kuntze, Patrick, Miltenberger, Annette and Tost, Holger. 2023. To be determined. To be submitted (as of November 2022)**
  For this work the idea was to combine and compare convection-permitting ICON simulations (in a local area model) with ICON simulations with parameterised deep convection (on a global domain). Since Patrick Kuntze (under the supervision of Annette Miltenberger) had the plan to do convection-permitting simulations (which was in my interest, to be able to do the comparison between both simulation approaches to describe deep convection - as also stated in the proposal of W2W project A1) and I planned to do simulations with parameterised convection, we agreed to keep in touch on the datasets and exchange data. After I analysed my ICON convection parameterised simulations and LES-simulations (Chapter 3), I developed the hypotheses to test on his simulation dataset, based on the result obtained with LES simulations (all three studies listed above). Then I developed the analytical methods to do so and analysed the results, supported by a few advices from Holger Tost. After doing the analysis, I wrote a draft manuscript and shared the analysis and draft manuscript with all co-authors, who helped improving it by reviewing it internally, before submitting the work to a journal eventually.

The following publication is not included as part of this dissertation:

- An expected publication, mainly in collaboration with Tobias Selz and Michael Riemer, is expected for later this year. **Title: to be determined.**

- **Simulaties van extreme neerslagsommen bij zware convectie, Groot, Edward. 2021. Meteorologica (no. 2, 2021; in Dutch). Nederlandse Vereniging ter Bevordering van de Meteorologie.**
  An English translation of the title: *Extreme precipitation sums in severe convection simulations.* The research for this manuscript was fully designed and conducted by me. The work covers an analysis of the precipitation sums in simulations used for the work included in this dissertation (Chapter 3) and was reviewed by two editors of Meteorologica, before the final publication.

1 Introduction

1.1 Mesoscale convective systems

The dynamics of convective systems has long been studied from the fluid dynamical point of view: buoyant parcels or thermals floating upward and downward, spontaneously or as a result of forcing of some kind. All starting as individual cumulus clouds, associated clouds can subsequently grow or merge into cumulonimbus clouds and eventually mesoscale convective systems (MCS), or even larger complexes. A historical overview of early technical descriptions, the discovery of cumulonimbus and organised convective systems and full recognition of organised (mesoscale) convective systems can be found in Houze [2018], Sections 1-7.
The subsample of clouds studied in this work are all of the cumulonimbus type. Even though not all of them fulfil the definition of a mesoscale convective system (typical definition: a convective system horizontal length scale larger than about 100 km), many of them are. From a dynamical point of view, these systems usually generate a system-scale dynamics [see Houze, 2004, for a more elaborate discussion].
Studying mesoscale convective systems is not only needed for improved understanding of the direct potentially hazardous effects of these systems [Wilhelm et al., 2021, Antonescu et al., 2017, Clark et al., 2012, Doswell, 2003, and many other studies] - also

- For the potential of those systems to impact weather predictability downstream [e.g. Rodwell et al., 2013, Baumgart et al., 2019, Clarke et al., 2019a,b]
- For improved understanding of variability and predictability of the convective systems themselves [e.g. Stechmann and Neelin, 2011, Keane et al., 2014, Groot and Tost, 2023, 2022, Groot et al., 2023, (Chapters 3, 4 and 5 of this work)]
- On the way towards improved representation of those systems in numerical weather prediction and climate modelling [e.g. Bechtold et al., 2014, Stein et al., 2014, Hanley et al., 2015, Bauer et al., 2015, Ollinaho et al., 2017, Varble et al., 2020]

The fundamental dynamics of convective clouds is discussed in the following section, including the association of those clouds with horizontal convergence below and horizontally divergent flow at the top. That dynamical pattern sets important boundary conditions for the scope of Chapters 3 and 4 of this work: the divergent outflow forms the red thread.

1.2 Flow perturbations around convective clouds

Convection is the process in which air spontaneously rises due to differences in buoyancy, which can be driven by contrasts in temperature and moisture and therefore buoyancy. Furthermore, in other cases it occurs in response to a forcing (e.g. land-sea contrasts and accompanied flow). It may lead to the formation of so-called cumulus clouds and ultimately cumulonimbus clouds, after further vertical growth of the cumulus. Here, the example cumulus clouds forming through positive buoyancy is described. Nevertheless, from a dynamical point of view, consequential flow perturbations and pressure fluctuations within and in the surroundings of the clouds have the same patterns - irrespective of the driving mechanism being buoyancy or a forcing.
Usually, a horizontal layer with a nearly homogeneous average *potential* temperature (symbol: θ) and water vapour *mixing ratio* has contrasts in those quantities at small scales of turbulent eddies (sub-km). Potential temperature is the thermodynamic quantity that is conserved in the absence of mixing in "dry" air (that means: air with relative humidity below 100%), when it moves upward or downward. Similarly, water vapour mixing ratio is the conserved quantity for water vapour upon vertical displacements and without mixing. If, however, phase changes occur as a consequence of vertical motion and accompanied temperature changes, the total water mixing ratio is conserved instead. The contrasts in potential temperature at small length scales will often lead to spontaneous upward motion. If the mixing ratio of water vapour in moist air parcels is sufficiently high and the top altitude of the (nearly) homogeneous layer is at sufficiently high altitude, this will lead to condensation and the formation of a cloud, once the moister air parcels reach the top of the layer.
In other cases, if a layer is statically stable, such vertical motion is constantly damped, because a negative vertical acceleration will be introduced when an air parcel rises spontaneously. That negative acceleration occurs due to its colder temperature and higher density than its environment at the same altitude.
The condensation leads to the release of latent heat, which can enhance the upward motion and helps the cloud to penetrate through a statically stable environment - at least shortly. The cloud air is warm compared to its environment, while rising, and warms if latent heat is released. Pressure perturbations with respect to a background state occur around such a cloud, due to temperature perturbations and motion associated with

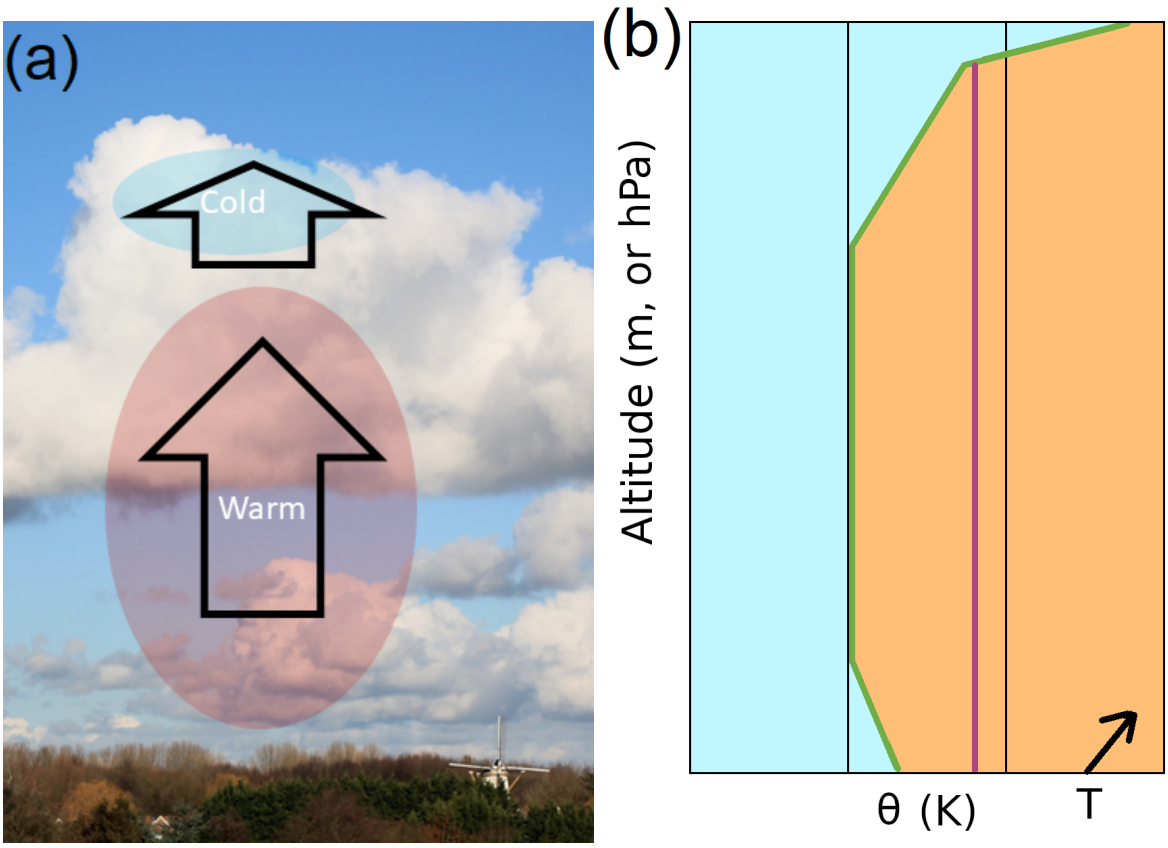

Figure 1.1: (a): Convective cloud (cumulus) with schematic indications of warm and cold anomalies, as well as arrows for vertical motion. Black outlined arrows indicate the relative motion schematically and transparent red (blue) indicate warm (cold) temperature perturbations with respect to the cloud's environment. The picture was taken in Rotterdam on the 2nd of February 2019 by the author. (b): Plot as typically used in atmospheric dynamics and meteorology when looking at convective motion, with on the y-axis the altitude in m or pressure in hPa (decreasing order) and black isolines of potential temperature (isentropes). An (approximately) conserved but varying quantity is displayed along the x-axis, here θ. As a result, isotherms are tilted (T). An environmental mean profile is depicted by the green line. To the right of it, parcels are cooler than their environment (light blue area) and to the left warmer than their environment (orange area). As a result of positive buoyancy, a random warm parcel at the surface may accelerate upward (violet; the parcel moves along this line if not diluted by environmental air). This parcel will stop accelerating and consequentially decelerate, once it meets the environmental temperature profile, at the top (green). If latent heat will be released by condensation, the parcel in violet will propagate upward and rightward, towards increasing temperatures and altitude. This is a typical way to display atmospheric profiles in meteorology. Similar profiles are used in this work.

the cloud [see for example Chapter 2.5 of Markowski and Richardson, 2010, Nascimento and Droegemeier, 2006, Morrison, 2016a, for a more in depth quantitative and theoretical treatment].
The pattern of relative motion and temperature perturbations with respect to its surroundings within a convective cloud is typically as shown schematically in Figures 1.1 and 1.2. Before the cloud initiates, a warm anomaly (perturbation with respect to a background mean state: here typical environmental air, Figure 1.1b, but usually mean or median of local climatological distributions) exists, leading to upward motion of positively buoyant air. At the same time, the warm anomaly reduces the mean density in the column, which also reduces the vertical integral of mass above the warm anomaly: a small-scale low pressure area is associated with the warm anomaly. This leads to convergent air motion towards the warm anomaly. While the air with warm temperature perturbation moves upward, it cools adiabatically (mixing neglected). At some point on its way up, it will meet a layer, with respect to which the parcel will have a cold temperature anomaly. That might be a *capping* temperature *inversion* topping the *planetary boundary layer*, any layer in the *free troposphere* that happens to be there, or the *tropopause* (see Appendix A for an explanation of those basic meteorological terms). With respect to this layer, the cloudy saturated air will become negatively buoyant very shortly after reaching this layer.
Strong upward motion occurs in the lower and/or middle region of the cloud (vertically), but air parcels are

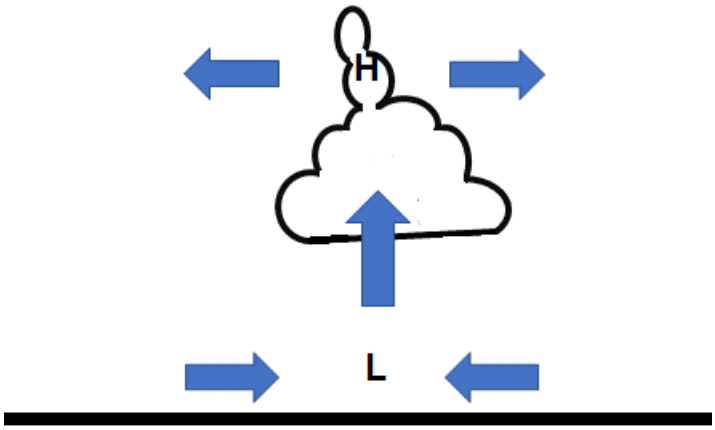

Figure 1.2: Schematic vertical cross section of relative flow and pressure anomalies induced by rising air and (usually enhanced) by the consequent heating pattern of a cumulus or cumulonimbus cloud. "H" indicates a high pressure anomaly and "L" a low pressure anomaly.

decelerated near the cloud top once the cloud meets the layer with respect to which it is negatively buoyant. That deceleration leads to an accumulation of air in the upper cloud region. However, the compression and accumulation is immediately followed by the formation of a region of high pressure and this is subsequently compensated by divergent motion in the horizontal plane, away from the cloud top. The origination of pressure perturbations can be described with equations, where regions of rotation and deformation are associated with low, respectively high, pressure perturbations. For the corresponding equations and their derivations one is referred to chapters 2.5 and 3.1 of Markowski and Richardson [2010] and Nascimento and Droegemeier [2006].
This type of motion (Figure 1.2) occurs in any convective cloud (cumulus, cumulonimbus) where the *updraft* (the core of the region of upward motion) is active. It is the divergent motion in the upper regions of deep cumulonimbus clouds reaching the upper half of the troposphere (as well as near-tropopause layers close to the interface between the troposphere and stratosphere) that will be studied Chapters 3 and 4. The predictability and variability of the magnitude of the mass divergence in different types of simulations of convective clouds will be assessed, in relation to other processes that are specific to the corresponding clouds: relations with specific precipitation rates (net latent heating), specific convective momentum transport (the momentum tendencies induced by vertical motion around convective clouds; introduced in detail in Chapter 2) and convective organisation/aggregation (also introduced further in the next section of this Chapter and continued in Chapter 2). The latter two are usually strong in mesoscale convective systems, but comparatively moderate or weak in an environment of few, isolated, cumulonimbus clouds.
Cumulonimbus clouds are more complicated than ordinary cumulus clouds in terms of associated flow. Once precipitation starts falling out of a convective cloud, evaporation occurs through latent cooling wherever precipitation reaches sub-saturated air (in terms of water vapour: relative humidity below 100%). *Downdrafts* are coherent downward air streams that usually contain precipitation or have contained precipitation. They may help organising convective systems, but may also help destructing convective clouds. Convective organisation could be seen as the tendency of cumulonimbus clouds to create a separate downdraft and updraft area within a cloud cluster, for example an MCS. Usually, good organisation is related to structured convergence and divergence zones and fosters convective aggregation of cumulonimbus clouds, maintaining spatial patterns within a precipitation system on time scales that exceed the lifetime of an individual cumulonimbus cloud (usually an hour or a bit less). For more in-depth introductory material on this topic, one is referred to Section 2.4.

1.3 Predictability of atmospheric dynamics

Predictability studies and descriptions of error evolution root mostly in the work of Lorenz [Lorenz, 1969a, 1963, 1996, 1969b,c] and rely on the important thoughts of Lorenz, that he disclosed in those studies.
Before moving to the actual matter of predictability and error, some definitions have to be introduced. Important is the method of ensemble forecasting, which is very widely used operationally for numerical weather prediction (NWP) [e.g. Bauer et al., 2015]. It is essentially a Monte Carlo method with a few dozens of meteorological simulations, where usually equally likely and closely related initial states of the

atmosphere at a given initial time are constructed from error distributions around observational constraints (data assimilation) that cohere in space and time [e.g. Miyoshi et al., 2014]. From these equally likely initial states, an NWP is run forward in time: often with the same governing (dynamical) equations, but sometimes (operationally) individual (e.g. unresolved, parameterised) processes may also be perturbed randomly [e.g. Ollinaho et al., 2017, Leutbecher et al., 2017]. For the remainder of this work, it can be assumed that initial states are perturbed, and the model evolution is not perturbed through any randomness in governing model equations.
If there are two NWP simulations in such an ensemble, their difference evolution can be calculated. This is also referred to as a possible error evolution. Lorenz was essentially the first scientist to compare the evolution of a pair of simulations - two ensemble members - doing the necessary assumptions (even though the representation of the atmosphere was highly simplified and idealised). To convert a difference evolution of a simulations pair into an error evolution, one has to do the *perfect model assumption* or the *perfect error assumption*: the physics and dynamics of the atmosphere is perfectly represented by the model (perfect model assumption) or the physics and dynamics of the error is perfectly represented by the model (perfect error assumption) [see Selz, 2019]. Both assumptions can be proven unrealistic if the scale of a phenomenon of interest has a scale small compared to the model grid. But at more than seven times the horizontal grid spacing of a numerical simulation, such an assumption becomes reasonable [Skamarock, 2004]. The assumption will be applied in part of this work and makes the evolution of error, spread and differences between ensemble members effectively equivalent.
Lorenz [1969c] described three methodologies, which have been used to study predictability of the atmosphere and have been key to the development of a couple sub-fields within meteorology since. Important are on the one hand the dynamical approach to predictability, the study of which was initiated with Lorenz [1969a], and on the other hand the empirical approach [Lorenz, 1969b, Van Den Dool, 1994], which lends well for many statistical and machine learning approaches, but can also be suitable for understanding specific meteorological phenomena [e.g. Weyn et al., 2019, Schulz and Lerch, 2022, Eisenstein et al., 2022]. In addition, both the dynamical and empirical approach have been highly important to the development of ensemble prediction much later. Ensemble prediction has led to many additional developments in meteorology, such as advanced data assimilation systems [e.g. Ghil and Malanotte-Rizzoli, 1991, Evensen, 2009, Bannister, 2017, Bauer et al., 2015].
However, restricting to the (for this work) more relevant dynamical approach to evaluate predictability: important (more practical) dynamical studies on predictability and errors have appeared only in the last two decades or so, since numerical weather prediction has bloomed and the use of ensemble prediction has become widespread. The more recent work has revealed that precipitation systems play an important role in error growth, with a large role for the parameterisation of deep convection (generating a substantial fraction of the precipitation in most state-of-the-art global simulations) in particular [e.g. Zhang, 2005, Zhang et al., 2007, Sun and Zhang, 2016, Baumgart et al., 2019, Zhang et al., 2019, Selz et al., 2022].

1.4 Scope of this work

1.4.1 Working assumptions from a convection point of view

In this work I would like to take a focused look at the predictability of deep convective divergent outflows in the upper troposphere. Hereby, I will illustrate the value of taking a conditional, essentially Bayesian, point of view. The viewpoint relies on conditioning on precipitation rate, or equivalently net latent heating rate, amongst others. These two are equivalent, if not using experiments to manipulate the specific heat associated with condensing 1 kg of water vapour (which is actually also done within this work) and if its small temperature dependency in the common tropospheric temperature range is neglected.
Taking this perspective, the implicit assumption will be done that any deep convective cloud produces non-negligible precipitation rates (at the surface!) and that its cloud top reaches the upper half of the troposphere. The troposphere is typically about 12 km deep in the simulation set-ups used in this work (see also Appendix A). If one makes use of this assumption, one important experiment is not considered, but ignored: an experiment with no precipitation, no convective outflows, no convective dynamics, no tropospheric divergent outflow and no way to generate variability in the listed quantities. This ignored $(0, 0)$ point in the space that is regularly presented in this work represents the case where insufficient buoyancy and forcing is available to produce deep convective clouds and accompanied dynamics. In some cases, buoyancy and forcing versus stratification may be in a subtle balance. Then, the possible occurrence of deep convection may very sensitively depend on the atmospheric state [e.g. Melhauser and Zhang, 2012].
Furthermore, shallow convection can occur, in which precipitation does not occur or otherwise is unlikely to reach the surface. In the circulation generated with this type of convection, the upper troposphere is usually not affected, unless over a highly elevated continental land mass. Similar circulations systems have recently been identified George et al. [2021, 2022] and are the small cloud equivalent of circulation investigated here.

However, here the focal point is the branch that consists of upper tropospheric divergence.
By investigating how the strength of upper tropospheric divergent outflows from deep convection relates to the state of convective organisation and varies among three types of model representations of deep convection, it is likely that some common conclusions on upper tropospheric divergent outflows from deep convection can be found among at least two of those representations of deep convection. Furthermore, using anterior knowledge on representation of (deep) convective flows in NWP, estimates can be made on how likely conclusions are to hold in the real world.
Analysing convection from the perspective used here, an implicit analysis is done on how processes targeted at, namely convective organisation, cloud geometry (see Chapter 2), and convective momentum transport (see also Chapter 2), can affect the coupling between convection and dynamics (Chapters 3 and 4). This means that convection does not only mix air masses, but also forces a flow pattern: through its precipitation and associated latent heating [e.g. Moncrieff, 1992, Schumacher et al., 2004, Hoskins and Yang, 2021]. In this work, not all aspects of variability in upper tropospheric divergent outflow from deep convection can be assessed simultaneously in much detail. The main focus is on the magnitude of these outflows, especially in the first two studies presented (Chapters 3 and 4). The variability in outflow altitude is mostly documented in these chapters, but is by setting a fixed integration mask in the vertical not evaluated directly in much detail. However, setting the bounds of this mask will be covered in the presentation and discussion. Additionally, relations to existing literature in this regard are also discussed. Furthermore, in the third study (Chapter 5), divergent outflows will not be the core topic, but it is implicitly investigated. Vertical penetration of deep convection in 2D of a so-called *squall line* of infinite length is treated somewhat more explicitly, including consequences for flow perturbations resulting from the deep convection, but still not a core topic. Nevertheless, an impression of the variability in altitudes of divergent outflows of deep convection under certain conditions can at least *roughly* be obtained with the results presented in this work.

1.4.2 Relevance of predictability studies and their working assumptions

The work is also motivated in connection to Baumgart et al. [2019]. The methods and findings of the Baumgart et al. [2019] study are in general a major motivation for various projects in Research Area A of Phase 2 of Wavestoweather, including this work. A key point from Baumgart et al. [2019] is that it illustrates that for an NWP ensemble with initially very tight spread in the atmospheric states, the parameterised effects are most influential to the (near-tropopause) difference growth diagnostic based on potential vorticity[1], which is probably the most important quantity in the field of atmospheric dynamics (at least outside of the tropics). Here, difference growth refers to the difference in state between a pair of ensemble members, which under the condition of a *perfect error assumption* also represents errors. Parameterised deep convection tendencies make up the largest contribution to error or difference growth among all tendencies, initially. Subsequently, after 12-48 hours, the divergent components of the wind dominate among the contributions to difference growth diagnostics (Figure 1.3). This has led to the hypothesis that convective systems, releasing latent heating and thereby initiating divergent motion, are of major impact on initial differences between a pair of ensemble members [Baumgart et al., 2019] in an initially (very) tight ensemble - one with initially a strongly reduced spread compared to the average of current operational forecasts [Selz et al., 2022]. According to this hypothesis, from a dynamical point of view, the divergent winds at the top of deep convective systems provide a feedback to their surroundings [Baumgart et al., 2019]. The possibility to predict the magnitude of such feedbacks is assessed in this work. The conditional variability and conditional stochasticity of the feedback under a subset of conditions is closely related to that possibility.
Subsequently, Selz et al. [2022] showed that the initial condition uncertainties in current operational systems are typically about five to ten times larger than those in which the convection parameterisation becomes dominant in an initial error growth stage. In the works by Baumgart et al. [2019], Selz et al. [2022] stochastic convective parameterisation has been used to represent deep convection: the mass of air transported vertically by a collection of cumulonimbus clouds in a horizontal area is randomly drawn from a distribution [Craig and Cohen, 2006, Plant and Craig, 2008]. Within this work, some of the implications of representing deep convection with a fundamentally similar non-stochastic parameterisation can also be illustrated [see Plant and Craig, 2008, Keane et al., 2014, for an elaborate technical discussion on the stochastic parameterisation]. On the other hand, this work will be of large benefit to the understanding of stochastic and systematic variability in upper tropospheric divergent outflows, which may improve future perturbation strategies around deep

[1]Potential vorticity is a dynamical quantity describing the ratio between absolute vorticity and stratification of the atmosphere. Using that quantity, one could in theory predict the large-scale dynamics of the atmosphere infinitely ahead, if there was no coupling to the small-scale dynamics leading to violation of the necessary assumptions, and, if its spatial distribution was known with infinitely high accuracy. However, due to the presence of to small-scale dynamics, limitations of computation accuracy and tendencies due to heat exchange between molecules (e.g. radiation, precipitation processes), such prediction is not possible. For the understanding of this work it is not essential, but it is essential for the understanding of many of the cited works in this section.

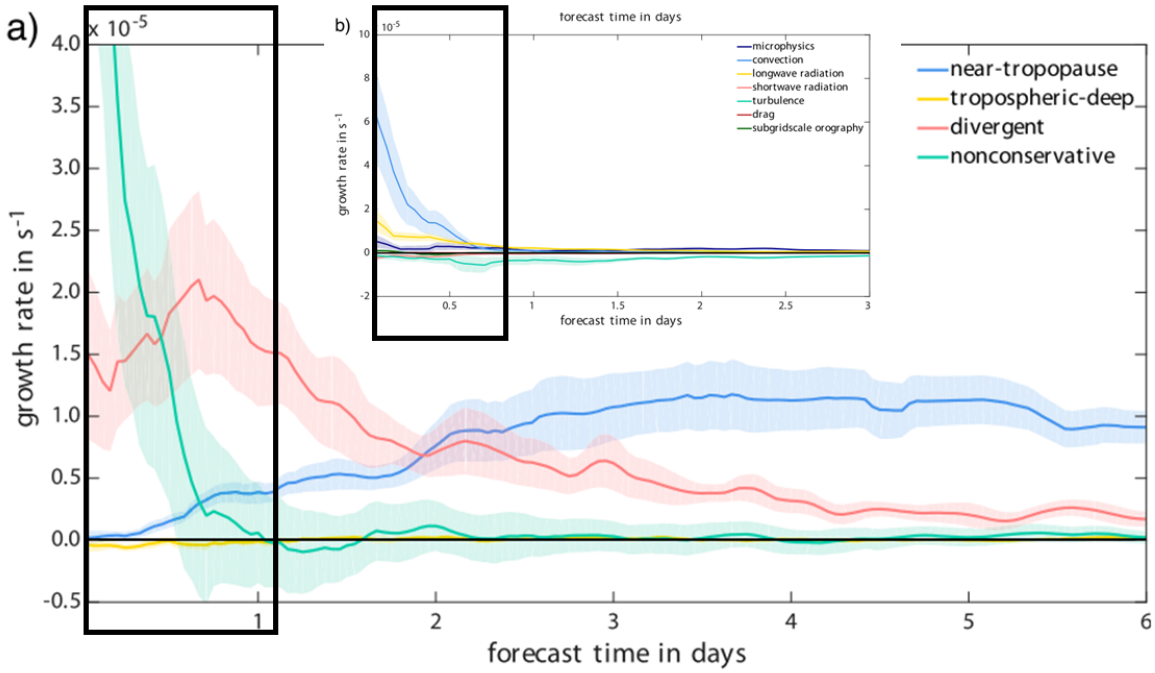

Figure 1.3: © American Meteorological Society. Used with permission. Taken from Baumgart et al. [2019] (Figure 7). Figure (a) represents the dynamical processes that correspond to the highest error growth rates and thus dominant error sources in their potential vorticity based framework. Figure (b) splits off the contributions of "non-conservative" in Figure (a): here, parameterisation tendencies originating from the deep convection scheme dominate on the first day (figure (b)). Non-conservative terms are overtaken by divergent modes of the wind on the later part of the first day and the second day (Figure (a)). It is the interaction between those two, the deep convection and resulting divergent winds, that is investigated in Chapters 3 and 4.

convective systems in some targeted (predictability) studies. Moreover, possible implications for error growth studies like those of Baumgart et al. [2019], Selz et al. [2022] when deep convection would have been resolved explicitly instead may be illustrated, and, eventually, understood with methods and insights based on this work.

1.4.3 Structure of this work

After further background on convection and atmospheric dynamics (Chapter 2), the main content of this work consists of three major studies, presented in Chapters 3, 4 and 5. The main studies are followed by overarching conclusions in Chapter 6 and another Chapter, 7, with a short review of further (potential) implications of the three studies. In Chapter 3, an attempt is made to understand upper tropospheric divergent outflows from deep convection theoretically in detail, using the most sophisticated state-of-the-art numerical models to represent deep convective systems: cloud resolving Large Eddy Simulations (LES) in Cloud Model 1 (CM1), [Bryan, 2019], in which the very largest turbulent scales (1-2 km) within an environment of deep convection are resolved, but most of the turbulence is still parameterised. Here, important dependencies of the outflows on convective organisation, latent heating rate and convective momentum transport are investigated by applying ensemble and physics perturbations to four types of idealised convective systems in LES. Then, findings about the representation of these outflows in model CM1 will be used for a follow-up study. In that study, a comparison is made between two representations of divergent outflows from deep convection in the ICON model [Zängl et al., 2015, Giorgetta et al., 2018] (Chapter 4), an operational forecasting (NWP and climate) model used by Deutsche Wetterdienst (the German national weather service). A case notorious for the Munich Hail Storm [also studied in e.g. Wilhelm et al., 2021, Barthlott et al., 2022a,b] will be analysed, covering Central Europe: the day and night of June 10^{th} and 11^{th} 2019. Simulations in which convection is parameterised ("PAR") in a global setting with 13 km nest[2] over Europe and simulations with a convection-permitting local area model ("PER") over a subdomain of Central Europe will be analysed. The global

[2]A nest refers a smaller simulation domain of an NWP simulation embedded within a larger domain, with a feedback at the boundaries of the larger and smaller domain in both directions. A Local area model (LAM) refers to a smaller simulation domain that only depends on the larger domain through a feedback at the boundary via lateral boundary conditions.

simulation with nest has also been repeated with explicit representation of deep convection at 13 km grid spacing (i.e. the parameterisation is switched off). Both studies will use a box approach, in which the upper tropospheric divergence around a set of (mesoscale) convective systems is integrated over a predefined mask in the upper troposphere - the same for each ensemble member. The analysis based on simulations of the local area model is done with a moving box and will be presented in Chapter 4. The box analysis can illustrate the main dependencies of the outflows from deep convection on processes occurring within the convection.

Subsequently, an analysis of the evolution of the growth of ensemble spread in a subset of the investigated LES is presented in the following chapter (Chapter 5), thereby leaving the box approach for a full domain assessment. The evolution of the ensemble spread in that subset of the simulations will illustrate some processes responsible for error growth in organised convective systems. Simulations of so-called *squall lines* (a specific linear form of strongly organised convection) will be used, as they have a symmetric quasi-2D geometry. These 2D properties have been explored in studies by Moncrieff and co-authors [e.g. Moncrieff and Miller, 1976, Moncrieff, 1978, 1981, 1992] and Trier et al. [1997]. The form of quasi-2D convection lends very well for such an analysis, because a system of this type has often homogeneous properties along the third axis over an extended length, especially when averaged over larger along-system scales. It will be illustrated that the differences in the LES ensemble grow through specific dynamical processes and that there is a time scale on which the ensemble spread has memory for convective dynamics, but not for preceding gravity wave dynamics.

Gravity waves and their relation with convective clouds will now first be introduced in the following Chapter (Chapter 2), together with some other important processes in (mesoscale) dynamical meteorology, including a short discussion about why deep convection organises into convective systems.

2 Background on mesoscale atmospheric dynamics

2.1 Aspect ratio in atmospheric motion

Motion in the atmosphere can be subdivided into two classes in several ways. In this work, it is generally assumed that rotational effects and consequent apparent accelerations (Coriolis terms in a rotating frame of reference) are unimportant - convective systems are studied on time scales up to a few hours after initiation, rather than about half a day and beyond. Therefore, more relevant here is the subdivision into a quasi-2D class of large-scale atmospheric dynamics in quasi-horizontal directions, in which vertical accelerations are negligible, and a turbulent 3D regime at smaller scales. Dynamics of convective systems mostly coincides with the larger length scales of 3D turbulent motion.
The existence of these two regimes can empirically be derived by replacing all terms in the Navier-Stokes equations in a rotating framework with two substitutes: the appropriate scaling terms and variables of order one. Similarly, without setting any scales in advance, the same derivation can be done. After the procedure, constraints on the relative magnitude of terms in the equations can be deduced, leading to dimensionless numbers as the Rossby number, aspect ratio of flows and Reynolds numbers, amongst others. Such a procedure is beyond the scope of this work; an example of the procedure can be found in most atmosphere and ocean dynamics lectures or books, e.g. Cushman-Roisin and Beckers [2011] (Chapters 2-4). However, among the dimensionless quantities mentioned, the aspect ratio is the one that separates the quasi-2D and the turbulent 3D regime.
The quasi-2D and 3D regimes are not truly separated [as one could simply argue based on e.g. Gage and Nastrom, 1986, Durran and Gingrich, 2014, Craig and Selz, 2018]: at the 1000 km scales, one can simply assume that motion is (quasi-)2D, as the troposphere is on the order of 10 km deep and vertical acceleration is negligible (*hydrostatic assumption*). At scales of order 10 km and less, atmospheric motion clearly becomes 3D and vertical acceleration may be of a similar magnitude as the horizontal one. At intermediate scales of several dozens or a couple of hundreds kilometres, the validity of the hydrostatic assumption may sometimes become questionable, depending on the practical or research interests. However, it is known that the dominant sources of vertical acceleration at those scales involve deep convection - mesoscale convective systems - and to a lesser extent also so-called gravity wave dynamics (Section 2.3) [Houze, 2004, Bretherton and Smolarkiewicz, 1989, Craig and Selz, 2018]. Non-negligible vertical accelerations that act on length scales of several dozens to a couple of hundred of kilometres involve well-developed mesoscale convective systems in practice (and still, average vertical velocities and associated vertical accelerations remain rather limited compared to actual updraft cores). This roughly coincides with the middle ranges of the mesoscales of atmospheric dynamics (full mesoscale runs from ≈ 1 km to ≈ 1000 km).
Given the aspect ratio of atmospheric motion shifting from the limit of nearly 0 to order 1 on the aforementioned length scales, only around convective systems and for even smaller scales as the planetary boundary layer (order 1 km), one could say that vertical advection has a similar magnitude as horizontal advection, if the gradients in any atmospheric property $\phi(x, y, z, t)$ are similar in the horizontal and vertical ($\frac{\partial}{\partial z} \approx \frac{\partial}{\partial y} \approx \frac{\partial}{\partial x}$). However, typically, vertical gradients are also larger than horizontal gradients in the troposphere and vertical advection is likely to dominate out of the two in case of aspect ratios close to 1. In the next section, consequences of the aspect ratio shift for mixing of momentum will be contrasted.

2.2 Mixing of momentum in the atmosphere

In principle, momentum mixing could take place on any scale and in any direction. The presence of a momentum gradient in at least one direction is required. Nevertheless, the aspect ratio of atmospheric flows imposes some constraints on momentum mixing: at very large scales, only quasi-horizontal momentum mixing could take place. However, typically, gradients are small at these scales - as implied by long time scales and the nearly geostrophic character of the flow, which is divergence-free in the purely geostrophic limit. Implicitly, gradients leading to deformation of parcels is very limited on the very large scales, which can also be induced from corresponding dimensionless numbers (as mentioned in the previous section). Mixing through viscosity or *apparent, effective* viscosity [Pope, 2000] - as induced by turbulent characteristics of the flow - is not important within the large-scale quasi-2D atmospheric flow regime.
At smaller scales, momentum mixing can occur effectively through gradients in the flow. Importantly, the strong vertical motion associated with deep convection (including mesoscale convective systems) drives an exchange of momentum between the lower troposphere and the upper troposphere [e.g. Badlan et al., 2017, Houze, 2004, Moncrieff, 1992]. The momentum mixing through vertical gradients can take place at the scale scale of mesoscale convective systems, because it is the largest scale process (horizontally) in which vertical acceleration becomes relevant - it is the largest scale horizontal process in which the aspect ratio shifts away from near-zero values, towards 1.
Other types of atmospheric motion in which momentum mixing takes place, are shallow convection and

motion in the planetary boundary layer [e.g. Brown, 1999, Schlemmer et al., 2017, Dixit et al., 2021, Salesky et al., 2017]. The vertical advection terms of momentum in an environment of deep convection are driven by deep convective systems and - related (in the presence of deep convection inseparable) - boundary layer dynamics. Hence, one could say that vertical mixing of momentum in the presence of deep convection can largely be attributed to the process of (deep) convection and associated convective systems. The vertical advection term of horizontal momentum will be perturbed in experiments of Chapter 3 and it will often be referred to as convective momentum transport (CMT), of which it is arguably usually the dominant component within a region of deep convective cells [see also Houze, 2004]. Together with pressure induced accelerations, CMT predominantly accelerates air in (mesoscale) convective systems [Badlan et al., 2017, Houze, 2004, and references herein].

2.3 Linear model of gravity wave adjustment to a heat pulse

2.3.1 Mechanism of gravity waves

Gravity waves are very well known from the sea surface and from their occurrence at a water surface, for instance when a stone has fallen into a pond. They also occur internally in fluid continua as the ocean and atmosphere.
If a parcel of fluid is displaced vertically, either convective adjustment or gravity wave adjustment will occur. Which of the two occurs, depends on the static stability of the fluid: the natural tendency to buffer or intensify vertical motion, which depends on $\frac{\partial \theta}{\partial z}$.
However, even if there is a natural tendency to accelerate upward vertical motion, a parcel will accelerate and at some point meet another environment, where deceleration occurs: the vertical motion is buffered by that layer. In a statically stable environment vertical motion slows down, but even if the environment below is statically unstable (or nearly neutral) and convective clouds have developed below, some gravity wave adjustment will occur. In case of a convective cloud field with small heating rates or an extent that approaches an infinite length scale, the associated gravity wave adjustment may be negligible in practice.
Essentially, gravity induces an adjustment in the continuum wherever waves are triggered, which have a propagation velocity as a function of vertical and horizontal wavelengths and stratification (static stability, vertical gradient of θ). Density perturbations with respect to the reference density at given altitude result in vertical acceleration, and together with inertia lead to oscillations of parcels: the wave motion (Figure 2.1). The parcels themselves do not move along with the wave signal. The signal is transferred by the density perturbations with respect to their surroundings and consequential vertical acceleration tendency.

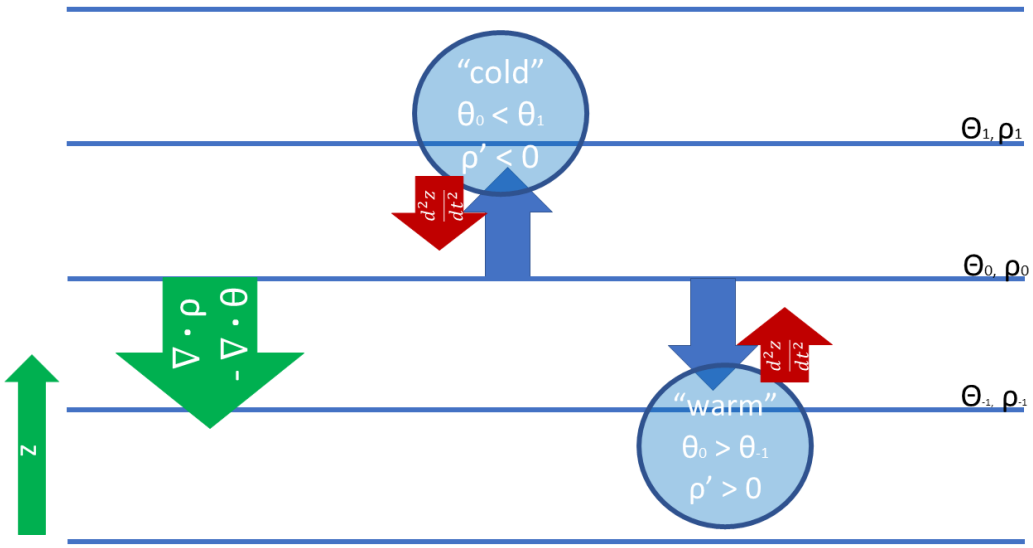

Figure 2.1: Restoring mechanism of gravity waves in a statically stable atmosphere, with isolines representing environmental mean density and potential temperature. Blue arrows indicate displacements and red arrows acceleration by gravity. The green arrows indicate orientation of the axes.

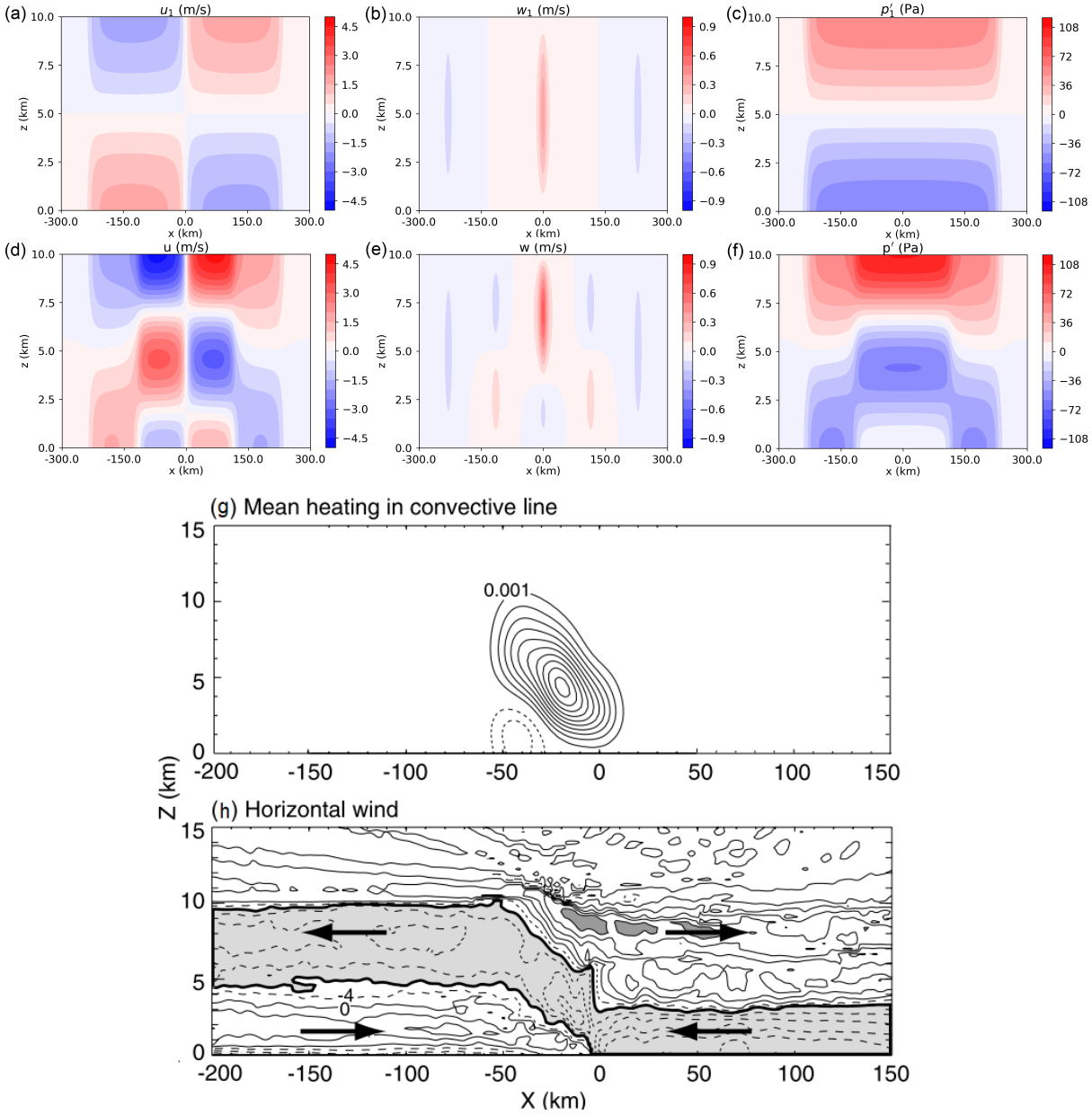

Figure 2.2: Panel of six (top, a-f) and two (bottom, g-h) vertical cross sections - (a-f): horizontal flow (a), vertical flow (b) and pressure perturbations (c) in the presence of continuous heating and a rigid lid top boundary, adjustment with only and first two gravity wave modes (d-f; same sequence of variables) after 2h; adapted from equations 12-15 and Figures 3 and 5 in Nicholls et al. [1991]. Bottom (g): localised thermal forcing (thick solid contours, top > 0, dashed < 0) to approximate real squall line flow, with corresponding flow below (h). Data and content (g and h) from Pandya and Durran [1996] as adapted in Houze [2004] and adapted further by the author.

2.3.2 Convective systems as heat pulses in a linear gravity wave response

Even though convective adjustment is the first of the two adjustment mechanisms in response to density perturbations - the one where acceleration of parcels persists for at least a short while - those perturbations may directly trigger the second of the two adjustment mechanisms: gravity waves.
Work fundamental for the interpretation of simulations in the following Chapters has been done in the late 1980s and 1990s [Bretherton and Smolarkiewicz, 1989, Nicholls et al., 1991, Mapes, 1993, Pandya et al., 1993, Pandya and Durran, 1996], with some related studies appearing recently [e.g. Bierdel et al., 2017, 2018, Adams-Selin, 2020a,b, Weyn and Durran, 2017]. The basic concept is that a warming tendency, representing the latent heating by cumulonimbus clouds as a localised heat source, continuously creates temperature and pressure, hence density, perturbations. Even though convective adjustment requires local convective instability, this convective instability can be very restricted spatially [see Pandya and Durran,

1996]. A continuous stream of upward moving parcels in a convective system results in continuously generated perturbations, leading to gravity wave adjustment within the convective system and in the surrounding atmosphere (Figure 2.2a-f). The flow that arises as a consequence of such an adjustment mechanism in the plane perpendicular to a quasi-2D convective system (mostly: squall line) contains the divergent outflow from deep convection and has been investigated in Nicholls et al. [1991], Pandya and Durran [1996]. In the first of the two references, explicit expressions for the linear component of the gravity wave response to prototype localised heating pattern are derived. Work by Pandya and Durran [1996] using a more advanced numerical simulation technique shows that the linear model by Nicholls et al. [1991] contains the dominant contributions to the resulting flow (linear terms) and that the omitted terms are comparatively less important. Furthermore, Pandya and Durran [1996] argue based on the superposition principle that if a prototype heating pattern (Figure 2.2g) is inserted, the model contains a flow response closely resembling the flow in a realistic squall line (Figure 2.2h).
One may wonder why an obvious wave signal is missing in the flow responses shown in Figure 2.2a-f. Adjusted atmospheric states do not bounce back to a background state, but are maintained for some time. Then, a secondary wave comes in (travelling at half the speed of the original wave and with a vertical wavelength half as long) and adjusts the atmospheric state again, which is subsequently maintained again for some time at any inner location ($X < 100$ km) (Figure 2.2d-f). The reason for maintenance of perturbed states is that the "convective system" as represented by a heating signal is switched on initially and then maintained. As a result, buoyancy and pressure perturbations travel outward and remain constant in this 2D set-up as long as the (constant) localised heat source is continuously present. The outflow pattern in Figure 2.2a/d is maintained, until the convective heating source is switched off. The role that fluctuations in the intensity of a convective system (or lack of them) play, has recently been documented and explained in Adams-Selin [2020a,b].
The positive heating branch of the flow recognised in Figure 2.2g compares to a limited extent to that associated with the consequence of temperature perturbations in Figure 1.2. Nevertheless, Figure 2.2g depicts a more advanced heating pattern due to the tilting of the positive heat source and heating patterns and temperature anomalies do not match one to one. The works and model discussed in this section will be an influential benchmark for the next Chapters, as it provides a background understanding of divergent outflows from deep convection.

2.4 The tendency of convective systems to organise and aggregate

Various mechanisms lead to the tendency for convective clouds to organise into varying types of convective systems. The term *squall line* has been introduced in Chapter 1, but additional modes of organisation include the *supercell* and other types of *multicells*. In case of the supercell, rotation and a vorticity centre aligned with the main updraft(s) plays an important role in the dynamics of the convective system: the aligned vorticity centre creates a persistent updraft at a specific relative location within the deep convective cloud system.
If deep convection does not organise into a coherent cell structure, a cumulonimbus cloud may be called a *single cell*. The term *multicell* is used to accentuate the contrast between any *single cell* convective system and other convective systems that consist of multiple cellular elements, which represent individual cumulonimbus clouds. Multicell cumulonimbus clouds often have a moderate or strong degree of organisation, where updrafts of individual cumulonimbus cells structure coherently in some way, creating a sub-region of updrafts. The same may also hold for one or multiple structured coherent sub-regions of downdrafts. However, once the multicell fulfils the definition of another subcategory of convective systems, i.e. supercell or mesoscale convective system (of which squall lines are a subcategory), systems are usually referred to as such. Larger supercells or collections of supercells may also be considered (part of) a mesoscale convective systems, as their *anvils* (icy shield near the cloud top of some cumulonimbus clouds) can incidentally grow sufficiently large. For an elaborate discussion on the formation and dynamics of the mentioned types of deep convective cells, one is referred to Chapter 8 in Markowski and Richardson [2010] and Houze [2004].
Convective systems tend to organise in various ways and there is a gradient in acting mechanisms between the tropics and higher extratropical latitudes.
One of the mechanisms that can organise convection is actively driven by **gravity wave dynamics** [e.g. Mapes, 1993, Lane and Reeder, 2001, Stechmann and Majda, 2009, Grant et al., 2018, Adams-Selin, 2020a,b]. The propagation velocity of gravity waves having different vertical wavelengths is inversely proportional to their wavelength [e.g. Grant et al., 2018], as counted over twice the vertical depth of the troposphere; so $n = 1$, $n = 2$ and $n = 3$ are nearly always or usually fast enough to propagate away from the convective system, in the presence of a typical background flow. These first few vertical modes of propagating gravity waves create regions of preferred upward motion (see also Figure 2.2b/e) and of preferred positive / negative temperature anomalies in the lower and upper troposphere, hereby increasing / reducing the tendency of

deceleration of upward moving parcels in certain layers (i.e. *convective inhibition (CIN)*) and modifying the *convective available potential energy (CAPE)*[3]. As the gravity waves propagate over an area, conditions can alternate between more and less favourable conditions for the initiation of deep convection (compared to the background state). Consequently, moving spatial patterns of locations favourable and unfavourable for convective initiation occur around pre-existing convective systems.

Another mechanism that may assist convective systems forming an organised structure is vertical wind shear, or simply **wind shear**. This is a particularly important mechanism at mid-latitudes, as wind shear is typically much smaller in the tropics. If deep convective clouds (cells) develop, their upward motion is amplified and partly driven by the latent heat release within the cloud, as released by condensation. As more condensate (possibly forming liquid water and ice, snow, hail and so-called *graupel* upon freezing) accumulates within the cloud, the mass of total condensate also increases. This condensate will partially fall out, with as a result downward acceleration induced by the water mass accumulation. The downward acceleration opposes the prior upward acceleration by positive buoyancy. As the downward motion and fall out of precipitation particles occurs, the updraft is basically destroyed, if it occurs at the same location (cooling of evaporating/sublimating precipitation will also help). However, vertical gradients in the wind speed and direction (wind shear) can displace the condensate (hydrometeors) with respect to the updraft and move the precipitation away to another location by relative motion. Fall out of precipitation will lead to evaporation below the (convective) cloud and induce cooling tendencies at low levels. So-called **cold pools** may form and on their turn also focus dynamic structures: motion in cold pools is usually divergent at low levels. Subsequently, convergence zones that arise at the edge of cold pools may lead to structured low-level vertical motion. Consequently, new initiation of deep convection - organisation by cold pools - may also be considered a separate mechanism leading to the organisation of convection.

Absence of wind shear may destroy cumulonimbus clouds, but too strong shear may also lead to very strong mixing and dilute convective clouds so strongly, that they may also disappear completely. For a more elaborate discussion on wind shear, cold pools and their roles in convective organisation, one is referred to work by Weisman and Klemp [1982], Rotunno et al. [1988], Coniglio et al. [2006], Markowski and Richardson [2010] (Chapter 8, and references herein) and many others.

Another mechanism that can lead to the tendency of deep convective clouds to organise into aggregated areas is the **warming and moistening of the boundary layer over larger regions**, and strongly related convergence of moisture [see Arakawa, 2004, Muller et al., 2022, for reviewing material][4]. Naturally, water vapour is brought into the atmosphere by evaporation from ocean and land surfaces and transpiration from vegetation and other organisms. Large-scale warming and moistening may exceed the cooling rate by radiation loss. The atmosphere will become statically unstable with respect to upward motion at places and convective clouds can be *forced* to initiate over somewhat larger regions and cooperate.

Convective organisation and aggregation is an active field of research and for a broad contemporary review on the topic, one is referred to Muller et al. [2022] (with many interesting references herein). Structures seen in deep convective clouds are inexhaustible - the core of the concept is that convective organisation and aggregation is the natural tendency for convective clouds to occur in the inexhaustible set of different formations, and often structure updrafts and downdrafts in coherent regions. The tendency towards well-aligned updrafts (downdrafts) demonstrates particularly strong degree of convective organisation. Often, multiple of the mechanisms introduced in this section can affect convective organisation simultaneously.

A major interest of this work is understanding the impact of convective organisation on the magnitude of upper tropospheric divergent outflows from deep convection. This can be motivated by the simplified understanding of divergent outflows in the upper troposphere that Bretherton and Smolarkiewicz [1989], Nicholls et al. [1991] provided, together with the still simple representation of flow around a squall line or 2D convection in Pandya and Durran [1996], Moncrieff [1992]. A configuration in which convective cells interact and cooperate can be understood much better these days with high resolution large eddy simulations. In these high resolution LES simulations, convective organisation and aggregation is represented in much detail: essentially all atmospheric processes can be incorporated that fall within the range of scales represented (from $7\Delta x$ up to domain length).

2.5 Tropopause as barrier: divergence profiles for deep convection (example)

Before moving to the main content of this work, the course of a vertical divergence profile for a typical deep convective system has to be discussed. A detailed inspection of such profiles and their relation to the condensation profile is and has been necessary to understand and interpret the connection between different

[3]Both CAPE and CIN represent vertical integrals of buoyancy for initial parcels that are vertically displaced, when no mixing with the environment is assumed

[4]However, one could say that moisture convergence is often associated with some of the other mechanisms discussed as well, but the horizontal scale over which the moisture convergence occurs is typically much smaller for, for instance, convective organisation by cold pools

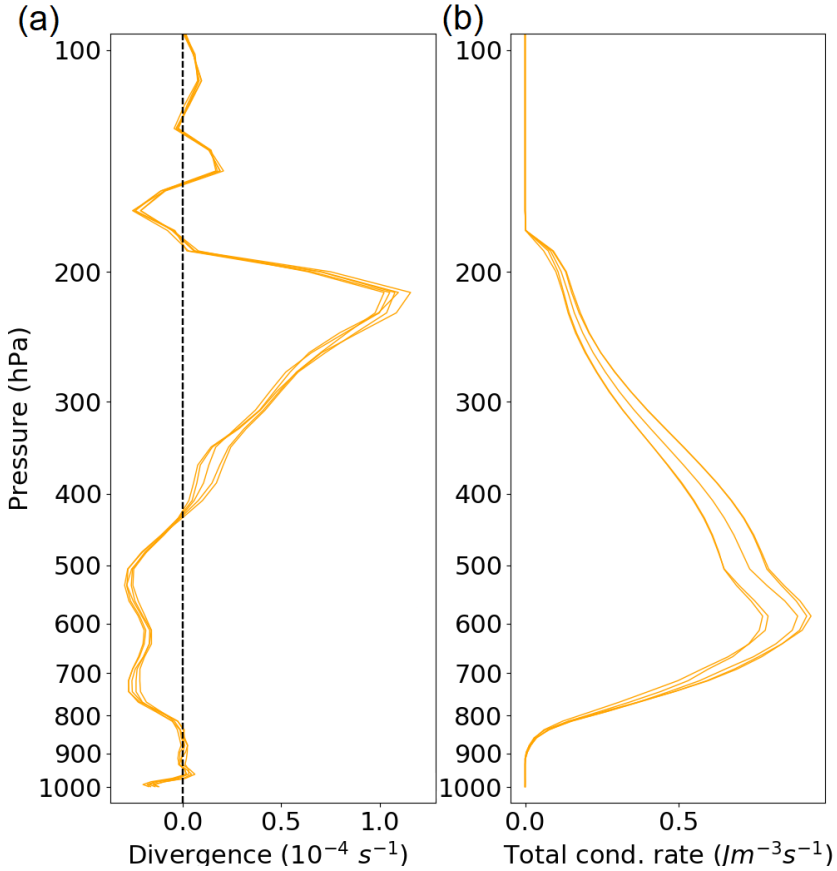

Figure 2.3: Vertical profiles of divergence (a) and condensation rate (b; including vapour deposition onto pre-existing hydro-meteors) for an example convective system included in the later parts of this thesis. Five ensemble members are displayed.

simulations constantly, throughout the project.
Many profiles have been inspected to create this work, but the profiles have often been omitted or only included in appendices of this work. The divergence and condensation profile for five ensemble members that over an area that represents one of the convective systems to be analysed in this work is depicted in Figure 2.3. The simplified model represented in Figure 2.2a-f is a benchmark: there, an eastward wind is found in the "upper troposphere", with the "tropopause" represented by a rigid lid in this case. The divergence occurs in the upper 2-3 km and lower 1.5 km, if one considers that the convective system is located at $x = 0$ km. Around 4-5 km, convergence occurs: westward winds. Similarly, going from left to right in Figure 2.2h, divergence away from the system in the centre takes place near the top of the heat source (outlined with black box), roughly in the upper half of the plot. The maximum of divergence probably occurs somewhere at 8-10 km altitude. Convergence roughly occurs in the lower vertical extent of the plot, $z < 4km$. The general pattern is what could have been expected based on 1.2.
In practice, Figure 2.3a shows that the divergence indeed occurs above and at the top of the source of latent heating (Figure 2.3b). However, a prominent maximum occurs close to 200 hPa. This maximum is to be expected when deep convection is intense and cumulonimbus clouds collide with the tropopause. The tropopause consists of a strong barrier - it is not a true rigid lid as in simplified studies [e.g. Nicholls et al., 1991], but nevertheless a discontinuity on top of the free tropopause layers with nearly constant stratification (static stability, $\frac{\partial \theta}{\partial z}$).
If one would imagine convective clouds as a huge balloon of air, with a large mass, this mass "collides" with the tropopause. The large mass decelerates quickly and has to spread out horizontally, as it is positively buoyant with respect to the layer below (at least part of the mid-troposphere) and negatively buoyant with respect to the layer above (stratosphere): it diverges just below and at the tropopause. This shape of the divergence profile is very typical for the outflow of deep convective clouds. For shallower convection, the outflow does not collide with the tropopause, but convective overturn takes place fully within the planetary boundary layer and the lower free troposphere. Given the relatively constant stratification ($\frac{\partial \theta}{\partial z}$), the shape of the outflow profile tends to be more symmetric instead of highly skewed in the vertical.
The sudden deceleration imposes a potential sensitivity: the destination of any convected air mass may

sensitively depend on initial potential temperature and moisture and the profile near the tropopause. Near the tropopause, there is a large gradient, especially in terms of potential temperature. Outflow at that gradient is a potential source of simulation errors, but in this work the potential temperatures and altitude at which outflow takes place is not a main concern. The main focus is the magnitude of the (mass weighted) divergence, which is integrated and averaged over selected levels in the upper troposphere.
The levels over which deep convective outflow is integrated vertically are usually set such that the upper bound of the integration mask lies in the lower part of the stratosphere - just above the tropopause barrier - cause much air departs convective cells only in the near-tropopause region. The lower bound is set at levels of typically about 400 hPa (about 7 km), where the level of neutral divergence is often located. It will be shown in Chapters 3 and 4 that an integration mask is set optimally this way.
Consideration of the condensation profiles has also been important in the aforementioned chapters: if a convective system gets stronger, a stronger latent heating source is implied and more latent heat is released. Divergence will often be normalised with respect to the net latent heating source, as expressed by column precipitation rate (Chapter 4) or net latent heating (Chapter 3), which are in real life equivalent: 1 mm/h precipitation rate is equivalent to a latent heat flux of 695 W/m2.

2.6 Further motivation

2.6.1 Representation of deep convection in numerical weather prediction

Currently, an important change is taking place in numerical weather prediction: the point is reached where deep convection and consequent mesoscale convective systems that form can be largely resolved explicitly with available computational resources at domains covering the whole globe [Bauer et al., 2015, Judt, 2018, Satoh et al., 2019, Brown et al., 2022]. Global so-called *convection-permitting* numerical simulations are about to become feasible [Brown et al., 2022] for operational purposes and have become increasingly common [see Satoh et al., 2019, for an overview]. Whereas classically, parameterisations were needed to represent deep convective processes in global simulations [e.g. Arakawa, 2004, Bechtold et al., 2014], numerical grids in weather simulations are becoming finer as a result of availability of increasingly large computational resources. Grid spacings of about 2-4 km or finer are required to fully replace parameterised convection in a numerical model [e.g. Weisman et al., 1997, Skamarock, 2004]. At that grid spacing, motions at length scales of typical cumulonimbus clouds (10 km) start to be sufficiently well resolved at the native model grid.
Nevertheless, when moving towards much finer grids, cumulonimbus clouds still benefit from representativity issues [e.g. Bryan et al., 2003, Hanley et al., 2015]. The root sources of improvements at grid spacings on the other of 100-250 m are typically attributed to improved representation of turbulence and associated sub-cloud scale mixing [Bryan et al., 2003, Hanley et al., 2015, Varble et al., 2020], which is strongly coupled to deep convection and mesoscale convective systems (see also Groot and Tost [2023] (Chapter 5)).
The main objective of parameterising deep convection has traditionally been to represent its mean effect on physical and dynamical atmopsheric processes, affecting the large synoptic flow [e.g. Craig and Cohen, 2006, Arakawa, 2004, and references herein]. Those atmospheric processes include the heating effect of deep convection and the production of precipitation, as well as mean upward motion in (sub-grid) convective clouds. Furthermore, adjustment of coupled processes is achieved - for example some mean effect on nearby horizontal atmospheric motion (as for instance explained in Section 2.3). Together, the effects are called convective adjustment. Attempts have been done to represent conditional variability associated with convective adjustment, as imposed by for example the process of convective organisation [e.g. Moncrieff, 1992, 2019]. In spite of these attempts, they have not lead to widespread explicit representation of convective organisation in deep convective parameterisations of operational numerical weather prediction models [Bechtold et al., 2014].
In convection-permitting numerical weather prediction set-ups deep convection is explicitly resolved. The atmospheric motion as a consequence of deep convection is directly coupled to, and thus solved by, the so-called *dynamical core* of the model. Adjustments occur spontaneously, as a result of the direct coupling.
The representation of deep convective systems in state-of-the-art numerical weather prediction models - both in parameterised and convection-permitting simulations - is assessed in detail for a single event and one numerical model in Chapter 4. Focal point is the divergent outflows from deep convection in these two types of model set-up. Convective outflow variability as a consequence of for instance convective organisation is explicitly revisited in the Chapter. Therefore, a more detailed discussion on the parameterised representation of deep convection in numerical weather prediction models is provided in Section 4.3.2.2.

2.6.2 Natural variability, representation and predictability

From the slightly philosophical perspective, many motivations are possible to learn about natural variability of a certain phenomena in atmospheric dynamics - in this case upper tropospheric divergent outflows from

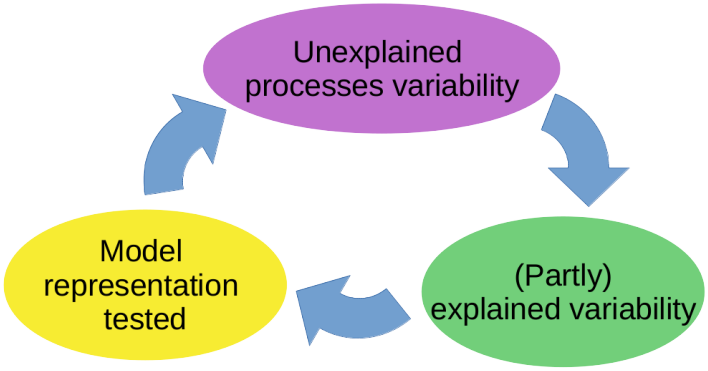

Figure 2.4: Understanding natural variability is important, and by iteratively understanding variability and its model representation better in time, progress in terms of prediction and model accuracy will come with it.

deep convection. Before moving to the main matter of this work, I would like to emphasise that it may be important to learn about views at *Natural* variability from as many perspectives as possible and feasible. *Natural* variability can consist of a component variability of a system that can be understood (Chapter 3) and component of the natural variability that may be impossible to understand and track in model simulations: *intrinsic* variability (Chapter 5). Predictability, and its potential limits, are closely related to the question of which components of variability can be understood and which cannot. Through an increasing understanding of variability, practical predictability may only be increased with time, as long as the limit identified by Lorenz [1969a] is asymptotically approached but not reached. Subsequently (see Figure 2.4), the representation of the obtained understanding of natural variability can be examined, as is done in Chapter 4. Without learning about variability and its representation in numerical weather prediction models, predictability will not grow (Chapters 3 and 4) [Bauer et al., 2015, e.g.]. Predictability at small and large scales are inseparable, as Lorenz [1969a] showed. Variability at large and small scales are inseparable too, and predictability and variability are inseparable as a whole (Chapter 5).
The strong coupling of large and smaller scales governs a connection of understanding mesoscale convective variability to large-scale predictability studies, which is overly emphasised in this work. The latter results from part of the project being rooted in the proposal of Research Area A of Wavestoweather Phase 2, which as a whole covers all those scales.
By shedding some light on convective predictability and variability I would hope that this work may add a new complementary way of looking at variability and predictability. However, each perspective or approach is among a long list of many perspectives that have been important to the understanding of (internal) variability of atmospheric dynamics. Only some important ones stand out among all those listed approaches.

- Representative ensemble prediction systems
- Spectral views onto variability and predictability
- Coherent and physically based stochastic modelling
- Dynamical process understanding of the evolution in spread within ensemble simulations
- New modelling approaches
- Experimental ensembles
- Spatial and temporal understanding and evolution of variability
- Model intercomparison studies
- Evaluation of targeted conditional variability and statistics

All these methods combined are the key towards improved predictability, even if the predictability of the *internal* part of variability in (tropospheric) atmospheric dynamics is thought to be intrinsically limited [Lorenz, 1963, 1969a, Zhang et al., 2019], whereas for example external forcing like ocean and stratospheric dynamics may govern skill beyond the internal atmospheric limit [Buizza and Leutbecher, 2015] - especially for forecasts applicable to substantially longer averaging periods. The listed study methods widen the understanding of variability.

3 Divergent convective outflow in large eddy simulations with Cloud Model 1

Large parts of this Chapter also appear in Groot and Tost [2022], while some sentences in Section 3.2 have previously been published in Groot and Tost [2023]. Furthermore, the experimental set-up as well as other elements in Groot and Tost [2022] and this Chapter have partial overlap with Groot and Tost [2020].

3.1 Introduction

Organised deep moist convection is not only a substantial precipitation source over the tropics and mid-latitudes, but also a driver of the global atmospheric circulation. The energy conversion, as it drives the global atmospheric circulation, is achieved by so-called latent heating in deep convection: condensation of water vapour warms rising air parcels while they move upward, expand and cool. The warming tendency of latent heating opposes the stronger cooling tendency (expansion) and provides (positive) buoyancy. Positive buoyancy "fuels" the moist convection that can keep it running, even accumulate and further organise.
Once organised systems of deep moist convection (from now on *convective systems*) have formed, they feed back onto the background atmospheric circulation. The background atmospheric circulation is typically hardly affected by tiny convective systems composed of one or two cumulonimbus clouds. On the other hand, the mesocale circulation can be entirely disturbed and even dominated by convective systems of sufficiently large size and intensity [Houze, 2004, 2018]: in case of so-called mesoscale convective systems (MCS) a complete re-organisation of the atmospheric flow around the MCS can happen. In other words: large systems with higher precipitation rates introduce an on average stronger feedback to the large-scale atmospheric flow (intuitively), i.e. the feedback is expected to increase with the precipitation intensity (or, equivalently, net latent heating). Consequently, the net latent heating can be used to quantify the intensity of convective systems. The feedback onto the background circulation has also significant consequences for downstream developments of the atmospheric flow sometimes [e.g. Rodwell et al., 2013, Clarke et al., 2019a,b].
An increase of the flow feedback strength with the amount of net latent heating is supported by the simplified linearised gravity wave model described in Bretherton and Smolarkiewicz [1989], Nicholls et al. [1991], Pandya et al. [1993], Mapes [1993]. Principles behind this linear gravity wave modelling approach have additionally been used for simulations of the flow feedback from squall lines by Pandya and Durran [1996]. Furthermore, the model has also been used in a very different set-up to study flow adjustments to localised heating by Bierdel et al. [2018]. Bretherton and Smolarkiewicz [1989] studied gravity wave responses to heat sources with a linearised model that supports gravity waves. Their linear model reveals increasing convectively induced circulation with an increasing latent heat source. The gravity wave adjustment signal propagates away from the convective system, but comparatively strong upper tropospheric outflow is maintained around the location of the initialised latent heat pulse (Figure 2.2 in Chapter 2). Moreover, their model describes how point and line sources generate different outflow responses and how responses depend on vertical wavenumber: in other words, the outflow may depend on the organisation of the convection (including storm geometry). Extensions of the linear model by Bretherton and Smolarkiewicz [1989] have later been used to understand preferential locations of convective initiation, e.g. in the tropics [Lane and Reeder, 2001, Stechmann and Majda, 2009, Lane and Zhang, 2011, Grant et al., 2018], and to understand error propagation in a rotational set-up [Bierdel et al., 2017]. The linearised model by Bretherton and Smolarkiewicz [1989] can serve as a benchmark for the irrotational cloud resolving and large eddy simulations with much more complexity, as presented here [for most important predictions of the gravity wave model, here partly used as assumptions, see Bretherton and Smolarkiewicz, 1989, Bierdel et al., 2017, 2018].
In Baumgart et al. [2019] and Zhang et al. [2007] it was found that numerical weather prediction errors can be initially established predominantly in regions of enhanced, and mostly convective, precipitation. Baumgart et al. [2019] were able to attribute initial error growth (< 12h into the simulation) in their stochastically perturbed simulations to non-conservative processes and, predominantly, to the deep convection parameterisation. That parameterisation represents the collective effect of organised convective systems and isolated convective cells. At later times, the induced ensemble variability corresponds predominantly to variability in the upper tropospheric divergent winds. Baumgart et al. [2019] inferred that this variability is likely associated with latent heat release below and corresponding deep convection as precursors.
Interpreting Baumgart et al. [2019], it is likely that convective precipitation provides the fastest feedback from *diabatic*[5] processes to the unbalanced flow at mid-latitudes (faster than for example radiation and microphysics, which are suggested to be secondary processes). Therefore, on the way to optimised downstream predictions and climatological representation of coupled unbalanced flow components, it is suggested that a reliable relation between convective precipitation and subsequent unbalanced (divergent) flow is a necessity.

In general, a good representation of this component of the *physics-dynamics*[5] coupling should reduce some of the existing model biases.
Quantitative understanding of upper tropospheric outflow and uncertainty quantification achieved here could support an extension of the potential vorticity diagnostics of Baumgart et al. [2019] towards smaller scales. Consequently, it may lead to improved insight in the role of individual convective systems in the appearance of certain forecast errors. Furthermore, it may reveal biases between certain *modelling approaches*, namely large eddy simulation, cloud resolving simulations with explicit deep convection and global simulations with parameterized deep convection. Intercomparison of divergent outflows among the LES investigated here and comparison of various simulation set-ups (Chapter 4) could provide structural insights in (potential) biases between each of them. Such insight in structural biases, depending on the treatment of deep convection, may be beneficial to the understanding of weather and climate simulations [e.g. Done et al., 2006]. In this work, a set-up for intercomparison of divergent outflows is established, focused on LES with advanced small-scale process representation. Effects of differential convective organisation or differential *diabatic* heating could potentially be followed to synoptic scale uncertainty days ahead, using thorough understanding of upper tropospheric divergence variability [e.g. Baumgart et al., 2019, Rodwell et al., 2013]. From this perspective, differential diabatic heating may force differential unbalanced[5] upper tropospheric flow, which would be a mediator to large-scale non-linear flow perturbations [Baumgart et al., 2019]. However, first it needs to be understood which main factors control the upper tropospheric divergence.
The main objective of this study is therefore to understand and diagnose the upper tropospheric outflow feedback of organised convective systems to its surroundings quantitatively for large eddy simulations, in which part of the turbulence is explicitly resolved. The divergence sets on as a horizontal wind compensation for vertical acceleration of convective upward airflows, accompanied by a high pressure anomaly aloft. Such a high pressure anomaly aloft exists as a consequence of abundant mass aloft.
More specifically, the upper tropospheric mean lateral acceleration over a control volume, as diagnosed with the mass divergence, is compared to the net latent heating. Furthermore, the relation of the mass divergence to accompanied convective momentum transport and organisational structure of the convective systems is assessed. Analysing a control simulation, an ensemble and tailored experimental simulations, the effect of net latent heating, convective momentum transport and convective organisation on the divergent outflow of convective systems can be evaluated systematically.
Ensembles and physics perturbations are applied to three selected organisational *modes* (organisational structures) of convection: a supercell, regular multicells and a squall line. The latter class is further sub-divided into two categories (finite-length and infinite-length squall lines), leading to four basic scenarios in total. Convective momentum transport is purposely switched off or adjusted by $\pm 50\%$. Additional physics perturbations are applied to the aforementioned basic *modes* of deep convection to test specific hypotheses and to improve the quantification of the impact of latent heating.
Diagnosed quantities are averaged over mesoscale boxes and compared for a large set of large eddy simulations. The box of integration is suited to the purpose of this study, which is understanding the upper tropospheric divergent outflow from deep convection. Hence, the ideal box contains this mass divergence completely, but little of the inflow and convergence signals. Fitting the box is done for the different types of convective organisation separately and is described within the results section, before looking specifically at the upper tropospheric divergence.
With the method presented in this study, the *physics-dynamics* coupling for convective systems can be assessed on mesoscales of order 100 km. Physical understanding of this coupling using idealised large eddy simulations (this Chapter) allows for further comparisons with operational numerical weather prediction models (next Chapter). In the current Chapter, aim is gaining physical understanding of the theoretical connection between convective precipitation on the one hand and resulting mesoscale divergent outflow as a feedback to larger scales on the other hand, using idealised large eddy simulations.
The structure of this Chapter is as follows: in Section 3.2 the model set-up (Section 3.2.1), initial conditions for four prototypes of convection and corresponding convective environments (both in Section 3.2.2) are described. Furthermore, all perturbation types (e.g. ensemble configuration) are covered in this section (Section 3.2.3) and the analysis windows are described (Section 3.2.4). In Section 3.3 the evolution of convective cells is first discussed for the reference simulations. Thereby, each of the four prototypes of convection are introduced separately (Section 3.3.1). That is followed by illustrations of accumulated precipitation, which

[5]One can split-off diabatic and adiabatic processes. Dynamical processes purely transport (redistribute) energy spatially. In absence of diabatic processes, which are parameterised and result in superposed tendencies (e.g. for moisture and temperature) locally, the evolution of atmospheric flow at sufficiently large scales is fully constrained by the spatial distribution of potential vorticity (outside of the tropics). Adiabatic processes conserve potential vorticity. Diabatic processes result in energy exchange, leading to apparent potential vorticity changes (see Figure 1.3, Chapter 1.4). Such processes are associated with the term *physics*, not being part of the dynamics itself (while strictly speaking physics means "atmospheric physics other than atmospheric dynamics"). Diabatic processes perturb balanced flow to make the flow unbalanced, but are not the only way to create unbalanced flow.

represents column integrated latent heating signal, and a general overview of the evolution of vertical motion signals. These vertical motions consist of the convective cells themselves and remote impact by for instance gravity waves, which represent an important feedback to the environment [Mapes, 1993, Lane and Reeder, 2001, and others]. Therefore, these two flow aspects (heating and vertical motion) provide information about the horizontal constraints on the feedback of the convective cells to the surrounding flow. Furthermore, suitable vertical integration masks of divergence are fitted for the ensembles in Section 3.3.4. A dataset of upper tropospheric divergence is obtained in Section 3.3.5, based on all aforementioned constraints. That dataset sheds light onto the relationship between latent heating and upper tropospheric divergence. After ultimately investigating the east-west and north-south components of divergence separately (Section 3.3.6), the Chapter is finalised with a discussion and a conclusion section.

3.2 Methods

3.2.1 Model set-up

Simulations presented in this study are conducted with the cloud resolving model CM1 [Bryan, 2019] (version 19.8). The default horizontal grid size is 120 by 120 km, with a default simulation time of 2 hours ($9600dt$, with $dt = 0.75$ s). The vertical extent of the domain is 20 km. A sponge layer exists in the upper 5 km, which damps upward propagating gravity waves. Output is stored per 5 minute interval. The simulations are run in large eddy simulation (LES) mode at $dx, dy = 200$ m and $dz = 100$ m by default. In addition, extra simulations are run with additional grids where $dx, dy = 100$ m, $dx, dy = 500$ m and $dx, dy = 1$km. In the latter two the vertical grids are adjusted to 250 m and 500 m spacing. In one last simulation with adjusted resolution, dz is set to 200 m.
In LES-mode, a so-called *turbulent kinetic energy-scheme* after Deardorff [1980] handles the flow's sub-grid turbulence. The default CM1 microphysics scheme is used to represent clouds and precipitation by means of parameterisation, which is the two-moment Morrison scheme with hail [Morrison et al., 2009] in version 3.6. In this scheme, supersaturation is resolved and condensation is based on saturation adjustment [see also Morrison et al., 2005]. In such a two-moment microphysics scheme both mass and number concentration of each of the represented cloud and precipitation substances (cloud water, rain, cloud ice, snow, hail) are separately simulated. The scheme is specifically developed for representation of clouds and precipitation in mesoscale convective systems, such as squall lines. Simulated radar reflectivity calculations (from here on *reflectivity*) in the CM1 scheme [Morrison et al., 2009] are based on the assumption of a 10 cm wavelength. The scheme estimates Rayleigh scattering by cloud ice, water and mixtures of those, integrating the water mass [Bryan, 2019]. The advection scheme applies a 5^{th} order advection algorithm and Coriolis acceleration is ignored. Radiation is not actively resolved and no background tendencies have been set for radiation. All simulations in Chapters 3 and 5 have used the aforementioned settings.
The boundary conditions are non-periodic in all directions, which leads to the theoretical availability of an infinite reservoir of inflow (warm and moist low-level) air for convective systems. Derivatives of all quantities are set to 0 at the boundaries. Wave signals can therefore partially reflect at the boundaries. By selecting subdomains in time and space, over which the main analysis is carried out, boundary effects are strongly reduced (Section 3.2.4 and Section 5.2.2 of Chapter 5). Further metadata and output datasets are provided in Groot [2022] and Groot [2023].

3.2.2 Environmental conditions

3.2.2.1 Overarching settings The initial thermodynamics is prescribed using the profile of Weisman and Klemp [1982] (Figure 3.1), a standard in CM1. Two basic local potential temperature perturbations have been set at $t = 0$ to trigger convective cells with various kinds of organisation. Furthermore, the initial wind profiles are varied at $t = 0$ to realise systems that manifest with a certain organisational structure of the convection, numbered # 1-3 on the left of Figure 3.1 [see Rotunno et al., 1988, Weisman and Klemp, 1982, Bryan, 2019, and Bryan's CM1 code]. Each of the four combinations of local temperature perturbations and wind profiles are introduced in the following, in Sections 3.2.2.2 to 3.2.2.5. These prescribed profiles establish the four modes of convection.
The convectively very unstable initial conditions associated with the selected sounding are introduced on purpose: the perspective is taken from which it is known that strong convection will initiate. Conditional on that initiation, the convective systems are studied. This perspective complements that of Melhauser and Zhang [2012] (mostly in Chapter 5), in which the criticality of initial convective initiation itself is explored.

3.2.2.2 Supercell A supercell scenario is constructed by applying an initial warm bubble disturbance. The warm bubble is initialised around the centre of the domain, with a radius of 10 km in the horizontal. It has a bell shaped amplitude, with a maximum of 1 K (in terms of θ) at the origin and $z = 1.4$ km. The

warm bubble forces upward motion in the domain centre, which in combination with the high CAPE leads to the growth of strong convective cells.
The strong wind shear profile induces a supercell structure (Figure 3.1, #1). Wind component u gradually increases from easterly winds (negative) of 12.5 m/s at the surface to 18.5 m/s from the west, at interface between the layer of wind shear and the layer without. This interface is located at $z = 6000$ m in the reference case [Weisman and Klemp, 1982]. This combination of strong easterly and westerly winds keep the convective system centred within the domain throughout its evolution. The other (northward) wind component v wind varies from -2 m/s, at the surface, to +2 m/s, at and above that same interface.

3.2.2.3 Regular multicell A regular multicell is generated in the same warm bubble initiation scenario as the supercell case.
Moderate wind shear is applied, in combination with the warm bubble scenario leading to ordinary multicell convection. However, the easterly inflow at the surface is set to 11 m/s, while u increases to +3 m/s at the interface height, which is set at 2.5 km altitude [adjusted from Rotunno et al., 1988, , Figure 3.1 #2]. Again, the wind profile is created to keep the convective system relatively centred within the domain throughout its evolution.

3.2.2.4 Infinite-length squall lines Below $z = 2500$ m, a potential temperature perturbation that decreases linearly in magnitude with z from -6 K, at the surface, to 0 at 2500 m is set at initial time for the western half of the domain: $x < 0$ km. Upward motion that initiates convection is generated at the boundary between the air masses in the west and the east ($x = 0$ km). The combination of high CAPE and the moderate shear profile perpendicular to this boundary leads to a strong line of convective cells.
A moderate wind shear is applied, as in the regular multicell scenario. With this moderate shear, the u-component of the wind varies linearly from 12.5 m/s of easterly inflow at the surface to weak westerly flow of 1.5 m/s above the top of the shear layer (Figure 3.1). That top is set at $z_{i,ref} = 2500$ m for this scenario in the reference run [adjusted from Rotunno et al., 1988, Figure 3.1 #3]. As in the other two modes of convection (#1, #2), the v-component of the wind varies linearly from -2 (surface) to +2 m/s ($z \geq z_i$) over the same layer. The latter is needed to develop some degree of three dimensionality in the simulation. Given fully-2D initial conditions in the infinite squall line simulations, the three dimensionality could have been absent without any differential meridional advection, in combination with the open boundary conditions.

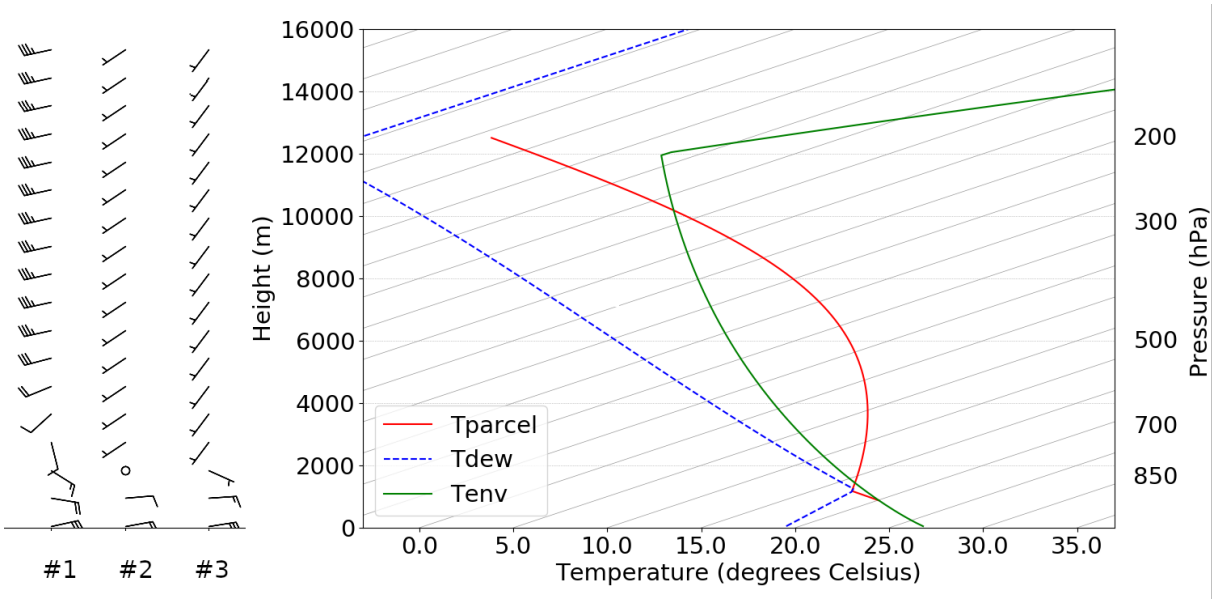

Figure 3.1: Vertical temperature and moisture profile following Weisman and Klemp [1982] and wind profiles 1-3 (left). Isotherms are the tilted isolines, every 5 K. Temperature state: green solid line; dew point state: blue dashed line; temperature of parcels when lifted from about 900 m altitude (no mixing is assumed): red line. The temperature difference between the red and the green line corresponds with the buoyancy of cloud air with respect to the environment (when expressed as a temperature and) in the limit of no mixing. The wind is visualised with a direction (orientation of the barb) and a full line at the end of the barb for each rounded 5 m/s of wind, or a half line for 2.5 m/s, which are subsequently added to get the full wind speed at a certain level. An open circle indicates that the wind is calm at a certain level.

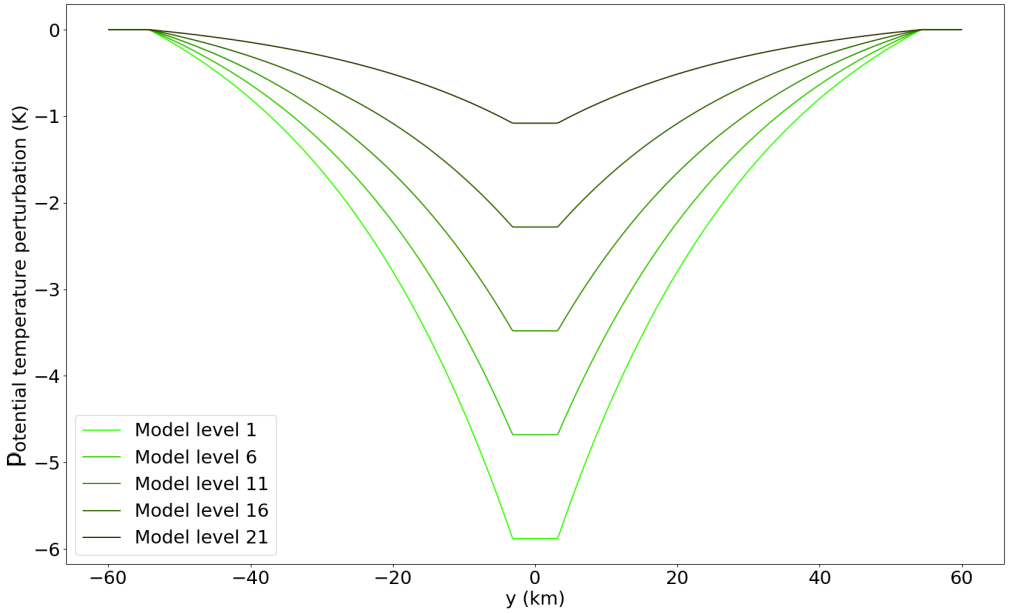

Figure 3.2: North-south profile of initial potential temperature perturbations along the length of the finite-length squall line for five selected model levels, counted upward from the surface level.

Note that the wind profile implies the omission of deeper shear (especially in #2 and #3), which on average reduces the depth of vertical displacements within squall lines and, therefore, the size of the convective systems [Coniglio et al., 2006]. This is beneficial for a reduction of the storm-relative flow and hence to reduce the across-line growth of the squall lines: the residence time of the convective systems within the domain is increased.

3.2.2.5 Finite-length squall line simulations Despite the substantial similarity to the infinite-length squall line, this additional class of organised convective systems is constructed to obtain convective cells arranged in a line, but with more potential for outflow in the y-dimension locally (at least at the squall line edges). This meridional outflow is substantially diminished in an infinite-length squall line. Most of the conditions are identical to the infinite-length squall line simulations (described above, Section 3.2.2.4). The main difference is a modification of the initial potential temperature perturbation in the cold pool damming scenario: in the central region of the domain, it maximises at 6K at the surface, but this surface maximum decreases outward to 0K near the meridional boundaries of the domain. The north-south profile of initial potential temperature perturbations associated with this scenario is shown in Figure 3.2. Quantities of interest are separately diagnosed over a central (with the same extent as infinite-length squall line) and an outer region in the finite-length squall lines. An outer region is assigned at both the northern and southern ends for this scenario; their spatial extents are defined in Figure 3.7.

3.2.3 Perturbations

3.2.3.1 Ensemble perturbations To test the robustness of the results, an ensemble is constructed in the following way, and for each scenario accordingly: the interface height z_i between layers in which initial wind shear is present and absent, is randomly perturbed. Thereby, the maximum deviation within the ensemble is 5% from the reference $z_{i,ref}$. Corresponding extreme deviation values for z_i are $2500 - 127$ resp. $6000 - 304$ m, with an ensemble mean deviation of 2.7% from the reference simulations. The relative magnitudes of the perturbations are equal for moderate and high shear profiles, and hence, all storm geometries.
Ensemble perturbations for the finite-length squall lines (Section 3.2.2.5) have been set-up in a slightly adjusted way compared to the other three scenarios: four perturbations were generated as a *narrow ensemble band* where the depth of the initial shear layer has been adjusted similarly as for the infinite squall line. On top of that, four additional ensemble members have been generated with stronger initial condition perturbations: one with a 1 km deeper cold pool, one with a deeper (climatologically more realistic) shear

layer and two with a 4K and 7.5K maximum of the potential temperature perturbation in the domain centre at the surface, referred to as a *wide ensemble band*.
Ensemble perturbations provide a background scatter of random variability in upper tropospheric divergence within a close proximity of the control runs, as caused by small random variations in initial conditions. After applying interface perturbations, winds are interpolated to the native vertical grid length of the corresponding simulation: 100 m. Effectively, a very slight contraction or expansion of the shear layer is achieved with the given perturbations. The magnitude of perturbations is equivalent to about one model level in typical high resolution simulations.
Note that the cold pool and warm bubble profiles, and hence the potential energy distributions, are not affected by the ensemble perturbations; the kinetic energy distribution of the initial conditions shows only weak deviations, located at low levels, within the ensemble (up to mid-levels for the supercell simulations).
It is not given that variability imposed by initial shear perturbations within the ensembles are maintained until the formation the organised convective systems and beyond. Nonetheless, as a result of the 5% variation in low level shear intensity, systematic variability of nearly the corresponding magnitude in net latent heating might be anticipated on: this would occur as a consequence in variability in layered overturning, if the variability maintains itself [based on arguments by e.g. Coniglio et al., 2006, Alfaro, 2017].

3.2.3.2 Physics perturbations Two types of physics perturbations are applied. These perturbations are applied for a comparison to the control simulation and ensemble of each of the three basic modes of convection (Sections 3.2.2.2, 3.2.2.3 and 3.2.2.4).
The constant of latent heating is adjusted to 60%, 80%, 90%, 110% and 120% of its actual value. This approach has been selected to serve as a proxy for perturbed cloud and microphysics tendencies (e.g. condensation, evaporation) or CAPE, without perturbing any of the other physics and the initial environment within the model. Conversions of energy fluxes (mostly: precipitation) in simulations with adjusted latent heating constant are naturally evaluated with the corresponding adjusted latent heating constant.
The adjustment of the latent heating constant feeds back non-linearly onto the conditions in convective clouds: the latent heat released by condensation of a given amount of mass of water vapour is reduced, which simultaneously affects the temperature evolution of any parcel ascending within those convective clouds. The temperature contrast with respect to the environment is therefore augmented at any point in time. The adjusted temperature contrast subsequently affects the vertical extent of a convective cloud. As the vertical cloud extent changes, the mass per unit area that "collides" with the tropopause, if the latent heating is sufficient to reach the tropopause. However, at the same time, the latent heating is affected by the perturbation. Irrespective of the aforementioned cascading effects, the research interest is rather the relative magnitude and, more specifically, the way that such latent heating perturbations and divergent outflows cohere.
In Figure 3.1, these feedback effects translate into a stronger curvature towards the left of the red curve (parcel temperature) at levels above about 1100 m, up to 12000 m. The distance between the red and green curve in this Figure is equivalent to the buoyancy, if cloud and environmental parcels would not mix.
The presence positive feedbacks in the response to latent heating perturbations motivate the selection of smaller perturbations of the latent heating constant (e.g. 10%) than for convective momentum transport.
The vertical advection term in both horizontal momentum equations has been adjusted to 0, 50% and 150% of its actual magnitude in another set of experiments to perturb the convective momentum transport. This is done to determine direct physical effect of the convective momentum transport process on upper tropospheric divergent outflows. The perturbation technique is similar to creating an artificial source/sink term of horizontal momentum at locations with strong convective (i.e. vertical) motion, which is driven by tendencies caused by vertical gradients in horizontal momentum.
It is not given that vertical advection of horizontal momentum (and hence CMT) adjusts by the percentage corresponding to the magnitude of the perturbation, unless CMT is actively switched off and cannot take place (i.e. when the perturbation is 100%). Since the evolution of the convective systems is perturbed by adjustments of 50% in the convective momentum transport, precipitation rates may change. As a consequence, CMT may adjust somewhat disproportionally. Nevertheless, all quantities diagnosed separately, including the vertical advection of horizontal momentum. Therefore, the effect on CMT can be tracked actively. As the set of experiments consists of three CMT perturbations in three modes of convection and one experiment in each mode of convection has no CMT, it is not strictly relevant whether diagnosed perturbations are exactly ±50% or deviate from the ±50%.
Systematic non-linear effects on the mass divergence are detectable, if processes other than the intensity of the convection affect mass divergence directly. Additionally, the role of other parameters, such as convective organisation and convective momentum transport, for the upper tropospheric divergence can be determined by the comparisons between simulations.

3.2.3.3 Adjusted low level temperature perturbations The dataset obtained with simulations introduced in Section 3.2.2 is complemented with additional simulations, in which the strength of the potential temperature disturbances (warm bubble(s) or cool pool damming) has been adjusted. These modifications result in slightly stronger / weaker triggering of convective cells and hence slightly stronger / weaker convective cells would be expected, compared to the other ensemble simulations. The perturbations are configured as follows:
For the **infinite-length squall lines**

- Default perturbations are halved
- Default perturbations are linearly reduced to zero, over a length scale equal to the domain length.

On the contrary, for the **regular multicell** and **supercell**

- A superposition of a half amplitude cold pool and half amplitude warm bubble
- A superposition of a half amplitude cold pool and full amplitude warm bubble

are applied to the region of the original bell-shaped perturbation only. The specific shape of those modifications is also defined in the output and metadata of the corresponding simulations, which are available via Groot [2022] and Groot [2023].
These simulations complement the dataset of this study with an additional class of stronger initial conditions perturbations, on top of the background ensemble. Two extra simulations for each of the three basic modes convection (left three columns of Figure 3.3) are integrated over time.

3.2.3.4 Simulations at extended domains The domain size that has been chosen in this study can perhaps be considered on the small end for studying the feedback from convective cells to their environment: especially for the supercells and squall lines during the last half an hour of the simulations. In the regular multicell simulations, however, the limited domain size should be of no concern: the convective cells cover only a limited fraction of the 120 by 120 km domain.
To test the effective limitations of the restricted domain, more robustly determine the patterns in the dataset and herewith strengthen the potential conclusions, one supercell and one finite-length squall line simulation are repeated at an extended domain (200 by 200 km). The simulation time is extended to 160 minutes,

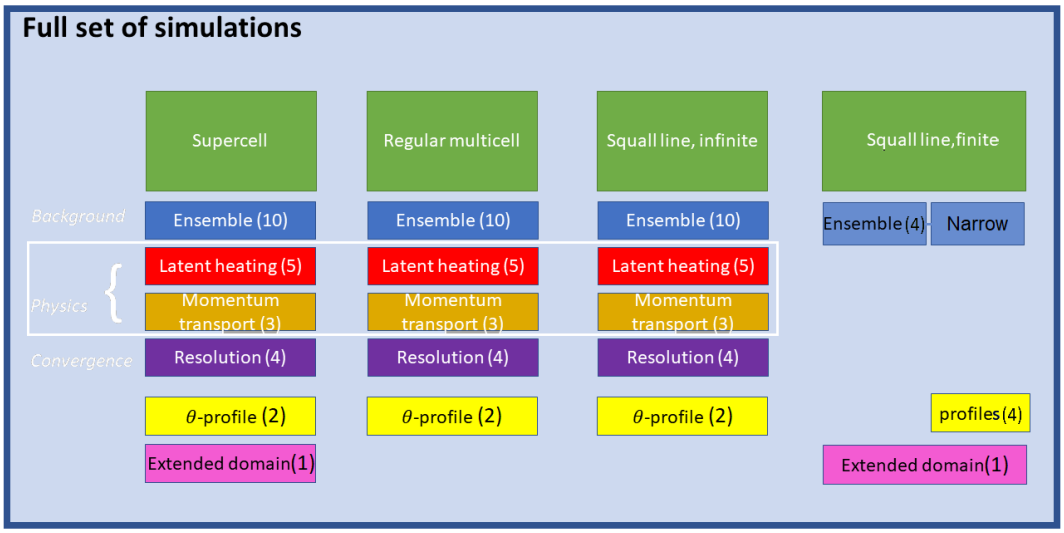

Figure 3.3: Overview of all CM1 experiments done in this study. The four scenarios represented in the columns of the display have been introduced in Section 3.2.2. The green boxes with white caption show each of the four prototypes of convection that are used, with a list of experiment groups following in the column below each of them. Below the column header, the perturbations applied to each scenario are represented, which are discussed in the order of display (downward; Section 3.2.3). Here, white text represents the regular basis set of perturbation experiments, applied to the first three modes of convection. Black text represents irregularities among the experiments, tailored at specific modes of convection and robustness testing. In the last column "narrow" denotes the narrow ensemble band, corresponding to the ensemble of the other three scenarios. "Profiles" denotes the wide ensemble band, which correspond to θ-profile perturbations in the other three scenarios (Sections 3.2.3.1 and 3.2.3.3).

but the analysis window is restricted to up to 120 minutes. For the finite squall line, the configuration of the large domain simulation is not identical to the reference squall line simulation. Conversely, it uses the conditions for an ensemble member with reduced potential temperature perturbations: maximum 4K only. This configuration is selected to reduce additional convective initiation, which also results in precipitation. Such secondary convective initiation is located further away from the squall line if the initial temperature perturbation is reduced to 4K. The additional convective initiation makes the evolution of the system less comparable to the ensemble simulations in the reference domain.
An overview of the simulations introduced in this section and the previous Section (3.2.2) is shown in Figure 3.3.

3.2.4 Spatial and temporal analysis windows

Diagnostics that represent latent heating by precipitation, upper divergent outflow and convective momentum transport are evaluated over two separate time intervals. The first time interval ends after 75 minutes for the squall lines and after 90 minutes for the regular multicells and supercells. Diagnostics are also evaluated over the second time interval, running from the end of the first interval until the end of the simulation (120 minutes). This approach with two time intervals creates temporal sub-samples. In the first interval's sub-samples, effects close to the selected box boundary are relatively unimportant. On the other hand, such effects have a comparatively stronger impact on the diagnostics during the second time interval. Comparison between the two intervals helps to determine the relevance of, for instance, propagation of gravity waves, influencing the larger scale environment.
Furthermore, a restricted rectangular horizontal area within the whole domain is selected, over which diagnostics are averaged spatially, to further limit boundary effects. The exact extent of the boxes is depicted in Figure 3.7 (Section 3.3.3).

3.3 Results

In this section, the development of the convective systems is described from a basic point of view, by first illustrating the radar reflectivity as simulated by the model CM1 and describing the evolution of the precipitation systems (Section 3.3.1). The temporal evolution is presented for the control simulation of each of the four modes of convection separately. Reflectivity at 3 km altitude is selected for illustration of reflectivity across a horizontal plane.
Then, the spatial distribution of accumulated precipitation is shown for some selected simulations (Section 3.3.2). The cumulative precipitation represents the latent heating over the atmospheric column over a given area to a good approximation. This is because the background wind field is set such that convective systems propagate slowly relative to the domain by design. Furthermore, the region with substantial precipitation accumulation coincides with the area over which the convective cells reside and is the area where outflow from the updrafts originates. The cumulative precipitation pattern explains the spatial distribution of convective heating, and variability herein, to a large degree.
Following on the accumulative precipitation, the effect of convective systems on mid- and upper-tropospheric vertical motion is discussed (Section 3.3.3). That does not only illustrate the direct location of convective cells, but also the dynamical effect of the convective systems on their surroundings, including for example patterns of gravity wave adjustment [see Bretherton and Smolarkiewicz, 1989]. Knowing the spatial distribution of the convective heat sources and flow adjustment, the last ingredient needed for integration is a vertical mask. The vertical extent over which the divergent outflow occurs is delineated in Figure 3.8, accompanied by a discussion on the evolution of this vertical extent (Section 3.3.4).
The section is continued with the dataset of diagnosed mass divergence and net latent heating over the column for all simulations and both time intervals. That mass divergence in the dataset is based on the horizontal and vertical extent of the box (Section 3.3.5). Finally, the zonal and meridional horizontal divergence are separately analysed for a selected simulation (Section 3.3.6).

3.3.1 Evolution of the convective cells

Figure 3.4 depicts the temporal evolution of the four convective systems in the control simulation, together with their corresponding simulated patterns of radar reflectivity.

3.3.1.1 Supercell The initial warm bubble is a source of buoyant air around the origin, which can freely ascend. Part of it develops into a deep convective cell and, in the conditions of high (wind) shear, it organises itself as supercell. After 25 minutes, the convective cell develops and simulated radar echoes appear at 3 km altitude (Figure 3.4, left column). The cell stretches out strongly in the east-west direction under the condition of a wind shear larger than 30 m/s (surface to the upper half of the troposphere). Maximum

reflectivity immediately reaches about 65 dBz and stays at this level, with a continuous growth of the high reflectivity regions (> 60 dBz). A so-called *hook echo* (feature that characterises most supercells [e.g. Markowski and Richardson, 2010, Chapter 8]) appears after about 45 minutes in a southern cell, about 10 km west of the origin, with an approximately antisymmetric cell as northern counterpart. The length of the cells is already about 50 km in the *zonal* (west-east) direction at this time, but the *meridional* (south-north) length of the box containing both cells is only about 20 km. The simulated radar echoes grow mostly in the meridional direction during the second hour (Figure 3.4). The southern hook echo starts accelerating southeastward and thereby still gains size. Its orientation remains mostly west-east, while the northern cell tilts its orientation in the horizontal plane by some 20-30 degrees and grows. On the western flank, initiation of much smaller convective cells sets on after about 85 minutes.
The evolution of the ensemble compares very well to that of the reference run, as it is described earlier in this section. There are also a lot of similarities in the patterns of convective initiation of much smaller cells after 90 minutes, west of the supercell. The details of cell intensities are different, but other patterns of cell initiation have strong correspondence between the ensemble members. Peak intensities are similar too.

3.3.1.2 Regular multicell From the warm bubble initialised at the origin, a convective cell is able to develop right next to the origin (Figure 3.4, second column) - as in the supercell simulations. This is a consequence of weak upper tropospheric flow and strong lower tropospheric inflow with high CAPE values, as provided by the Weisman and Klemp [1982] initial conditions and a buoyant warm bubble.
After 25 minutes of simulation time, the first reflectivity signals appear at $z = 3$ km, directly below melting level. A first convective cell remains small during the first hour, with a size of 10 by 20 km in the horizontal direction and maximum reflectivity around 60-65 dBz. A small cold pool develops on the downdraft side (west; not shown). During the next output time steps, the convective precipitation system remains contiguous, but also develops two cores (around and just after 60 minutes): a southerly and a northerly cell. Herewith, a two-cell system, a multicell, has developed. It increases in size to about 30 km in each horizontal direction and the northerly cell propagates northwestward, while the southerly cell remains very near to the origin. After 120 minutes, the systems has grown to some 50 by 30 km, with slightly more linear characteristics appearing on the northwest and south end of this structure (last 5-10 minutes). The orientation is mostly perpendicular to the west-southwesterly shear and accompanying (developing) cold pool near the surface.
Basically, one could say that the description above applies to the reference simulation and to all ensemble members, which means it also covers the ensemble envelope. Furthermore, most of the other regular multicells also behave the same way, with the exception of those with the strongest physics perturbations (latent heating constant -40%, modified CMT and to a lesser extent -20% latent heating constant). That statement is generally also true for the supercell and infinite-length squall line simulations to which the physics perturbations have been applied.

3.3.1.3 Infinite-length squall line In the infinite-length squall line simulations deep convection develops along the initialised cold pool edge, which sits at the y-axis (Figure 3.4, third column). Convective initiation occurs as upward motion is triggered at the interface between warm air to the east and cooler near-surface air to the west. With substantial amounts of CAPE, shear helps to organise the convective storms along the y-axis.
The first convective precipitation cells appear along the y-axis after 15 minutes. A secondary phase of convective initiation occurs a few kilometers ahead of the main squall line after 30-40 minutes of simulation time, which is more extensively discussed in Groot and Tost [2023] and Chapter 5. Newly initiated convective storms exceed reflectivities of 55 dBz, with values up to about 65 dBz locally. This is followed by an onset of eastward displacement of the line of convective cells. The squall line also starts to reveal some inhomogeneity along the y-axis by then, while convective cell cores continue to display high reflectivities in excess of 55 dBz. The shear also helps to efficiently increase the size of the partly precipitating convective *anvil* in the zonal direction.
The evolution of the squall line ensemble spread is discussed very extensively in Groot and Tost [2023] and Chapter 5. The key finding is that the developments essential for the evolution of ensemble spread occur during the second phase of convective initiation, with consequent differences in cold pool acceleration within the ensemble. The intensity of the secondary convective initiation varies substantially among the ensemble members. It is also associated with contrasts in intensity and corresponding precipitation rates of the convection within the ensemble envelope. For more detail on the evolution of the squall line reference simulation and ensemble spread one is referred to Groot and Tost [2023] and Chapter 5.
Infinite-length squall line simulations with perturbed physics show discrepancies with respect to the control simulation in terms of exact propagation velocity of the cold pool, development of the convective area and total area covered by strong convective cells. Furthermore, the corresponding evolution of the convection is

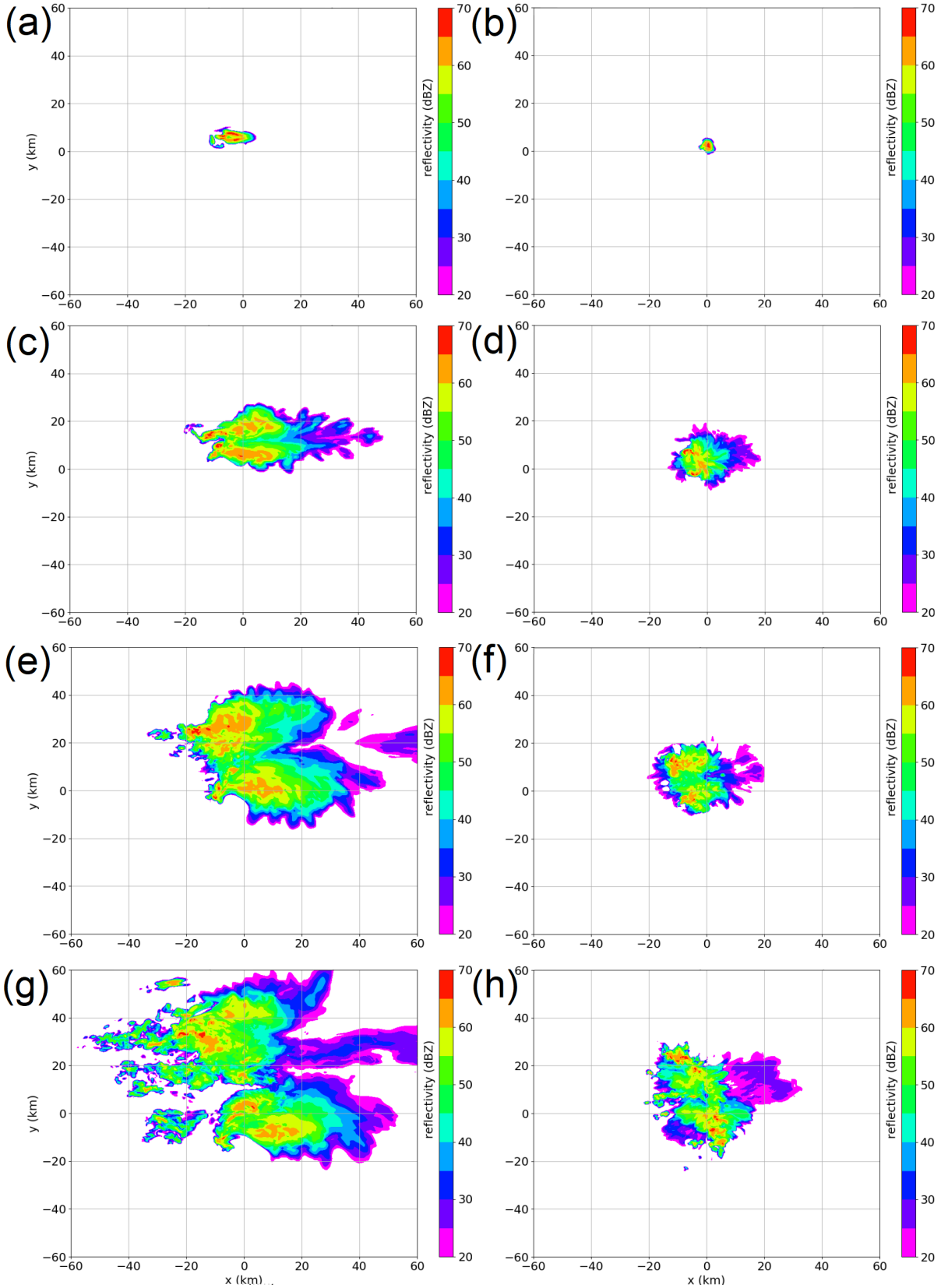

Figure 3.4: Top view of simulated radar reflectivity at 3 km altitude in the control simulation for each of the four modes of convection. From left to right supercell (a, c, e, g) and regular multicell (b, d, f, h; squall lines on the next page). From top to bottom time increases: 30 min (top row, a and b), 60 min (second row, c and d), 90 min (third row, e and f) and 120 min (bottom row, g and h). Figure continues on the next page.

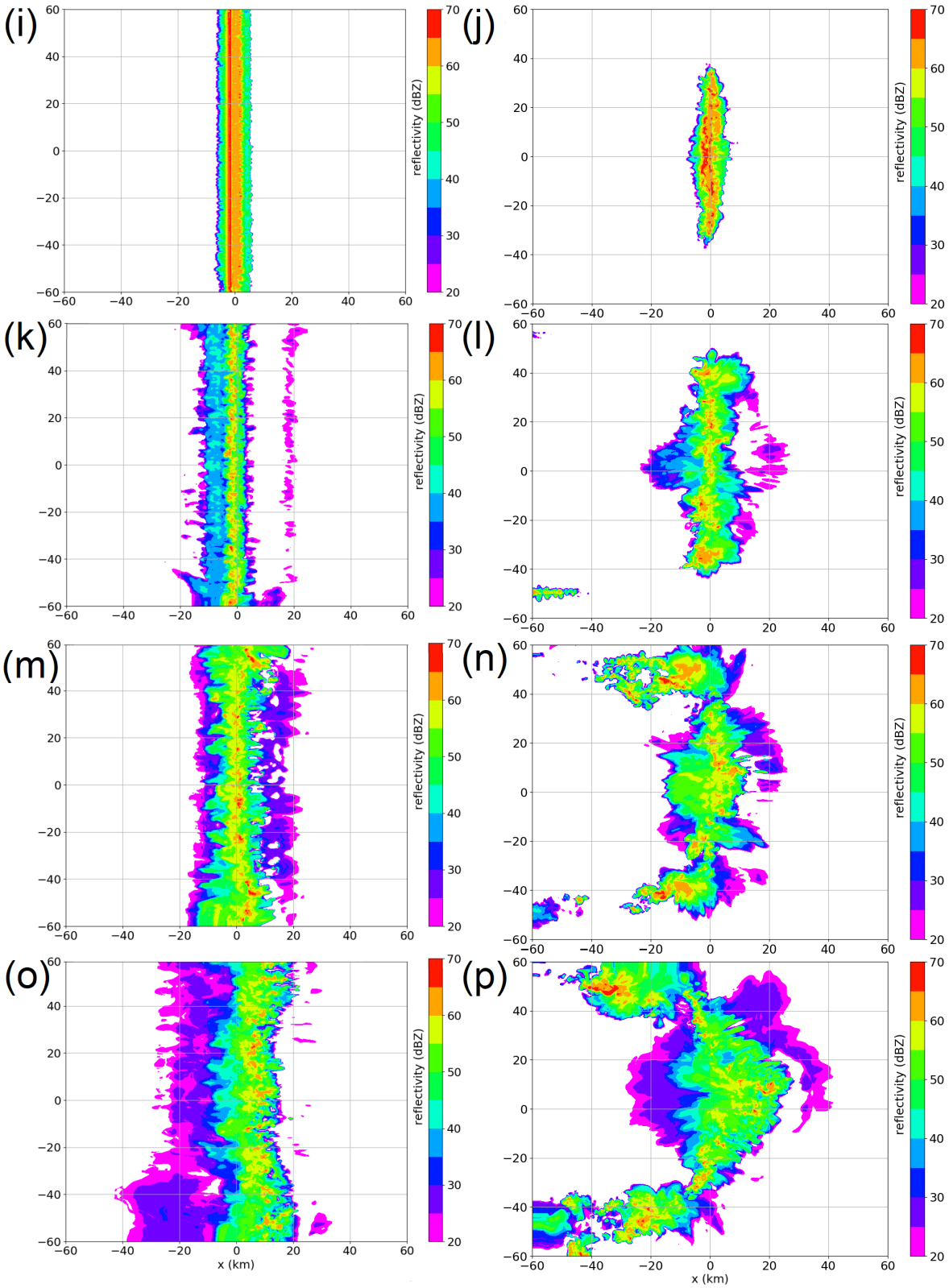

Figure 3.4: Continuation of previous page. Infinite-length (left, i, k, m, o) and finite-length squall line (right, j, l, n, p) with a display of the same snapshots (30, 60, 90, 120 min) and downward increasing simulation time.

slightly quicker (slower) than in the control in some simulations and the *anvil* can be larger or absent. The most contrasting differences occur, understandably, in the -40% latent heating simulation. Areas with high reflectivities change accordingly.

3.3.1.4 Finite squall line The finite squall line starts precipitating after 15 minutes over a length of about 50 km along the y-axis (Figure 3.4, last column). After 20 minutes, reflectivities above 65 dBz already appear in the model output and the precipitating region grows in each horizontal direction. Cellular structures are not yet present, but start appearing after 30 minutes of simulation time. By this time, its length is about 75 km, centred at the origin. The width of the squall line reaches about 30 km in the centre after 45 minutes and a small blob of anvil precipitation is sent westward from the origin, against the wind shear (*upshear*).
While the core region maintains its position near the centre of the domain, an extension of the squall line at both ends ($y \approx \pm 40$ km) adjusts the geometry of the convective system to an arched shaped line after 60-65 minutes. Simultaneously, some convective initiation occurs locally, west of $x = -40$ km at $y = \pm 40$ km. These small cells live for maximum 5-10 minutes. The associated precipitation accumulation is negligible compared to the rest of the squall line (initial conditions were selected to reduce the size and duration of cells as much as possible on purpose).
With the development of the arching geometry, the simulated reflectivity signal strengthens and the convectively active area in the outer regions (close to the northern and southern boundary) increases as well. The squall line centre region starts to accelerate eastward and moves to about 15-20 km east of the origin over the last 40 minutes of the simulation. However, this acceleration is mostly restricted to a 30 km region around $y = 10$km. After about 115-120 minutes, the 55+ dBz echoes become discontinuous along the arch (Figure 3.4) and the reflectivity pattern suggests that a *mesoscale vortex* may have appeared just north of the centre (near $x = 10$ km and $y = 10$ km).
Each of the patterns described above is representative of all ensemble members. The most significant contrast between individual members is the location of individual cell cores, mostly later on in the simulation. If the wider ensemble band with stronger initial condition perturbations is considered, conditions with slightly stronger cold pools and increased shear correspond to a somewhat faster growth and to a slightly larger system with a larger precipitation area. The initiation at the flanks of the systems is also increased a bit. Lastly, the central cells of these systems propagate faster in those simulations. On the other hand, those systems with reduced initial cold pools remain a bit smaller and have reduced convective initiation at the flanks of the arch.

3.3.2 Cumulative precipitation

In Figure 3.5 one can see the mean precipitation accumulation for each mode of convection, as well as the ensemble spread for some thresholds of cumulative precipitation. It is shown for the background ensemble and the perturbed convective momentum transport simulations. The latter set is shown, because the area of precipitation accumulation is generally displaced or deformed the most within these experiments compared to the reference simulation (which itself is included in the *spaghetti* plots). Other perturbations introduce weak(er) displacements and are shown in the complementary Figure B1 of Appendix B. Furthermore, perturbed latent heating in particular affects mostly the amplitude of the precipitation signals.
The figure shows that the latent heating is injected into the column within a rather compact region: in particular for the regular multicell (Figure 3.5c, d). The ensemble spread is small. In simulations with physics perturbations, the precipitation cells also occur in a condensed area during the two hours simulation time. Furthermore, the high degree of symmetry along the length of the infinite-length squall line stands out (Figure 3.5e, f).
A compact and persistent region of high precipitation accumulation is achieved, as intended: the precipitation cells do not move far from their original position near the origin, as displayed in each of the panels in Figure 3.5. As the divergent outflows could reasonably be assumed to be co-located with cumulonimbus clouds (the region of *diabatic heating*) and their close proximity, and thus with the precipitation signal, net outflow has to (mostly) stick to that region near the central part of the domain. This suggests that an integration over a subdomain of the simulation domain suffices for rigorous assessment of outflow magnitudes in the simulation datasets.

3.3.3 Near-tropopause and middle tropospheric vertical motion

A selection of panels with the evolution of mid-level and near-tropopause vertical velocity in the control simulation of the four modes of convection is first presented, before the upper tropospheric divergence itself

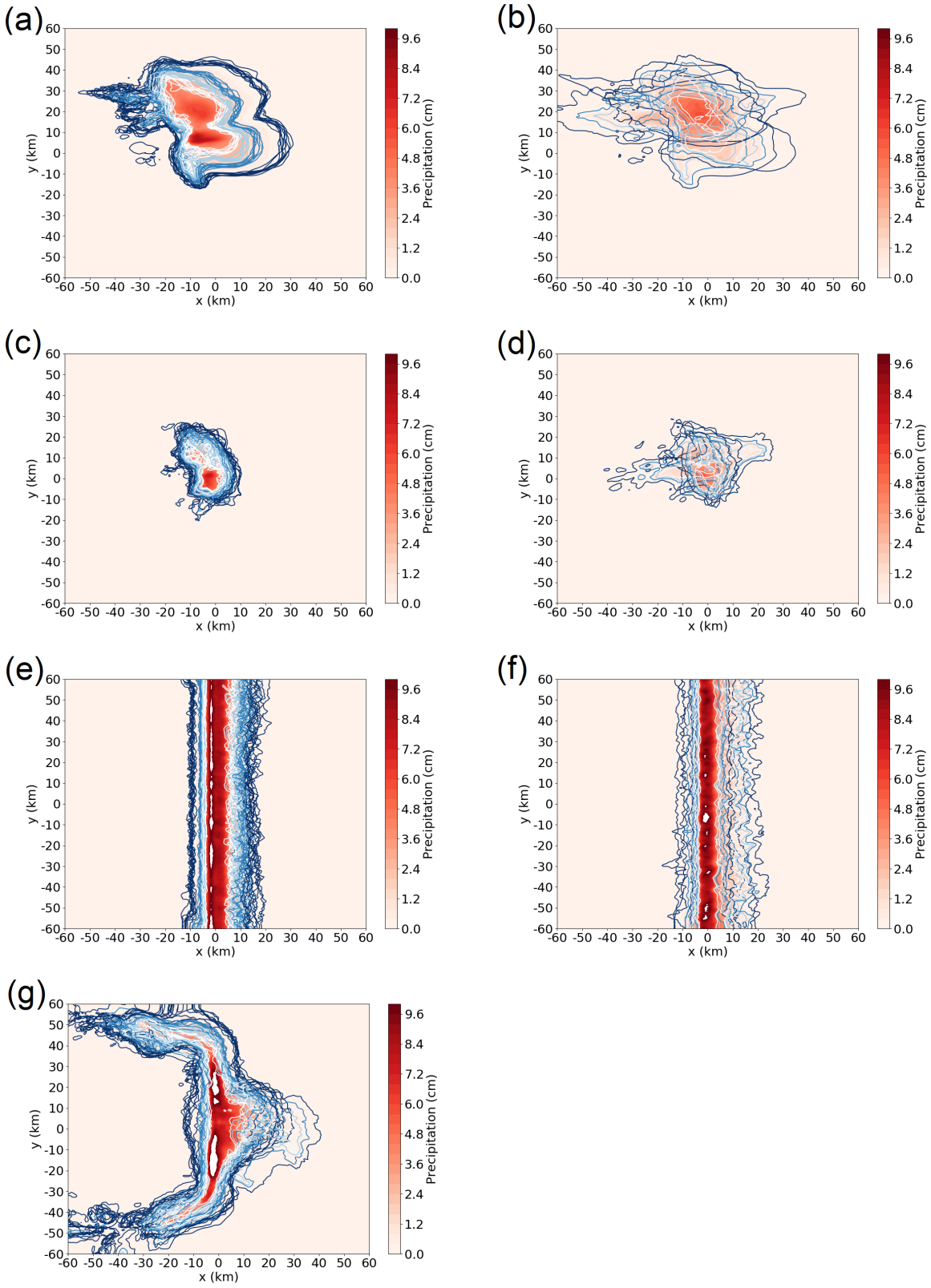

Figure 3.5: Spatial distribution of mean precipitation accumulation (red colour scale; if a mean of 100 mm is exceeded: white) and isolines for 1, 10, 20 and 30 mm (dark blue to white). Top (a, b): spaghetti plots for supercell; second row (c, d): regular multicell; third row (e, f): infinite-length squall line; bottom (g): finite-length squall line. The left column (a, c, e and also g) displays the ensemble and the right column (b, d, f) perturbed convective momentum transport simulations (in case of the infinite-length squall line, only the ensemble is available).

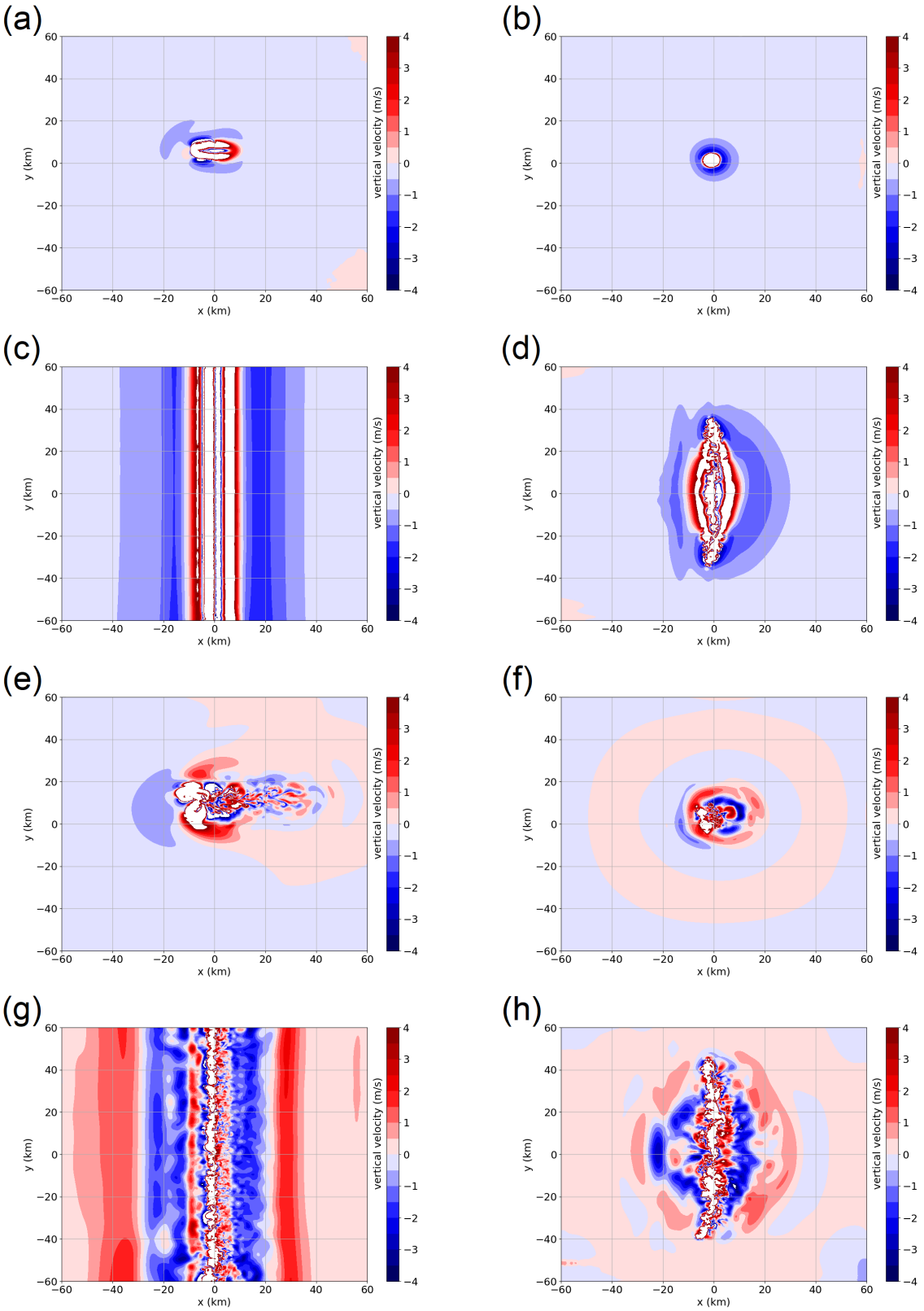

Figure 3.6: Spatial distribution of vertical velocity w at 6 km altitude for the control simulations. Top four panels: after 25 min for (a) supercell, (b) regular multicell, (c) finite-length squall line, (d) finite-length squall line. The second set of four panels shows the evolution after 50 minutes (e, f, g, h, same order, bottom four panels) and the part on the next page shows the evolution after 90/90/75/75 min (i, j, k, l). The convective cell cores appear in white, as they (largely) exceed ±4 m/s. The figure is continued on the next page.

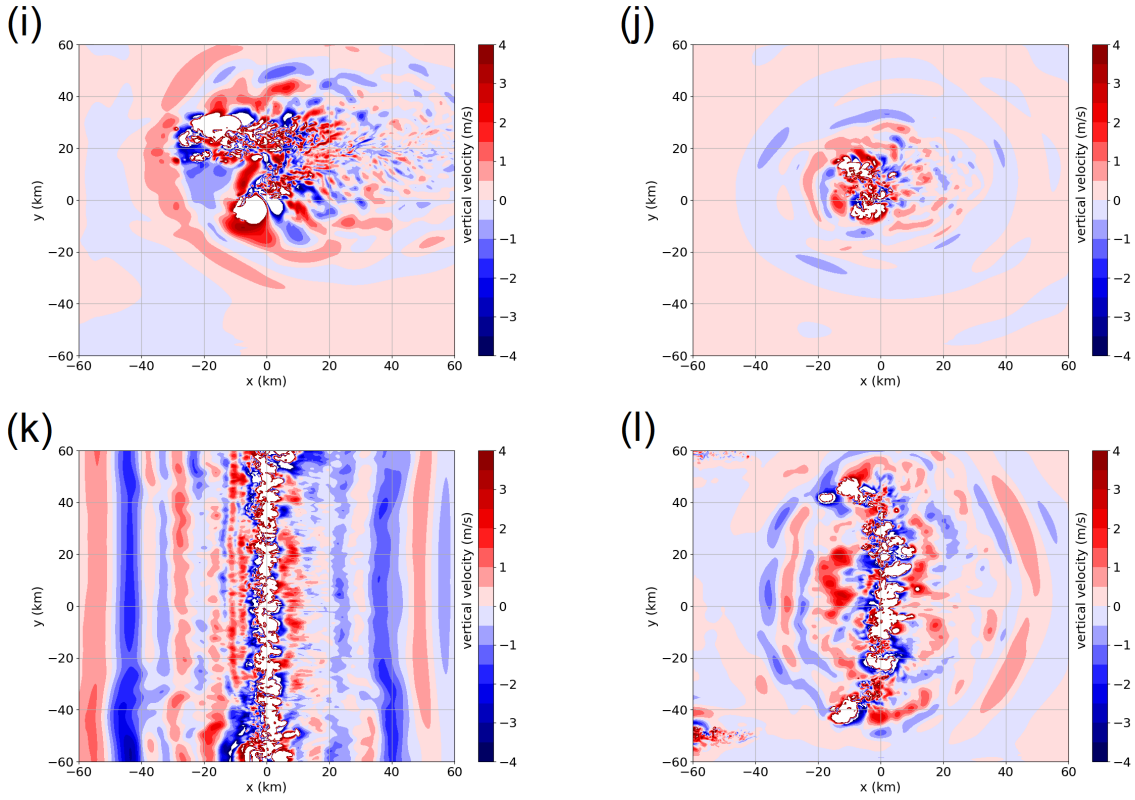

Figure 3.6: Continuation of the figure on the previous page (i, j, k, l).

is analysed in detail (Section 3.3.5). The vertical velocity in the middle troposphere is shown in Figure 3.6. After 25 minutes of simulation time, the gravity wave signal that propagates away from the convective cells (which themselves are white) is represented by an outer ring of weak downward motion (so-called *subsidence*) in the supercell and the regular multicell simulations. That ring is still restricted to a very small region within 20 km (10 km) of the convective core, located close to the origin. In both of the squall line simulations, the convection develops a little bit quicker and the subsidence ring has already grown further, reaching more than 30 km outward from main convective line. Such a ring of subsidence has been documented regularly in literature (see Figure 2.2b at x =200 to 250 km in Chapter 2; Bretherton and Smolarkiewicz [1989], Mapes [1993] and many after them, e.g. Bierdel et al. [2017]). This is a response to and compensation for the upward mass transport that the convection imposes: the conditions in the environment surrounding convective cells is adjusted by this process.

Looking at w after 50 minutes (Figure 3.6), subsequent gravity wave signals partially lead to upward motion in the middle troposphere. In the supercell case (Figure 3.6e), the signal is clearly much more extensive in the direction along the wind shear than in the meridional direction, nearly perpendicular to the wind shear. Substantial gravity wave activity occurs over the area 20-40 km east of the supercell core, where higher frequency gravity waves are superposed onto one another. Upstream of the supercell, the motion is still downward.

The signal associated with the regular multicell is still largely circular, with alternating upward and downward motion. Looking at the infinite-length squall line, a lot of upward motion in the middle troposphere occurs, which has propagated slightly further upstream than downstream to an area covering a range up to about 40 km away from the y-axis. However, the wavelengths are relatively long (still). In case of the finite-length squall line, the pattern is similar to the infinite-length squall line. However, the area covered is comparatively reduced, reaching locations up to 30 km away from the y-axis.

In the last panel (90 and 75 minutes), waves with shorter length also spread out substantially: for the supercell case, about half of the domain extent in the northeastern corner is dominated by the shortwave signal. The asymmetric propagation occurs due to the strong westerly upper tropospheric flow, leading to a mean tropospheric wind that is also eastward. However, the convective cores remain near the centre (especially the southern one).

The shorter wavelength signals for the regular multicell still stick to a portion of the domain within about 30-40 km radius of the convective cores. The convective cells also nicely stick to the centre. Similarly, weak

(slightly eastward) propagation of the infinite-length squall line has occurred. Associated shortwave gravity waves have occupied more or less the whole domain by now, as opposed to the finite-length squall line, where most effects are restricted to a region up to about 40 km from the y-axis. The southern most 10 km of the domain also does not show strong gravity wave signals. Exception to the latter is the first local signal from newly initiated convective cells at the southwestern corner of the domain.
Figure 3.7 shows the vertical velocity at a level near the tropopause (within 0.5 km). The boxes over which further diagnostic quantities are integrated (following Sections) are also outlined accordingly, with black and purple rectangles. The simulations are split into two time intervals, as mentioned in Section 3.2.4: the first interval before the snapshot in Figure 3.7 and the second interval covering the part of the simulation afterwards. The box is chosen such that the flow effect of the convection, visible as ripples in the wave signal at the tropopause level, is still limited to the region (mostly) within that horizontal extent. By the time of the snapshot in the Figure, only a small fraction of the longwave gravity wave signal left the region of the box.
Comparing the four modes of convection, Figure 3.7 shows clear contrasts. The supercell simulation (Figure 3.7 a) has a comparatively large region over which shortwave signals occur near the tropopause. The box size over which outflow is diagnosed has to be sufficiently large that it covers the adjustment region of shortwave gravity wave activity. On the other hand, shortwave variability only occurs in an oval that is restricted to a comparatively smaller region in the regular multicell simulation (Figure 3.7b). For a fair comparison, both integration boxes are set over the same spatial extent. A region where near-tropopause boundary reflection effects are suspected to occur can be identified in the infinite-length squall line simulation: regions away from the centre ($y = 0$) have a wider zonal extent over which shortwave w variability is strong, compared to the central region. That pattern in w is not present in the display of the finite-length squall line as a consequence of the arch shape, which covers only a restricted part of the domain.
The significance of propagating gravity wave signals for the divergence can be inferred from the comparison of two time intervals diagnosed in this study. An important contrast between the two time intervals is to which extent the propagating signal of gravity waves, and other turbulent motion away from the core region of the convection into the ambient region, has taken place, as Figures 3.6 and 3.7 show. If the two time intervals reveal substantial deviations in the magnitude or conditional behaviour of their upper tropospheric convective outflow, it implies that the propagating gravity waves actively modify the feedback from the deep convection to its environment. If no contrast between the two time intervals is detected, the effect of the escaping gravity waves has to be unimportant.

3.3.4 Divergence profiles

The next section explores the main quantity of interest in this study within the four ensembles. For each of the four organisational types of convection, the evolution of basic characteristics of the tropospheric divergence profile is presented and evaluated to set an appropriate vertical integration mask.

3.3.4.1 Ensemble evolution Figure 3.8 shows the time evolution (x-axis) of the vertical divergence profiles (y-axis) for each of the four basic types of convective organisation (starting from $t = 5$ minutes). Initially, the convection has not developed. It requires roughly 30-50 minutes before intense convection develops, as suggested by isolines in the figure. Note, that the colour scale of the isosurfaces and the isolines use different values to allow for a distinction between the pattern of individual ensemble members and the ensemble mean value of strong divergence. In the top and bottom row, strong low-level convergence ($z < 3$ km) starts to exceed the isoline threshold after about 45 minutes ($\pm$20 minutes). With a slight delay (about 15-20 min), strong signals of mass divergence set on and stick to a layer between 8 and 13 km altitude, around and just below the tropopause.
The mass divergence (convergence) signals in the regular multicell both set on after an hour in the upper (lower) troposphere. Afterward, they expand their vertical extent with time. In this set of simulations, the upper tropospheric divergence also sticks to the 8-13 km layer. The low-level convergence expands quite much after about 1.5 hours, as to nearly cover the full lower half of the troposphere.
The ensemble spread is narrow for the two upper panels (Figure 3.8a, b), as suggested by the spaghetti lines. Among the squall line ensemble members, there is more spread: the lower panel suggests a typical spread of up to about 1-2 km in the vertical for each contour of mass divergence (convergence) during the second hour (maximum/minimum level of isoline; see also Appendix B, Figure B3). Therefore, Chapter 5 and Groot and Tost [2023] provides a detailed analysis of the ensemble evolution in this set of simulations.
Of particular interest is the mid-tropospheric contour of neutral divergence in Figure 3.8 (white isolines): this marks the boundary between the upper tropospheric divergent outflow and the *entrainment*/inflow region of convection in each simulation. It settles at about 5-6 km altitude, after rather noisy behaviour in the first 30 minutes due to (mostly) undeveloped convection. It rises to 7-8 km altitude for each mode of convection

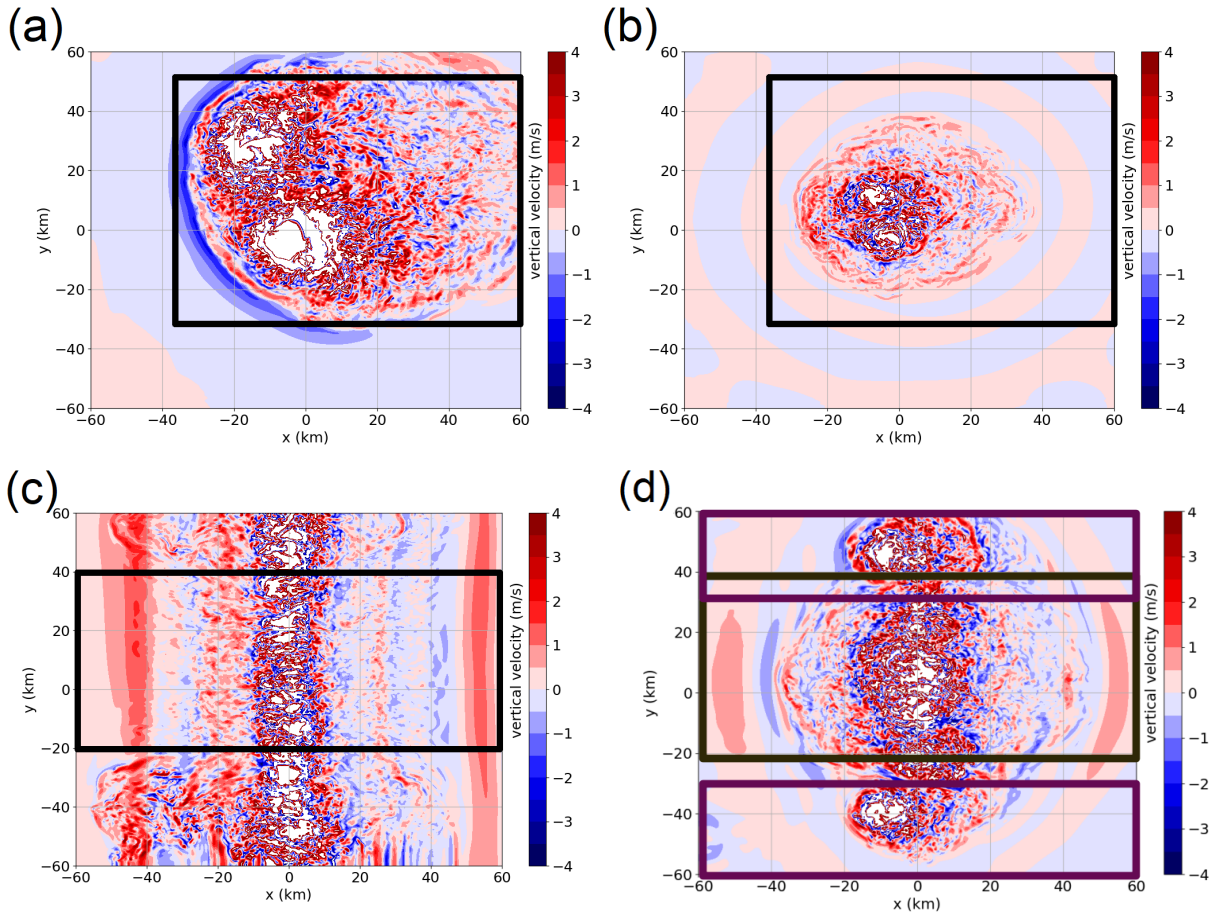

Figure 3.7: Top view of w at tropopause level after 90 minutes for the control simulations of (a) the supercell simulation, (b) regular multicell and 75 minutes (c) for the infinite-length squall line and finite-length squall line (d). The thick black outline of the rectangle defines the outer region of the horizontal box over which diagnostics are integrated and the time stamp that belongs to it defines the end point of the first integration interval. That stamp corresponds to the start of the second integration interval as well. As in Figure 3.6 regions that mostly exceed ±4 m/s (white) indicate direct convective motion, which means that an updraft (downdraft) core is present locally.

eventually (after about 90 minutes of simulation), but not before shortly dropping to about 4 km altitude in the infinite-length squall line simulations (at about 60 minutes). The strength of the upper tropospheric divergence signal gradually increases towards the end of each simulation.
Moving to the right panels with the finite-length squall line, a substantial amount of ensemble spread is identified. Nevertheless, it is mostly smaller than for the infinite-length squall lines. The outflow divergence has settled to levels of about 7.5 to about 13 km quite soon and remains at those levels along the outer parts (at the edge of the finite-length squall line). The convergence zone at low levels seems to slowly lift with time in this ensemble, reaching an upper bound of about 7 km after 100-120 minutes. The divergence signal seems to be much stronger in the edge region of the finite-length squall line than at its centre as well. Even though the time evolution of divergence (convergence) in the finite squall line simulations (centre region) share many similarities with the infinite-length squall line, the first hour has a contrasting evolution. Signals are nonetheless rather weak in general during that hour.
Divergence profiles complementary to Figure 3.8 for the physics experiments are provided in Figure B2 of Appendix B.

3.3.4.2 Outflow integration mask From the previous section, it could be concluded that the lower boundary of the upper tropospheric divergence signal hovers mostly at levels between 5 and 8 km. However, after 80-120 minutes, a clear convergence signal occurs in all three modes of convection at 5-6 km height. The lower boundary of the integration mask for the upper tropospheric divergence is best set at 7 km, as this boundary is most suitable to differentiate between the regions of convergence and divergence. Therefore, results using this altitude threshold are used for the analysis of the next Section. The upper boundary is

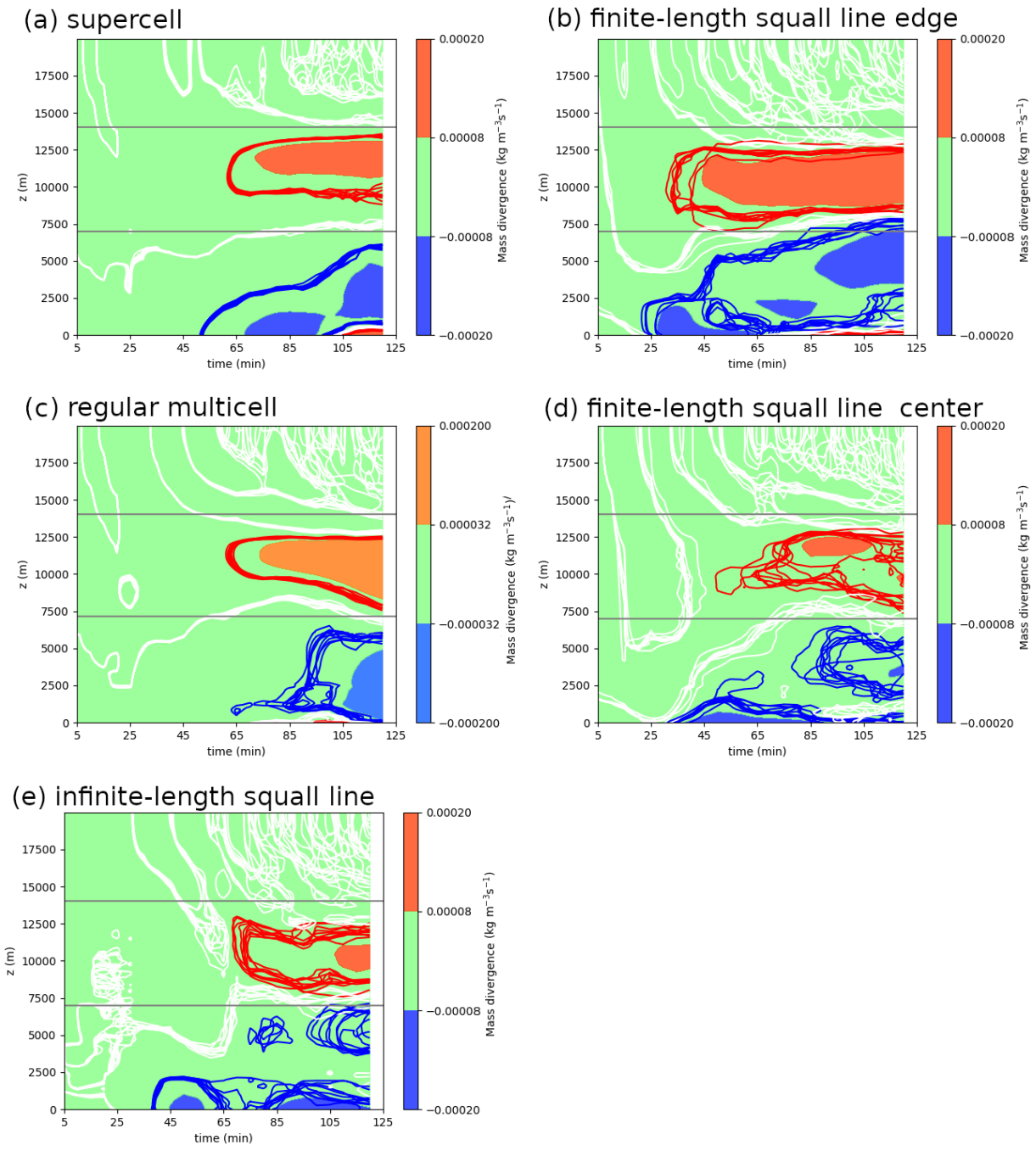

Figure 3.8: Vertical cross section of time evolution of mass divergence (convergence) as a function of altitude for three basic modes of convection, averaged over the ensemble (filled) and for the individual members (spaghetti contours; blue: -5×10^{-5} kg m^{-3}s^{-1}, white: 0 kg m^{-3}s^{-1} (i.e. neutral divergence), red $+5\times10^{-5}$ kg m^{-3}s^{-1} (four of the five plots) and $\pm2\times10^{-5}$ kg m^{-3}s^{-1} (only c)). Note that the contouring values differ from those corresponding to the colour fill. The finite-length squall line is further split-up into its edge and centre regions (right column).

quite stagnant at 13, sometimes 14, km altitude and therefore the upper boundary is set to 14 km, which is about 2 km above the tropopause (see also Figure 3.1).
Note that the figures illustrate the ensemble spread. That means, they exclude physics perturbations. Especially for these perturbed physics perturbations (notably −40% latent heating constant) the vertical profiles may substantially differ from the ensemble, due to lower tops of the convective clouds (see Appendix B).

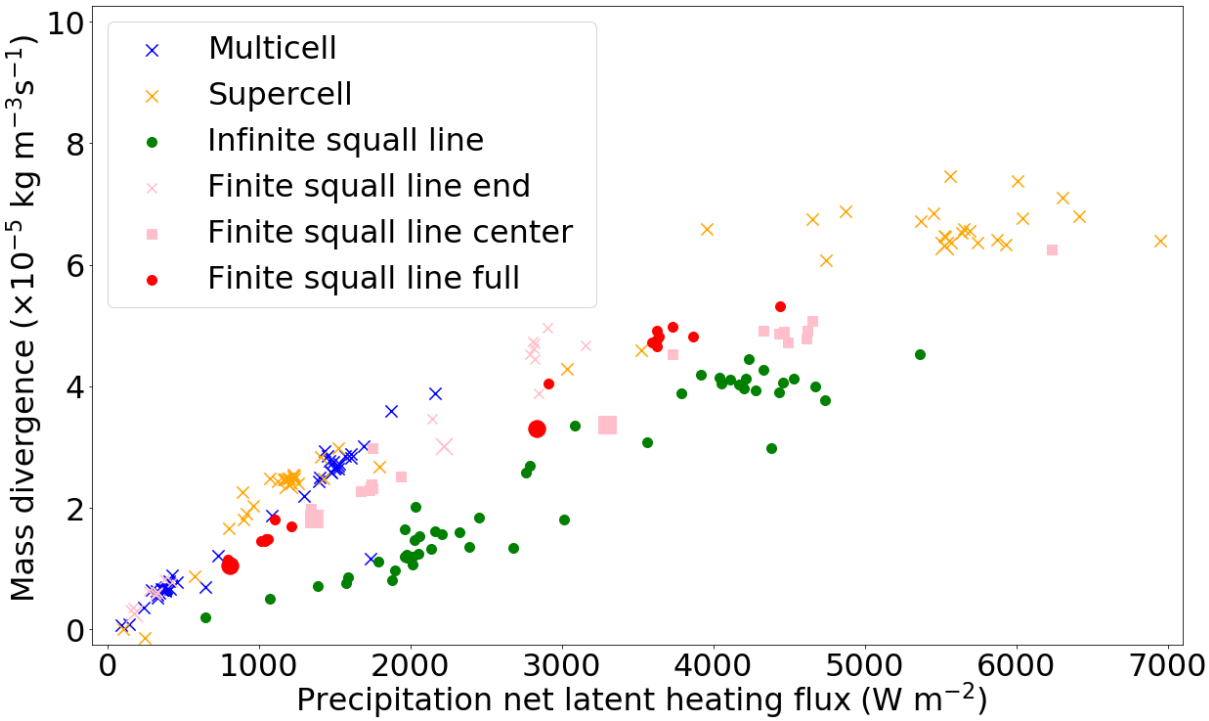

Figure 3.9: Full dataset of upper tropospheric mass divergence integrated over the layers 7-14 km versus net latent heating. Included are 206 records, covering 4 modes of convection during two time intervals. The larger symbols indicate simulation data from extended domain simulations (8 in total).

3.3.5 Relation between mass divergence and net latent heating

Figure 3.9 presents the vertically integrated strength of divergent outflows as a function of net latent heating by precipitation. Purely focusing on the three main scenarios (see leftmost three of the four columns in Figure 3.3), the separation between the infinite-length squall lines on the one hand and both the supercells and regular multicells on the other hand at given net latent heating is obvious: the latter two have increased divergence compared to (almost) all the squall line simulations. Nonetheless, this contrast is reduced at higher latent heating rates (i.e. over roughly 3000 W m^{-2}).
The expected increase of divergence with increasing net latent heating is generally present within each mode of convective organisation.
More specifically, the initial slope that signifies the ratio between mass divergence and latent heating is much higher for the regular multicells and supercells than for the squall lines. For increased precipitation rates, the slope seems to decrease compared to that at low latent heating rates. On the contrary, the squall line slope even appears to increase with precipitation intensity, although this not so clear. The robustness of the slope increase of squall lines is questionable. The lower slope for the supercell reduces the gap between the two regimes at higher latent heating rates: on the one hand regime that the supercell and regular multicell seem to follow and on the other hand a regime that the (infinite-length) squall line seems to follow.
Interestingly, the physics perturbations do not substantially affect the suggested regimes and resolution also has no noticeable effect in the plane of Figure 3.9 (it should be noted that simulations with physics perturbations are included in this Figure!). The isolated convection regime (i.e. nearly-3D outflow, applicable to regular multicells and supercells) is surprisingly linear at precipitation intensities up to about 2000 W m^{-2}. Moreover, the contrast in slopes between the two regimes that are identified is suggested to exceed a factor two: on the one hand, the steep sloped line that would describe the two isolated modes of convection reaches an upper tropospheric divergence of almost 4×10^{-5} kg $m^{-3}s^{-1}$ at 2000 W m^{-2}. On the other hand, only one record of the infinite-length squall lines reaches about 2×10^{-5} kg $m^{-3}s^{-1}$ at about 2000 W m^{-2} (≈ 3 mm h^{-1}) precipitation rate.
When one now focuses on the finite-length squall line simulations (pink/red, Figure 3.9), the records that belong to its end region are very much in line with the mass divergence of supercell simulations. At low precipitation intensities, the mass divergence increases as rapidly as for the supercell. In addition, both supercells and end regions of finite-length squall lines have a slope between mass divergence and precipitation that reduces at higher precipitation intensities in very similar ways.
That decrease of the slope with higher precipitation rates also occurs for central regions of the finite-length

squall line, but the mass divergence is systematically reduced compared to the end regions of the finite-length squall lines. Hence, the behaviour of the finite squall line centres aligns better with the infinite-length squall line simulations. In spite of that, the mass divergence is systematically reduced even stronger compared to the finite-length squall line centres in the infinite-length squall lines.
In general, the full domain integration of the finite-length squall line leads to intermediate behaviour, with the amount of divergence in between those amounts for the centre and line end. That is a consequence of averaging over the centre and end regions. Reduced slopes at high precipitation intensity also occur for the full integration of finite-length squall line divergence.
The initial slopes between precipitation intensity and mass divergence suggests that the low precipitation intensity can obey to two limit regimes:

- a 2D outflow regime, with reduced mass divergence
- a 3D regime, with comparatively increased mass divergence in the outflow region

The quasi-2D regime occurs as neighbouring cells compensate each other's divergent outflows efficiently in squall lines. Even though three dimensional outflow from the individual cells in a squall line exists, the meridional component is largely compensated by the neighbouring convective cells, as they also produce (opposing) meridional outflow. In the integration of the divergence over all convective cells, these meridional components compensate. Hence, they produce no net divergence along the y-axis of the simulations. Therefore, the zonal component of the net divergence is an order of magnitude larger in an infinite-length squall line than the meridional component (the next Section highlights the effect for finite-length squall lines, Section 3.3.6). The ratio between mass divergence in the two regimes could be around a factor of three, according to the dataset visualised in Figure 3.9! At higher precipitation intensities, these regimes are apparently not obeyed in the simulations. So a line at intermediate slope between the two regimes around which all data points scatter at high net latent heating rates might exist.
Given these two idealised regimes that are approached by some simulations, infinite-length squall lines represent a nearly-2D form of convection [similar to argumentation by e.g. Moncrieff, 1978, 1992, on archetypal models for convection]. On the other hand, initially isolated convective cells that are circular in an environment without convection follow the 3D regime. At increasing precipitation or latent heating rates, outflows from deep convective cells are more likely to collide. They mimic idealised point (i.e. 3D convection) or line (i.e. 2D convection) sources less well. The collisions would result in an interference of outflows, which effectively creates an intermediate outflow dimensionality between 2D and 3D. The conceptual model of collisions and intermediate effective dimensionality may largely explain the variability in divergent outflows as detected. It could be seen as a non-linear effect of deep convection on its divergent outflow, induced by convective organisation. Without an upscale convective organisation effect, resemblance of idealised 2D or 3D regimes could have maintained during over both of the two time intervals. In the finite squall line case, the mixed or intermediate dimensionality is already effective at low precipitation intensity. This concept with qualitative explanation connects the findings of the LES-simulations with Bretherton and Smolarkiewicz [1989],Nicholls et al. [1991] and Mapes [1993], who derive a separate equation for flow induced by line and point sources of heating. Their model can be used to represent convective systems and resulting gravity wave response [e.g. Pandya and Durran, 1996].
Investigating the set of larger symbols in the scatter plot (Figure 3.9) - those symbols that represent a supercell simulation at an extended domain - they appear within the range of data points covering the simulations with small ensemble perturbations. Similarly, for the finite-length squall line simulations, the mass divergence to net latent heating ratio is often slightly lower than that associated with the ensemble mean. Nevertheless, divergence in the extended domain simulations is never substantially outside of range of most perturbed and ensemble simulations within each mode of convection.
The ordering of the different modes of convection in Figure 3.9 is unaffected by all the studied experimental factors - with regular multicell, supercell and finite squall line ends inducing most mass divergence at a given net latent heating rate, followed by the full domain integration of the finite-length squall line, the finite-length squall line centre and lastly the infinite-length squall line with weakest mass divergence. That ordering clearly indicates that mass divergence at given precipitation rate depends on the organisation of a convective system. Initially, it is suggested to manifest as a 2D outflow regime (line source) with weaker mass divergence on the one hand and a 3D regime (point source) enhancing mass divergence on the other hand. At high precipitation or net latent heating rates, and over the course of time, the convective systems do not stick to these idealised regimes.
By focusing on the multicell simulations in Figure 3.9, it can be deduced that contrasts in the normalised divergence (relative to net latent heating) between the first and second time interval do not or hardly exist. Based on this argument, and closer inspection of the spatial distribution of divergence patterns in the simulation dataset, it is very likely that the spatial precipitation (heating) pattern is solely accountable for the extent over which upper tropospheric divergent flow occurs.

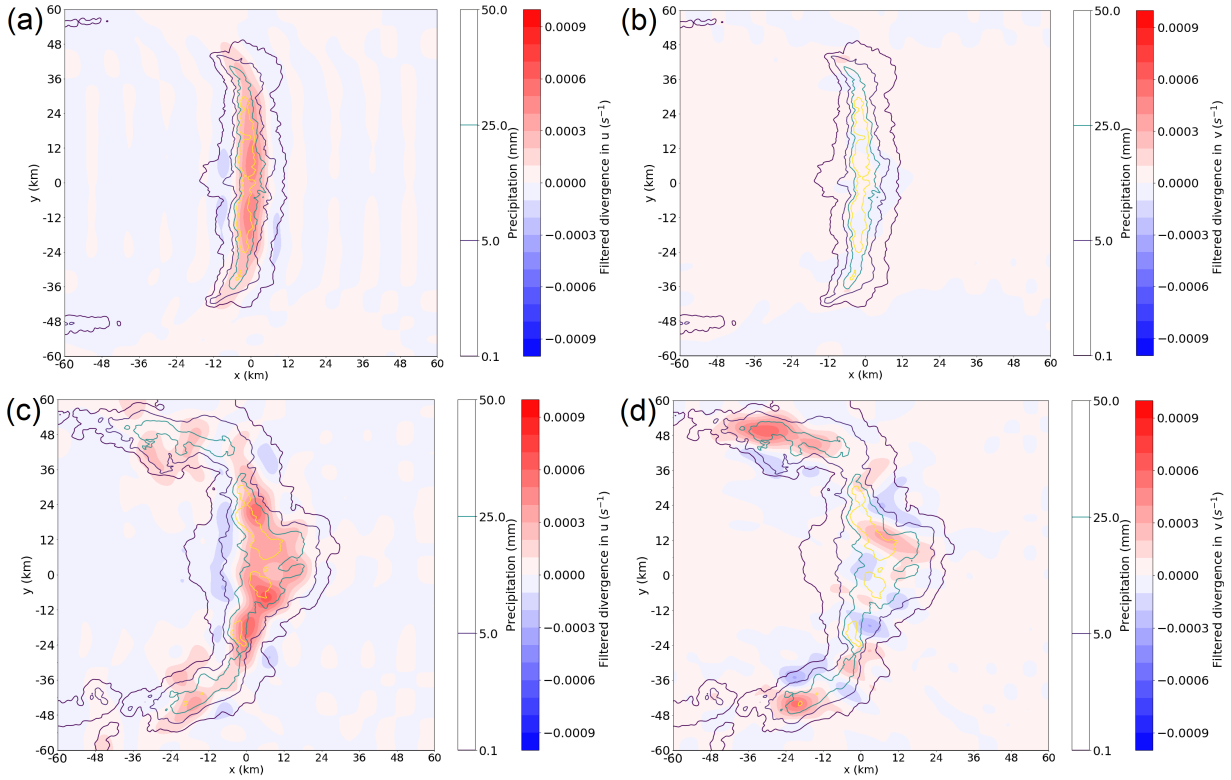

Figure 3.10: Spatial distribution of filtered divergence integrated over altitudes of 7-14 km for a finite squall line during (a, b) the first and bottom (c, d) the second time interval. Wavelengths that fit more than 20 times in the domain have been removed with a discrete cosine transform. Contours indicate the accumulated precipitation pattern during each of the two time intervals (0.1, 5, 25, 50 mm, as displayed in one of the two colour bars). Both the zonal (a, c) and the meridional divergence components are displayed (b, d).

3.3.6 Zonal and meridional divergence components in finite squall line

The existence of two outflow regimes (2D and 3D divergence) has been

- Suggested in the previous section
- Suggested by analytical expressions of flow perturbations derived from a linearised gravity wave model forced by heating [Bretherton and Smolarkiewicz, 1989, Nicholls et al., 1991, Mapes, 1993, Pandya and Durran, 1996, Nascimento and Droegemeier, 2006]
- Documented for related pressure perturbations and updraught strengths by Morrison [2016a,b]

In this section, the u- and v-components of the upper tropospheric divergence are separately investigated for the finite-length squall line to complement Section 3.3.5 and the mentioned studies.
Figure 3.10a, b shows that during the initial time interval, the meridional component of the divergence is negligible throughout most of the domain. The comparatively small contributions by the v-term arise predominantly at the end points of the squall line: at the northern and southern edge. The pattern in the v-term of the divergence is consistent with this part of the finite-length squall line resembling the 3D outflow regime. Similar patterns have been identified for the infinite-length squall line (not shown), but without an enhanced meridional component of divergence at the squall line end there. Practically all divergence occurs in the u-component initially, which is consistent with the manifestation of a 2D-like outflow regime in the infinite-length squall line and the centre region of the finite-length squall line (Figure 3.9).
During the second time interval, the shown v-components develop particularly strongly on the northern and southern arching regions of the squall line. Both components are of the same order of magnitude, but that is to be expected for a strongly curved squall line. The pattern of squall line curvature is clear from the accumulated precipitation (and, similarly, the simulated radar imagery in Figure 3.4l). The possibility that outflow collisions occur and the effective flow resembles a regime governed by a mixture of 2D and 3D regimes - as a result of interference between outflows from individual convective cells - is strongly supported by both Figure 3.9 and 3.10. Hence, Figure 3.10 provides further evidence for the conceptual interpretation proposed Section 3.3.5.

The mean divergence in Figure 3.10a is about an order of magnitude larger than in Figure 3.10b in the squall line centre. This is consistent with the infinite-length squall line, in which the difference is about one order of magnitude too. In the bottom panels of the figure, that contrast has strongly reduced, as a result of curvature in squall line - accordingly with expectations of bending mixed 2D-3D convection. Therefore, the leading order divergence variability in Figure 3.9 can confidently be attributed to the dimensionality of outflows (2D versus 3D) and, correspondingly, the presence of a pulse or line source of latent heating.

3.4 Discussion

3.4.1 Coverage of outflows: spatial and temporal analysis windows

Upper tropospheric outflow from deep convection has been investigated in an extensive set of large eddy simulations by integrating the mean mass divergence in 3D over a region surrounding the convective cells (horizontally) and over 7-14 km altitude. Figure 3.8 and divergence profiles (see also Appendix B, Figures B2 and B3) revealed that the lower boundary is the most critical of the two. Therefore, the integration has been repeated for the 6-14 km layer. The appearing patterns in a latent heating versus divergence diagram comparable to Figure 3.9 are not sensitive to the lower boundary.
The integration procedure has been executed for two time intervals separately: a first time interval, in which only the fastest gravity waves escape the box of integration, and a second, in which a large proportion of the gravity wave signal has escaped the integration mask. Even though some potentially relevant gravity wave effects with consequences for upper tropospheric divergence could have escaped this integration box, the results suggest that this is not the case. That such an escape did not have consequences for diagnosed upper tropospheric divergence can be justified with the following arguments:

- As a first argument, the mechanism of gravity waves is to restore density anomalies with fluctuations, which are averaged out when integrated over longer distances in the quasi-horizontal plane.
- Second, the similarity of the slope between mass divergence and net latent heating (1) during the first and second time interval for regular multicells and (2) the similarity of that slope to supercell simulations during the first time interval suggests that an escape of gravity waves plays no role to the mass divergence. It certainly does not dilute the divergent outflow by underdetection.
- Furthermore, mass divergence of the outflow cannot initiate at a location outside of the convective cell's updraft itself and spatial distributions of the divergent winds (e.g. Figure 3.10) support that argument.
- Lastly, as an extension of the previous argument: by testing different integration masks for the large domain supercell simulation, it has been verified that mass divergence only decreases relative to the precipitation rate (!) when integrating over a too large domain. This is a sign of a substantial increase in the subsidence within the integration mask, as soon as the mask is altered; the subsidence develops in the near surroundings of convective cells as gravity waves propagate away [see Bretherton and Smolarkiewicz, 1989, Mapes, 1993, and Figures 3.6 in this chapter and 2.2b in Chapter 2]. The tests essentially suggest that the essential divergent outflows are included by including the precipitation cores within the integration mask. This is consistent with the spatial distribution of the divergence signals found and with the linear gravity wave adjustment model triggered by convective heating patters, as documented in Bretherton and Smolarkiewicz [1989], Nicholls et al. [1991], Pandya and Durran [1996].

An integration mask covering the convective cores and ending just outside of the area of precipitation accumulation leads to the detection of a large proportion of the divergent outflows. Little dilution from convergence/inflow may occur, if the appropriate vertical levels are selected for vertical integration.

3.4.2 Deviations of perturbed simulations from main upper tropospheric divergence structure

3.4.2.1 Responses to physics perturbations In Figure 3.9 one can see a very robust signal of convective organisation, with significance for the divergent outflows. However, a few odd data points occur. By design and nature, the strongest physics perturbations (e.g. -40% latent heating constant) suppress the deep convection (see Section 3.2.3.2). While some deep convection, and consequent precipitation, still occurs in the simulations with the strongest physics perturbations, the divergent outflow does vertically not fit in the integration mask as well as for the ensemble and the large majority of other simulations. It is verified that data points appearing as outliers in Figure 3.9 shift toward those of similar organisation type, if the vertical mask of divergent outflow integration is shifted appropriately to other vertical levels (with appropriate density weighting). An extension of Figure 3.8 can be found in Appendix B. The dataset visualised in Figure B2 of this appendix shows how the integration masks of outliers have to be shifted for better alignment of particular simulations with the general pattern in Figure 3.9.

3.4.2.2 Specific role of convective momentum transport The strong order in Figure 3.9 directly suggests that convective momentum transport does not have a direct systematic impact on divergent outflow from deep convection in the presented experiments. That does not imply that convective momentum transport does not play a role at all: it can modify the evolution of convective systems, affect convective aggregation indirectly and thereby affect the precipitation intensity. The latter two do affect the upper tropospheric divergent outflow, as the dataset presented in Figure 3.9 revealed. Even if some scatter in the mass divergence occurs at a given precipitation rate and convective organisation or aggregation, it turns out that it does not systematically relate to increases or decreases in convective momentum transport. Such scatter mainly occurs at high precipitation rates for the infinite-length squall lines and supercells in Figure 3.9.

The absence of a direct effect of convective momentum transport on divergent outflows from deep convection may appear surprising. Firstly, Badlan et al. [2017] suggest that proper simulation of an effect of convective momentum transport on the dynamical evolution around convective systems is not ought to be investigated on small domains. However, this implication specifically applies to simulations with periodic boundary conditions, whereas open boundary conditions have been applied here. Furthermore, the potential concern about small domains is addressed specifically with large domain simulations in this Chapter. Therefore, the experimental design to detect the possible effect of CMT on the convective systems' outflows can be regarded appropriate in this work.

Furthermore, parts of the momentum redistribution in convective systems studied in Badlan et al. [2017] are caused by horizontal pressure gradients. In the models of Bretherton and Smolarkiewicz [1989], Nicholls et al. [1991], Mapes [1993], these horizontal pressure gradients around organised convective systems typically occur because of the gravity wave signals triggered by heating (remotely) and the convective heating itself (locally; see Figure 2.2c, f). Here, the role of these horizontal pressure gradients in the redistribution of momentum is considered separately from the vertical advection of horizontal momentum (mean eddy term in Badlan et al. [2017]). This vertical advection term is treated specifically as the direct effect of convective momentum transport on deep convective divergent outflows in this work. The horizontal pressure gradients resulting from gravity wave propagation partially determine the main signal identified in this Chapter (Figure 3.9).

A more elaborate discussion on the LES, with some additional profiles of simulations with perturbed vertical advection of horizontal momentum, is provided in Appendix B.

3.4.2.3 Adjusted low level stratification The signal of convective organisation in Figure 3.9 is robust. This is because the ordering of the different modes of convection is robustly present among a dataset with the background ensemble, physically perturbed simulations, the simulations on extended domains and simulations at different resolution. Additionally, initial potential temperature profiles are perturbed in an another set of simulations (see Section 3.2.3.3 and Figure 3.3) to test whether the stratification of the low levels has a substantial impact. The dataset obtained suggests that this is not the case. Low-level perturbations are also used for the *wide ensemble band* of finite-length squall lines. The structure in Figure 3.9 is well established. This implies that a wider range of initial conditions than just those of a very specific thermodynamic profile is explored with the dataset. The dataset strongly suggest that the magnitude of divergent divergent outflow relates to net latent heating primarily and in a coherent way, irrespective of the strength of near-surface inversions and the magnitude of moist instability.

3.4.3 Two mass divergence regimes at low precipitation rates

Figure 3.9 suggests that there is about 1500 W m^{-2} of latent heating rate needed for 1×10^{-5} kg $m^{-3}s^{-1}$ of divergence in an infinite-length squall line. On the other hand, this is only about 500 W m^{-2} for the regular multicell and supercell regime. The proportionality between these two regimes is well over a factor two, and likely very close to three and π.

The idea of the finite-length squall line simulations is that the outer part at both of the squall line ends represents a regime where convective cells can freely induce their outflow in a 3D space - as both ends are combined (as if the centre is "removed"), the divergence regime appears to be 3D: similarly to the case of a multicell and supercell. The centre, however, is geometrically somewhat restricted, as in that of an infinite-length squall line. Infinite-length squall lines only allow for outflow in one horizontal direction. The conceptual understanding is confidently supported by the magnitudes of two components of the mass divergence in infinite-length squall line simulations: outflow in the zonal direction exceeds that in the meridional direction by an order of magnitude, consistently with findings pointed out by Nascimento and Droegemeier [2006]. Similarly, in the finite-length squall line centres, divergent outflow is initially much larger (an order of magnitude) in the direction normal to the finite-length squall line than in that parallel to the squall line. Thereby, dynamics induced by small cells (at short wavelengths) are compensating each other in the parallel

direction (Figure 3.10). That provides further support for the idea of two outflow regimes.
Outflow simulations with analytical expressions based on the numerical model of Bretherton and Smolarkiewicz [1989], as derived by Nicholls et al. [1991], suggest that the ratio of convective outflows between a line source and point source is a factor of 2π in their limit case. That stems (in their calculations) from a conversion of the delta function from radial geometry to an x-y plane [Nicholls et al., 1991]. A mechanism that could explain the deviation of about factor two between the linear gravity wave models and large eddy cloud simulations has not been found yet. Theoretical support for different regimes of updraft and pressure perturbations between 2D (line source) and 3D (a point source) in a weak shear environment is also provided by Morrison [2016a]. The updrafts and pressure perturbations as studied by Morrison [2016a] drive the outflows studied here; outflows relate to updrafts through continuity. Morrison [2016a] derived a deviation factor of two theoretically and subsequently compared the findings to cloud resolving simulations [Morrison, 2016b].
The robustness of the results, together with the arguments above, give confidence in the impact of outflow dimensionality on the magnitude of the divergent winds. Furthermore, the intermediate slope between outflow divergence and precipitation rate, in comparison to the initial 2D (shallow slope with precipitation rate) and 3D (steep slope with precipitation rate) regimes, suggests that convective aggregation likely affects the dimensionality of convective outflow in the upper troposphere. This is suggested, since the intermediate slope appears to be a general feature at high precipitation intensities. Outflow likely follows a mixture of 2D and 3D regimes due to the convective organisation and interference between outflows of individual cells, as caused by collisions and subsequent interference. When aggregates of convective cells collide with upper troposhperic outflows of other convective cells, the effective dimensional constraints to the outflow would be something intermediate between 2D and 3D: the outflows first collide along the line through the updrafts and become nearly-2D along the line. In contrary, on the outer regions the outflow can still move as if the convective cell was isolated. That outer region resembles a 3D outflow regime, and any mixture conceptually creates ovals of outflow similar to the finite squall line (even if the supercells also reveal the intermediate behaviour between two the regimes and collisions of outflow after some time).
The key finding is thus that outflow strength from deep convection is linearly linked to net latent heating rate in the idealised case of isolated convection, resembling a point source, or 2D convection along an infinite-length line. But on the long term, convective organisation and aggregation likely modifies the relationship to something that depends non-linearly on latent heating rate, as the outflow develops less a idealised structure: the geometrical constraints, representing something intermediate between a line and point source, restricts the divergent outflows.

3.4.4 Implications

The mass divergence found in the dataset (Figure 3.9) is in good agreement with linear gravity wave adjustment models, in which heating is imposed as proxy for a convective system in terms of its magnitude [Bretherton and Smolarkiewicz, 1989, Nicholls et al., 1991, Mapes, 1993, Pandya et al., 1993, Pandya and Durran, 1996].
The initial 2D versus 3D regime behaviour, with reduced divergence at higher precipitation intensities due to convective aggregation, that is suggested contrasts with the modelling and observation studies by Mapes [1993], Mapes and Houze [1995]. To understand why, a discrimination needs to be made between convective and *stratiform* parts of mesoscale convective systems. The stratiform part is the part of a mesoscale convective system characterised by layered clouds, much lower vertical velocities than the convective part. In this part, rain fall of reduced intensity may occur. Rain may also evaporate, before reaching the ground, and low precipitation rainfall is relatively homogeneously distributed in space.
Stratiform contributions to heating profiles of MCS (including squall lines) are often developing with time. These contributions to the heating profile mostly excite the second vertical mode of gravity waves, due to their typical vertical shape. On the other hand, the deep convective parts of the system (which are yet present at the start of an MCS) excite the first mode [e.g. Houze, 2004, and references herein]. These two modes were thought to be responsible for producing divergent winds at different rates as a consequence of a given local heat source. More specifically, in Mapes [1993], it is suggested that a stratiform contribution by the vertical half wavelength due to a stratiform fraction of a mesoscale convection system actually increases the ratio of divergence to net latent heating rates. Therefore, as the relative importance of the stratiform contribution to the heating in an MCS typically has to increase, a significant increase of the normalised divergence (with respect to latent heating) with life time would be expected for squall lines. This implication contrasts with the results presented here (see Figures 3.9 and 3.8).
On the one hand, this could imply that the convective systems simulated in this study do not extend sufficiently and yield any sizeable stratiform contribution to the precipitation. Indeed, the stratiform extent of the simulated squall line and supercell clouds in this study is not substantial, especially when considering

the stratiform precipitation that reaches the surface (which is turned into net latent heating); see Figures 3.4 and 3.5 and Chapter 5. The formation of a stratiform precipitation regime is expected to coincides with lifting of the level of neutral divergence, on average [Mapes, 1993, Houze, 2004]. The expectation is based on the superposition of the stratiform and convectively generated gravity wave modes in combination with a growing relative contribution of the stratiform part. In Figure 3.8, such a continuous gradual rising of the level of neutral divergence for supercells and squall lines during the second hour cannot be detected. However, at least some small fraction of stratiform system formation would often be expected within the second hour. This suggests that the results found in this study are only representative of purely convective systems, or those with very minor stratiform fractions, which is a reasonable approximation for convective systems in certain regions [Schumacher et al., 2004] (but not in others). In spite of this, these purely convective systems are important to study for a better understanding of the role of deep convection in the climate system and to improve NWP or climate models in general, or specifically parameterisations of deep convection.
On the contrary, using Figure 3.9, one could argue that a stronger increase of the mass divergence with latent heating rate occurs for the infinite-length squall line simulations at high latent heating rates, rather than at low latent heating rates (as the highest latent heating rates occur in the second hour). Furthermore, stratiform precipitation system may form out of the squall line anvils. That would be in agreement with arguments by Mapes [1993] and Mapes and Houze [1995], assuming that the stratiform fraction of the system should increase with time. However, an infinite-length squall line is in practice not very representative of most deep convection in the real world. In addition, the level of neutral divergence does not seem to rise at all for the infinite-length squall lines in Figure 3.8, which would not support arguments of Mapes [1993] and Mapes and Houze [1995]. Furthermore, the more realistic finite-length squall line is not behaving in agreement with the arguments. In the finite-length squall lines, the ratio between mass divergence and net latent heating decreases at higher precipitation rates during the second (later) time interval, as shown in Figure 3.9.
Theoretical 2D squall line models have extensively been studied by Moncrieff and co-authors [e.g. Moncrieff, 1992, and references herein]. In Moncrieff [1992], it was argued that such 2D models could be very beneficial for parameterising convective momentum transport. Trier et al. [1997] pointed out that one should be careful with assigning dimensionality of convection. Processes such as convective momentum transport in actual squall line convection can have characteristics of a mixture of 2D and 3D convection. Certain sections have more characteristics of a 2D convection regime and others more of a 3D convection regime. The finite-length squall lines suggest that the same holds for divergence profiles. Therefore, comparisons of traditional or theoretical models of idealised convection (e.g. 2D models) to cloud resolving and large eddy simulations are desired. By stimulating such model intercomparisons, the applicability of traditional practices and findings to the more complex simulation techniques can be scrutinised, as Pandya and Durran [1996] and Morrison [2016a,b] also did.
Theoretically, convectively induced divergence profiles are suggested to mimic 2D or 3D regimes in some cases. On the contrary, intermediate behaviour is suggested to be more realistic in organised convective systems, especially for intensive systems. That can be a worthwhile consideration for the development of convective parameterisations taking convective organisation and aggregation into account [e.g. Moncrieff, 2019].

3.5 Conclusion

LES simulations of four convective scenarios with ensemble, physics, resolution and other perturbations have shown that upper tropospheric mass divergence, associated with deep convective systems, depends on net latent heating (i.e. precipitation intensity) and on the convective organisation. Divergent outflows have been integrated over a fixed area and 7-14 km altitude. Thereby, the main precipitation cores for each type of convection have been covered and split over two time intervals (Figure 3.7). Wind profiles were imposed such that the convective cells propagate slowly with respect to the domain, and therefore their flow perturbation accumulated in a condensed region. The relation between mean mass divergence and net latent heating rates has been analysed and intensively discussed:
At low precipitation rates and in initial development stages, the four basic scenarios strongly suggest the existence of a 3D outflow regime for isolated convective cells (i.e. supercell and regular multicell). In addition, another 2D outflow regime exists, as demonstrated by the infinite-length squall lines. In each regime, a linear dependence of mass divergence on net latent heating is found. In practice, a more realistic finite-length squall line is suggested to conform to a mixture of the 2D and 3D regimes, with two components (*zonal*, west-east, and *meridional*, south-north) of the divergent outflow behaving accordingly. At higher precipitation intensities, the outflow does not strictly follow these two regimes anymore. The magnitude of the mass divergence at high net latent heating rates appears to be intermediate between the initial 2D and 3D regimes, but ordering between different organisational types of convection still occurs at high net latent

heating rates. Given an outflow dimensionality, upper tropospheric divergent convective outflow therefore depends linearly on net latent heating accordingly. This dependence in LES is the key finding of this study. Additionally, non-linear dependence occurs through convective aggregation. The aggregation changes effective outflow dimensionality.
Simulations on extended domains strengthen the confidence in the results, in addition to an ensemble of simulations. Convective momentum transport plays no direct role for the mass divergence in the simulations. Nevertheless, by affecting convective organisation and precipitation rates within a system, it may indirectly affect upper tropospheric mass divergence.
An important implication of the results of this study may be a strong bias in upper tropospheric divergent flow. Biases are suggested if the convective organisation is unknown, substantially misrepresented or even unrepresented (as it is generally the case for deep convective parameterisations in NWP). The implication exists, even if the precipitation rate or some kind of distribution, describing the precipitation rate in a statistical way, would be known. That specific potential implication represents an important finding and is investigated in the next chapter, Chapter 4.
The findings are in good agreement with the behaviour of outflows explained by linear gravity wave adjustment models triggered with heat sources [Bretherton and Smolarkiewicz, 1989, Nicholls et al., 1991, Mapes, 1993, Pandya and Durran, 1996]. In such a model, the heat source represents a (mesoscale) convective system. The identified 2D regime corresponds to a line source. The identified 3D regime to a point source in Nicholls et al. [1991] and Morrison [2016a,b]. The agreement with Nicholls et al. [1991] is restricted to the case of purely convective heating regimes. This is a consequence of absence of any substantial contributions from *stratiform* fractions of mesoscale convective systems [Mapes, 1993, Houze, 2004] in the simulations. Therefore, no conclusions on the role of individual vertical modes can be drawn. Additional simulations, beyond the scope of this study, would be necessary to understand the response of upper tropospheric divergence to mixed stratiform-convective heating profiles. Such simulations would then have to be focused on the finite and infinite-length squall lines at larger domains specifically. Furthermore, an extended integration time would be needed to inspect the effect of higher order gravity wave modes.

4 Divergent convective outflow in ICON deep convection-permitting and parameterised deep convection simulations

Large parts of this Chapter also appear in Groot et al. [2023].

4.1 Introduction

Flow variability may be defined as the evolution of difference winds between at least two simulations that are initiated with very similar initial conditions. However, it may also be defined as the distribution of a specific flow characteristic, for example with respect to a mean or median of that distribution. Lorenz derived expressions for difference evolution of a flow [Lorenz, 1969a], which he used to conduct early, but highly influential, research on predictability of the atmosphere (restricted to the dynamical evolution). His work also demonstrated growth characteristics of initial condition derived flow variability towards the climatological distribution (i.e. the second possible definition). In the last two to three decades, important studies have been undertaken to elaborate on predictability and related flow variability, as well as its representation in numerical weather prediction models.
Flow variability can manifest at many different scales in atmospheric dynamics: turbulence down to the small dissipative scale, but also planetary Rossby wave variability and its climatology. Here, a form of flow variability on the scale of mesoscale convection is assessed with the ICON numerical weather prediction model, which represents a state-of-the-art operational forecasting and research model. The structure of divergent outflow variability induced by deep convection will be investigated in detail for a convective event, which means the initial condition view of flow variability is addressed. Nevertheless, the case study is only a first attempt to improve understanding of the addressed divergent outflow variability. The tested hypotheses are thought to be valid independently of the considered case: they may represent climatological physics-based characteristics of divergent convective outflows [Groot and Tost, 2022, Bretherton and Smolarkiewicz, 1989, Nicholls et al., 1991, Morrison, 2016a]. The role of convective organisation and dependence on precipitation rate will be assessed, based on hypotheses put forward:

- In the large eddy simulations of Chapter 3 by Groot and Tost [2022],
- Consistent with older idealised models [Bretherton and Smolarkiewicz, 1989, Nicholls et al., 1991, Mapes, 1993].

The understanding of convective outflows in Groot and Tost [2022] and Chapter 3 builds in an important way on Bretherton and Smolarkiewicz [1989], Nicholls et al. [1991] and Mapes [1993]: based on a linearised gravity wave adjustment model, an expression of outflows from deep convection was constructed by Nicholls et al. [1991]. In their highly idealised settings, deep convection is represented by a localised heating source. The obtained expression is different for line and point sources of localised heating. Furthermore, outflow depends linearly on the net latent heating source, when the geometry of the heating source is prescribed. Mapes [1993] investigates the consequences of the gravity wave adjustment process conceptually for convective organisation: gravity wave activity may lead to convective aggregation, which was suggested to affect outflow dimensionality in turn by Groot and Tost [2022] (Chapter 3). Outflows from real convective systems therefore typically organise into something that may be interpreted as a mixture of an idealised point ("3D") and idealised line ("2D") source [Groot and Tost, 2022]. Mapes [1993], Mapes and Houze [1995] have also used the linearised gravity wave adjustment model to identify vertical mode-dependent responses of gravity wave adjustment, induced by heating profiles of convective systems, in theory and in actual convection. They found out that higher frequency waves (in the vertical) in an organised convective system should reduce the ratio between mass divergence and net latent heating, compared to a purely convective heating profile. These higher frequency waves are typically excited in case of a (partially) *stratiform* heating profile [e.g. Houze, 2004]. In the LES simulations of Chapter 3, the pattern was probably absent as a consequence of a weak stratiform contribution to the convective systems [Groot and Tost, 2022] (Chapter 3).
The development and growth of flow perturbations from initial condition uncertainties have long been difficult to research, from a dynamical process point of view. However, in the last two decades or so, improvements of NWP have shaped the landscape for improved understanding of the growth of flow perturbations and its implications for predictability of atmospheric dynamics. A strong (initial) connection of perturbation growth with precipitating systems and convective precipitation has become clear in those two decades [e.g. Zhang, 2005, Zhang et al., 2007, Rodwell et al., 2013, Selz and Craig, 2015a,b, Baumgart et al., 2019, Zhang et al., 2019, Selz et al., 2022]: using a potential vorticity perspective, this link has become particularly clear if an ensemble experiment, in which a tight initial condition envelope is evaluated [Baumgart et al., 2019, Selz et al., 2022] (much smaller than in operational NWP). Nevertheless, a limitation on predictability directly induced by (mesoscale) precipitation-related variables is currently rarely applicable [Selz et al., 2022,

Baumgart et al., 2019, Rodwell et al., 2013]. A possible induction of small-scale uncertainty (perturbations) directly imposed by the large-scale may even imply that large-scale variability will forever play a role in the growth of flow perturbations [Lorenz, 1969a, Durran and Gingrich, 2014]: through the inseparable connection between large and small scales in atmospheric dynamics. Nevertheless, studies continue to suggest that improvements can be made by reducing sources of uncertainty at small scales [Selz et al., 2022, Zhang et al., 2019].

A precipitation or latent heating-dependent perspective on convectively induced flow variability is taken in this study. Based on some of the cited works, it is noted that the precipitation conditioning stratifies the most probable magnitude of potential perturbation sources in the flow. The analysis from the conditional perspective will be compared to results obtained with an LES-model and the idealised gravity wave model [Chapter 3, Groot and Tost, 2022, Nicholls et al., 1991]. Furthermore, indirectly, a pathway via which organised convection could play a role in processes of perturbation growth may be identified. This role of organised convection for error growth has been suggested by Rodwell et al. [2013] and Clarke et al. [2019a,b], for instance. Baumgart et al. [2019] have investigated the sequence of dynamical processes that (on average) contribute to mid-latitude error growth and proposed, based on their analysis, that latent heating tendencies from their deep convection scheme in ICON may induce differential divergent winds in the upper troposphere. Subsequently, further non-linear error growth in the upper troposphere [Baumgart et al., 2019] can occur as a result of differential advection. Therefore, the error growth as a consequence of organised deep convection may be important [Rodwell et al., 2013]: one could for instance wonder whether variability of flow perturbations induced by deep convection are represented well within the ensemble of NWP, when using parameterised deep convection.

More specifically, it has been suggested that convective momentum transport may modify upper tropospheric flow perturbations induced by deep convection [Rodwell et al., 2013]. The 2013 study found that mesoscale convective systems over the North-American continent could affect European weather predictability. Furthermore, convective momentum transport (CMT) of strongly organised mesoscale convective systems can play a crucial role for downstream perturbation growth [Rodwell et al., 2013]. Groot and Tost [2022] (Chapter 3) noted that the effect of CMT could be separated into a direct and an indirect effect: CMT could affect divergent flow and associated horizontal acceleration directly, resulting in flow perturbations around convective systems. In addition, CMT can affects the convective organisation and precipitation rates only, resulting in an *indirect* modification of upper tropospheric flow. Changes in precipitation rates directly lead to a modification of the divergent outflows, as divergent outflow scales with net latent heating. A direct effect on divergent outflows was not identified in LES-simulations of Groot and Tost [2022] (Chapter 3). In this Chapter, the direct effect of CMT on divergent outflows from deep convection will be assessed for ICON simulations.

The missing - but crucial - weather modelling strategies will be examined in the current investigation. The understanding of operational modelling complements idealised models, like the linearised gravity wave adjustment model [Bretherton and Smolarkiewicz, 1989, Nicholls et al., 1991] and idealised LES [Groot and Tost, 2022], from which basic physical understanding of processes could be gained (Chapter 3). Bridging the gap to operational NWP - in this case ICON 2.6 - is a step towards a (very) *basic* understanding of divergent deep convective outflow magnitudes across a broad range of simulation set-ups. At the same time, the relationship between net latent heating and divergent convective outflows in the upper troposphere is assessed in the most complicated setting. Both parameterised and explicitly resolved deep convection (*convection-permitting*) settings will be used: thereby, potential limitations of the parameterised treatment of deep convection may be exposed.

Altogether, the following hypotheses will be tested on convection-permitting ICON simulations, in line with that recent work:

- The dimensionality of convective systems can substantially affect the magnitude of divergent outflows. Specifically, when the divergent outflow of isolated convective cells is compared to the outflow of convection closely resembling a line source of heating (e.g. elongated squall lines), a contrast in ratio between divergence and latent heating is expected: at the same area mean intensity of latent heating, less divergence is expected for a linear geometry than for a corresponding point source [Groot and Tost, 2022, and Chapter 3]
- Convective aggregation and organisation affects the magnitude of divergent outflows - the outflow is expected to increase at a rate slower than linearly, when convective aggregation leads to increases in the mean precipitation rate (probably partly explained by adjusting the outflow dimensionality) [Groot and Tost, 2022, and Chapter 3]
- CMT does not affect the magnitude of divergent outflows from deep convection and, hence, normalised convective momentum transport does not have a statistically significant relation with the normalised ratio between mass divergence and precipitation rate [Groot and Tost, 2022, and Chapter 3].

As in Groot and Tost [2022] and Chapter 3, a box integration is used to compute diagnostics in this study. As a flow perturbation generated by deep convection and latent heating may travel downstream [see for example Rodwell et al., 2013, Baumgart et al., 2019, Clarke et al., 2019a,b], convective systems are also tracked in the convection-permitting ICON simulations. In the parameterised deep convection setting, it was chosen to not track the system. Conversely, a one hour window is selected for each convective system instead (the motivation for that choice is discussed in Section 4.3.2.2). The relationship between net latent heating and the magnitude of divergent outflow in the upper troposphere is evaluated, based on the findings by Groot and Tost [2022] (Chapter 3). In Groot and Tost [2022], a linear relation with the net latent heating and superposed variability induced by outflow dimensionality was found. The hypotheses will be tested by using an ellipse fitting algorithm to track the elongation of convective systems with time (a concept which has been used before by Grant et al. [2020] and references herein). A validation procedures assures a consistent parameter evolution. Furthermore, in convection-permitting simulations, extra attention will be paid to convective systems that resemble an elongated squall line, which are supposed to resemble line sources of heating more closely. Convective momentum transport, divergence and precipitation rates will be integrated over boxes that are independent of the ellipse detection and complete the datasets.
In the case of simulations with parameterised deep convection, a static box approach with ensemble (and physics) perturbations, similar to Groot and Tost [2022] and Chapter 3, is chosen. A case of strong organised convection over Central Europe occurring on June 10^{th} and 11^{th} 2019 is selected for all the assessments.
A short synoptic discussion of the simulated case is provided in the next section (Section 4.2). After a discussion of the model and simulation set-up in Section 4.3, an example track of a convective system and its evolution of fitted ellipse parameters will be presented in Section 4.4. Then, the upper tropospheric (250 hPa) divergence variability among convective systems in parameterised convection and convection-permitting ensembles will be assessed, in relation to the location of convective features in Section 4.5.1. Subsequently, the divergent outflows will be compared between parameterised convection and convection-permitting simulations (Section 4.5.2). This is followed by an assessment of the three hypotheses presented in this introduction (Section 4.6) for convection-permitting simulations. Subsequently, a synthesis and discussion section is presented to wrap-up (Section 4.7) and conclude (Section 4.8).

4.2 Synoptic and convective situation

An upper tropospheric low pressure system was located over Western France on June 10^{th} 2019 (Figure 4.1; see also Figure C1 in Appendix C), with a southerly flow advecting warm, moist air northward over Central Europe (red areas in Figure 4.1). The associated pattern, with cold air west of the upper air low pressure system, led to strong thermal gradients and *baroclinicity* (i.e. density gradients on a quasi-horizontal surface of constant pressure) over France, the Alps and (later) Germany. The presence of strong horizontal gradients in *equivalent potential temperature*[6] (θ_e) implies that a front is present over the far northeast of France. Cold near-surface air creeping northeastward, directly ahead of the co-located cold front, supported the initiation of some strong convective systems. These systems are present in nearly all simulations, albeit at slightly different locations in nearly all simulations than in reality, including east of the front in the region of warm near-surface air.
As one can see in Figure 4.2 (in combination with Figure 4.1), the strong mid-level (mid-tropospheric) front has moved a bit eastward during the evening of the 10th of June over Western Germany and Switzerland, close to the French border (the border itself is not shown). The cross section shows an associated zone of convergence around 600 hPa, with divergence above and forced upward motion near the frontal plane, sloping as a cold front. Given the strong cross-frontal contrasts at 600 hPa (and the presence of the Alps, near the front), this particular level was selected for illustration of synoptic and larger mesoscale conditions, in combination with the jet stream levels (Figure 4.1). The frontal convergence zone is suitable for strongly forced *elevated* convection from the mid-troposphere, while it is not suitable for *surface-based*/boundary layer-based convection.
The area where deep convection may be triggered is roughly represented by the convergence zone of Figure 4.2b and all locations to the east of the zone. Over that area, the southerly flow (Figure 4.1) is advecting the warm air mass. The warm air mass, east of the frontal zone, is much more suitable for convection based in the planetary boundary layer, with mid-tropospheric θ_e lower than low-level θ_e (i.e. conditionally unstable static stability). As a result of the θ_e-distribution, the deep convection in the simulation set-up with parameterised deep convection ("PAR") was surface-based over the Alps. The mid-tropospheric front was still west of the Alps during convective initiation, which occurred around 19-20 UTC. However, in the lower layers, some colder air seemed to be advected into the Western Alps already, slightly ahead of the actual

[6]Equivalent potential temperature is a potential temperature that takes into account the energy contained in moist air, which can be extracted by the phase change between water vapour and liquid water. It would be conserved in moist convective processes, if no mixing and no precipitation would occur, and is a useful quantity to identify fronts.

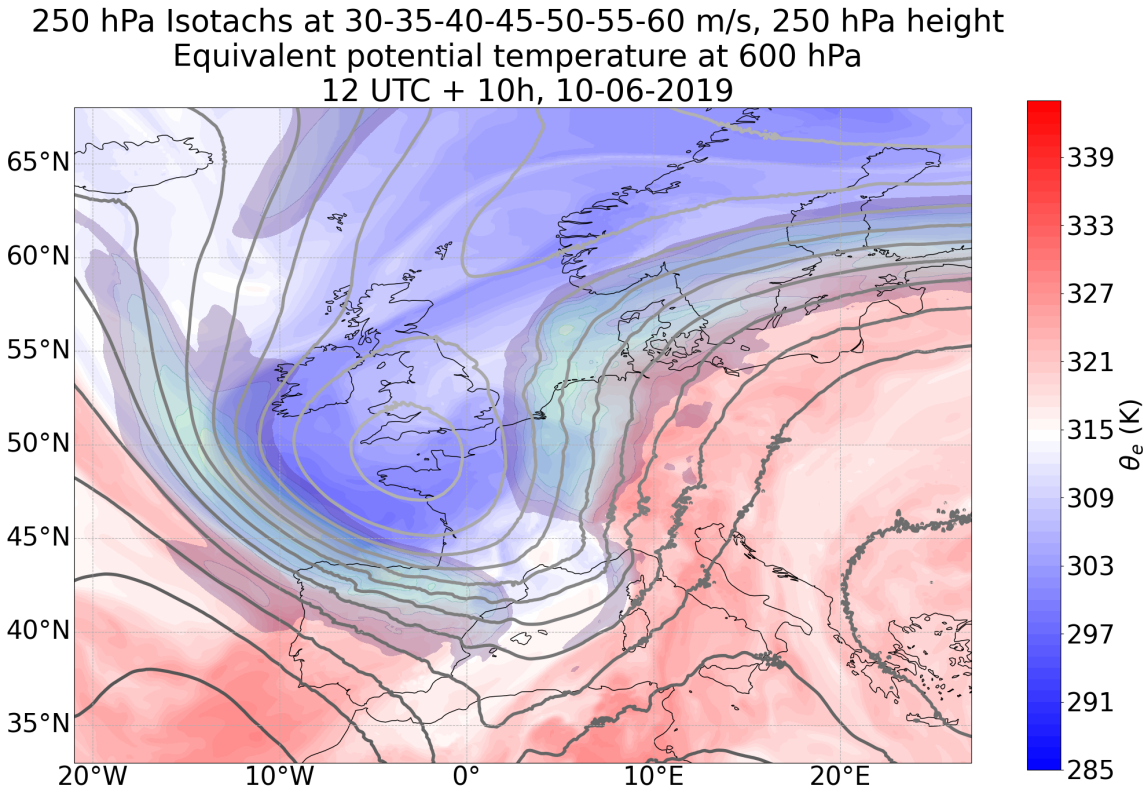

Figure 4.1: Spatial distribution of equivalent potential temperature at 600 hPa (blue-white-red), lines of equal wind speed (*isotachs*) at 250 hPa (30 to 60+ m/s at 5 m/s intervals, partially transparent colour fill) and geopotential height of the 250 hPa surface (at ca. 11 km altitude) at 50 m intervals. Displayed is the forecast for 22 UTC on June 10th over Western Europe.

mid-tropospheric front (Figure 4.2). The θ_e cross sections suggest that the (comparatively) cold near-surface air helps to initiate convection along an initially subtle (orographic) convergence zone.
Later on in the PAR simulations, the zone with convective systems moves northward along the front. From the same patch of convective activity, another strong convective system moves over Central Germany just after midnight UTC, feeding from mid-tropospheric air along the front.
The nearby jet stream, with strong southerly flow, and much weaker low level winds helps to organise the convection, after the convection is triggered at the front. Given a strong *bulk wind shear* over the lower 6-7 km, of $\approx 25m/s$, the environment is suitable for well-organised deep convection. In the convection-permitting simulation set-up ("PER"), convective activity starts earlier in the day than in PAR. The jet stream is located further to the west, which may reduce the average degree of organisation, by slightly reducing the *effective wind shear* (i.e. wind shear over the layer with convective motion). (Note, however, that the elevated base of convection in turn may also reduce the effective shear that cumulonimbus clouds can use in the west, despite the closer proximity of the jet stream.) Nevertheless, supercell and squall line organisation of convection could still occur over Southeastern Germany in the presence of high shear. Furthermore, the convection in the PER simulations is much more scattered and associated with the warm air mass - with the larger systems occurring mostly along a specific trajectory (Figure 4.7a). The frontal zone does not play a role as significant as in PAR simulations. The convection in PER-simulations seems to be driven mostly by large thermals of vertical motion, escaping the warming and moistening boundary layer (advection from the south; not shown).
After all, several co-located systems with mesoscale convective activity developed over Germany and the Alps in a vast majority of the PAR simulations during the afternoon and evening. Similarly, convection was relatively active in PER over Southern Germany in the (late) afternoon of the 10^{th} of June (Figures 4.4 and 4.7a, that appear later, show this; observed convective systems are also shown there). Well-organised convection occurred over regions with strong local relief in the southwest, as well as towards the east. In the east, initially surface-based convection occurred during the late afternoon and early evening. The strong southerly to southwesterly upper tropospheric flow helped to organise convection in PER to a varying degree: a few convective systems in the east of Southern Germany developed into squall line-like structures. On the contrary, other structures only organised into smaller multicells. This mixture may be very suitable for the

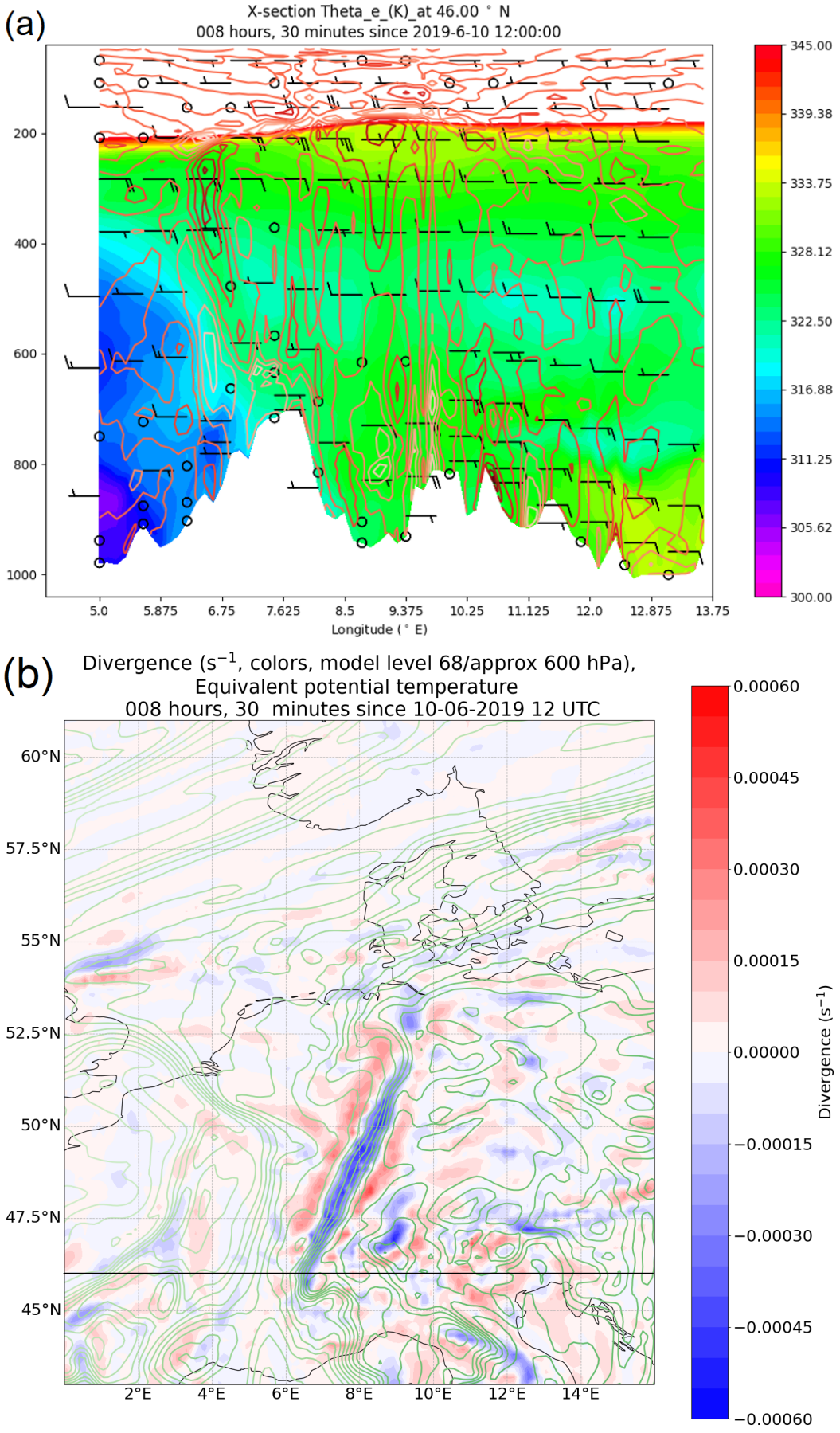

Figure 4.2: Equivalent potential temperature θ_e and convergence (divergence) in the troposphere. Top (a): vertical cross section through the Alps (46 °N) as a function of pressure levels. Isolines: divergence; colour fill: θ_e. Bottom (b): top view at about 600 hPa. Isolines: θ_e; colour fill: divergence. A black solid line marks the location of the cross section in the top panel (a).

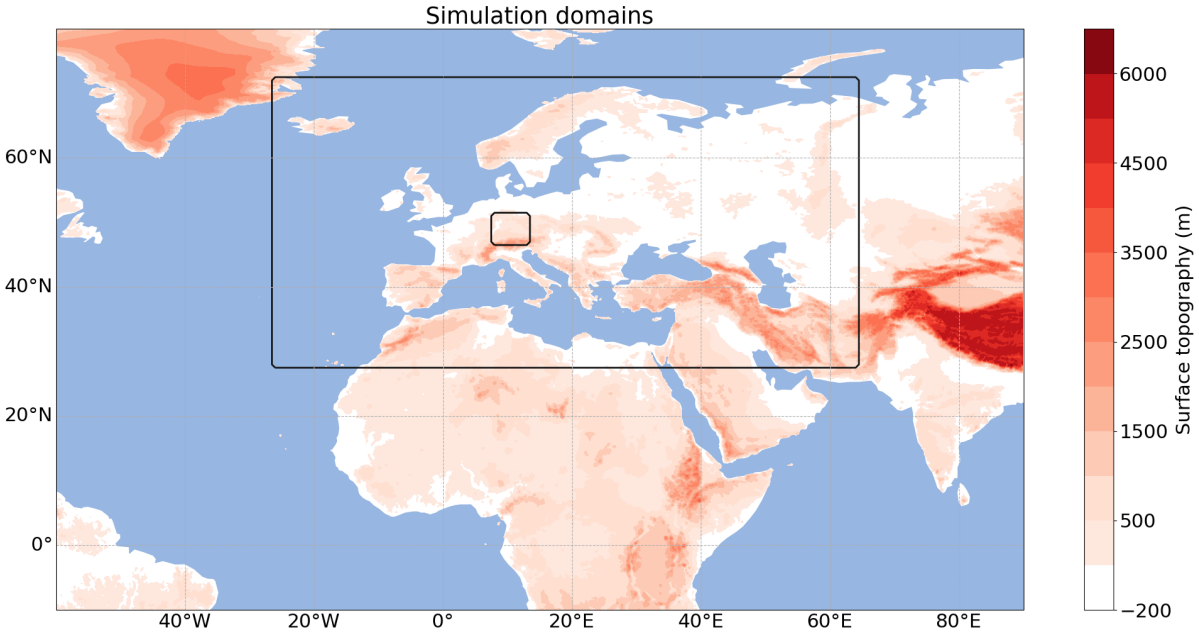

Figure 4.3: Two simulation (sub-)domains used in this study: the nest over Europe (outer outline) and the Southern German LAM domain (inner outline).

assessment of divergent outflows from deep convection, since idealised LES simulations of Groot and Tost [2022] and Chapter 3 suggest that convective organisation, geometry and aggregation may be crucial aspects for the outflow - these aspects may determine the normalised outflow strength with respect to net latent heating rate (Chapter 3). A more detailed discussion of the synoptic configuration around this event is provided in Wilhelm et al. [2021].
The contrasts in precise location of the convection between PAR and PER simulations are not essential for the analysis carried out in this study: more important is that convection occurs on the same day and in the same area. That means that it is associated with the same large-scale synoptic setting and roughly similar characteristics of convective environments and the convective adjustment. If representation of deep convection would not substantially differ between the two types of simulations, overlap in background conditions should yield similar dependence of divergent upper tropospheric outflows on the intensity of the convection (as quantified by the precipitation rate, for instance).

4.3 Methods

4.3.1 Model set-up

4.3.1.1 Domains, grids and parameterisations In this study, numerical simulations with ICON 2.6 have been conducted and analysed at two different resolutions and in the following two corresponding set-ups:

- Global simulations, with a nest over Europe
- Convection-permitting simulations over Southern Germany, using the local area mode (LAM)

The model ICON has been developed and used operationally by the German Weather Service and Max Planck Institute [Zängl et al., 2015, Giorgetta et al., 2018].
Global simulations have been performed with the non-hydrostatic numerical weather prediction model ICON, in version 2.6.0. A global domain at 26 km grid spacing (R03B06) was used for that purpose, with a nest at 13 km grid spacing (R03B07) over Europe (Figure 4.3) and with 90 vertically stretched levels, reaching up to 75 km above the sea level. Here, R0xB0y defines how the ICON grid has been constructed. The parameterised convection simulations have been initiated at 12 UTC on June 10^{th} 2019 and were run out to +33 hours. Generally, standard (operational) parameterisation options have been used in this set-up: a Tiedtke-Bechtold convection scheme [Tiedtke, 1989, Bechtold et al., 2014] and *single moment* microphysics with rain, snow, cloud water, cloud ice and graupel [Seifert, 2008]. When single moment microphysics is utilised, only the mass concentration of each reservoir of water is simulated - as opposed to the number concentration, which is additionally taken into account by two moment microphysics schemes. The non-default Ritter-Geleyn parameterisation was applied to radiation fluxes though, because files for the default

parameterisation scheme were missing in the available model version. For cloud cover, turbulence, *saturation adjustment*, *sub-grid orography* and *gravity wave drag*, default/operational ICON schemes have been used [for more details, see also Prill et al., 2019, 2020]. A model time step of 100 seconds was used. The convection scheme and sub-grid orography scheme in the inner nest were executed every 10 minutes and in the outer domain every 20 minutes. The gravity wave drag scheme was called every 20 minutes everywhere. A coarsened radiation grid (at twice the model grid spacing) has been used with a calling frequency of 30 minutes for the computation of radiation fluxes.
Convection-permitting ICON simulations have also been used. The convection-permitting ICON LAM (version 2.6.2.2) has been run for a domain over Southern Germany (Figure 4.3), with a time step of $dt = 10$ seconds, starting at 3 UTC on June 10^{th} 2019 and running until 19 UTC. The horizontal resolution is 1km (R05B09 grid) in the native ICON grid. The model output has been re-gridded to regular lat-lon coordinates at 2 km grid spacing. In this simulation, two moment microphysics after Seifert and Beheng [2006] was used. Furthermore, the model top of convection-permitting simulations was located much lower than for the global simulations: at 22.5 km above the sea level, with Rayleigh damping being applied above $z = 12.5$ km. 90 vertical levels were used to represent the atmosphere over a depth of 22.5 km. Parameterisations were also run at lower frequencies than the model time step, for instance, once per 600 seconds for radiation. Deep convection was not parameterised in the convection-permitting simulations, but a shallow convection parameterisation was included.

4.3.1.2 Ensemble and perturbation settings Perturbations have been applied to both simulation set-ups. Ensembles have been run with the aim to sample an unspecific form of background convective variability: ICON simulations using global parameterised deep convection with nest over Europe (PAR) have been perturbed by using the available outdated surface tile datasets (2015-2018; in addition to the latest dataset of 2018 at the time; $n = 6$). The parameterised convection simulations have been initiated at 12 UTC on June 10th 2019 and were run out to +33 hours. The combined variability imposed by selecting various convective systems, over a time range and through the dimension of ensemble members, allows one to study the characteristics of convective variability in a precipitation rate normalised framework.
In addition, physics perturbations have been applied to the convective tendencies in additional PAR simulations. These physics perturbations are designed to match those of Groot and Tost [2022] and Chapter 3 in essence. Therefore, convective momentum transport and latent heating are perturbed by a constant proportionality in theory (nevertheless, feedbacks can usually also affect the actual magnitude of perturbations, as described in Section 3.2.3.2). However, the relative strength of latent heating perturbations was reduced to ± 5, ± 10 and $\pm 20\%$. CMT tendencies have been perturbed by $\pm 50\%$ and, in another experiment, CMT has been switched off entirely, as in the LES simulations of Chapter 3. Since the PAR simulations last only slightly longer than a day, consequent latent heating effects on the energy distribution should not accumulate to large (potentially highly unrealistic) biases during the simulations. Application of corresponding perturbations to PER simulations was not considered a necessity, based on the understanding built with the large eddy simulations [Groot and Tost, 2022, and Chapter 3] and PAR simulations presented here in a preliminary study - sufficient variability in convective precipitation, organisation and divergent outflows will automatically be induced by the ensemble perturbations. Furthermore, some CMT variability occurs among convective systems, which means it will be possible to test each of the posed hypotheses. After all, an important purpose of this study is to understand the induced divergent outflow variability and its representation in realistic ICON simulations.
In addition to the ICON-PAR ensemble and physics perturbations, four separate simulations with adjusted settings in the convection scheme have been conducted:

- A simulation with no parameterised convection at 13 km resolution
- A simulation with a parameterisation for shallow convection only
- Two simulations where the calling frequency of the deep convection parameterisation was reduced to every 20 resp. 30 minutes everywhere.

For the setting without any convection parameterisation, an ensemble was constructed in the same way as for the other PAR-simulations.
The ICON convection-permitting (PER) simulations have been perturbed with a representation of the initial condition uncertainty at June 10^{th} 2019, 03 UTC. The initial condition uncertainty has been sampled using the the Kilometer-scale ENsemble Data Assimilation framework (KENDA, Schraff et al. [2016] , 2 km grid spacing). This initial condition dataset has been provided by Matsunobu et al. [2022]. The 20 member initial condition ensemble closely resembles the ensemble perturbations of the operational DWD ICON D2. Lateral boundary conditions have been derived from the ICON global ensemble (40 km grid spacing) with

ICON-EU nest (20 km grid spacing), initiated at 3 UTC. These boundary conditions were available at one hour intervals. The simulation domain was restricted to Southern Germany (Figure 4.3). Output available at 5 minute frequency from 10 until 19 UTC has been used for the analysis, which means that the time range covered by the PAR and PER simulations overlaps partially.
The results presented will mostly be focused on the comparison of the PAR and PER ensemble and on the PER ensemble itself.

4.3.2 Extracting convective system properties in ICON simulations

Extraction of convective system properties (shape, area, etcetera) is a more than feasible task in PER-simulations. On the contrary, parameterised treatment does not lend itself very well to extract the such properties, because it assumes that a statistically averaged effect of convection over larger scales exists and is represented [e.g. Done et al., 2006, Craig and Cohen, 2006]. Therefore, any description of local (sub-grid) variability, induced by convective cells and convective organisation, is represented less accurately in PAR than in convection-permitting simulations with a finer grid, or not at all. The extraction procedure of organised convective systems, and parameters to represent those systems, from the first set of simulations (PER) is described in the following Section (4.3.2.1), followed by a section with corresponding considerations for PAR (Section 4.3.2.2).

4.3.2.1 Convection-permitting simulations, PER It is important that the dataset with properties of convective systems is able to describe the degree of convective aggregation, orientation and the relative state of the system's geometric elongation in time and space (by means of a dimensionless number). Consequentially, it is possible to single out whether an almost 2D- or almost 3D-outflow regime can be expected [Groot and Tost, 2022, and Chapter 3]. These factors have been found to determine the relative magnitude of outflow from idealised deep convection modelling [Bretherton and Smolarkiewicz, 1989, Nicholls et al., 1991, Groot and Tost, 2022, and Chapter 3]. In order to estimate parameters describing the elongation and state of aggregation for any convective system, an ellipse fitting algorithm has been designed. In parallel, an independent moving box is initiated to track a convective system. The independent box is needed to conserve an integration volume, moving (approximately) with the convective system's main updraft, over which divergence and precipitation are integrated.
The following steps are involved in constructing the dataset of convective systems and ellipse parameters:

- Ellipse fitting
- Validation of obtained ellipse parameters
- Construction of precipitation rate, filtered mass divergence and convective momentum transport diagnostics
- Moving box integration of the constructed diagnostics along a convective system's track
- Matching between ellipse parameters and moving box diagnostics
- Final check of the matched records

The full procedure is explained in the following part of this section and contained in the dataset of Groot and Kuntze [2023].
Ellipse fitting is applied to any area, larger than about 400 km^2 (100 grid cells with "convective" precipitation),S with a precipitation rate over 10 mm/h in the PER simulation output. Before fitting the ellipses, the obtained binary representation of convective precipitation areas is first smoothed spatially ($\sqrt{r}$ dependence) with a kernel of 20 km radius. The first step, after fitting ellipses, consists of an initial validation procedure that assesses the stability of the fitted ellipse parameters over the course of a one hour window. Thereby, short lasting strong fluctuations are filtered out. Only fluctuations that match any prior and successive record within one hour were maintained, based on some predefined measures (for the details: see the code of Groot and Kuntze [2023]). A removal of each independent record is possible: at least one plausible predecessor and successor needs to be present for each record, among all the other ellipse records, both forward and backward in time (within one hour). Note that the corresponding prior or successive records might have been removed themselves in specific cases! Additional validation steps are done to check the distance between an ellipse centre (set to be < 20 km) and the track of a convective system, as identified with an independently moving box. A full list of ellipse and moving box parameters used for the dataset is provided in Table 4.1.
Independently from the ellipses, a moving box has been initiated subjectively and moves with a convective system. The box is used for integration of precipitation and divergence over an horizontal subspace that

is constant in time (with respect to the moving box centre). The convective systems propagate with relatively constant velocity north- or northeastward and only 1-3 convective systems in each member of the 20 ensemble members have been tracked (see also Figure 4.6a). Manually defined boxes, moving at a constant velocity, could therefore be used to define the box outlines. The moving boxes are initiated and then track the systems, independently from the ellipse fitting procedure, because merging events (such as between smaller satellite ellipses and larger ellipses) occur frequently in the ellipse dataset. In case of a merging event, ellipse parameters will weakly vary in time, but the spatial integration mask of the moving box should not change accordingly. If ellipse parameters vary strongly, the validation procedure is not passed. The signal of divergence and precipitation within a box should predominantly be affected by the main, central, convective system within the box, and only be weakly affected by satellite systems that develop from time to time around some of the systems. Nevertheless, some satellite systems may contribute to the precipitation and divergent outflow signal occasionally. This contribution is not a problem and possibly unavoidable: as convective systems tend to organise anyway (Chapter 2), satellite systems may be inherent byproducts of another, larger, convective system and occur even as a part of the larger system. The evolution of satellite systems may be inseparable from that of the larger system (see also Section 2.4).
For each box and time step, the following variables are calculated: firstly, the strength of convective momentum transport (CMT) over a moving box is computed to determine whether and how this acceleration (deceleration) affects the upper tropospheric divergence. The estimate of CMT is based on the eddy covariance of perturbations ($'$) in u, v and w from domain mean values. Separate estimates of meridional and zonal correlations with vertical velocity, representing (resolved, vertically integrated) convective momentum transport fluxes, are made at model level 25: located at 315 hPa or about 9 km altitude. This level is selected, because the eddy flux in the upper troposphere turns out to be mostly maximal at, or near, this level during studied event. The mean of $u'w'$ and $v'w'$ represents a vertical integral over the acceleration at all levels below as a result of convective momentum transport. The box averaged values of $u'w'$ and $v'w'$ at the given altitude, in the surroundings of any convective system, are then normalised with precipitation rate (resulting in C; similarly for divergence, resulting in D). This normalisation is done to compensate for the effect that stronger convective systems are typically associated with enhanced resolved CMT. Hence, the relation between anomalous CMT and anomalous relative mass divergence is investigated. Subsequently, both normalised upper tropospheric divergence (D) and normalised CMT (C) are compared within precipitation rate bins. The conditional comparison allows one to detect signals of anomalous mass divergence (potentially) directly induced by anomalous CMT in a more robust way. Secondly, the mean precipitation intensity and the filtered mean divergence is computed. Wavelengths > 45 km in both u and v are kept, whereas flow variability at shorter wavelengths is removed. Divergence is on the one hand filtered for longwave signals to remove shortwave variability introduced by shortwave gravity waves from the dataset (although net divergence over a full wavelength should go to 0), but also to make the comparison between 13 km and 1 km resolution ICON much more legitimate - smallest scale decently resolved motions in 13 km resolution simulations occur at wavelengths of about 50-90 km [Skamarock, 2004]. The three quantities can only be computed and validated if the whole integration box lies within the extent of the simulation output at any given time. Finally, the ellipse characteristics of the ellipses contained within each box (elongation A: length ratio between two ellipse axes; orientation; area of the ellipse) are then matched with the corresponding records, averaged over the moving box. An example of the path of a moving box and (contained) ellipses, with corresponding ellipse parameters and moving box diagnostics for one convective system, is provided in Section 4.4.
The ellipse dataset fulfilling all validation conditions contains 456 records, in which the time evolution of 22 out of a total of 28 convective systems is represented. This dataset is the basic dataset for the assessment in Sections 4.5.2 and 4.6. With a slightly weaker box-center-to-ellipse-centre distance criterion, a second dataset of 866 records is obtained. For this larger dataset, the distance criterion was set individually for each convective system (based on e.g. box size), or replaced with an ellipse area criterion. In the larger dataset, all 28 convective systems are present. Since the validation algorithms turned out not to be fully waterproof, ambiguous records have manually been inspected before finalising both datasets: 5 additional matches were ambiguous (duplicates fulfill all validation criteria at one specific time stamp) in the dataset of 866 (+5) and two of those occurred in the dataset of 456 (+2) records. The double matches among those ambiguous records were manually selected (removed), based on area and centre location of the ellipse.

In the Section 4.4, the evolution of precipitation and ellipse parameters is discussed for an example system.

4.3.2.2 Convection parameterising simulations (PAR) In past times, most computationally feasible NWP simulations required the application of a parameterisation to represent deep convection. Only recently, global convection-permitting simulations have been utilised for research purposes (up to now) [e.g. Judt, 2018, 2020].
Philosophy behind the representation of deep convection is, and has been, generally different between pa-

Table 4.1: List of parameters in the dataset of ellipse records, with their descriptions.

Name of parameter	**Unit**	**Explanation (if necessary)**	**Symbol**
Ellipse id	#	Each ellipse has a corresponding ellipse id	
Time stamp	# 5 min	Each corresponding output time step has a time stamp	
Axis ratio	-	Ratio between major and minor axes lengths of an ellipse	A
Mean precipitation rate	mm/h	Mean surface precipitation rate over convective system's track (moving box integral)	
Mean mass divergence	kg $m^{-3}s^{-1}$	Mean upper tropospheric (380-180 hPa) mass divergence over convective system's track (box integral)	
Div/precip ratio	$\frac{kg \cdot mm}{m^3 s^1 h^1}$	Ratio between box's mean mass divergence and box's mean precipitation rate	D
U-component of CMT eddy flux	$^2s^{-2}$	Mean value of $u'w'$ at model level 25, about 315 hPa	
V-component of CMT eddy flux	m^2s^{-2}	Mean value of $v'w'$ at model level 25, about 315 hPa	
Absolute vertical integral of CMT acceleration	m^2s^{-2}	Mean value of $[(u'w')^2 + (v'w')^2]^{\frac{1}{2}}$ at model level 25, about 315 hPa	
Ratio absolute integral of CMT acceleration and precipitation rate	$\frac{m^2 h}{s^2 mm^1}$	As above, but relative to precipitation rate in mm/h (also computed for U and V component separately)	C
Xcentre	grid cell #	Centre location of the fitted ellipse in zonal direction	
Ycentre	grid cell #	Centre location of the fitted ellipse in meridional direction	
Ellipse angle/orientation	°	Orientation of the major axis of the ellipse with respect to a reference direction	O
Major axis length	km	Major axis length of fitted ellipse	
Minor axis length	km	Minor axis length of fitted ellipse	
Ellipse area	# grid $cell^2$	Area of the ellipse that has been fit, can be converted to square km (1 grid cell is approximately 4 km^2)	
Mean precipitation rate over ellipse	mm/h	Mean precipitation rate, over ellipse only	
Area >10 mm/h precipitation rate	-	Fraction of ellipse area exceeding 10 mm/h ("convective") precipitation rate	
Area >1 mm/h precipitation rate	-	Fraction of ellipse area exceeding 1 mm/h ("stratiform + convective") precipitation rate	
Distance ellipse and box centre, x-component	km	Distance between box centre and fitted ellipse in x-direction	
Distance ellipse and box centre, y-component	km	Distance between box centre and fitted ellipse in y-direction	
Total distance ellipse to box	km	Total distance obtained from its x- and y- component	

rameterised and convection-permitting approaches - for simulations with parameterised deep convection:

- Convective cells are not advected with the background flow, but have their full life cycle within a cell: there is a split between dynamics and the parameterisations in each grid cell [Lawrence and Salzmann, 2008, Prill et al., 2019, 2020].
- An equilibrium assumption is used [e.g. Done et al., 2006, Palmer, 2019, in particular Figure 1 of the latter], where (deep) convection represents the adjustment mechanism of the atmosphere to the presence of static instability. Adjustment occurs under the condition that convection can be triggered, through the potential availability of ascend through a small CIN layer. The trigger may be represented passively, through indirect estimates of sub-grid variability. Grid cells in NWP and (some) climate models are so small nowadays, that the equilibrium between a forcing of the convection and its consumption by adjustment applicable to large areas (containing many convective cells) does not hold anymore. The equilibrium assumption is violated and can affect the evolution of the atmospheric state [Done et al., 2006]. Furthermore, a predefined time scale for this convective adjustment mechanism is often assumed [Cohen and Craig, 2004, Done et al., 2006], which turns out tunable and cannot be generalised.

As a consequence, the representation of deep convection by parameterisation does not only tend to smoothen

precipitation through its coarser resolution, but also through underestimated spatial variability [Keane et al., 2014]. Not all deep convection parameterisations apply the same assumptions - they can be categorised, and hence, the two key points listed here do not have exactly the same implications for each deep convection scheme [Arakawa, 2004, Dudhia, 2014]. A more in-depth discussion of the equilibrium assumptions and its relation to convective variability is found in Done et al. [2006], Craig and Cohen [2006] and Plant and Craig [2008]. A broader discussion on the philosophy and limitations of parameterising deep convection is found in, for instance, Arakawa [2004] and Lawrence and Salzmann [2008].
The arguments above, and the comparatively large grid size, suggest that convective organisation is not directly represented in simulation set-ups with parameterised deep convection. Furthermore, even though attempts have long been done to represent aspects of convective organisation in parameterised deep convection [e.g Moncrieff, 1992, 2019], operational parameterisations do not represent convective organisation Bechtold et al. [2014]. Categorisation through convective organisation is poorly - if at all - justifiable [see also Satoh et al., 2019]. Consequently, application of a complex tracking algorithm, following parameterised deep convective systems, is not suitable. The decoupling from the dynamical model core could lead to failure of tracking: a statistical sample of convective cells technically regenerates irrespectively on an hourly time scale, while precipitation system moves through an area favourable for deep convection. Furthermore, the PER simulations have a domain of only 400 by 500 km, whereas the nest with parameterised convection covers the whole of Europe (Figure 4.3). A typical (mesoscale) convective system, of a (couple of) hundred kilometers, is contained over at least several dozens grid cells in the nest. Therefore, a set of static boxes can be compared among the various ensemble (and physically perturbed) simulations to investigate a convective system. The static boxes are prescribed such that the dominant precipitation and divergence signals of the systems are contained within. Three very different deep convective systems are systematically compared across the six ensemble members and the perturbed experiments are also included in the comparison. An elaborate description of the three systems is provided in Appendix C.1.

4.4 Example of a convective system's track in ICON-PER

The track of one of the two convective systems in ensemble member 14 of the PER simulations is illustrated in Figure 4.4a. The box centre is indicated by a red line, with markers along the way at regular intervals of two hours. The first snapshot at 12:30 UTC shows that the ellipse detection algorithm detects an aggregated convective system at the edge of the box. This large system does not fully fall into the box. The algorithm, that validates the ellipse fits, automatically reports a failure (represented by an X in the plot), because of a too large distance between the box centre and the convective system.
Subsequently, small convective cells develop near the centre of the box (14:30 UTC). One of these systems, the easternmost system, obtains an ellipse centred around itself that is actually located within close range of the box centre. Another one to the west also corresponds with an ellipse fit, but the distance to the box centre is quite large. The system is at the edge of the box and the match is rejected, based on the maximum allowed distance.
Two hours later, again two matches are found: one very near the box centre and one to the north of the centre, but within the box. The larger central one matches through the distance rule, but the northern one is rejected during the validation process.
At the end of the simulation (18:30 UTC snapshot), an elongated convective system develops in association with the earlier central system (14:30, 16:30 UTC). It still sits close to the box centre and is the only ellipse that is detected within the box.
In Figure 4.4b, the development of fitted ellipses over short time intervals is illustrated. The differently coloured precipitating and box features slowly move to the northeast in this plot. However, the ellipse features undergo various changes here. This is associated with a slight reorganisation of the convective structures (see also Figure 4.4a). The reorganisation is induced by the formation of new cells in close proximity of the older system. The northeastern feature is detected throughout, but as revealed by the blue crosses, the match is initially rejected. The box is slowly closing in on the system, as revealed by the possible match, or square marker, at the last of the six time steps. For the southwestern system, one can see that the initial system (larger purple ellipse associated with it) breaks up into smaller pieces for two successive time steps and eventually disappears. The northeastern cells are then left on their own. One of the ellipses fitted to the southwestern system (blue circle) matches with the box at the given time (green), due to the close distance between the ellipse centre and the convective box centre.
However, the northeastern system gets a match with just one of the ellipses: at the last time step. This match is only valid for the larger dataset, with a relaxed ellipse-to-box-centre threshold. This illustrates how convective (re-)initiation, and small displacements, can lead to changes in the ellipse parameters. Corresponding jumps in the time series of ellipse parameters can be identified here and are filtered out. The interval around the jumps is indicated by the dark red outline, at 17:30-18:00 UTC (Figure 4.5a). Most of

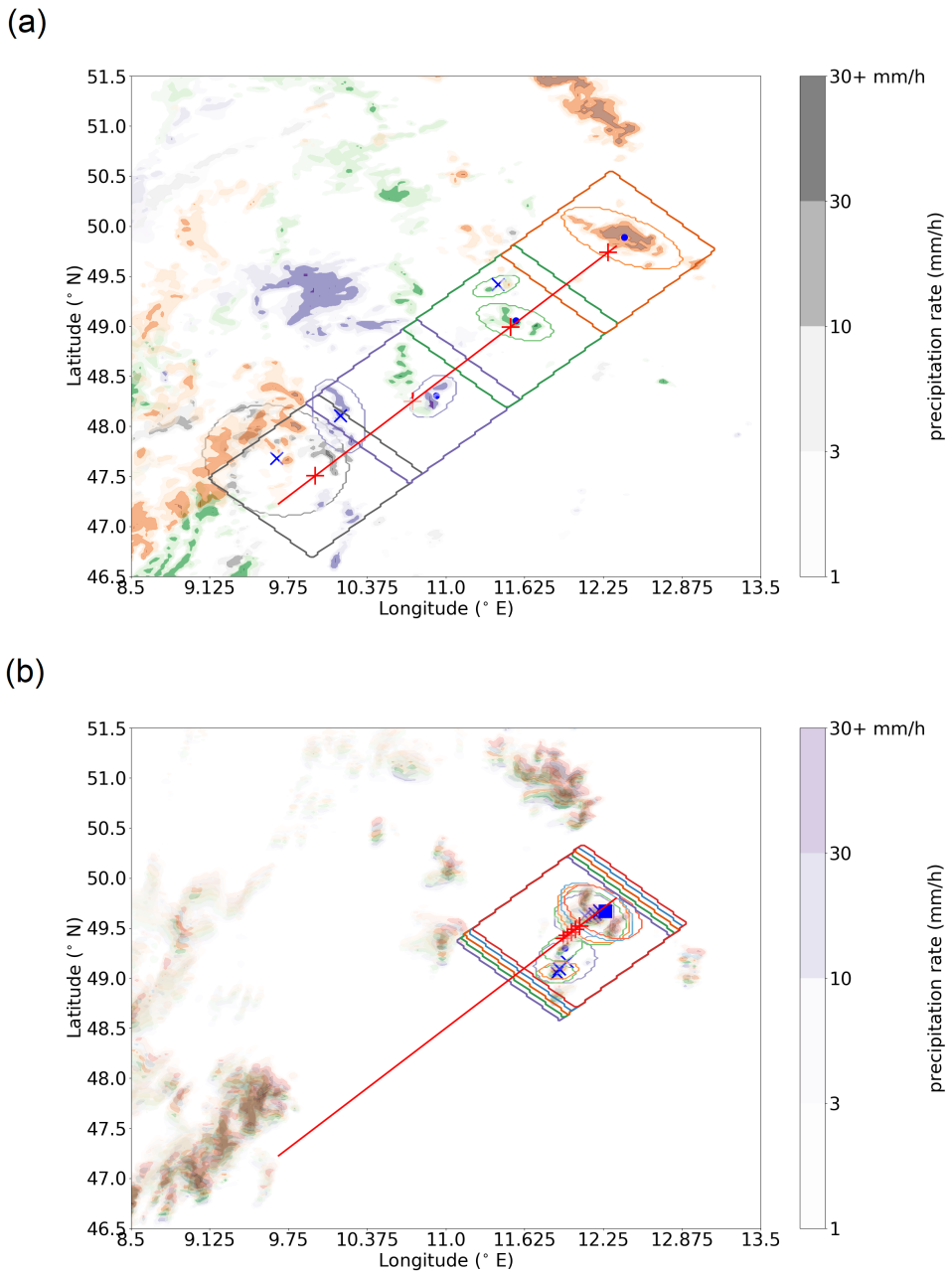

Figure 4.4: Spatial distribution of the precipitation rate (mm/h) in ensemble member 14 of the PER simulations at (a) 12:30 UTC (grey colours), 14:30 UTC (purple), 16:30 UTC (green) and 18:30 UTC (orange). The colour intensity represents precipitation rate, according to the colour bar shown for 12:30 UTC. Bottom (b): same for 17:30-17:55 UTC at 5 minute intervals. The box outline (tilted rectangles), designed to track the convective system, is displayed in the same colour. The edges of ellipses matched with the box outline are also indicated. The track of the box is indicated by a red line and its centre location is indicated by a +. The distance from that red plus-sign to the ellipse centre (blue markers) is evaluated and marked with an *X* , for distances larger than 11 grid cells (about 25 km), a blue circle, for those within 20 km, and a blue square, for those at 20-25 km distance.

the ellipses in this interval are rejected due to such behaviour, but some are retained during the interval. A temporary shrinkage of the axes lengths is seen, but records are nonetheless not rejected in the validation process, due to the design of the validation algorithm: the assessment of the stability of ellipse parameters and interpolated parameter values from nearby records assure plausible records. Another jump within the same time interval is seen in the offset of the matched ellipse from the box centre. Nonetheless, the general behaviour tends to be very smooth over the five hours. That behaviour illustrates that the regenerating convective cells can successfully be detected, covering the temporal evolution of the system.

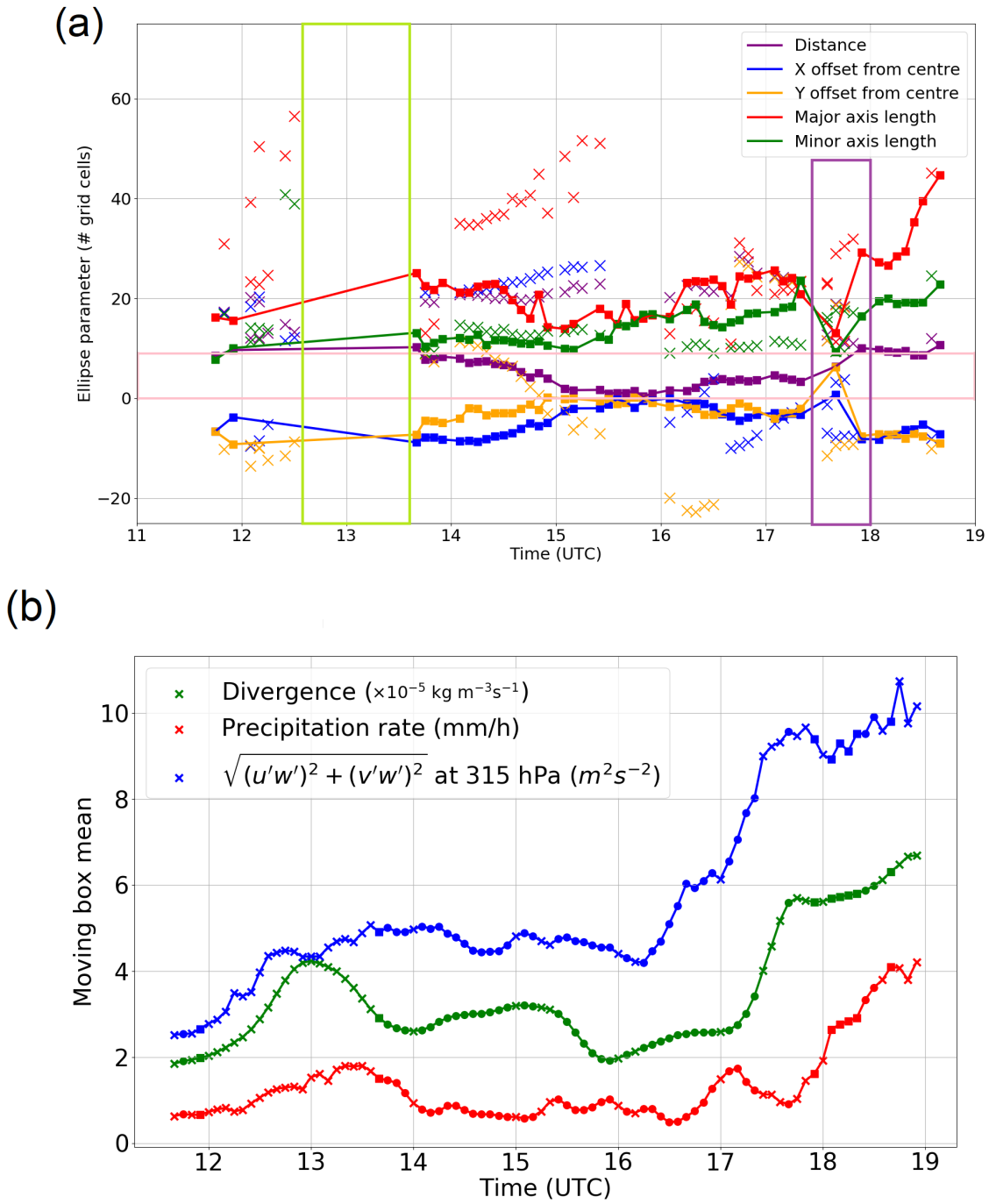

Figure 4.5: Top (a): example of time evolution of ellipse parameters in the dataset, for the same convective system as shown in Figure 4.4, halfway through the validation process. Different colours indicate various ellipse parameters. Distance is calculated from the box centre (+ in Figure 4.4). Crosses represent rejected ellipse records for any of the final datasets. Square markers with a line indicate accepted records. The subset within the thin pink solid outline indicates the records in the small dataset of 456 records. Bottom (b): temporal evolution of the average divergence, precipitation rate and CMT diagnostic over the moving box. Here, circled markers represent records appearing in both datasets and squares only appear in the $n = 866$ dataset.

Figure 4.5a shows the time evolution of ellipse parameters matched with one convective system's box in time - together with the independent, moving box-averaged, values of (filtered) divergence, precipitation rate and the CMT diagnostic (Figure b). No validated ellipse records for a time window around 13 UTC remain in the dataset of this convective system: they have been removed in some step of the validation process (light green solid outline in Figure 4.5a).
Between 14 and 15 UTC, two convective systems have actually been matched with the box represented in

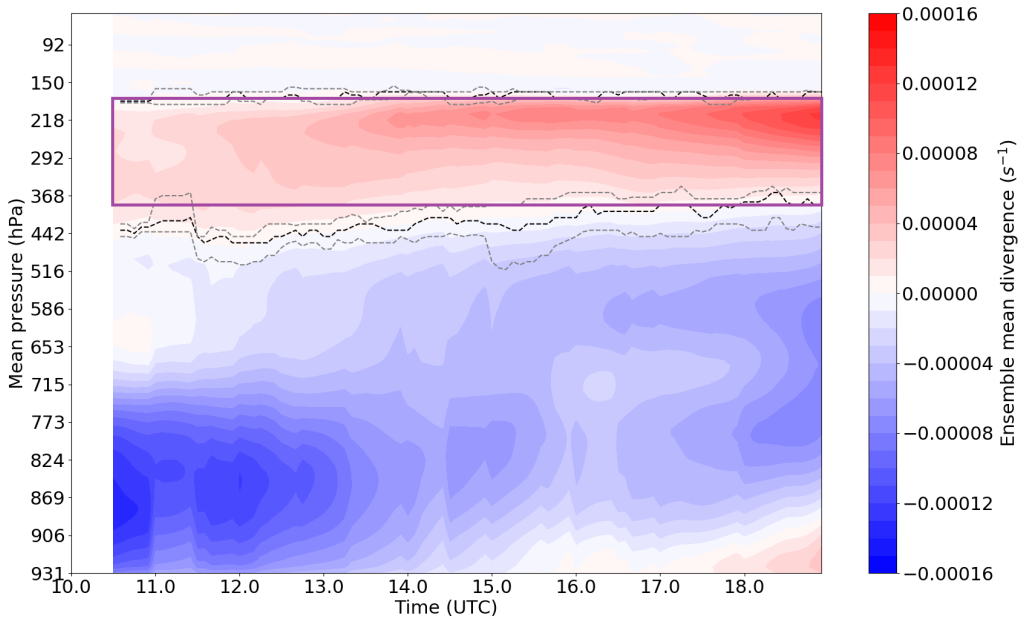

Figure 4.6: Vertical cross section of the evolution of the mean divergence (convergence) along the track of 28 convective systems as a function of mean pressure. Note that, at each instance, only a subset of the 28 convective systems is actually active. Black dashed lines indicate the median level of neutral divergence at any t and grey dashed lines the corresponding 75^{th} and 25^{th} quantiles (nearest to the vertical maximum of divergence). The purple dashed outline indicates the levels, between which the divergent outflow has been integrated in PER.

Figure 4.5. One of them is travelling at an equivalent distance of about 20 grid cells (about 40-45 km) from the box centre and the other at about 4-9 grid boxes from the centre (10-20 km).
The distance between the centre of an ellipse and the associated convective box centre has been set to maximum 9 grid cell distances (20 km) for the more strict dataset, leading to the 456 records dataset (purple series versus pink dashed outline in Figure 4.5a).
In this work, it is not the actual question whether a set of convective cells is actually the *same convective system*, or a prior, or succeeding set of cells. More crucial is to set a criterion, in order to remove the substantial outliers: about these outliers, one can certainly say that two snapshots of a convective system are not representing the same system. The deeper philosophical question of what defines a convective system clearly lies beyond the scope of this work. The main objective of this work is to generate a dataset that covers the variability of deep convective systems, permitted by a certain large-scale background setting (e.g. air mass, jet stream), and the corresponding variability in convective organisation.

4.5 Intercomparison of divergent convective outflows in PER and PAR

4.5.1 Convective systems and associated patterns in divergence (variability)

Figure 4.6 depicts the evolution of the vertical profile of horizontal divergence averaged over 28 convective systems in PER, although at no point in the evolution all 28 systems are simultaneously present. The time evolution of the median level of neutral divergence among the individual systems is superposed as black dashed lines. The grey dashed lines represent the time evolution upper and lower quartiles of the same distribution.
The figure shows some clear signals: dominant inflow of deep convection is in the boundary layer (931 to 800 hPa mean pressure), initially. Subsequently, the convection becomes elevated on average (16-19 UTC) in ICON-PER, with inflow predominantly originating at levels between 800 and 600 hPa, between 17 and 19 UTC.
Furthermore, inflow and *entrainment* (i.e. mixing of environmental air into convective clouds) typically occurs at levels up to about 450 hPa. A strong vertical gradient in the mean of the horizontal divergence is found around 180-190 hPa, close to the tropopause. About and slightly above this level, many convective

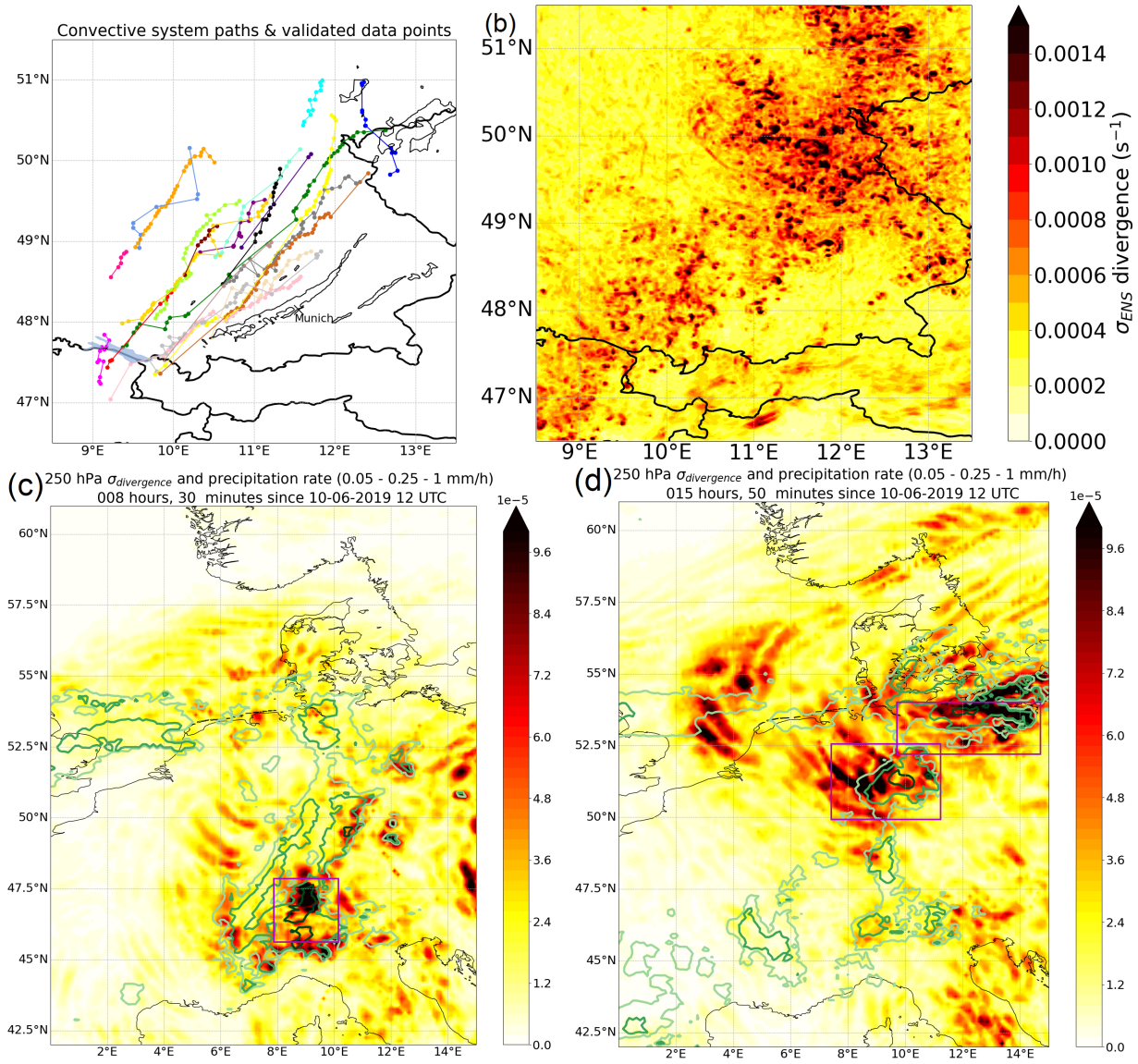

Figure 4.7: Left top (a): paths of convective systems over Southern Germany, as included in the dataset of 456 records for ICON-PER. In thin black contours, tracks of observed convective systems with > 55 dBz reflectivity are shown for the same day, which generally appear further to the southeast than those in ICON. Right top (b): σ_{ENS} of 255 hPa divergence over the same area, on 10^{th} of June 2019, at 18:00 UTC. Bottom (c, d): same at 250 hPa, for ICON-PAR. Isolines in light to dark green indicate precipitation intensities over 0.05, 0.25 and 1 mm/h (ensemble mean; bottom plots only); the boxes, surrounding three convective systems, are outlined in purple. 20:30 UTC (c); 3:50 UTC (June 11^{th}) (d).

systems have a second level of neutral divergence (dashed green lines). Hence, this is the upper boundary of divergent outflow from deep convection in ICON-PER.

Most dashed lines of neutral divergence in Figure 4.6 are located at levels between 350 and 450 hPa. The mean divergence increases gradually with height (from about 0 near 400-440 hPa and even negative below). In PAR, similar profiles also reveal a strong divergence maximum directly underneath the tropopause (Appendix C.1-6). The level of neutral divergence occurs at similar levels, as one would expect, but with slightly more variability: roughly within the envelope of 500 to 350 hPa. The strong decay of divergence at the tropopause is similar.

According to Figure 4.6, the maximum of divergence occurs in the uppermost layers of the troposphere, between 200 and 300 hPa. The spatial variability of horizontal divergence in this layer is illustrated in Figure 4.7 for ICON-PAR and ICON-PER ensembles, in combination with surface precipitation rate (PAR). Figure 4.7a shows the tracks of 22 of the convective systems passing over Southern Germany in PER. The tracks of convective systems in PER generally move from southwest to northeast through the domain. As only a subset of the records were validated, straight sections without markers can occur along the tracks for a series of rejected ellipse fits. Few systems move northward (e.g. the one that has its first record the

furthest to the east, in the Czech Republic). Generally, the precipitation systems tend to increase their intensity and size with time - correlation coefficients between output time and (1) precipitation intensity and (2) ellipse area are 0.22 and 0.25 respectively (see also Figure 4.11). While the overall mean of the precipitation rate over the moving boxes is 3.1 mm/h, the value increases to 4.4 mm/h between 17:30 and 19:00 UTC. Furthermore, the average position of the box centres moves toward the northeastern quadrant of the simulation domain in the last 1.5 hours: to 11.6°E and 49.5°N on average. This region coincides with the highest ensemble variability in the 255 hPa divergence. In other words, large variability in the divergence is associated with the proximity of increasingly active convective systems.
Results for PAR simulations are shown in Figure 4.7c and d: regions of maximum upper tropospheric divergence variability are, again, in close proximity to regions of enhanced precipitation and convective activity. However, not all regions with (strong) precipitation signals are one to one connected to enhanced upper tropospheric divergence variability. One possible explanation for a weaker relation may be the release of latent heat far below 250 hPa, which may lead to divergence in the middle troposphere, instead of the upper troposphere. Another reason for a weaker connection may be that the deviations from the ensemble mean are low, both in precipitation rate and mass divergence. Furthermore, the presented ensemble mean precipitation intensities tend to smoothen precipitation maxima in space.
In Figure 4.7c and d, the convective systems over the Swiss Alps (9°E, 47°N, panel c) and those over Northern-Central Germany (51°N, 10°E and 53.5°N, 12°E, panel d) are the most interesting features, with large upper tropospheric divergence variability. The next section will present results of the box analysis over those three convective systems. The red rectangular boxes in the regular latitude-longitude grid cover the enhanced variability feature of order 200 km length (Figure 4.7). The upper tropospheric divergence is compared to the net latent heating for PAR and PER simulations, as in Section 3.3.5 [Groot and Tost, 2022].

4.5.2 Comparison of the relationship between net latent heating and outflow divergence in PER and PAR

The instantaneous precipitation intensities of three separate convective systems, that develop into squall line-like structures at the end of the simulation, are illustrated in Figure 4.8. The Figure shows in brown (at the end of the squall line formation) that nearly linear segments of high precipitation intensity occur in the northeastern corner of the domain (Figure 4.8a/b) and in the central part of the domain (Figure 4.8c). These nearly linear segments have formed along a line that has a northwest-southeast orientation, often with a sharp gradient in precipitation intensity along the northeastern flank. The line segments are sometimes curved. Figure 4.9 shows the relation between outflow mass divergence and precipitation rate in all of the analysed ICON-simulations. Records ($n = 456$) with valid ellipses and corresponding ellipse parameters are included (Figure 4.9a). The systems that develop into squall line-like structures are thought to resemble 2D convection closer than other single cell or multicell systems. The three coloured lines show the precipitation rate and divergence of these three systems, just when the squall line-like structures develop. Time increases with increasing precipitation intensity (towards the right). Some records are included as both the coloured lines and the background dataset of 456 records, while some other records representing squall line-like structures have been rejected in the validation process.
Figure 4.9a shows that, as time evolves, the normalised mass divergence D is within, or propagating towards, the lower half of the distribution D as squall line structures develop (colored lines). That means mass divergence is, or becomes, low compared to a typical value at a given precipitation intensity, as squall line-like structures develop. The linear least squares fit of one of the three coloured systems in the plane of Figure 4.9a has a slope that even negative in this plane (Table 4.2): the green system with lowest precipitation intensities. The slope with respect to precipitation rate signifies that it moves towards the lower half of the D distribution, while squall line-like structures develop. The other two curves, corresponding to the blue and red line of Figure 4.9a, have a positive gradient with respect to precipitation rate: that is rather typical for the background scatter in this plane. However, a linear fit with intercept value at 0 mm/h precipitation rate lies below the intercept value representative of the background slope and brings those systems in the lower half of the distribution too (Table 4.2). Furthermore, one could see that for those two systems, the gradient with precipitation rate seems to decrease as precipitation rate increases (with time and as the squall line-like structure develops). The weighted (and unweighted) mean slopes of the three coloured systems of 4.9a is well below the representative background slope (Table 4.2). The behaviour of those squall line-like systems fits the expected impact of dimensionality on convective outflows, as put forward in Groot and Tost [2022] (Chapter 3) and supported by Nicholls et al. [1991] and Morrison [2016a,b].
PAR-simulations in Figure 4.9b that represent three different convective systems, as marked with crosses, squares and dots suggest, a roughly linear relation between mass divergence and net latent heating (both for the parameterised deep convection and explicit deep convection ensemble at 13 km grid spacing, black

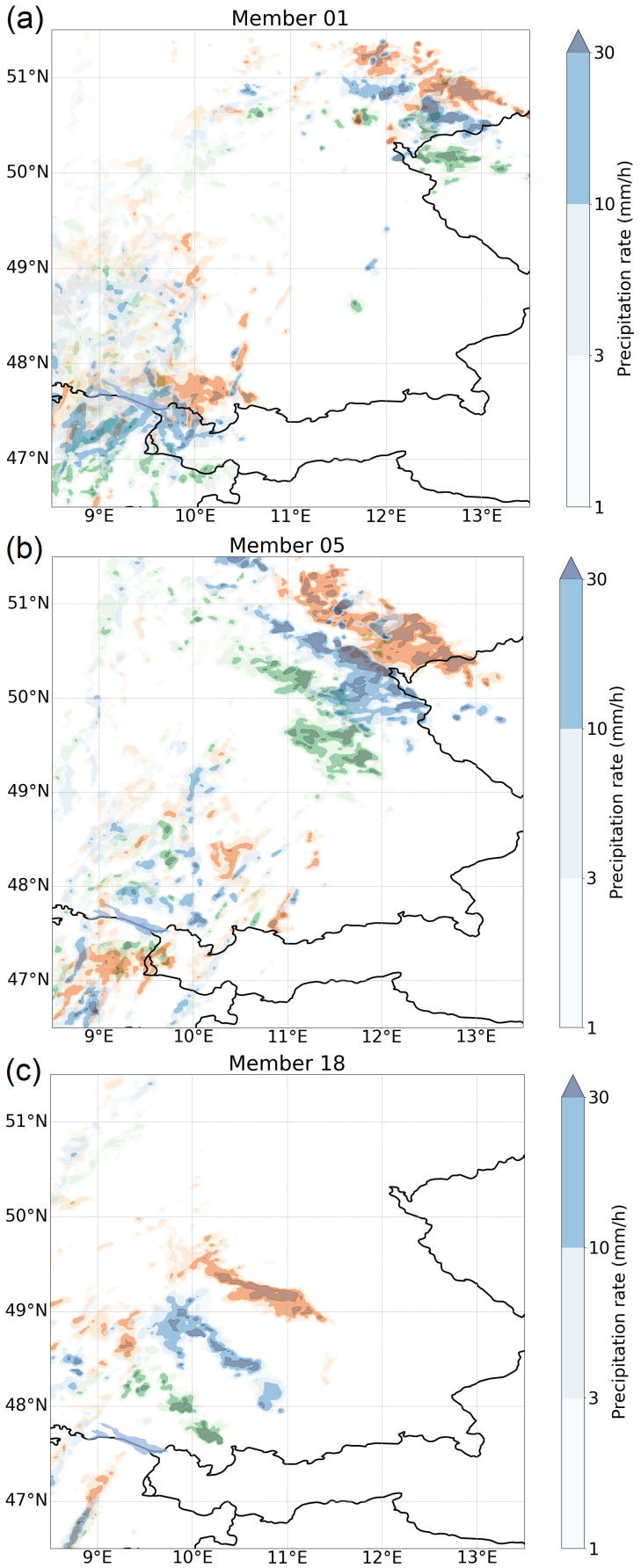

Figure 4.8: Spatial distribution of precipitation intensity at three time intervals (different colors) for three ensemble members of PER (a, b and c) that best resemble a squall line at the end time. Green: at the start of squall line formation process; blue in the middle of the squall line formation; brown at the end of the squall line formation.

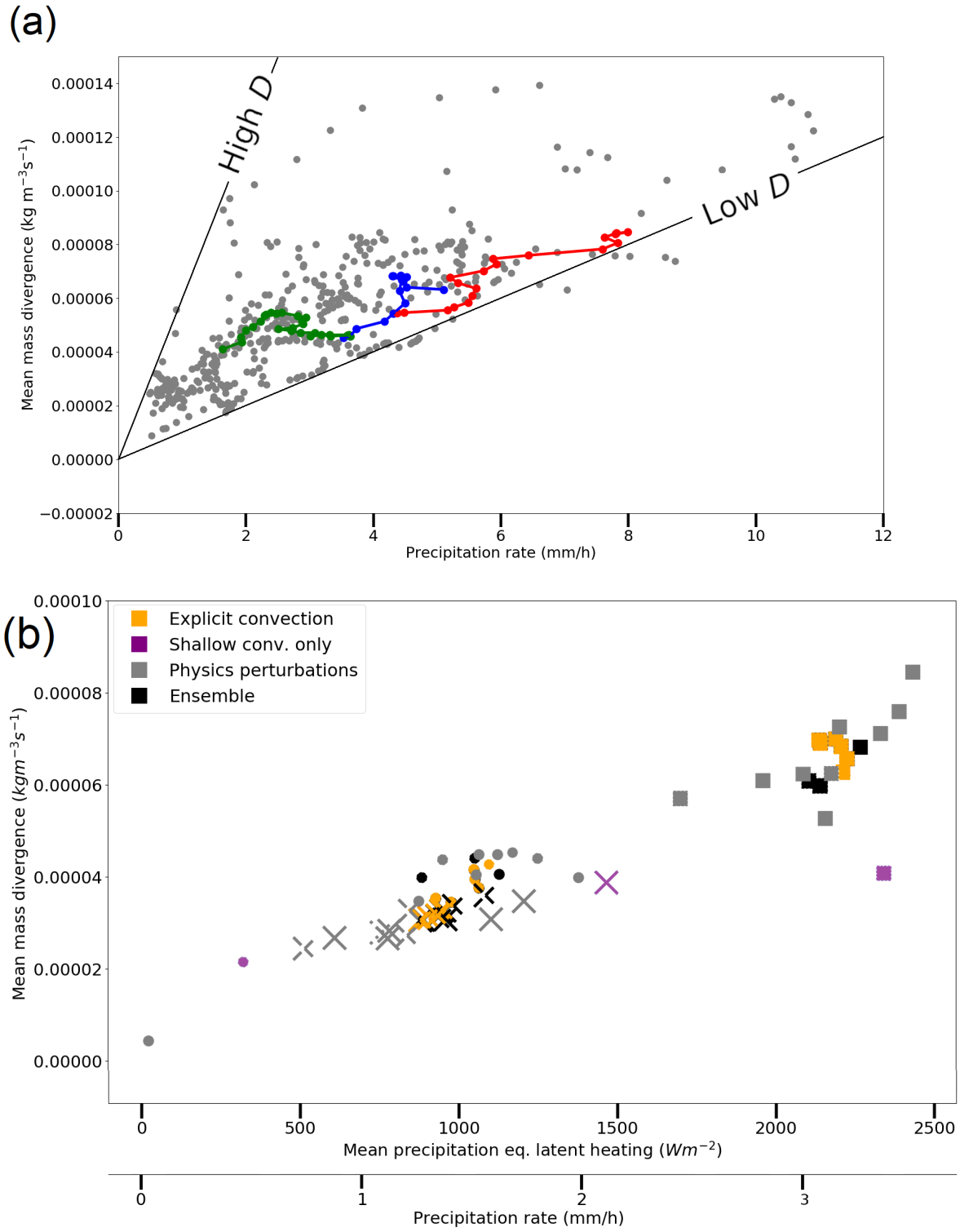

Figure 4.9: (a) Divergence-latent heating relationship of PER simulations for the validated dataset of 456 records (grey), plus the time evolution of three convective systems that form a short squall line-like feature in three ensemble members (colors). Divergence is integrated over the 380 to 180 hPa layer. Added are two black lines of constant parameter D: $D = 6 \times 10^{-5}$ $\frac{kg \cdot mm}{m^3 s^1 h^1}$ and $D = 1 \times 10^{-5}$ $\frac{kg \cdot mm}{m^3 s^1 h^1}$. (b) Same relation integrated over model levels from 420-430 hPa up to 175 hPa for parameterised convection simulations black: ensemble and parameterisation calls at lower frequencies; grey: perturbed physics simulations; orange: explicitly resolved convection as in PER, at 13 km grid spacing; purple: shallow convection parameterisation only. All at 13 km resolution over Europe. Three different markers, crosses, circles and squares, correspond to three different convective systems, as outlined with purple boxes in Figures 4.7c and 4.7d.

Table 4.2: Parameters of least square linear fits for three squall line-like systems in Figure 4.9a, with their corresponding marker colors in the Figure.

Subsample	**Slope** ($\frac{kg \cdot mm}{m^3 s^1 h^1}$)	**Intercept (kg m^{-3}s^{-1})**	**Size of sub-sample**
Background, grey	1.0×10^{-5}	2.2×10^{-5}	414
Green system	-6.5×10^{-6}	6.7×10^{-5}	29
Red system	8.5×10^{-6}	1.7×10^{-5}	21
Blue system	1.7×10^{-5}	-1.2×10^{-5}	16
Linearly weighted mean of green, blue and red system	4.0×10^{-6}	3.2×10^{-5}	66

and orange respectively). Even though the integration depth is about 250 hPa for PAR, versus 200 hPa for PER (Figure 4.9a), a quantitative comparison is sensible. The expected impact of the difference between both integration masks would translate to a $\approx \frac{250}{200}$, or 25%, stronger outflow in PER (Figure 4.9a), if neutral divergence is assumed over the layer excluded from both masks.
In any case, a generally stronger outflow from deep convection occurs in the PAR-simulations at a given net latent heating rate. The relationship for unperturbed parameterised deep convection (black, Figure 4.9b) appears to be very close to linear: no information on mode of convective organisation, such as the appearance of a squall line structure, could be taken into account in these simulations (Section 4.3.2.2). The relationship is also very close to linear for the ensemble of simulations at 13 km resolution without any convection parameterisation (orange). If only shallow convection is parameterised (magenta markers), the outflow deviates clearly from the linear relationship of explicit and parameterised deep convection ensembles (orange and black markers). The deviation is caused by a downward shift of outflow levels (not shown). The analysis of the three convective systems in different ICON-PAR simulations suggests that simulations at 13 km resolution linearise the precipitation rate-divergent outflow relationship. Furthermore, (un)physical perturbations, applied to the parameterised convection set-up, produce small deviations from the seemingly linear relationship (grey, Figure 4.9b).
Parameterised deep convection seems to overly linearise the relationship between upper tropospheric convective outflow and latent heating rate. The behaviour is in agreement with expectations from the absence of convective organisation in the parameterised deep convection. Resolving deep convection "explicitly" at 13 km resolution does not affect the suggested overly linear relationship. On the other hand, the relationship is more flexible in actual convection-permitting simulations, at 1 km horizontal grid spacing. The envelope, with a more variable relationship between mass divergence and net latent heating, is roughly consistent between ICON-PER and idealised CM1 simulations (Chapter 3, Groot and Tost [2022]). The results and discussion in Groot and Tost [2022], and references herein, provide reasons to consider an envelope with variable mass divergence per unit latent heat release more plausible, as an accurate representation of the divergent outflows, than a near-linear relationship with little spread.
Patterns within the relationship of Figure 4.9a, among convective systems in the PER-simulations, are analysed in detail in the next section (Section 4.6). Equivalent patterns, superposed on the nearly linear relationship of Figure 4.9b, existing within PAR cannot be identified (i.e. as a result of physics perturbations that have been applied; see Appendix C.1-6 for a more detailed analysis).

4.6 Dependence of divergent deep convective outflow on properties of convective systems in convection-permitting ICON simulations

4.6.1 Elongation of convective systems

The elongation of convective systems was quantified, using the axis ratio A between two ellipse axes of representative ellipse fits to the convective systems. Based on Groot and Tost [2022] (Chapter 3), one would expect an on average lower A for systems with low values of ratio D (representing divergence over precipitation rate) at a given precipitation rate. Furthermore, it would be expected that, while a convective system evolves, A correlates positively with D. Positive correlation of A and D would then be consistent with the low values of D for the squall line-like systems in Figure 4.9a and 2D-like convection. Finally, it is expected that 2D convection corresponds to a strong component of the inflow, and outflow, perpendicular to the mean tropospheric steering winds. As a result, an ellipse orientation O perpendicular to the mean wind vector is expected to dominate systems with 2D convection. As the steering flow is southerly to southwesterly, eastward or southeastward ellipse orientations are also expected to occur more frequently than other orientations, for low D.
Figure 4.10 suggests that low A indeed corresponds with low D at high precipitation intensities ($>$ 6 mm/h). However, at low precipitation rates, the axes ratio classes are more mixed. At lower precipitation intensities,

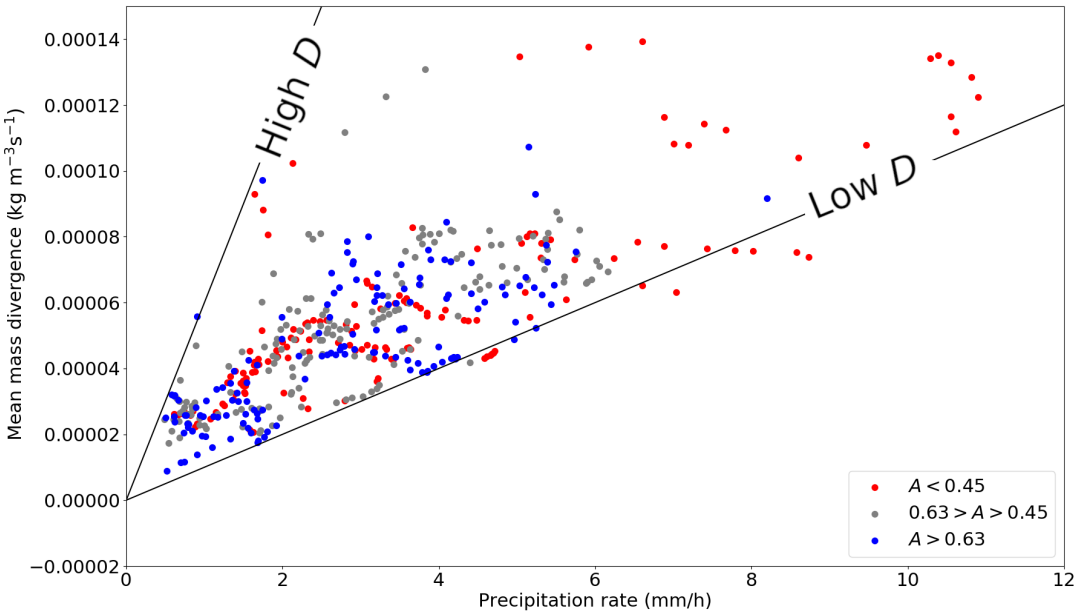

Figure 4.10: Divergence-precipitation dataset of PER simulations, with colours indicating three similarly sized classes of axes ratios. Added are two black lines of constant parameter D: 6×10^{-5} $\frac{kg \cdot mm}{m^3 s^1 h^1}$ and 1×10^{-5} $\frac{kg \cdot mm}{m^3 s^1 h^1}$.

the figure looks relatively chaotic. This suggests that the elongation of convective systems is not the only parameter accountable for anomalies in the mass divergence-latent heating space. Note that the classification into three classes of A can be sensitive to thresholds of A, but it is clear from Figure 4.10 that coherent behaviour is not supported at low precipitation intensities.
Contrasts are nevertheless present, when sub-setting the dataset first to all precipitation intensities above 2.5 mm/h and then to two classes of strong D anomalies (at least ±15% from conditional mean of D). Larger D is associated with an average A of 0.602 in the subset, versus 0.542 for low D. The mean value over the whole dataset is 0.56, with σ of 0.18. Therefore, the difference is significant at 95% confidence and of the expected sign. Nevertheless, the difference in A between the two classes is lower than expected, based on insight from idealised simulations [Groot and Tost, 2022, and Chapter 3].
Furthermore, variability in O within that low D class is strongly reduced, compared to instances with high D: $\sigma = 32°$ for low D, versus $\sigma = 44°$ for all records and $\sigma = 45°$ for the high D subset (significant at 95% confidence too). Orientations of major axes are mostly eastward to southeastward within the low D subset and this is corresponding with expectations.
The within-system evolution of A also does not reveal the expected sign of correlations with D. Signals are rather varied. Overall, relations between D and A are suggested to be non-existent. Similarly, correlation signals of D within bins of similar precipitation rate inconclusive. An overview of some important correlations studied in the whole of Section 4.6 is provided in Figures 4.11 and 4.12.

4.6.2 Aggregation of convective systems

Figures 4.9a and 4.10 suggest deviation from the linear relationship towards larger precipitation rate, i.e. reduced D for convective systems with increasing precipitation rates. Therefore, mass divergence is non-linearly related to precipitation rate in the convection-permitting ICON ensemble, in contrast to simulations at 13 km resolution (Figure 4.9b). Structure in ratio D is investigated in detail here, to improve understanding of the subtle non-linearity for the PER dataset.
A reduction in mass divergence may be caused by the collision of individual 3D outflows from individual deep convective cells, as induced by convective aggregation (see also Chapter 3 and Groot and Tost [2022]). Hence, convective aggregation may reduce divergence, relative to isolated convective cells, as more precipitation cells develop within an area. Analysed measures that indicate developing and aggregating convective systems are ellipse area and area over which a precipitation threshold of 10 mm/h is exceeded (Table 4.1; 4.11). Furthermore, precipitation intensity itself will generally tend to increase as the number of mature

precipitation cells increases with convective aggregation.
Expected negative correlation of the amount of mass divergence per unit precipitation intensity D with increasing size and (precipitation) intensity of the convective systems are found in the presented dataset (see also Figure 4.11). The most important relation connects precipitation intensity and D, with a correlation coefficient of -0.59 in the fully validated dataset and -0.52 in the larger dataset of 866 records. The negative correlation curves the pattern of scattering, in for instance Figure 4.10, towards lower mass divergences than in case of a linear relationship (like in Figure 4.9a).
The robust negative correlation coefficient between D and precipitation rate implies that it is possible to predict some of the non-linear behaviour within the envelop of Figure 4.10: a non-linear best fit between divergence and precipitation rate is expected. A power law with power < 1 could be assumed to reflect the optimal relation between mass divergence and precipitation rates in Figure 4.10 and indeed a fit, optimised for the 456 record dataset, approximates a power law with an exponent of 0.704. When a transform with that power is applied to precipitation rate, the best linear fit is obtained, in terms of least squares. For the larger dataset of 866 records, an exponent of 0.606 is found. Bootstrapping was applied to investigate the uncertainty in the transformed linear least squares fit of the smaller dataset. The 95% confidence of the power transform was estimated at 0.526 to 0.851. However, since multiple highly correlated parameters contribute to the fit (intercept, slope, exponent), the actual parameter uncertainty is smaller.
Conditional correlations between the ellipse area and D within precipitation bins also support the presence of the signal of convective aggregation in ICON-PER. These conditional correlations are summarised in

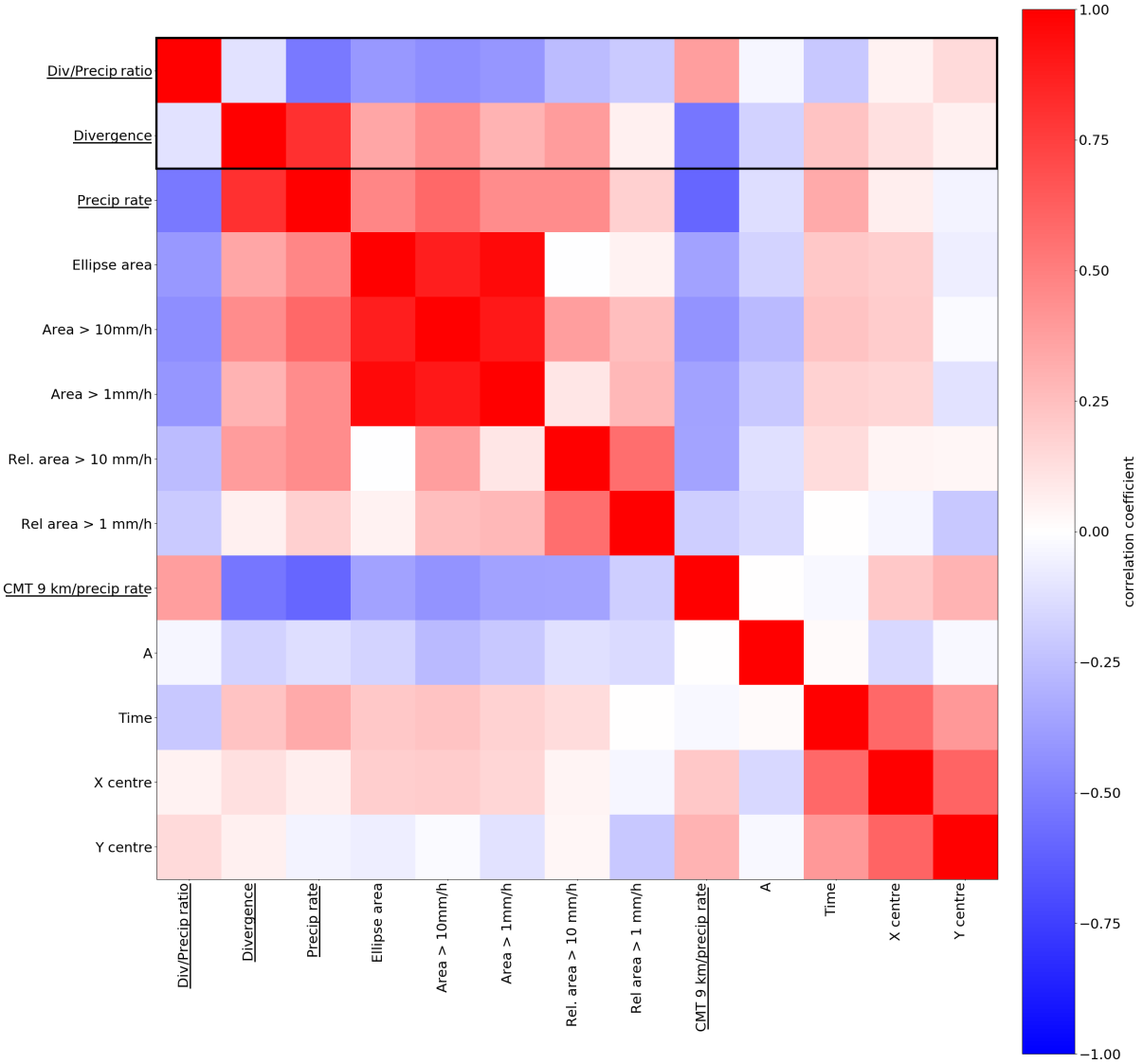

Figure 4.11: Overview of the correlation structures assessed in Section 4.6. Underlined variables indicate those that have been derived from the moving box integration, while those without the line indicate variables extracted from ellipse parameters. Estimates are based on larger dataset with $n = 866$ samples.

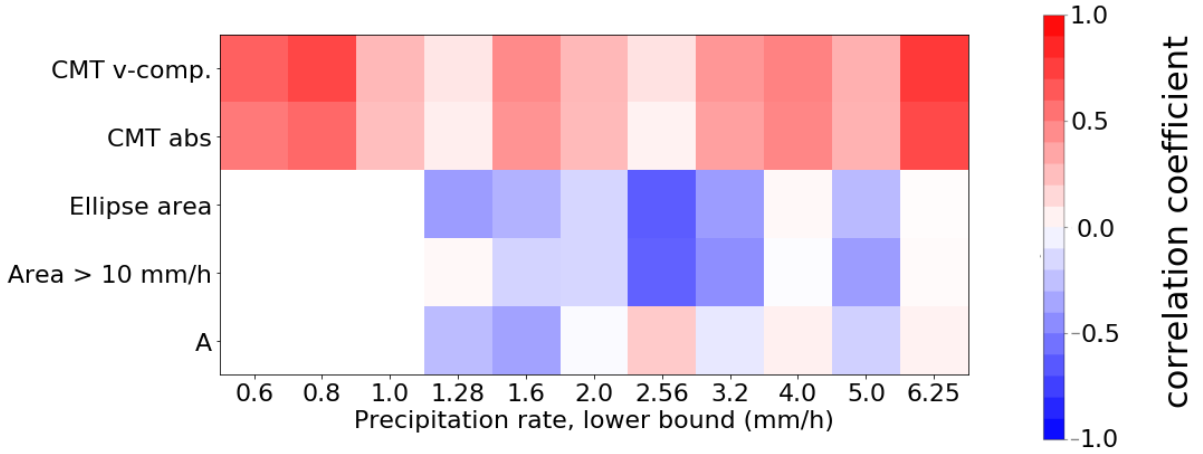

Figure 4.12: Overview of the correlation structures, conditional on precipitation rate, as assessed in Section 4.6. Based on the smaller dataset ($n = 456$ samples). Low precipitation signals are partially omitted, due to small sample sizes and weak convection (under 1.28 mm/h mean precipitation rate over integration box).

Figure 4.12: the (sample size) weighted mean correlation coefficient is -0.32 and this is significant at 95% confidence. Furthermore, the area > 10 mm/h precipitation rate reveals the same pattern, with a weighted mean correlation coefficient within precipitation bins of -0.29 (bins containing at least 30 records and with finite precipitation rate bounds are included in this estimate).
The given statistical relations, detailed on so far, suggest the following evolution of convective systems and impact of aggregation thereon: increasing precipitation intensity linearly forces a given amount of mass divergence in the upper troposphere, initially. But once the precipitation intensity is growing further, the mass divergence does not keep up with the initially linear relation anymore. At higher precipitation rates, mass divergence is typically growing at a comparatively slower rate (i.e. a negative feedback). This signal was exemplified by the developing squall line-like structures in Figures 4.8 and 4.9a. The non-linear mass divergence reduction is stronger in squall line-like structures than in the average of all sampled convective systems. These convective systems seem to move towards the right lower corner in Figure 4.9a. Overall, the non-linearity in mass divergence suggests that the expected impact of convective aggregation on the ratio D is present within the PER dataset. Furthermore, the impact of convective aggregation is qualitatively consistent with that in idealised LES simulations in CM1 [Groot and Tost, 2022].

4.6.3 Surface-based subsampling

If the ICON-PER divergence dataset is subsampled by selecting the systems with surface-based convection, the envelope of Figure 4.9a tightens (Figure 4.13). The selection of such a subsample excludes systems with elevated inflow, or a mixture of surface-based and elevated inflow. A tightening divergence envelope is consistent with expectations: convective systems with similar inflow levels are more likely to have similar outflow levels in the upper troposphere, under the same atmospheric background conditions. Therefore, inflow and outflow are likely more accurately integrated in such a subsample if pressure at upper and lower boundaries are altered (Section 4.5.1): possibly, transient integration boundaries would be optimal. Dilution of the mass divergence signal by local convergence between the lower and upper boundary of the integration mask is less likely in the subsample.
Importantly, the subsampling removes one outlier convective system. Furthermore, the linear correlation coefficient between mass divergence and precipitation rate increases, as the envelope tightens: from 0.80 to 0.85 (Figure 4.13). Therefore, the width of the natural mass divergence envelope for perfectly coherent environmental conditions is probably slightly overestimated in Figure 4.9a. Note that elevated convective systems dominate the dataset between 16 and 19 UTC and surface-based systems dominate before 16 UTC (Figure 4.4).

4.6.4 Role of convective momentum transport

For the dataset with 866 samples, the effect of convective momentum transport on mass divergence has been investigated, by normalising both quantities with the precipitation rate (C and D). Conditional correlation of C and D within precipitation rate bins are analysed. Thereby, the first-order linear effects of precipitation intensity on mass divergence and the aggregation effect (Section 4.6.2) are filtered out. Precipitation rate bins are constructed at the interval 0.6-6.25 mm/h, such that ratio between upper bound and lower bound

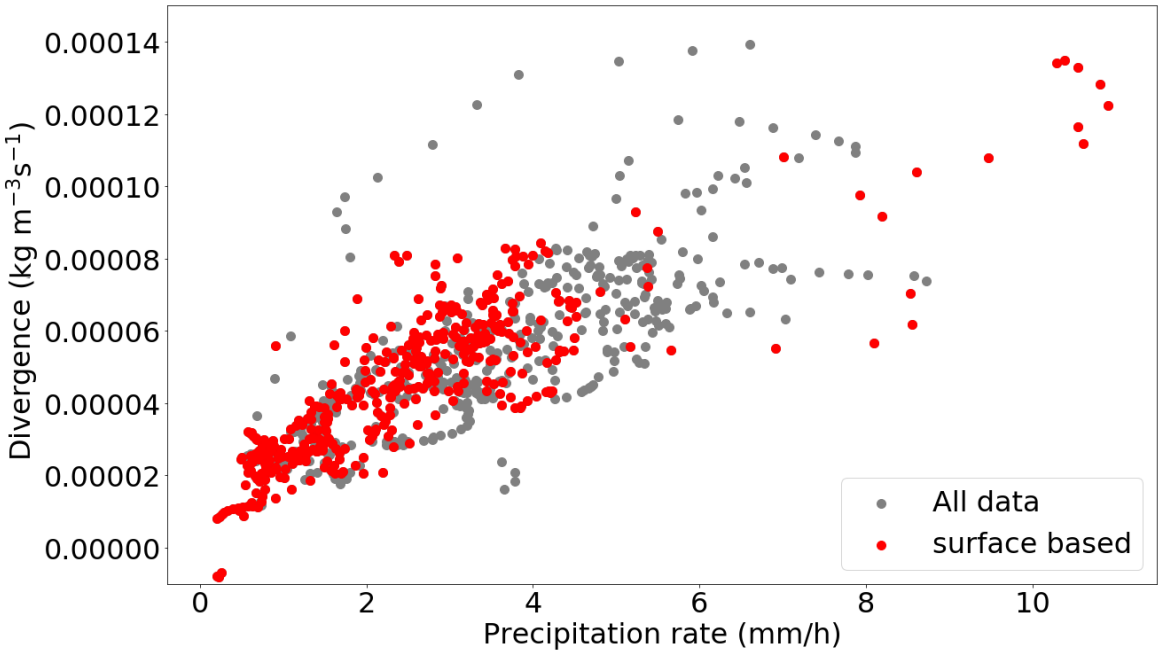

Figure 4.13: Divergence-precipitation relation for the large subset (n = 866), classified as either surface-based (red) or mixed/elevated convection (grey).

of precipitation rate bins is about 4 to 5 (see Figure 4.12).
Over all 11 bins, containing 39-150 samples each, the weighted average of the conditional correlation coefficient is 0.31. The equal weight average is 0.34, with exclusively positive correlations, up to about 0.7-0.8, within the individual bins. Furthermore, when the (dominant; Figure 4.14a) meridional component of the CMT diagnostic is selected, correlations tend to increase slightly: the weighted mean becomes 0.33, with an equal weight mean of 0.38. If the dataset is reduced to the 456 samples, correlations tend to strengthen slightly (not significant). Given all these statistics, it could be assumed that the true correlation coefficient lies very likely on the interval 0.2-0.5, which would imply that a small fraction of mass divergence variability in the convective systems can be explained by the magnitude of the CMT diagnostic (Figure 4.14b, c).
Note that no single data point with upgradient transport occurs among the investigated convective systems (Figure 4.14a). The sample of 866 data points is not fully independent, as only 28 independent convective systems are represented, with records at small time lags being correlated. Investigating the temporal evolution of several convective systems in a single high shear synoptic environment is of course somewhat biased towards a specific scenario. On the other hand, the large coherence of background flow is of benefit for the detection of subtle patterns in the dataset. In that respect, there is a strong contrast with the experimental method in Groot and Tost [2022] (Chapter 3) and its CMT effects on mass divergence.

4.7 Synthesis

4.7.1 Summary of the results

This study has investigated the envelope of divergent outflows from deep convective clouds, conditional on the precipitation intensity (equivalent to column latent heating) in ICON. Both ensembles of parameterised (PAR; grid spacing 13 km) and explicitly resolved convection (PER; horizontal grid spacing 1 km, remapped to a 2 km output grid) during one convective event have been analysed.
Prominent flow variability is co-located with convective system outflows in both PAR and PER-simulations during the event (Figure 4.7). The pattern of variability suggests that deep convection can be an important source of flow variability in the upper troposphere during the early stages of NWP-simulations, consistently with Baumgart et al. [2019].
The analysis of PAR reveals a highly linear relationship between net latent heating and divergent outflows from deep convection, with little spread. Conversely, in PER, a non-linear relation between precipitation rate and upper-level divergence, as well as significant scatter away from the mean relationship, is found. Even if the precipitation of climatology is well represented, the systematic difference between the two experiments implies that the feedback from deep convection to its larger scale surroundings is likely not accurately represented by parameterised convection. The convective flow feedback to larger scales is likely on average overestimated in PAR and using PER at 1 km grid spacing, the representation issue is suggested to be

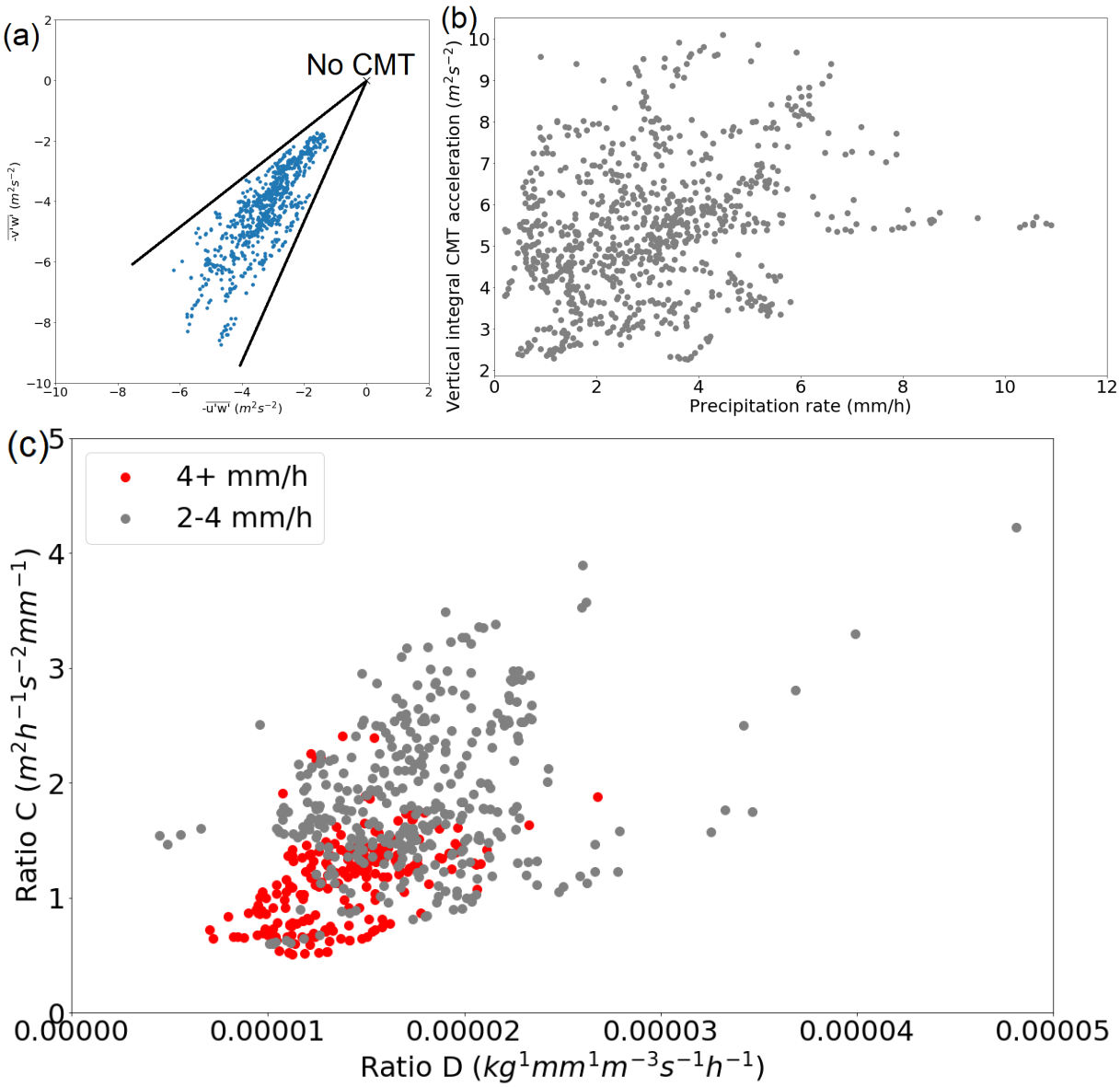

Figure 4.14: (a) Two components of the diagnosed vertical CMT integral at 315 hPa (over-bar denotes mean operator); (b) relation between the absolute acceleration, based on these two components, and box mean precipitation rate. (c) Relation between upper tropospheric mass divergence and the CMT diagnostic C, both normalised to precipitation rate, and for two different classes of precipitation rates (red and grey).

resolved. An on average overestimated deep convective flow feedback at given global average precipitation rates may have substantial effect on regional circulation in weather and climate models and may therefore contribute to their regional circulation biases.

The convection-permitting simulations have been utilised to test hypotheses, derived from idealised studies [Groot and Tost, 2022, and Chapter 3], on the impact of convective organisation, convective aggregation and convective momentum transport on upper tropospheric divergence in real-case simulations.

The first hypothesis, based on Groot and Tost [2022] (Chapter 3, and references herein), is that the dimensionality of the outflow (2D versus 3D and, therefore, the elongation of the system) affects the magnitude of upper tropospheric mass divergence in deep convective outflows. Three convective systems, developing a squall line-like structure, have been identified and they exhibit the expected behaviour over their lifetime: as the squall line-like structure is developing and precipitation intensity increases, the mass divergence does not necessarily follow and often remains in the lower half of the background distribution of conditional mass divergence. However, in a statistical analysis, varied signals have been identified among the expected relations between several ellipse parameters and normalised upper tropospheric mass divergence D and, as such, the first hypothesis is not clearly confirmed.

The second hypothesis is that convective aggregation and organisation modifies the strength of divergent

outflows, when systems with similar net latent heating are considered. This hypothesis can be corroborated by the analysis of the real case ICON simulations: correlations between divergent outflow magnitude and convective system area and intensity are clearly negative. Furthermore, fitting mass divergence to a power-transformed precipitation intensity confidently shows sub-linear growth, suggesting a negative feedback as a consequence of convective aggregation and organisation in the dataset.
Finally, the last hypothesis, about an absent direct impact of CMT on upper tropospheric divergent, outflows has to be rejected: conditional correlations within precipitation rate bins reveal that the magnitude of convective momentum transport also has a small, but significant, impact on the magnitude of upper tropospheric divergence, as opposed to expectations [Groot and Tost, 2022, and Chapter 3].

4.7.2 Discussion

The used method gives very reasonable results to gain insight into divergent outflow variability in ICON for the studied event, as hypotheses can be investigated in a multivariate way. Outflow variability will not collapse onto a linear relationship, without variability (ICON-PER set-up), due to robust effects of convective organisation that have been identified in a multivariate way. A careful selection of moving boxes has been applied to determine diagnostic quantities for all convective systems. In addition, many validation rules were applied before deriving ellipse parameters from ellipse fits. A substantial introduction of noise may result from variability in the outflow (inflow) levels, but by subsampling surface-based systems, it is shown that signals in for instance normalised mass divergence D are not affected: statistical outliers, which are caused by partial detection of deep convective outflows, are removed only (Figure 4.13). By even more careful detection of the outflow levels, the envelope of divergent outflow variability might tighten even further. Nevertheless, it is clear that structural spread and non-linearity in the relationship between outflow mass divergence and net latent heating is evident in the ICON-PER set-up, since the second hypothesis has been corroborated. To emphasise, the idealised large eddy simulations have also provided strong support that convective organisation plays a role in the magnitude of divergent upper level outflow. The idealised LES-study by Groot and Tost [2022] (Chapter 3) suggests that the variability is explainable, when appropriately conditioned on latent heating. This study provides substantial further evidence.

4.7.2.1 Dimensionality hypothesis The dimensionality hypothesis is not strongly supported by the outcomes of analyses in this study, albeit some indirect evidence points to an impact of dimensionality on divergent outflows. Three suggestions are made, why the dimensionality hypothesis is not strongly supported by the statistical analysis, but only weakly:

- The chosen metric is sub-optimal: it is not able to distinguish well between nearly-2D and nearly-3D convection
- The (elevated) shear profile of this case does not lead to a sufficiently large variation in dimensionality of the deep convection
- Opposing statistical patterns compensate each other, even within precipitation bins.

Each of these three suggestions will shortly be discussed in the following paragraphs, one by one. Consequentially, the outflow dimensionality seems to contribute only weakly to the variability of divergence, with the effect of organisation and aggregation present strongly in the outflow variability. However, the signal identified in systems with squall line development supports the dimensionality argument, consistently with Bretherton and Smolarkiewicz [1989], Nicholls et al. [1991], Mapes [1993], Nascimento and Droegemeier [2006], Morrison [2016a], Groot and Tost [2022] and Chapter 3.
The first possibility is that the metric for system dimensionality, namely the elongation of ellipse fits, is not fully adequate, in particular as many convective system in the ICON simulations are relatively small and only few develop clear structures. Two solutions to investigate if a poor metric buries the signal are, on the one hand, to apply the method to a larger set of PER-like simulations that includes various cases, and on the other hand, to investigate if other algorithms, using for example a storm-relative flow analysis, could be of benefit to examine the dimensionality of a wide mixture of organised convective systems. The latter may be combined with the current method and is technically doable [Chapter 3 and Groot and Tost, 2022, Trier et al., 1997].
Furthermore, the second possibility is that the shear profiles used in LES simulations with CM1 [Groot and Tost, 2022, Chapter 3] impose a much clearer separation of 2D and 3D outflow regimes than simulations of the event investigated here. That effect seems plausible, because the shear profile in CM1 was nearly perfectly perpendicular to the background flow, resulting in efficient formation of 2D convective systems. Nevertheless, ellipse parameters demonstrated that orientations of convective systems in PER were highly mixed. Among low D values - where convection is likely more 2D - the possible presence of a convection

regime resembling 2D convection better was suggested. Still, a different shear profile, with stronger low level shear (0-3 km), would better support squall line formation and initiate corresponding convection resembling the 2D regime closer. Such a wind profile probably lends itself better for separation of convective systems into nearly-2D and nearly-3D classes. It would worthwhile to revisit the dimensionality hypothesis with a larger ensemble of convective systems in particular, including cases of well-developed squall lines with a (sub-)ensemble of less strongly organised convection. In particular, the development phase of squall line structures could be of large interest for a comparison to the this work.
Lastly, as a consequence of compensating anti-correlation between A and convective aggregation (see Figure 4.11), axis ratio A may hide the direct dimensionality signal in amount of outflow divergence. The signal may even be hidden if conditional correlations within precipitation rate bins are considered (Figure 4.12). This can be the case if A is a sub-optimal proxy for the dimensionality of convective outflows. Two correlation effects within precipitation bins could oppose another, namely convective aggregation and A (as a proxy for outflow dimensionality). Such patterns could explain outcomes of this study, even if the dimensionality hypothesis would explain a substantial proportion of the examined divergent outflow variability.
Nevertheless, if the dimensionality (first) and aggregation (second) hypotheses are strongly interrelated, as suggested in Groot and Tost [2022] and Chapter 3, it would not be expected that the apparent potential compensation between correlation signals found in this study would exist. It would be more likely in such a case that the dimensionality hypothesis is easier to prove than the aggregation hypothesis. Therefore, a deeper study, with a squall line ensemble versus less strongly organised deep convection, is thought to be needed to resolve this possible paradox. On the other hand, the impression of a paradox does not imply that the method used in this study is unsuitable: it suggests that the methods used are particularly suitable to disentangle the three hypotheses.

4.7.2.2 CMT hypothesis The impact of CMT on divergence strength is found to be much more pronounced here than in the idealised an LES study by Groot and Tost [2022] (Chapter 3). A possible reason why convective momentum transport was not found to (directly) affect upper tropospheric divergence from deep convection in the CM1 simulations [Groot and Tost, 2022, and Chapter 3] is that the imposed shear layer was too shallow. Upper tropospheric wind shear was even completely absent in that set-up, whereas in any real world case (such as in this study), the wind shear is non-zero in the upper troposphere. In the LES simulations, the shallow shear set-up was used to reduce cell propagation in the small domain set-up. Shallow shear profiles can reduce the average height that parcels in convective cells reach [Coniglio et al., 2006] and the associated reduced vertical overturning then suppresses the interaction between the shear layer and the upper tropospheric divergent outflow (in agreement with Brown [1999]). Therefore, the impact of CMT on upper tropospheric divergence is perhaps suppressed in Groot and Tost [2022] (Chapter 3). It is also plausible that other mechanisms may be at least as important for hiding impact of CMT on upper tropospheric divergence in the LES set-up [Groot and Tost, 2022, and Chapter 3], but the author is not aware of any particular mechanism responsible that is similarly plausible.
Lastly, PER simulations in this study are arguably (much) more suitable for detecting subtle (but reasonable, in real cases) impacts of CMT on divergent convective outflows in the upper troposphere. On the contrary, it does not lend itself very well for in-depth understanding the mechanism underlying divergent outflow variability, due to the complexity of the flow scenario and the amplitude of systems in close spatio-temporal proximity. Additional LES experiments targeting CMT could provide further physical understanding, but are not within the scope of this study.

4.7.2.3 Further research To summarise, this study shows that further investigation is needed to thoroughly understand the role of dimensionality for the magnitude of divergent outflows in a practical NWP setting. Furthermore, convective organisation and aggregation is a key player for the magnitude of the divergent outflows in practice, which is only accounted for by convection-permitting simulations at sufficiently fine (for instance 1 km) horizontal grid spacing.

4.7.3 Implications

This study once more confirms the strong link between precipitation variability and flow variability in an ensemble. This close connection may lead to error growth in a forecast, or ensemble spread, in a set of simulations. While the downstream propagation of perturbations is not directly addressed here, the divergence variability (Figure 4.7) suggests a potential role for divergent outflows in propagating precipitation variability and other convectively imposed variability (e.g. CMT) to large-scale dynamics. The potential downstream impact of variability in convection characteristics via this (and other) mechanisms is addressed by Baumgart et al. [2019], Zhang et al. [2007], Zhang [2005], Rodwell et al. [2013] and Selz et al. [2022] (and others). Furthermore, based on this study, it could be argued that the contribution to flow perturbations, from the

convective scale's perspective, can be split-up into a component of precipitation variability and another component of superposed conditional mass divergence variability (D variability). The second component is induced by convective organisation and aggregation, amongst others. Such a role of convective organisation could advocate to the results found by Rodwell et al. [2013]. Nevertheless, examination of a selected case with upscale impact of the convection (e.g. Rodwell et al. [2013]) would be needed to thoroughly assess the role of acting mechanisms to understand downstream impacts of convective organisation on the large scale. The split-up of divergence variability into the two components, namely precipitation variability and superposed variability in outflow divergence (for instance, due to convective organisation and aggregation on divergence variability), has consequences for weather and climate simulations. Only the first of the two components can be modelled with regular deep convection parameterisation schemes. The second of the two components is (nearly) eliminated when deep convection is parameterised, but is accounted for in a convection-permitting high resolution set-up. To illustrate the two components of variability, conditioning deep convective variability on precipitation rate offers a highly important perspective onto convective variability. The perspective can be highly beneficial to better understand the feedback between deep convection and its environment. Variability associated with both precipitation rate and upper tropospheric dynamics within convective systems has also been evaluated in Groot and Tost [2023, 2022] (Chapters 3 and 5).
Rodwell and Wernli [2022] studied how ensemble spread in IFS is affected by various contributors, such as the deep parameterisation scheme, model uncertainty representation by stochastic perturbations of parameterisations and excitation of *singular vectors* (representing flow sensitivities to perturbation growth) in two cases. The difference in the divergence envelope at given rates of net latent heating, found here, may explain the localised impact of organised convection on the evolution of upper tropospheric spread, when they switch their IFS set-up from parameterised to explicit treatment of deep convection. Parameterisation of deep convection and other sources of uncertainty tend to spatially diffuse uncertainty signals, compared to explicit convection schemes [Rodwell and Wernli, 2022]. This may be beneficial, if additional diffuse sources of uncertainty are underrepresented. However, that is somewhat speculative, as their evolution of spread is controlled by an interplay between many contributors.
Findings in this work on the second, and to a lesser extent third, hypothesis imply that incorporating tailored diagnostics to address the effect of convective organisation and aggregation in error growth studies is needed. Then, the potential of extending such studies all the way from the convective to the planetary scales can be utilised: findings of Baumgart et al. [2019] and Rodwell et al. [2013] may be complemented. For that, the conditional perspective on convective variability, shaped in this study, needs to be connected with for example the perspective of Baumgart et al. [2019].

4.8 Conclusion

The multivariate exploration of divergent outflows of deep moist convection in ICON simulations shows that their dependency is not as simple as it may seem based on LES [Groot and Tost, 2022, and Chapter 3]. Additional factors likely play a role. However, a significant portion of variability is explained by effects that were also present in the analysis based on LES.
The following can be concluded on variability in upper tropospheric divergent outflows from deep convection ("this outflow"):

- This outflow is responsible for major ensemble spread in the divergent part of the upper tropospheric wind field during a convective event
- Convection-permitting high resolution simulations (horizontal grid spacing 1 km) represent the effect of aggregation on divergent outflow from deep convection and an envelope of divergent outflow variability for a given net latent heating rate
- Using simulations at coarser resolution seems to imply a (near-)linear relationship between this outflow and net latent heating rate
- Some indications show that the fingerprint of dimensionality is represented in variability of this outflow in ICON convection-permitting set-up, but a case study, comparing squall lines that highly resemble 2D convection with less organised convection would be needed to increase the confidence in this finding
- Convective momentum transport seems to weakly affect this outflow directly, conditional on, or normalised, with precipitation rate
- To understand the convectively induced flow perturbations better, a split these perturbations is useful: 1. variability associated with predicted precipitation intensities (on the mesoscale); 2. superposed precipitation-dependent flow perturbations, which can depend on representation of deep convection: convection-permitting or parameterised

5 Evolution of squall line variability in an ensemble of idealised LES

Large parts of this Chapter also appear in Groot and Tost [2023].

5.1 Introduction

Squall lines are a complex meteorological phenomenon, consisting of an elongated linear area with convective cells, that usually induce a coherent mesoscale circulation. They often develop into a mixed stratiform-convective precipitation system, with horizontal extents of up to several hundred kilometers, and have a lifetime exceeding several hours. Understanding and simulating squall lines has been an active field of research for several decades [Houze, 2004, 2018]. The goal of this study is to understand the dynamical processes that govern ensemble spread in large eddy simulations of idealised squall lines.

Due to the increasing computational resources, high resolution numerical simulations in convective studies have become feasible. Throughout the last 25 years, simplified cloud resolving km-scale simulations [Weisman et al., 1997] have been supplemented with systematic sets of fully three dimensional large eddy simulations (LES) at high resolutions [Adams-Selin, 2020a,b]. This allowed for an improved understanding of the impact of shear profiles on convective organisation [e.g. Weisman and Rotunno, 2004, Coniglio et al., 2006, Adams-Selin, 2020a], including squall line organisation. Moreover, by investigating convergence of simulations at high resolution, the effect of model resolution has been evaluated [Weisman et al., 1997, Bryan et al., 2003, Lebo and Morrison, 2015] (implicitly evaluating model representation). Bryan et al. [2003] found that even LES simulations do not result in true convergence of solutions, but still, resolving the hundred-meter scales strongly increases the confidence in squall line simulations compared to 1-4 km simulations. The need for parameterising processes, meanwhile, shifts to sub-grid turbulence in a partly represented *inertial sub-range* and microphysics [Bryan et al., 2003]. However, statistical (bulk property) convergence occurs already at coarser grid spacing, while local numerical convergence may not occur at all [Langhans et al., 2012]. How squall lines can sensitively depend on microphysics, shear and magnitude of conditional instability has been investigated by now [e.g. Morrison et al., 2009, Grant et al., 2018, Adams-Selin, 2020a,b].

Squall line ensembles, and their *error growth*, have been investigated by Melhauser and Zhang [2012], Hanley et al. [2013], Weyn and Durran [2017]. Individual ensemble members were compared to each other, with a focus on the differences in their evolution. Even though squall line development and sensitivity has been addressed in LES, e.g. Adams-Selin [2020a,b], error growth has not been addressed at sub-km grid spacing to the author's knowdlege, but only at km-scale convection-permitting resolution, e.g. by Weyn and Durran [2017]. At LES-resolutions (100-200 m), smaller scale processes can be included in a process-based analysis: updrafts [Varble et al., 2020], cold pools [Grant et al., 2018] and gravity waves are represented explicitly and their dynamics can be addressed directly, which is needed for improved understanding of small-scale error growth. Error growth studies at large scales suggest that deep convection is an important process to address in error growth studies [e.g. Selz et al., 2022, Baumgart et al., 2019, Rodwell et al., 2013].

Application of the word *error* (and related terms) to ensemble differences requires a *perfect model assumption* or a *perfect error assumption* [e.g. Selz, 2019]: the physics of errors has to be assumed to be represented perfectly in a numerical model, which is reasonable for error features larger than seven times the horizontal grid spacing, but not for smaller scale features [Skamarock, 2004]. Melhauser and Zhang [2012] and Hanley et al. [2013] looked at a set of simulations, featuring a real squall line case, in a local area model from the larger mesoscale and synoptic point of view. The realistic squall line was the core feature of both sensitivity studies, even though downscale "contamination" from the synoptic scale was present and considered. Melhauser and Zhang [2012] found that an intrinsic limit of predictability can affect squall line ensemble forecasts: by reducing initial condition spread by a factor of 8, their simulations could still diverge about as much as with the original (unreduced) initial condition spread. Furthermore, the eventuality of convective initiation was found to be key for the extent of the ensemble spread, a process of which the limited predictability would be expected to be driven by spatio-temporal variability at even smaller scales [Lorenz, 1969a]. Convective initiation was also found to be a key process by Hanley et al. [2013].

Weyn and Durran [2017] have looked at error growth in mesoscale convective systems with squall line-like features in isolation. The simulations of Weyn and Durran [2017] had a resolution of 1 km on a domain with horizontal scales of about 500 km. Most of their error growth analysis was done from the spectral point of view, which implies that there was much less attention on convective and accompanying processes in physical space. Despite this focus, they have compared the error growth of divergent and rotational wind components and found that divergent winds are mostly leading to larger scale errors. Furthermore, an important finding was that by reducing initial condition spread, by factors of 5 and 25, only about 1 hour of predictability was gained. Compared to their error saturation time scale (forecast time at which a majority of the predictable component of a signal is lost, for example 80%) of about 5 hours, this is not much.

In this study, sensitivity analyses will be carried out from a dynamical point of view, with squall line simulations in isolation from a synoptic and larger mesoscale environment. Error growth will be analysed in high resolution simulations (200 m) with 10 ensemble members. The dynamical aspects that will be analysed are the following - including a short review for each dynamical aspect:

- **Gravity wave dynamics**
  Interaction between gravity waves and a convective environment has been investigated using a linear gravity wave model [Bretherton and Smolarkiewicz, 1989, Nicholls et al., 1991, Mapes, 1993]. Mapes [1993] argued that propagation of the gravity waves is important for upscale organisation of convective systems as it happens in the tropics. In these studies, a localised heating signal was used as a proxy for a convective system, mimicking the latent heating source. Subsequently, cloud models have been used to investigate how gravity wave dynamics can concentrate regions of upward motion. Accordingly, it has been found that several vertical gravity wave modes favoring certain regions of convective initiation exist, which can subsequently assist in the formation of coherent patterns in vertical motion and organise convection upscale [e.g. Lane and Reeder, 2001, Stechmann and Majda, 2009, Adams-Selin and Johnson, 2013, Lane and Zhang, 2011, Grant et al., 2018, and references in the latter two]. In addition, Bierdel et al. [2017] have created a model to improve the understanding of the error propagation from convective scales to large mesoscales and (sub-)synoptic scales, caused by differences in convective heating, based on the linear gravity wave model [Bretherton and Smolarkiewicz, 1989, Nicholls et al., 1991]. However, they focused on the role of rotation on these larger scales and *geostrophic adjustment*[7] of difference flow. These scales are substantially larger than (sub-)squall line scales investigated here.

- **Convective initiation**
  Looking from the convective initiation point of view, Fovell et al. [2006] showed how gravity waves affect squall line regions on smaller scales. In their simulations, with explicitly resolved deep convection, it was shown how gravity waves can trigger the development of *discrete* convective cells. These cells form ahead of a squall line and can subsequently merge with the main system. A sensitive eventuality of these discrete convective cells was identified, which leads to a diverging evolution, as a result of contrasts in convective initiation, depending on the radiation treatment. The sensitive eventuality of convective initiation has played an important role in Melhauser and Zhang [2012] and Adams-Selin [2020a,b]. The sensitive dependence can nowadays be resolved more accurately, due to finer grid spacing.

- **Cold pool-relative motion: u in the x-z plane, averaged along squall lines**
  Pandya and Durran [1996] have looked at the (sub-)system scale variability, explained by thermally forced gravity waves, and found that the mesoscale squall line circulation in their system depends to a large extent on the magnitude and shape of thermal forcing. Low-level features, notably the *rear inflow jet*[8], depend on the low-level conditions, especially static stability ($\frac{\partial \theta}{\partial z}$). Their study has a strong focus on the squall line-relative circulation (u), in the plane perpendicular to the squall line orientation. The work also assesses the impact of modified physical processes and background state (e.g. microphysics tendencies, stratification) on the system-relative flow (see also Figure 2.2g, h in Chapter 2).

- **Updraft and downdraft motion**
  Updraft and downdraft characteristics can be sensitive to grid spacing. This sensitivity may lead to biases in updrafts (or downdrafts), and their evolution, when a comparison to radar images is made [e.g. Varble et al., 2020, Lebo and Morrison, 2015, Varble et al., 2014, Stein et al., 2014], which could propagate to other aspects of squall line simulations [Varble et al., 2020, 2014]. However, since no comparison between simulations at different resolutions or observations and simulations is made here, such sensitivities are not relevant here (see also Appendix D). Furthermore, the grid spacing is believed to be fine enough for accurately resolving updraft and downdraft characteristics [Bryan et al., 2003, Lebo and Morrison, 2015, Varble et al., 2020].

This study is restricted to the analysis of just one idealised squall line case, with weak ensemble perturbations. Considering just one case also allows for detailed assessment of the dynamical aspects listed. Nevertheless, some conclusions cannot be generalised, based on this Chapter alone. Furthermore, the squall line evolution is quasi-2D initially, due to the nearly-2D flow and initial conditions. However, this nearly-2D structure is of benefit for the analysis of squall line-relative flow. The magnitude of ensemble perturbations that are applied are equivalent to a vertical wind profile uncertainty of about, or less than, one model layer in the vertical, in

[7] Geostrophic adjustment is the process in which winds are accelerated by a pressure gradient initially, and, as time progresses during the first (typically half) day, the apparent Coriolis force balances those pressure induced winds. This process results in a nearly geostrophic circulation, around large-scale pressure systems at synoptic scales, and is beyond the scope of this work.

[8] A specific type of mid-tropospheric inflow from the rear side of squall lines encountered regularly, for relevant review material see for example Houze [2004]

typical convection-permitting model set-up. Altogether, the aim is to get a comprehensive overview of the processes through which errors propagate in a high resolution squall line ensemble, following such a small initial condition perturbation. How these errors may be transferred from one process to another is also addressed.
Furthermore, the issue of *intrinsic predictability* can be addressed, given the small magnitude of initial condition perturbations. Here, intrinsic refers to the fact the evolution of errors starting at very small magnitude within an ensemble can be examined (as in, for instance, Baumgart et al. [2019], Selz [2019], Selz et al. [2022]), much smaller than errors applicable in practical NWP nowadays (see also Sun and Zhang [2016], Melhauser and Zhang [2012] and Figure 18 in the latter). Relative to practical NWP, these small-magnitude errors approach a theoretical zero-limit of error magnitude. Zonal shear in a shallow layer is perturbed with magnitudes of 0-5% and randomly, as opposed to the often used systematic iterative approaches [e.g. Selz, 2019, Zhang et al., 2019, Selz et al., 2022, Melhauser and Zhang, 2012].
In this study, some analysis techniques are applied that are not so commonly used in studies of mesoscale convective systems. Next to more widely used *passive tracers* [e.g. Grant et al., 2018], an *ensemble sensitivity analysis* [Hanley et al., 2013, Torn and Romine, 2015, Bednarczyk and Ancell, 2015, but the latter with parameterized convection] and a *difference kinetic energy* metric are used. Passive tracers are an important tool to identify variability in convective transport, but by targeting the main inflow layer, differences between pairs of simulations can be identified early on. Variability in a second phase of convective initiation is revealed this way. In combination with a tailored ensemble sensitivity analysis, which allows to connect the strength of the convective initiation with subsequent evolution of the squall line circulation (u), the effects of this phase of initiation on squall line evolution can be followed in time. System-relative flow is evaluated and its relation with a second phase of convective initiation is analysed. The difference kinetic energy metric for error growth analysis, and other specific diagnostics, can provide further insights in the evolution of system-relative motion and its role in error growth [Zhang, 2005, Zhang et al., 2007]. Each of the three methods is introduced more extensively in the sections where these methods are applied.
The characteristics of the simulations used in this study have been documented in Chapter 3, Section 3.2, as well as the initial conditions and ensemble design. Furthermore, the spatio-temporal focus of the analysis and the statistical verification techniques are described in Sections 5.2.2 and 5.2.3 of this chapter. In Section 5.3 of this chapter, the main analysis is carried out, preceded by a description of diagnostics tools used in the respective subsection. The Section starts with a general evolution of the simulated squall line echoes. After looking at the simulated radar reflectivity, the comparison section (Section 5.3.2) describes secondary convective initiation and identifies a relation with gravity wave signals. This is followed by an investigation of the cold pool propagation (Section 5.3.3.1). Then, ensemble sensitivity analysis (Section 5.3.3.2) assesses the connection with the squall line-relative flow, followed by an investigation of downdrafts, and additional statistical considerations (Section 5.3.3.3). Section 5.3 ends with an error growth (Section 5.3.4) analysis, in grid point space and a system-relative perspective, to highlight associated contrasts in error growth. The set of analyses is synthesised in Section 5.4, followed by a discussion (also in that section). This discussion leads to the conclusions, as given in Section 5.5.

5.2 Methods

5.2.1 Model configuration and ensemble experiments

The ensemble of infinite-length squall lines is identical to the ensemble presented Chapter 3; the analysis and discussion of the current Chapter only covers these infinite-length squall lines (and no other simulations). Technical details of the conditions, and the reasons why their conditions have been selected, have therefore been covered in Sections 3.2.1, 3.2.2.1, 3.2.2.4 and 3.2.3.1. The corresponding thermodynamics and dynamics is displayed in Figure 3.1 (wind profile #3). The output of the simulations is available via Groot [2022].

5.2.2 Spatial and temporal windows for diagnostics

The presented diagnostics are applied to a central portion of the squall line region, where 40 km $> y > -20$ km. This selection is applied to reduce the effects of the boundaries, and their wave reflections, on the analysis of the squall line evolution. Generally, boundary effects in the central part of the domain become noticeable only during the last 30-40 minutes of the simulation. The boundary conditions are solely based on the evolution of state variables at the domain edge, with the first derivatives set to zero right at the boundary. The evolution of state variables at the boundary is therefore different among ensemble members, even though the same type of boundary conditions is applied to each ensemble member.
Some analyses (e.g. ensemble sensitivity analysis, Section 5.3.3.2, and the error growth analysis of Section 5.3.4) are carried out relative to the *cold pool edge*, of which the detection algorithm is defined in Section 5.3.3.1.

This study focuses on the evolution of the simulations up to 75-80 minutes. Nevertheless, the last 40 minutes of simulation time are also considered, wherever relevant.

5.2.3 Statistical assessment of the robustness of signals

As an ensemble sensitivity analysis is used to investigate spatio-temporal variability in this study statistically, a statistical criterion has been defined to evaluate if test statistics are globally significant, to complement grid point-based significance tests. To determine the robustness of analysed signals in the presence of a small ensemble size ($n = 10$), a statistical test criterion, based on t-tests, has been defined. With the given ensemble size, correlation coefficients exceeding $|r| > 0.631$ are significant at α of 0.05. That means, their frequency of occurrence in any large random sample is expected to be about 5%, at $p = 0.05$, and 1.25% for random occurrence of $|r| > 0.75$ ($p = 0.0125$).
In this study, statistical grid point testing will be applied to spatial patterns within the squall line, to determine the statistical significance of a signal. This is achieved in case of a significant correlation of a certain feature of interest over a large fraction of the grid points, located within its area. In the limit case, this fraction f needs to theoretically fulfill a criterion close to $f > 2p$ [Wilks, 2016]. On the contrary, other features, without signals associated with it, would simultaneously reveal small fractions of grid points with statistical significance. This is valid for most of the signals in the stratosphere (z of $15-20$ km), for instance. If fully random, a significant area fraction f of about 0.05 is expected, with $f \leq 2p = 0.1$, for $p = 0.05$, and $f \leq 0.025$, for $p = 0.0125$.

5.3 Results

5.3.1 Evolution of squall line radar reflectivity

For an overview of the general properties and representative behaviour of squall lines within the ensemble, the evolution of the simulated radar reflectivity is discussed for one ensemble member with strong squall line development.

5.3.1.1 Squall line evolution (one example member) As a response to the (1) large latent instability, (2) relatively strong low-level wind shear, perpendicular to the cold pool, and the (3) strong forcing of upward motion by the cold pool, deep convection soon develops along the full length of the y-axis. Narrow echoes of about 40 dBz, right above the initial condition discontinuity at $x = 0$ km, appear after 15 minutes into the simulation (Figure 5.1a). About five to ten minutes later, echoes exceeding 20 dBz reach above $z = 10$ km, as can be deduced from Figure 5.1c and 5.1d. Echoes also widen and exceed 60 dBz in the core region of the line. For the following 30 minutes, the squall line echoes grow monotonically at both anvil level and low/mid levels. The increase in areas with reflectivity $> 20dBz$ occurs both *upshear*[9] and *downshear* of the convective core (as could be deduced from Figures 5.1g, h), which itself is more or less stationary above $x = 0$ km. However, then the growth halts for a while on the downshear side after about one hour and on the upshear side after about 75 minutes (Figure 5.1k). Shrinkage of the areas with substantial cloud reflectivity occurs. After 80-90 minutes, a stratiform region of precipitation starts to develop on the upshear flank of the system (Figure 5.1j) and the anvil expands in both directions toward the end of the simulation, growing to about 100 km length, which is equivalent to nearly the length of the full domain. However, the stratiform precipitation area remains rather restricted to a very limited region at the rear flank (Figure 5.1j, at 3 km) and precipitation intensities remain rather low.
Starting from initial conditions that depend on x and z but not on y, initially, the system is nearly homogeneous in y (see Figure 5.1). The system gradually develops into a 3D squall line. Gradients develop along the y-axis, with convective cells of higher reflectivity embedded within the line after 50 minutes and beyond this time. However, this Chapter will mostly focus on results averaged in the y-direction, as contrasts are largest in x- and z-directions, and tend to be smoother along the y-axis.

5.3.1.2 Second phase of convective initiation In Figure 5.1, the evolution of the squall line in ensemble member 3 is shown. From the convective point of view, this member is on the very active end of the ensemble distribution. After 15 minutes (Figure 5.1a), the first convective cells are forming; after 25 minutes, this initial line of cells, which is very homogeneous in the y-direction, is maturing. Within the first 30 minutes of the simulations, ensemble variation is barely detectable.
Following upon this mature stage of the first line of cells, a phase with secondary initiation happens at $t = 30$ to 40 minutes. This second phase of convective initiation is most distinctive in ensemble member 3, in which

[9] Upshear refers to the direction against the wind shear vector: upstream of that vector; downshear refers to the opposite direction downstream of the shear vector.

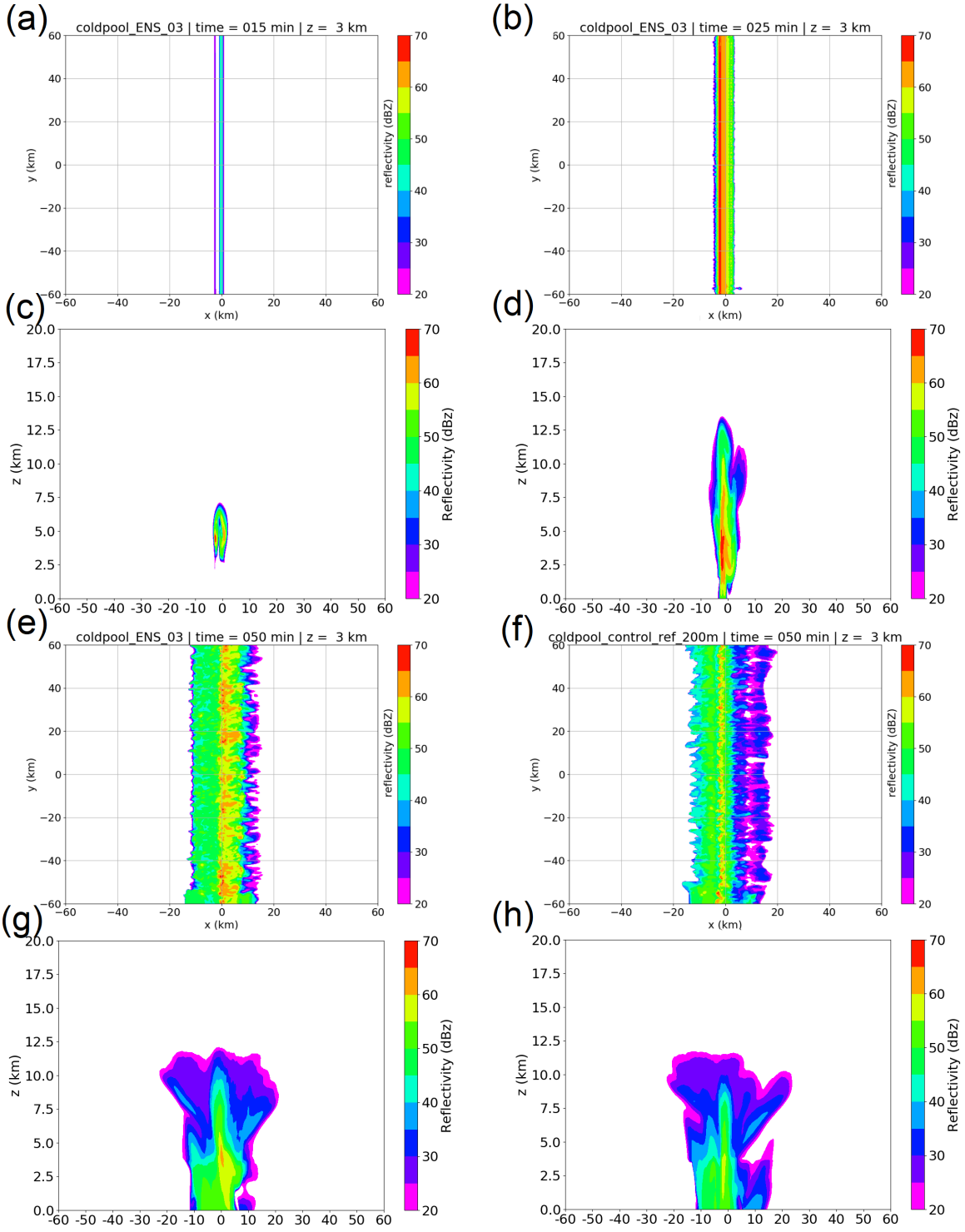

Figure 5.1: Evolution of simulated reflectivity for ensemble member 3 and the reference simulation (only $t = 50$ minutes) at $z = 3$ km. A top view is followed by corresponding vertical cross section (x-z) directly below, with the median of the reflectivity distribution along the length of the squall line. Left top (a, c): $t = 15$ minutes, right top (b, d): $t = 25$ minutes, left bottom (e, g): $t = 50$ minutes (all: ensemble member 3), right bottom (f, h) $t = 50$ minutes (reference simulation). The figure continues on the next page.

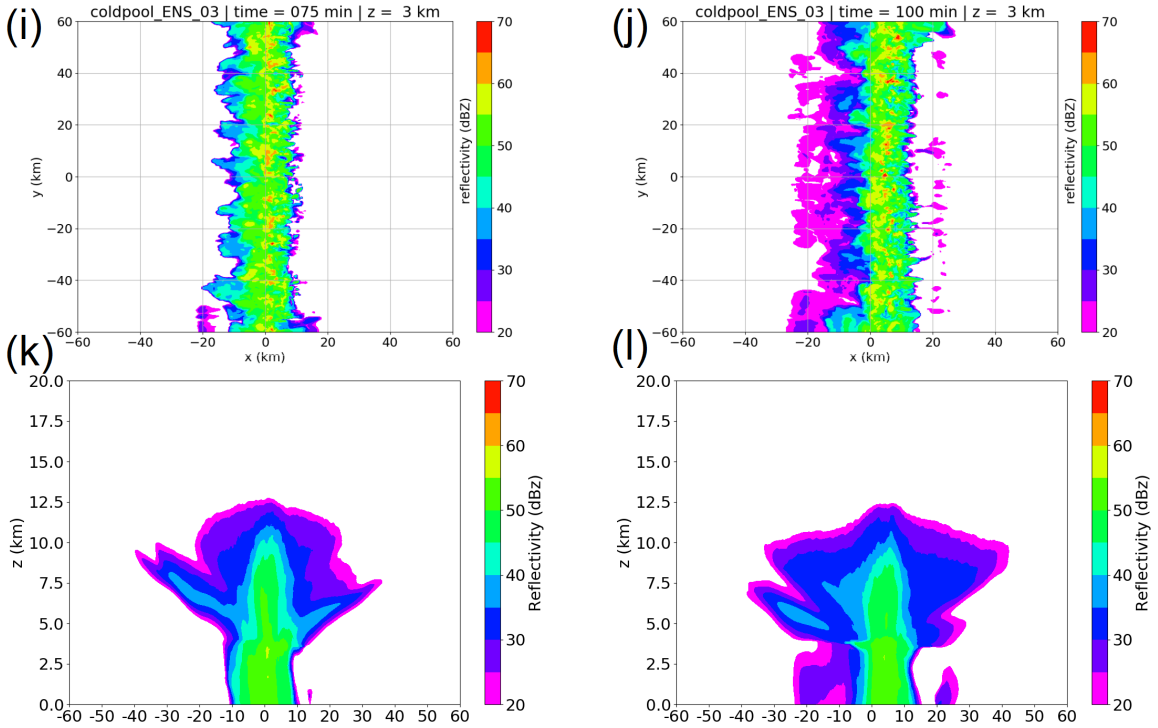

Figure 5.1: Continuation of the figure on the previous page. Left (i, k): $t = 75$ minutes, right (j, l): $t = 100$ minutes (all four represent ensemble member 3).

a secondary line of cells is triggered just ahead of the former line of cells, and leads to forward displacements of the squall line core. The reflectivity at $t = 50$ minutes clearly illustrates the forward displacement of convective cells and an increased area of reflectivity > 55 dBz on the forward flank, when the evolution of ensemble member 3 (ENS-03; Figure 5.1e) is compared to the reference run (Figure 5.1f). The reference run is not supporting the development of the second phase of initiation and, hence, the squall line appears to be practically stagnant until $t = 50$ minutes (Figure 5.1f). If any of the echoes in the reference simulation reach $x > 5$ km, it is anvil precipitation with reflectivity that locally reaches about 40 dBz, just below melting level, as opposed to newly initiated updrafts: those new updrafts locally exceed reflectivities of 55-65 dBz (Figure 5.1).
Following upon the second phase of convective initiation, the line of cells starts accelerating eastward, with the reflectivity signals exceeding 45 dBz at $z = 3$ km propagating to $x = 10$ km, after 75 minutes, and almost $x = 15$ km after 100 minutes (ENS-03). The line becomes increasingly inhomogeneous in the y-direction and exceeds 45 dBz at $z = 3$ km (about a km below melting level) over a longitudinal stretch of 15-20 km during this period, with very intense cores of 65 dBz. The latter is a consequence of the low-level cold pool, in combination with about 2000 J/kg CAPE [see Weisman and Klemp, 1982] and 14-15 m/s of wind shear over the lower 2.5 km. These are favourable conditions for very intense linear convection.

5.3.2 Detailed comparison of two example simulations

The upcoming section focuses on two illustrative simulations, before moving on to the variability between all ensemble members in Section 5.3.3. A comparison is made between the reference simulation and ensemble member 3 (see also Figure 5.1) in detail, because they often appear at opposite ends of the distributions, in most diagnostics. The evolution of convergence and divergence zones in space and time is described, for further analysis of the contrasts between the two simulations (Section 5.3.2.1). A respective description of their motion is necessary to understand how the (mass) sources and sinks of convective updrafts displace over time.
Passive tracers in the simulation pair are analysed in Section 5.3.2.2.

5.3.2.1 Convergence and divergence zones Figure 5.2 shows a set of *Hovmöller diagrams* (space-time plot) of divergence (red colours) and convergence (blue colours) in the lower and upper troposphere. The upper row of the figure illustrates that the low-level convergence zone accelerates eastward in both simulations, after a nearly stagnant position in approximately the first 30 minutes or so. The stagnation,

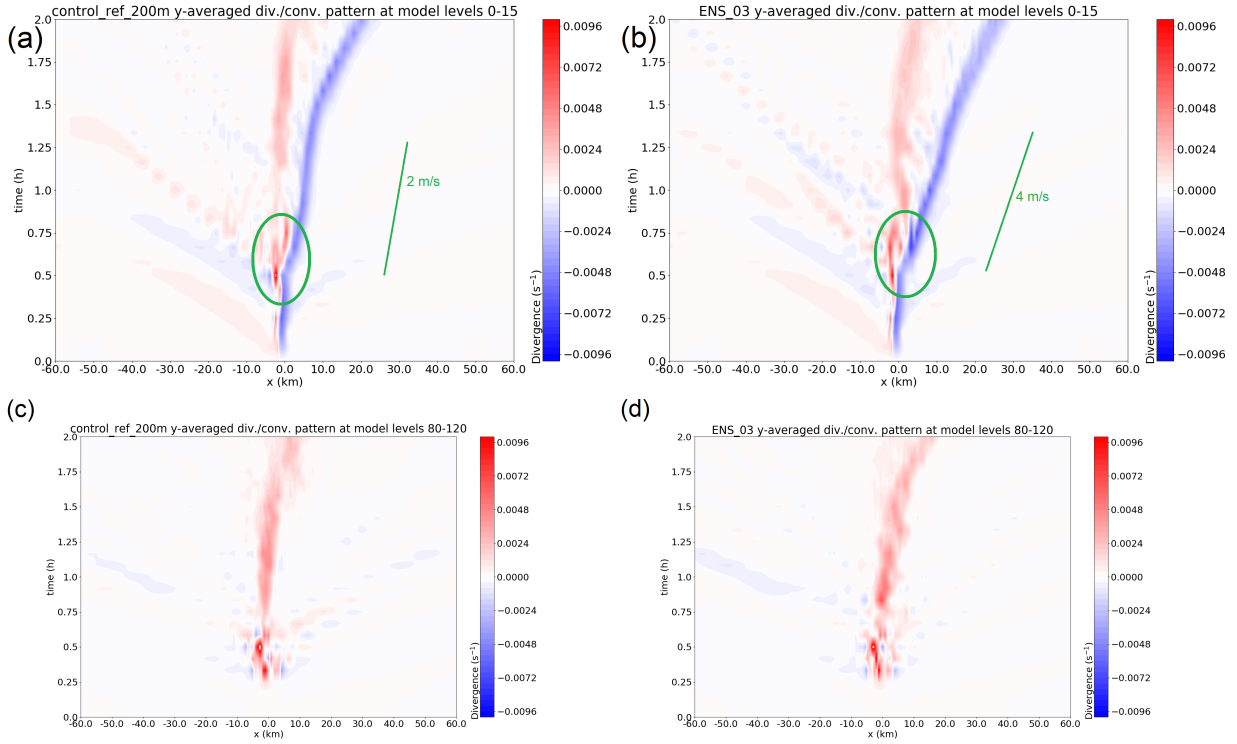

Figure 5.2: Space-time distribution of low-level (0-1.5 km; a, b) and upper tropospheric (8-12 km; c, d) convergence (s^{-1}) features in the reference simulation (a, c) and ensemble member 3 (b, d), averaged over all y and given z. A stage of particular interest that is analysed in the text is highlighted with a green oval, as well as the slope of the convergence zones, halfway the simulation.

and subsequent acceleration, is in agreement with displacements of convective cells, as described in the previous section (Section 5.3.1). After this stagnant stage, convergence and divergence zones accelerate eastward. Three patterns dominate the propagation of convergence and divergence zones in Figure 5.2:

- In the reference simulation, the convergence zone quickly accelerates to stationary eastward propagation of about 2.5 m/s in the following 45-50 minutes, whereas it is substantially faster in ensemble member 3, with $\approx$ 4.3 m/s.
- A weak acceleration of the divergence zone in the wake of the former zone occurs, most prominently in ENS-03.
- Another stage of acceleration of this zone occurs at the end of the simulations (90-120 minutes, $x = 0$ to 30 km). However, this might be a consequence of differences in reflections at the domain boundary and is not analysed further in this work.

In addition to these main low-level convergence features, convergence and divergence patterns associated with gravity waves are also visible in Figure 5.2. These comparatively weak waves lose amplitude in time. Apparent intermittent behaviour in both Figures for the western half of the domain is probably caused by the output interval of 5 minutes, approximately corresponding to the apparent pulse frequency of these features. A sudden displacement of the low-level convergence zone happens after about 0.6 hours (green oval, Figure 5.2), with a double maximum in the divergence in its wake, in ensemble member 3 (as opposed to the reference simulation). The amplitude of the convergence increases, directly after. In the reference simulation, this event happens in a smoother way: without a strong increase in amplitude of the convergence. On the contrary, the convergence zone also jumps by about a couple of km in ENS-03 and does not in the reference simulation. The jumpy displacement and amplitude increase of the convergence zone in ENS-03 is related to the initiation of secondary cells, ahead of the squall line core (Section 5.3.1). The panels in the lower row of Figure 5.2 depict a nearly stagnant and slightly diffuse patch of upper tropospheric divergence at $x \approx 0$ km, co-located with the squall line core. Propagation of this upper tropospheric divergence is clearly restricted to the second simulation hour for ensemble member 3. Furthermore, the consequences of developing convective cells (Section 5.3.1) are visible only after the first 15 minutes. Lastly, as in the lower troposphere, one can also see convergence-divergence patterns associated with comparatively weak gravity

waves propagating in the upper troposphere (given the propagation velocity of these patterns). These waves originate from the initial and secondary convective cells and leave the model domain after the first hour.

5.3.2.2 Second phase of convective initiation and tracers Passive tracers are a useful tool to describe convective circulation of air masses, as they provide quantitative information on the destination of specific inflow layers. Notably, the circulation in the squall line and its individual convective cells can be described with this approach, in a way comparable to a Langrangian analysis. Of course the tracer analysis is restricted to the identification of transport from the time of installation until any output time, for a specific air mass. In the simulations, tracers PT1 and PT2 are initiated below altitudes of 2.5 km, ahead of the squall line. Consequently, the mixing of air masses initially present at low levels, ahead of the squall line, can be investigated. On the other hand, the effects of rearward entrainment from the mid-troposphere and its diluting effect can only be analysed with much more difficulty. To evaluate the contrast between the simulation pair (Section 5.3.2.1) in more detail, passive tracers are injected in the inflow of the reference simulation and ENS-03. Tracer PT1 is inserted below 800 m altitude, between $x = 0$ and $x = 30$ km at $t = 0$, and PT2 is simultaneously initiated over the same horizontal region, at all model levels where $1600 < z < 2400$ m. All concentrations are initially set to 0.001 kg/kg. These tracers are advected with the flow, with computations based on the applied advection scheme, but also the built-in sub-grid turbulence of the LES. No sedimentation or other (microphysics-like) tendencies contribute to their redistribution.
In Figure 5.3a, the concentration of PT2 after 30 minutes is displayed for the two example simulations, namely the reference simulation and ENS-03. Looking at the red shading (reference simulation), the tracer is transported towards negative x-values as a result of westward flow at low levels, but it meets the updraft near $x = 0$ km. It can be seen that the second tracer, initialised at levels of about $z = 2$ km, has entered the updraft near $x = 0$ km, and it has been transported upward by the updraft, up to about $z = 10$ km. Shifting the focus to the blue isolines (which represent ENS-03), mostly the same patterns are seen, but with a slight westward shift of the updraft. Furthermore, while to the east PT2-concentrations in both of the simulations align nearly perfectly, a strong undulation is localised about 5 km to the east of the updraft in the PT2-pattern, when compared to the reference simulation. Therefore, in the evolution of the concentration difference after 25, 30 and 35 minutes is examined in the following.
The differences of PT2 concentrations between ENS-03 and the reference after 30 and 35 minutes are found in Figure 5.3 (b, c and d). A surplus in PT2 is visible at the location of the black "X" in ENS-03 and a surplus is found about 1 km lower in the reference simulation after 30 minutes, amongst others. More precisely, a dipole structure in the PT2 surplus, from $z = 4$ km to $z = 6$ km around $x = 0$ km at $t = 25$ minutes, suggests a slight shift between the developing convective updrafts in the simulation pair in Figure 5.3c. At $t = 30$ minutes, the dipole has elongated vertically: the updraft core is shifted eastward by a few grid cells in ENS-03, compared to the reference. Furthermore, the PT2 surplus at the location "X" in ENS-03 is very notable. At this location, PT2 concentrations are much higher in ENS-03 than in the reference simulation at $z = 3$ km, a few km east of the x-axis. About a kilometer below "X", PT2 concentrations are lower in ENS-03 simultaneously, at the lower flank of the source layer (Figure 5.3b). A difference of opposite sign occurs at the top of (red; and below: blue) the PT2 source layer, about 10 km to the east of X. After 35 minutes, the same signal has propagated eastward by about 5-7 km and the blue signal at location X has extended upward, but the red has not.
Consequently, PT2 transport is substantially different between ensemble member 3 and the reference simulation, from t = 30 until t = 45 minutes: only 7.0% of the PT2 mass moves from its low-level source layer to levels above 4 km height in these 15 minutes in the reference simulation, whereas 17.6% does in ensemble member 3. Furthermore, 11.7% (ENS-03) of PT2 is flowing to the upper troposphere ($z > 6$ km), versus 6.0% (reference simulation). This implies a very large difference in convective tracer overturn and, hence, convective mass fluxes are significantly larger in ensemble member 3 than in the reference simulation.
Figure 5.4 displays the PT1 distribution after 55 and 75 minutes. Both PT1 and PT2 (not shown, similar patterns) indicate that the top of the region with tracers, initiated in the lower troposphere, is lower in the reference simulation compared to the ENS-03. As the passive tracers are initiated at the main inflow air of the convection, they reveal the dominant patterns in the redistribution of air by squall line overturn.
Two additional patterns are visible in the aforementioned figure: first, the near-surface eastern boundary of PT1 moves faster eastward (in blue, ENS-03) than in the reference simulation (red). Second, the passive tracer is laterally spread out further in ENS-03 (green contour, 5.4b) than in the reference simulation.
The three aforementioned patterns in PT1 (Figure 5.4) are a consequence of differential mass transport within the convection. Together with the patterns seen in PT2, earlier in this section, increased convective overturn in ENS-03 may lead to all of the identified patterns. Extra mass overturn is consistent with the reflectivity patterns from Section 5.3.1.
The upper tropospheric divergence, as visually demonstrated by the passive tracers, is strongly increased in the ENS-03 (green) after 75 minutes compared to the reference (a link to the analysis of Chapters 3 and 4,

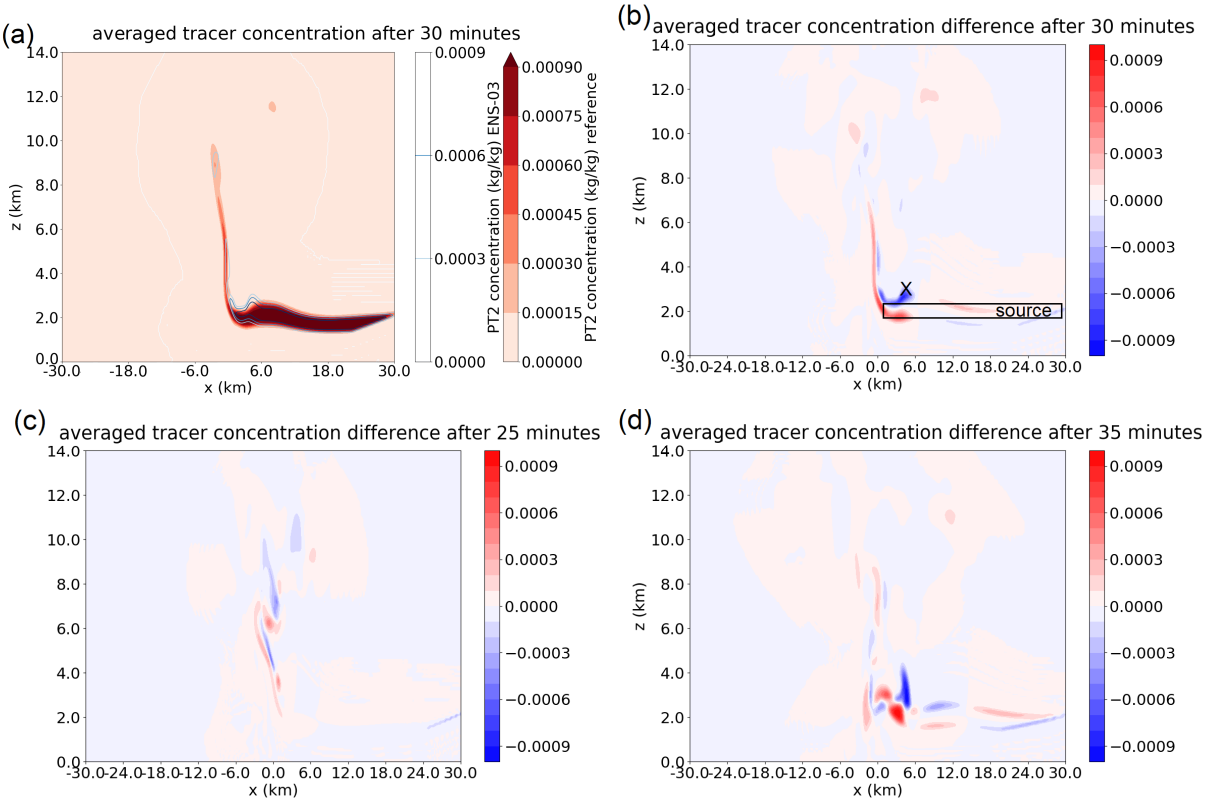

Figure 5.3: Vertical cross section (x-z) of (a) PT2 concentration in reference (shading) and ENS-03 (isolines) and (b, c, d) PT2 concentration difference between reference and ENS-03, after 30 min (b), 25 min (c) and 35 min (d). Red indicates a tracer surplus in the reference simulation, blue in ENS-03. The black X (b) marks the gravity wave crest, in which vertical displacement leads to the triggering of a new line of convective cells in the squall line (see also Section 5.3.2.3). Note that only half of the 120 km zonal domain extent is shown.

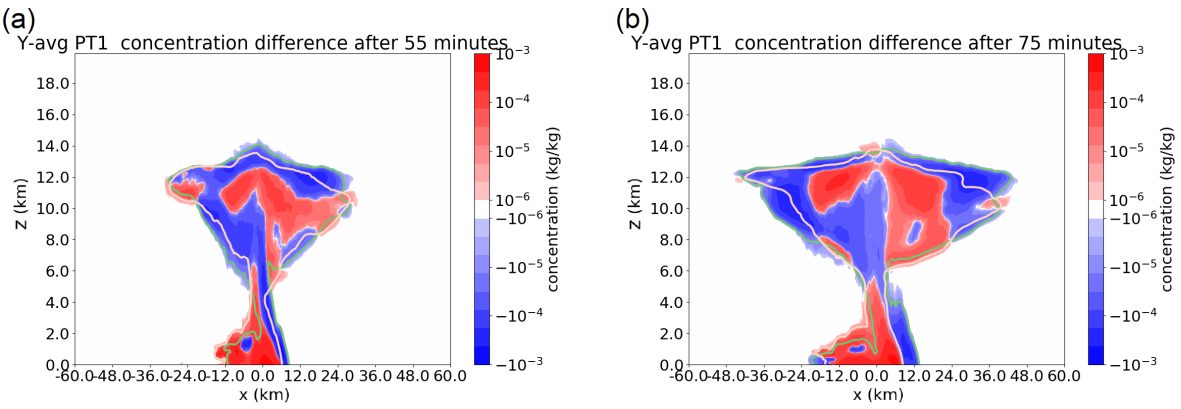

Figure 5.4: Vertical cross section (x-z) of difference in PT1 concentration between ENS-03 (blue: higher) and reference (red: higher) in colour fill, after (a) 55 minutes and (b) 75 minutes. In addition, the $q_{PT2} = 1 \times 10^{-5}$ kg/kg isoline is shown for both simulations (salmon/bright pink colour: reference; green: ENS-03). The y-average is now taken over the limited subspace, consisting of 40 km$> y > -20$ km.

Groot and Tost [2022] and Groot et al. [2023]). Upper tropospheric mass divergence, as averaged over the first 75 minutes and the rectangular box volume around the convective system (see Figure 3.7), differs by 38 % between the simulation pair. Nevertheless, the net latent heating left behind is only 24% higher in ENS-03 than in the reference simulation, over the corresponding surface area and time interval.

5.3.2.3 Vertical velocity at "X" Location "X" in Figure 5.3 has drawn specific attention, with a contrast between upward and downward displacements of PT2 in the simulation pair. These downward / upward displacements in the trough / crest are resembling gravity wave patterns, as it has been identified

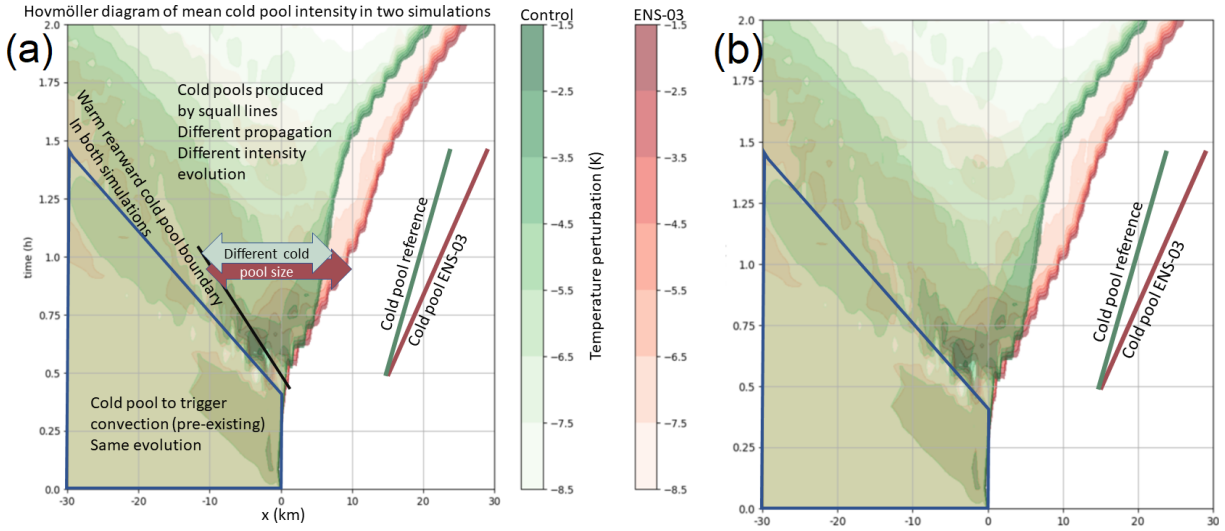

Figure 5.5: Hovmöller diagram of potential temperature perturbations, compared to the upstream source air at the lowest model level, for the reference simulation and ENS-03. Perturbations smaller than 1.5 K (outside of the cold pool) are left blank. A version with annotations (a) and without (b) is shown.

in the previous section (Section 5.3.2.2). Furthermore, consequent differential vertical overturn of mass has been identified with tracer evolution, directly afterwards.
The patterns identified in Section 5.3.2.2 appear to have a strong connection with vertical velocities at location "X". This local vertical velocity could be affected by both variability in the gravity waves, passing by first, and then possibly by consequent variability in the potential for convective initiation (for which lifting of air parcels above the *level of free convection* threshold is generally needed, hence, local $w > 0$). The mean w along the squall line at location X (t = 30 min) is +0.35 m/s in ENS-03 and -2.76 m/s in the reference, with along-line deviations of up to 1.5 m/s about the mean. Therefore, a large portion of X, along the length of the squall line, consists of favourable locations for the initiation of convection in ENS-03: $w_{X,mean} > 0$. Conversely, w is well below 0 at that position in the reference simulation. Other ensemble members experience intermediate values between those two opposites, with a mean of -0.93 m/s. Given the spread of about 1.5 m/s in local w about the mean, most members contain some limited areas favourable for the secondary convective initiation.
Immediately after the secondary initiation, the cold pool area of the rapidly developing new convective cells increases at a higher rate in ENS-03 than in the reference simulation. This can be seen in Figure 5.5, in which the low-level potential temperature perturbation, compared to the upstream source air at initialisation, is displayed. The expansion of the cold pool area occurs on the forward side, at the convergence line. The cold pool accelerates at a different rate in both simulations, as seen from the slope in the Hovmöller plot. The patterns of cold pool displacement in the 35-100 minutes time interval will be analysed in more detail in Section 5.3.3.1.

5.3.3 Ensemble squall line variability

In this section, the focus of the analysis is shifted towards the full ensemble. The former two simulations, at both ends of the ensemble distribution, have already illustrated some important characteristics of the squall line variability. Key aspects of this section are the lag correlations of the cold pool edge location with itself and the vertical velocity w at X (Figure 5.3). The relation of the latter with the meridionally averaged zonal cold pool-relative flow (u) within the ensemble envelope is investigated. In the latter case, w of each ensemble member at location X acts as an independent variable. Additionally, other variables are investigated in this section, such as downdraft mass flux. The obtained statistics complement the holistic picture of the squall line ensemble spread.

5.3.3.1 Location of the cold pool edge in the ensemble The cold pool location and its time derivative, the propagation speed v_{cp}, are computed at each output step by taking the maximum of $\frac{\partial \rho}{\partial x}$ at the lowest model level. This computation over the zonal direction is done for each location in the y-direction. The cold pool position and velocity are obtained by taking the average value of the resulting x over y. This way, a cold pool edge is defined as a function of ensemble member and time.

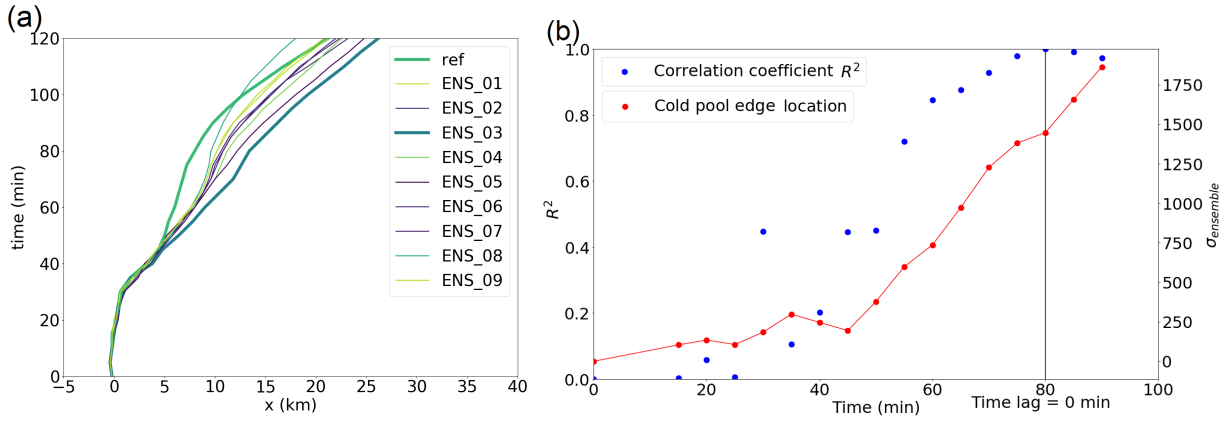

Figure 5.6: (a) Hovmöller diagram of cold pool edge propagation, with colors in the order of their initial z_i. Low interfaces are displayed in lime and high interfaces in purple (reference and ENS-03: bold). (b) R^2 of time lag correlations as a function of simulation time (indicated) for the cold pool position among 10 ensemble members, with the position at $t = 80$ minutes as reference correlation of 1 (blue; left y-axis). Also shown is the temporal evolution of the standard deviation of the cold pool edge position in m (red; right y-axis). The points at $t = 5$ and 10 minutes are omitted, as there is no variability in cold pool edge location among the ensemble members (yet).

With this definition, v_{cp} differs by up to a factor of 1.7 over the interval 30-75 minutes between the reference and ENS-03: 2.5 vs. 4.3 m/s. That simulation pair only differs by 47 m in initial interface height of the shear layer, z_i (< 2 %)! These simulations are on the outer ends of the ensemble distribution of cold pool velocity.
The temporal evolution of the cold pool edge location is depicted in Figure 5.6a, in which it is seen that a large contrast between the reference simulation and ENS-03 develops after about 45 minutes. Acceleration of the cold pools takes place after 30-40 minutes. The spread gradually develops after 45 minutes, with a kink in the propagation after about 80-100 minutes: towards further acceleration.
The average displacement of the cold pool edge at the surface is evaluated and lag correlated with its own location at $t = 80$ minutes. This t corresponds approximately to the instance when the first dynamically relevant effects of the squall line (fast gravity waves) are about to leave the domain, in the zonal direction (Figure 5.2).
The ensemble spread of the cold pool edge location is undetectable (up to 1 grid cell; Figure 5.6b) during the initial phase of the squall line development; consequentially, and as a result of the small ensemble size, resulting lag correlations are frail. As the ensemble spread in the cold pool location increases to 4 grid cells, after 40 minutes, and keeps on increasing linearly beyond (Figure 5.6b), the sensitivity of lag correlations due to limited ensemble spread is substantially reduced and then (practically) eliminated. Consequently, beyond 30 minutes, the time evolution of the lag correlation provides insight into the evolution of ensemble spread.
Figure 5.6b depicts an S-like shape of the lag correlation function. Roughly, three stages can be distinguished:

- A stage prior to establishment of the intra-ensemble variability in cold pool location (low reliability of lag correlation curve: little or nothing can be inferred from the curve).
- A stage where the intra-ensemble variability of cold pool location is establishing, corresponding with the growth stage of the S-curve. In this stage, the growth rate is maximised, around 40-45 minutes, and the growth stage of the ensemble spread lasts from about 35-50 minutes.
- A stage in which the intra-ensemble variability has been established: from about 50-55 minutes, onward. The cold pool location variability is maintained until 80 minutes (where $r = 1$) and beyond. In this stage, the cold pool locations have been set relative to each other: cold pools move jointly (at a nearly constant velocity).

The structure in ensemble variability, as manifested by the cold pool edge, is maintained. Both the standard deviation and the difference between maximum and minimum x of the cold pool edge increase nearly linearly beyond $t = 45$ minutes (Figure 5.6b), consistently with the apparent slope in Figure 5.2.

5.3.3.2 Ensemble sensitivity analysis The *ensemble sensitivity analysis* technique is applied to assess statistical patterns that exist in the squall line ensemble. Essentially, the ensemble sensitivity analysis finds

the regression line through the dimension of the ensemble members that describes the best (in principle linear) fit between two variables x_1 and x_2, like in any analysis of covariance patterns [see also Hanley et al., 2013, Bednarczyk and Ancell, 2015, where the method is also used to investigate convective systems]. That means that perturbations, or excursions, in an x_2 with respect to an ensemble mean can be investigated in relation to those in variable x_1. Furthermore, the evolution of these perturbations of x_2 with time can be followed, as they are structured within the ensemble envelope. The structure of conditional variability in x_2, conditional on x_1, is revealed and, hence, conditional coherent behaviour of a spatial flow pattern related to x_1 later in time can be identified.

Bednarczyk and Ancell [2015] discuss some limitations of this analysis for a convective case, which apply specifically if the (spatial) extent of the independent variable is not exactly known and a proxy has to be used, as in their case: deep convection was parameterized and precipitation- or reflectivity-related output had to be used, instead of more direct representations of convective motion (e.g. local vertical velocity, masked with threshold). In contrast, the spatial extent of a variable of interest is clearly delineated for this case, in Section 5.3.2.2 and Figure 5.3. The analysis of Section 5.3.2.2 also directs towards the independent variable, local w at X (Figure 5.3b).

Since the ensemble variability of quasi-2D squall lines is investigated from a dynamical perspective here, the y-averaged variation in u in the x-z plane is of particular interest - especially within the squall line core. This core area - with the updrafts, downdrafts and an inner portion of the anvil - is the target variable of the ensemble sensitivity analysis. Tailored statistical testing will be used to investigate the robustness of the most important signals (as it has been described in Section 5.2.3).

The sensitivity of the squall line circulation to a precursor pattern in the velocity field is explored. Therefore, an ensemble sensitivity analysis targeted at u, in relation to w at location X, is done. This w at X is averaged along the length of the squall line over five by five grid cells in the x-z plane: w_{loc}. The temporal evolution of covariance between w_{loc} and the y-averaged u in the x-z plane (i.e. u_{avg}) is analysed; a chronological discussion follows in this section.

Note that the ensemble sensitivity analysis is carried out in a cold pool edge-relative framework. As this cold pool edge moves by up to 30 km during the simulations, correction for its displacement in x overlays various x-coordinates and limits overlap between the ensemble members. As a result of the procedure, the available domain for the ensemble sensitivity analysis shrinks by approximately 30 km from 120 to about 90 km, in the zonal direction. Furthermore, the cold pool edge is co-located with $x = 0$ km in all members and at all times, as a result of the correction.

Initially, during the first 15 minutes of simulation time, the signals revealed by the ensemble sensitivity analysis contain very low amplitude patterns, that are virtually unnoticeable in terms of u_{avg} associated with it. These waves have to be low frequency sound waves, with wavelengths on the order of 5 km (Figure 5.7a,b), based on their geometry and fast propagation speed [see also Hohenegger and Schär, 2007]. Such waves can spontaneously develop from density anomalies. As the acoustic waves are from a practical perspective unrelated to the convection, their relation to the squall line developments can be ignored.

After 15-20 minutes, the area within and in the immediate surroundings of the convective bubble (near $x = 0$; developing convective cell) shows some covariability with w_{loc}. Initially, this signal is restricted to parts of the middle troposphere and the immediate wake of the cold pool edge. The magnitude of the covariability is initially small, generally below 0.1 m/s, but very locally reaches 0.5-1 m/s by 20 minutes.

The (somewhat turbulent) signal, from the updraft of the aforementioned developing convective cells, has propagated vertically after 25 minutes. Then, it extends from the surface up to about $z = 12.5$ km. This altitude range and location corresponds to the spatial extent of developing convective cells. The signal's amplitude is now also noticeable in terms u_{avg}: in the whole troposphere about 0.5 m/s. At this same instance, w_{loc} is associated with an undulating wave signal, travelling at the interface level z_i, for the first time. This is exposed by a trough around z_i and air that has sunk (Figure 5.7c). That signal resembles a gravity wave, consistent with contemporary signals from the tracer analysis (Section 5.3.2.2). None of the signals in the first 20-25 minutes pass the statistical robustness threshold: the amplitude may be considerable, but they are not strongly correlated with w_{loc} (linearly) over sufficiently large coherent regions.

After 30 minutes, small undulations, around the initial interface height z_i, are visible in the obtained correlation patterns. A crest develops in the immediate wake of the cold pool edge ($x = -10$ km). Simultaneously, ahead of the cold pool edge, gravity wave activity is now more apparent ($x = 5$ to $x = 15$ km; Figure 5.7c). Through w, this wave signal is associated with the strong signal of convective initiation, in ENS-03. On the contrary, the second phase of convective initiation does apparently not occur in the reference simulation. In the following three time steps (of 5 minutes each), many more, faster, gravity wave signals propagate away from the source region. This source region of warm air upstream of the squall line ($x > 0$ km) definitely passes the statistical significance test, as a robust signal, for $t = 30$ until $t = 60$ minutes. As the circulation is effectively almost 2D, this is partly inherited by the fact that the circulation in the x-z plane contains both of the lagged variables of the statistical analysis: w_{loc}, at t = 30 minutes, and u_{avg}.

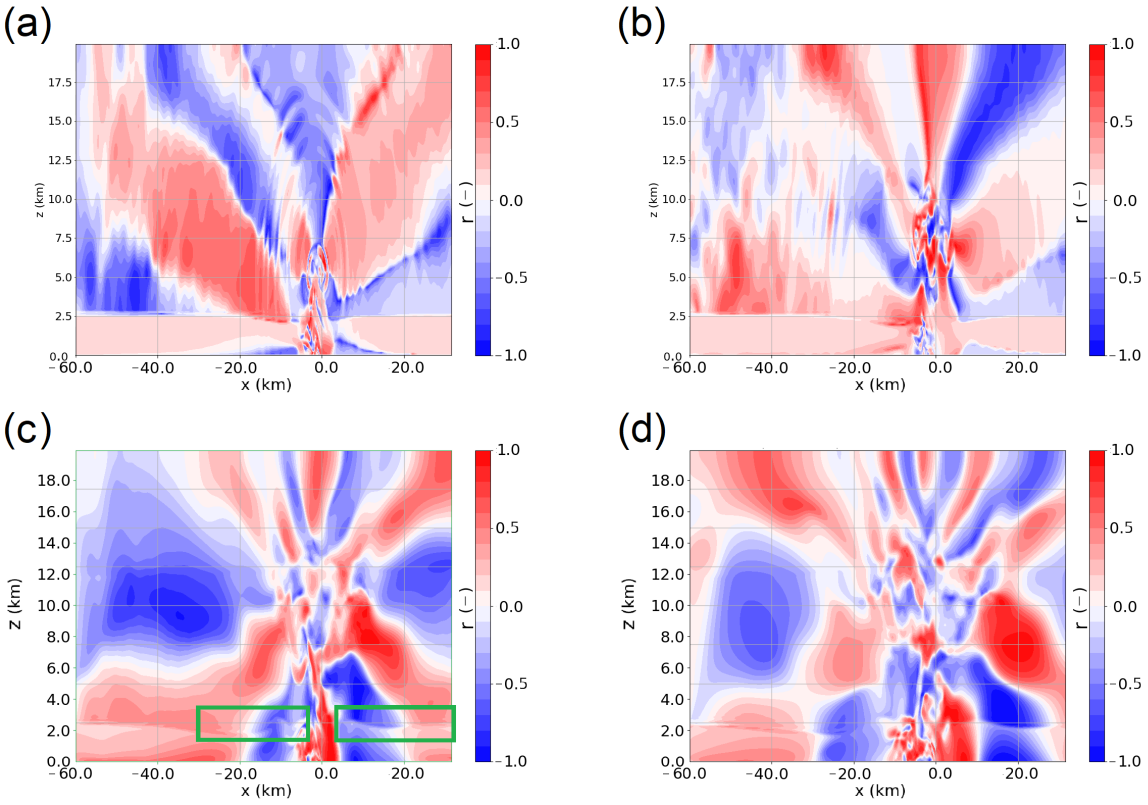

Figure 5.7: Vertical cross section (x-z) of correlation structure between w_{loc} and u_{avg}, obtained from the ensemble sensitivity analysis, after (a) $t = 15$ minutes, (b) $t = 20$ minutes, (c) $t = 30$ minutes and (d) $t = 35$ minutes. In (c), the green rectangles are illustrating where "undulating wave signals" (see text) that resemble signals of gravity wave activity, are located. One can see a gravity wave crest at $z_i \approx 2500$ m, propagating from $x = 4$ km to $x = 9$ km. With positive vertical velocity perturbations and inbound/converging u winds upon this crest, enhanced forcing of convective initiation ($x = 4$ km, $z = 3$ km, $t = 30$ minutes, X in Figure 5.3) is correlated with u_{avg}.

Following this stage of apparent gravity wave activity, a new stage in the evolution begins. To investigate this second stage, the focus is shifted from the correlations of the ensemble sensitivity analysis to the variability in the second covariant: u_{avg}, which is depicted in Figure 5.8. Among the main features in this Figure are enhanced convergence in u, around $z = 2.5$ km and $x = -4$ km, and enhanced divergence at $z = 7$ to $z = 13$ km. The signals in u_{avg} have moved from upright, multi-wavenumber in the vertical (centered at the convective cells), to one that is aligned with the tilted cold pool and another second contribution that causes

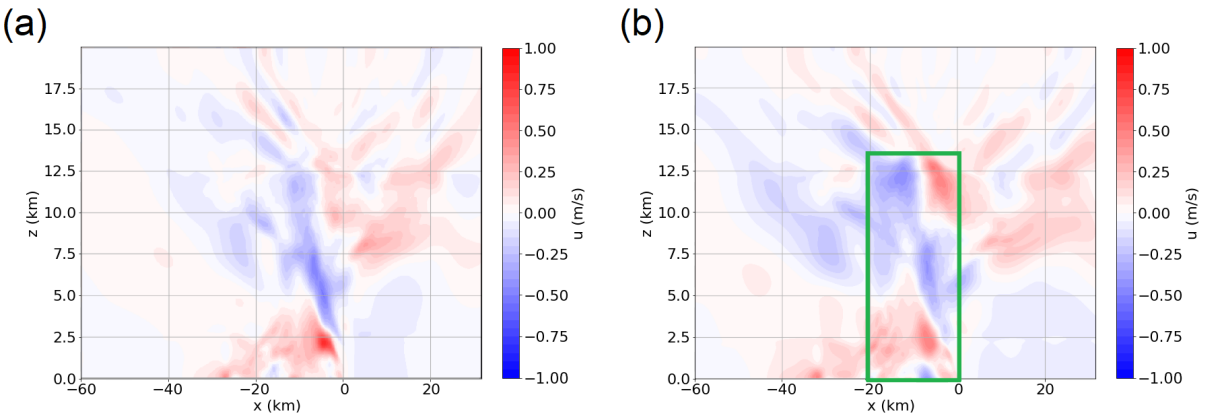

Figure 5.8: Vertical cross section (x-z) of y-averaged u_{avg} variance associated with w_{loc} after (a) $t = 50$ minutes and (b) $t = 55$ minutes. The central area of squall line circulation (see text), used for significance testing of the identified squall line circulation anomaly, is marked with a green rectangle (only in b).

upper tropospheric divergence away from the cells (in the anvil). Both the convergence signal, in the lower troposphere, and the upper tropospheric divergence signal are associated with the squall line circulation. They occur after 40-50 minutes. Synchronously, the associated u variability also exceeds 1 m/s, maximising at altitudes of 1.5 to 8 km (Figure 5.8a). On the right panel of the Figure, one can see extended divergence patterns, (slightly) above $z = 13$ km, which are likely associated with an *overshooting* cloud top. The cloud top is co-located with divergent outflow in u_{avg} (about $x = 10$ km). The features in u_{avg} still amplify in the higher regions of the troposphere and even up to the region of convective *overshoot*[10]. Signals of u_{avg} gradually propagate away from their source region, in the following 30-40 minutes.
The signal of this stage is statistically very robust: in the central 20 km of the squall line and at altitudes up to the tropopause, a fractional area f of 0.56 passes the statistical significance test at $p = 0.05$ and $f = 0.35$ at $p = 0.0125$ (Figure 5.8b). This is more than an order of magnitude larger than random values [see also Wilks, 2016]. Even when applying the statistical test to the whole tropospheric domain, over which the ensemble sensitivity analysis is applied, the fraction surviving the prescribed test at both p-values is statistically still robust.
After 80 minutes, the u-variability associated with w_{loc} has considerably weakened (Figure 5.9b). Later, some renewed variability occurs at $t = 90$ minutes, which behaves similar to ensemble variability in the previous stage (between $t = 30$ and $t = 80$ minutes): propagating away from its initiation region, slowly, while dying out. The exact location of the initiation has moved slightly upstream (relative to the cold pool edge at $x = 0$ km) and slightly higher up in the troposphere. In addition, the signals that likely occur due to gravity wave activity, around and below z_i, remain to be associated with the independent variable, but that signal is statistically not robust.
The first of two main circulation features, revealed by the ensemble sensitivity analysis, demonstrates anomalous convergence of mass at $z = 2 - 4$ km, rearward of the cold pool edge (Figure 5.8; $x \approx -4$ km). The convergence signal consists of enhanced easterly flow in the updraft region, which gradually rises and moves upstream relative to the cold pool, due to the updraft tilt. The feature with easterly flow anomalies moves upward, extending initially ($t = 45$ minutes) from the surface to 8-9 km altitude. On the rearward side of the convergence anomaly, a westerly flow anomaly does roughly the same, but sticks to lower levels and dissipates earlier (red shading in Figure 5.8, $z \approx 2$ to 3 km and $x \approx$ -20 to -4 km).
At the same time, a second main feature in the signal of ensemble sensitivity occurs in the upper troposphere: an enhanced upper tropospheric divergence at $t = 50$ minutes, which *overshoots* into the first 1-2 km of stratosphere at $t = 55$ minutes (Figure 5.8). This upper tropospheric pattern itself diverges over time and fades outward, after about $t = 80$ minutes (Figure 5.9b). Some patterns with reversed anomaly signs appear from $t = 90$ to $t = 115$ minutes, outside of the focal time frame of this study. These patterns have no relevance to the remainder of this study and are therefore not discussed in further detail.

5.3.3.3 Downdraft variability and cloud tops In this section, the downdraft characteristics are discussed in more detail. Furthermore, the ensemble variability in cloud top height is evaluated. Subsequently, the statistical relations between a few important diagnostic variables, describing the squall line characteristics, and their identified precursors (w_{loc} and cold pool edge acceleration to v_{cp}) are quantified.

[10] An overshooting top is a term, used for a cumulonimbus cloud top that 'shoots' to altitudes above the cumulonimbus anvil. It usually enters the lower stratosphere (Figure 5.8b).

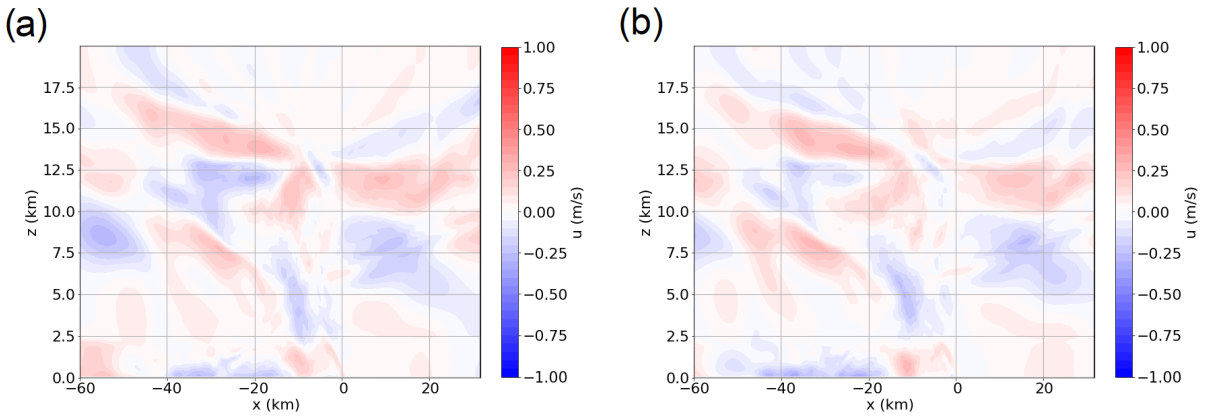

Figure 5.9: Vertical cross section (x-z) of u_{avg} associated with w_{loc} after (a) $t = 75$ minutes and (b) $t = 80$ minutes.

Downdraft detection To compute (1) the downdraft mass flux, (2) area profiles of downdrafts and (3) conditional vertical velocities in downdrafts, first, all grid cells with negative (positive; for corresponding updraft detection) vertical velocities ($w < 0$ m/s) and a minimal total cloud hydrometeor density of 1×10^{-4} kg m^{-3} are selected. The downdraft area is given by the number of grid cells occupied in each layer. This computation method is inspired by and adapted from Varble et al. [2020]. Subsequently, gravity wave contributions from saturated parcels to downward motion are removed. Accordingly, any grid cells where the total density ($\rho_{moist\_air} + \rho_{water}$) is lower than its horizontal average over that model layer are ignored (that means: positively buoyant parcels). Downdraft parcels with negative vertical velocity, but positive buoyancy, would be manifestations of downward moving parcels with hydrometeor content that would not maintain their negative velocity. Given their positive buoyancy, they rather have tendency towards upward acceleration. Without the correction for gravity waves, downdrafts are highly overestimated in the near-tropopause region. In this region, gravity wave activity is leading to substantial vertical transport of air with cloud hydrometeor content that is compensated by reverse motion in the vicinity [see also Pandya and Durran, 1996].
Any grid cell, classified as downdraft, is then used to calculate the conditional mean of the vertical velocity w. The product of air density and conditional vertical velocity, averaged over the full domain, provides an average downdraft flux.

Cloud top detection Among several tested cloud masks, a cloud top definition is selected, using the simulated reflectivity beyond 15 dBz as a cloud mask. The relative (fractional) area covered by the cloud mask, just after the convective *overshoot* (55-60 min, Figure 5.4), is aggregated in time (60-90 minutes) and along the squall line length as a function of z, as the anvil spreads out almost horizontally around equilibrium level. From several parameters, the maximum altitude with a fractional cloud cover of 0.1 is selected as most

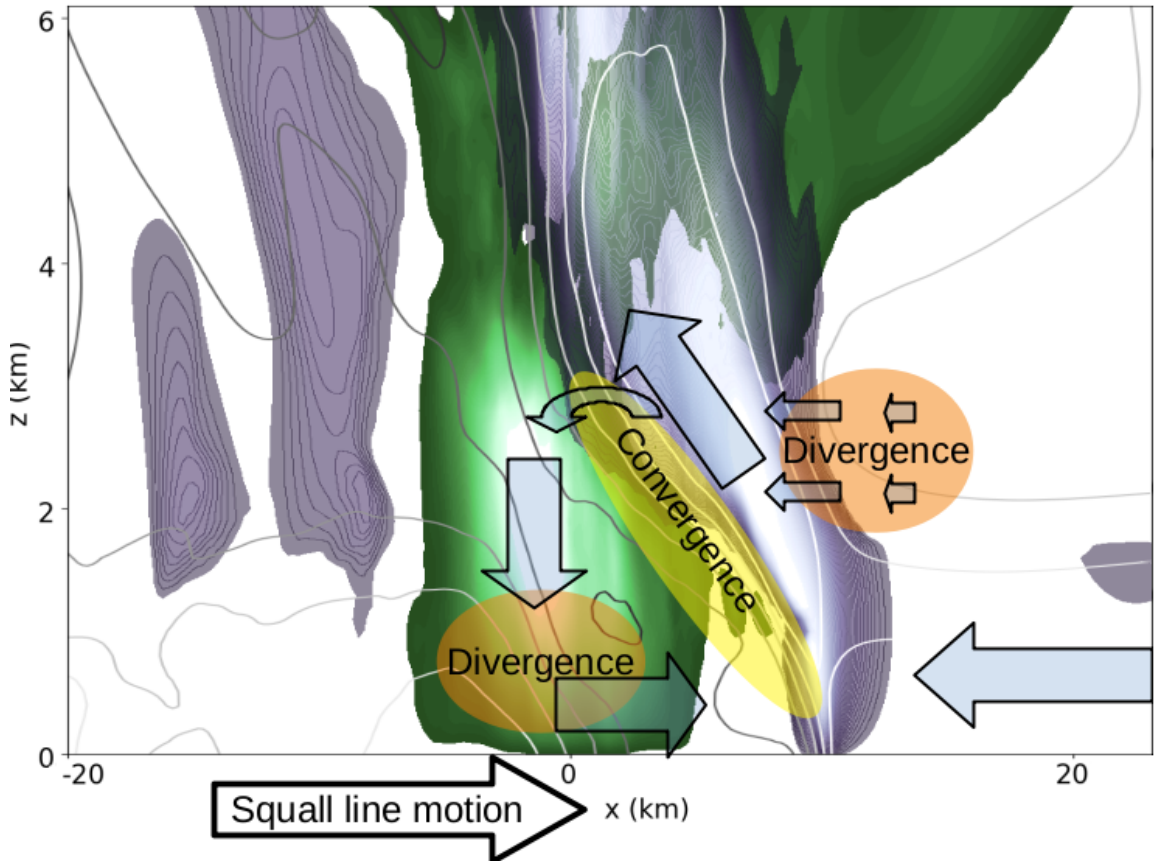

Figure 5.10: Schematic vertical cross section (x-z) of the cold pool circulation: green colouring shows updraft mass fluxes and purple colouring shows downdraft mass fluxes. The white isolines indicate easterly flow (-9 m/s, every 3 m/s), while darkest grey isolines indicate westerly flow (+6 m/s). One can identify convergence and divergence zones from these contours, which are conceptualised with semi-transparent yellow and orange ovals. The cold pool-relative flow is given by light blue transparent arrows. Note that the upper (roughly) half of the troposphere is omitted. The direction of squall line propagation is given by the arrow, at the bottom.

representative of the ensemble spread of cloud tops.

Analysis First, the y-averaged downdraft and updraft fluxes are displayed in an x-z cross section in Figure 5.10, for one random ensemble member. This view analytically represents detected updraft and downdraft mass fluxes for that simulation, but also includes a schematic overview of the circulation in the lower part of the squall line. It shows the updraft region on the forward flank (right) of the squall line and a region of horizontal divergence (acceleration into the updraft) at about 2 km, ahead of the main ascent region. A substantial fraction of air masses in the upward branch continue their ascent into the upper troposphere. However, a certain fraction is also entrained into the downdraft region, at, or behind, the cold pool edge. This edge is characterised by a region of convergence between the ascending and descending air masses. The downdraft, which is located mostly on top of the cold pool, causes low-level divergence. Furthermore, the downdraft also causes propagation of the squall line and cold pool edge, towards the right. A so-called *rear inflow jet*, that often occurs in squall lines, is absent in the set-up [Houze, 2004, and references herein].
Most of the downdraft variability within the ensemble is found in the downdraft area diagnostic. This is depicted in Figure 5.11. The left panel shows the downdraft mass fluxes, whereas the middle panel displays the conditional vertical velocity and the rightmost panel the area occupied by the downdrafts. While vertical maxima of the time averaged low-level downdraft fluxes vary by up to 40%, based on the ensemble envelope, the area of the downdrafts, at the level of maximum fluxes, explains about two third of this variability within the ensemble (even though the low-level mean area in time varies by only half of that 40%). Additional contributions to the variability come mostly from the conditional mean of the downdraft velocity.
In Section 5.3.3.2 (the ensemble sensitivity analysis), a tilted convergence feature was identified (Figure 5.8), of which the intensity is amplified with increased w_{loc} - as revealed by the ensemble sensitivity analysis. A portion of the extra strong easterly flow in the updraft regions reaches the tilted convergence zone and leaves the updraft on the upstream side for the convergence zone, located at the (upstream) tilted cold pool edge. As a consequence of the convergence with nearly stagnant air, moving at (approximately) v_{cp}, the downdraft fluxes below melting level are amplified at $z = 1 - 4$ km (Figure 5.11). The circulation, described in the

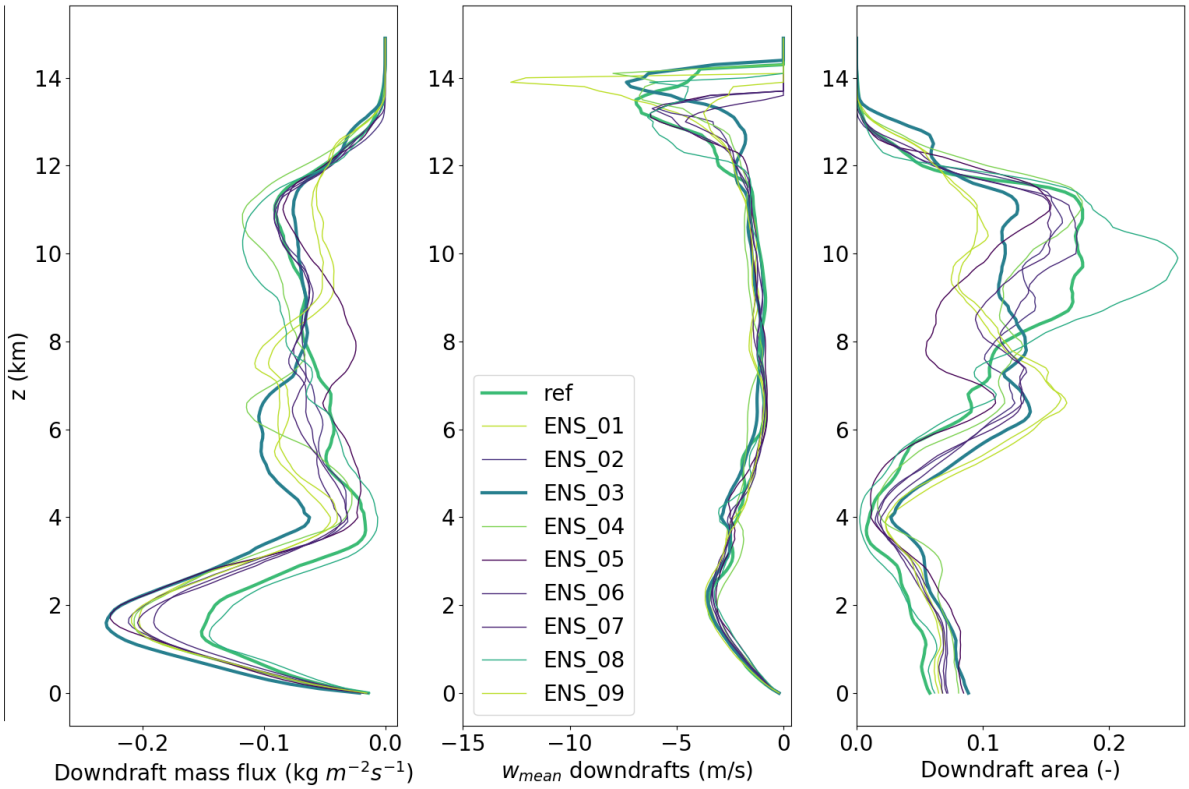

Figure 5.11: Instantaneous vertical profile of squall line downdrafts at $t = 75$ minutes for (a) their mass flux, (b) mean conditional w and (c) fractional area (reference and ENS-03: bold). Note that this figure shows instantaneous values, in contrast to the time averaged values over 30-75 minutes used for statistical diagnostics (Table 5.1). The simulations are colored in the order of their initial z_i, with low interfaces in lime and high interfaces in purple (reference and ENS-03: bold).

Table 5.1: Statistical relations the main diagnostics. $R^2 > 0.4$ is significant at $\alpha = 0.05$. z_i refers to the top altitude of the shear layer, perturbed in the initial conditions and Z_{max} in the table refers to the level where the low-level downdraft flux maximizes (over the range $z < 4$ km).

Precursor, Possible driver	**Effect, target**	**Time interval precursor (min)**	**Time interval target (min)**	$\mathbf{R^2}$
z_i	w_{loc}	0	30	0.020
w_{loc}	v_{cp}	30	30-75	0.612
v_{cp}	Downdraft area at z_{max}	30-75	30-75	0.611
v_{cp}	Downdraft flux at z_{max}	30-75	30-75	0.799
v_{cp}	Precipitation flux	30-75	0-75	0.927
v_{cp}	Upper tropospheric divergence	30-75	0-75	0.595
v_{cp}	Cloud top height	30-75	60-90	0.559

above, could be thought of as a sub-circulation within the squall line (Figure 5.10): a cold pool circulation. Given the convergence anomaly in Figure 5.8, positive covariance of the updraft and downdraft variability within the ensemble is found. That covariance may also imply a response of downdraft mass flux to the secondary convective initiation, which is discussed in Sections 5.3.1 and 5.3.2.
The statistical links between initial perturbations, mean v_{cp}, w_{loc}, downdraft characteristics and other variables are presented in Table 5.1. Significant correlations between the downdraft properties and w_{loc} are found, but not between initial conditions and the indicator of secondary convective initiation, w_{loc}. w_{loc} affects convective initiation, relates to overturned mass and in the end to the squall line-relative flow perturbations. In Section 5.4, these and other connections will be synthesised and discussed in more detail.

5.3.4 Error growth in the squall line simulations

In this section, the error growth is investigated, i.e. the increasing magnitude of the ensemble spread of the simulated squall lines. The ensemble spread of the horizontal winds, with and without a correction for the cold pool propagation, is analysed for that purpose. The latter approach allows for a comparison between a quasi-Eulerian and a feature-relative perspective. This enables one to differentiate between a process-based error growth and a feature location based increase of the ensemble spread. Additionally, an attempt is done to infer information about the processes, contributing to the errors, during the main development stage of ensemble spread (after about 25 to 60 minutes of simulation time).
A limitation of this method is that only net growth of errors can be detected. Some processes can also reduce errors (e.g. diffusion) and so the method provides additional insight only when it finds growth in the error: a process leading to highly unbalanced tendencies has to dominate error tendencies. Thereby, dominating error growth processes can be identified, and a sequence of error growth processes might be found [Zhang et al., 2007, Baumgart et al., 2019]. On itself, the metric has limited abilities to describe dynamical patterns and processes, but the combination with other diagnostics makes it a useful tool to learn about the relevant processes. Furthermore, negligible initial errors typically lead to error growth towards a certain climatological envelope, after approximately a given time, which makes the error growth analysis a useful tool here.
Similar to the ensemble sensitivity analysis, diagnosis of error growth is targeted at variability in squall line-relative flow, here, and therefore applied to the u winds in the x-z plane. The zonal wind is averaged along the y-direction, wherever the cold pool-relative framework is used (i.e. u_{avg}). The zonal wind approach differs from a more complete energy metric [e.g. Selz, 2019, Zhang et al., 2007, Zhang, 2005], which includes u^2, v^2 and may include T. The error growth, as a measure of ensemble variability, is mapped by the difference winds between ensemble pairs. The simulations, that such a pair consists of, are usually assumed to fulfil a *perfect error assumption*, analogous to a *perfect model assumption* [see Selz, 2019, and Section 1.3]: note that only the error needs to fulfill this assumption and not the full model itself.
The v-component is not included in the error metric, but it is typically at least comparatively much smaller than u, in the simulated scenario, and therefore u reveals the dominant error patterns. Nevertheless, the part of the domain, downstream of the squall line, is not fully included for the feature-relative analysis. The cold pool-relative framework leads to a direct comparison of u winds at x-coordinates that are a function of the ensemble member. As the series of x-coordinates, that can be covered, depends on the cold pool position in each ensemble member, about a quarter of the domain is lost by taking the cold pool-relative view (as in Section 5.3.3.2). Keeping the considerations mentioned in this section in mind, growth rates of error energy (difference kinetic and/or difference total energy, Zhang [2005]) can be compared with expected behaviour for both of the two perspectives: quasi-Eulerian and cold pool-relative.

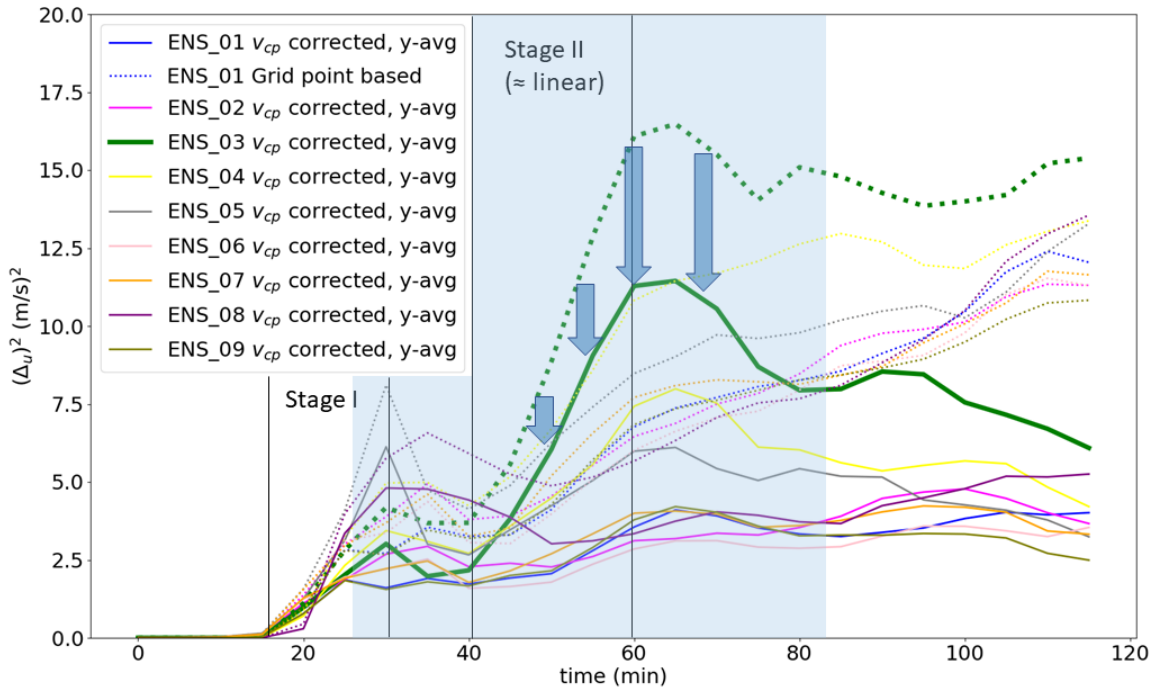

Figure 5.12: Error growth, as measured by the ensemble variance in u, where each other member is paired with the reference simulation. Both cold pool-relative curves (solid lines) and grid point-based comparisons (dotted) are displayed. The growth stages discussed in the text are also annotated in the Figure (see text) and the key interval discussed in the text is highlighted by blue shading.

Figure 5.12 shows the error growth curves. A first major stage of growth occurs between $t = 20$ and $t = 30$ minutes, both in the "absolute" and "relative" $(\Delta u)^2$ curves (Figure 5.12). This stage of the error growth is likely driven by de-correlation of the gravity waves, both their phases and amplitudes, and to some extent by differences in the convective initiation; see also Section 5.3.2.2 and Appendix E. This early stage does not cause much variation between the cold pool-relative and quasi-Eulerian error curves, because the cold pool edge has hardly moved in the early stage. However, some variation can occur, due to the inclusion of the full domain for the grid point-based comparison, versus only about three quarter of it for the cold pool edge-relative curves. In practice, differential error growth between the two classes of curves is first detectable after 25-30 minutes (Figure 5.12).
Another second major stage of error growth occurs from 40 or 45 minutes to 60-65 minutes. The variability in the squall line flow (Figure 5.8) strongly develops during this stage. In this stage, the slope between the quasi-Eulerian and cold pool edge-relative curves is systematically different, with much larger slopes for the former grid point-based curves. This means that a substantial portion of variability in squall line-relative circulation can be explained, and is probably induced by, variability in the cold pool edge propagation velocity v_{cp}. However, even in the cold pool-relative framework, some of the ensemble members still demonstrate strong error growth, whereas others hardly show error growth, compared to the reference simulation. The impact of non-linearities and feedbacks, that affect error growth as well, are certainly present. Nevertheless, during this stage non-linearities definitely do not dominate over v_{cp} effects. With a very rough estimate, one could say that, after about 60 minutes of simulation time, about a third to half of the error is related to differential cold pool propagation. Another third to half of the total errors was pre-existing after 30 minutes. Even though the latter two contributions are not fully independent, this means that non-linearities must be of a magnitude that is somewhat comparable to, or slightly smaller than, the other two.
Moreover, both the of the two classes of error curves seem to grow linearly in the second stage. In combination with the relatively constant v_{cp} values in each simulation (Section 5.3.3.1), it suggests that the cold pool acceleration linearly explains a substantial proportion of variability in the squall line circulation and possibly even the majority of the errors.
Another notable feature in the error growth curves, in between the two identified main stages of error growth, is the relatively low slope of v_{cp}-corrected curves (from 25-30 to 40-45 minutes). This can be explained by a

combination of regions of error growth and other regions where errors decay. Error growth mostly occurs in the region of secondary convective initiation. The spatial distribution of difference winds strongly suggests that the decay of errors mostly happens at locations of difference wind maxima after 25 minutes in the upper tropospheric region with cell cores, around $x = 0$ km (not shown). This implies that the relatively flat curve, after 30-40 minutes, is not inconsistent with local error growth due to secondary convective initiation.
After the first 60-65 minutes (Figure 5.12), the cold pool-relative curves do not seem to grow anymore, but errors remain rather stable. Moreover, the ensemble members with large $(\Delta u)^2$ do seem to have a stable cold pool-relative $(\Delta u)^2$ in the second hour.
Summarising this section, two main stages of error growth have been identified, with no growth in between those two stages of accelerated error growth. The second of the two stages reveals interesting near-linear relations with the cold pool edge propagation.

5.4 Synthesis and discussion

5.4.1 Evolution of ensemble spread

5.4.1.1 First amplification of ensemble spread: second phase of convective initiation The ensemble sensitivity analysis has demonstrated a statistical correspondence between w_{loc} and flow patterns in the x-z plane, elsewhere in time and space. In the section on the passive tracers (Sections 5.3.2.2), it has been shown that the updraft position after about 25 minutes of simulation time is already connected to differential w_{loc}. The temporal evolution and spatial patterns of a trough (resp. crest), both in the tracer distribution and the ensemble sensitivity, confirm that the propagation of differences in (both amplitude and phase of) gravity waves is leading to a local vertical velocity difference, w_{loc}. This vertical velocity contrast is able extend the size convective cells by a few km to the east, after about 30-35 minutes - the secondary convective initiation in part of the ensemble and most notably in ENS-03. The secondary initiation directly impacts convective overturning: subsequently, ENS-03 and the reference simulation reveal a large difference in upward tracer flux of PT2 to levels above 4 and 6 km associated with the deep convection. This increased convective overturn also translates into increased average precipitation intensities (24%) and upper tropospheric divergence (38%) in ENS-03, when averaged over the first 75 minutes of simulation time.

5.4.1.2 Second phase in the evolution: cold pool acceleration After the second phase of initiation happens (30-35 minutes), the upward mass flux within the squall line system is not just affected. The cold pool is also accelerated (around 35-45 minutes) to a speed that is later on maintained, as it was suggested by the lag correlation function of the cold pool edge location (Section 5.3.3.1). The cold pool velocity is higher for ENS-03, which has strong secondary convective initiation and more convective overturn. One could anticipate that more convective overturn (updrafts) also leads to increased downdraft intensities. As the strengthening of updrafts is caused by an eastward extension of the updrafts, a consequent increase in downdraft area could also be expected. Statistics reveal significant intra-ensemble correlation between the maximum downdraft flux, as well as downdraft area at the level of maximum downdraft flux (30-75 min), with cold pool velocity (30-75 min).
Further support for the importance of cold pool acceleration in this stage is provided by the error growth curves in Section 5.3.4. This error growth curve starts to grow strongly in the gravity wave de-correlation and first convective initiation phase (20 minutes). The curve continues to do so during the first part of the secondary initiation phase (30-35 minutes). Directly after the start of the secondary initiation, the error growth stagnates for a short period (around 35-40 minutes). Curves, in which a correction is made for cold pool velocity, clearly demonstrate less error growth in the subsequent phase than the uncorrected curves. By removing the contribution of cold pool propagation from the grid point-based error curves, the error is reduced substantially, implying that much of the error is contained in the spread in cold pool position. The evolution of the slope of the error curve implies a relevance of feedbacks and interactions, other than direct effects of cold pool propagation spread, as a source of ensemble variation. Nevertheless, a dominant mode of variability, contained within the ensemble, is certainly associated with the contrasts in the cold pool velocity. The linear contribution of cold pool propagation is thought to be at least as important to the errors as other, non-linear, feedback mechanisms, in the second stage of error growth (40-60 minutes).
The second phase of convective initiation (30-35 minutes) and subsequent cold pool acceleration (30-45 minutes) is the most important event for the ensemble spread.

5.4.1.3 Common mode of variability and possible common driver The common driver for a substantial fraction of the squall line variability, including the cold pool acceleration to a stable value of v_{cp}, is the gravity wave development originating from the first convective initiation. It influences the secondary

convective initiation and the cold pool propagation. In the example of strong secondary triggering (ENS-03), convergence originating from the gravity wave crest compensates for upward motion. This convergence pattern, below the gravity wave crest, implies that the cold air on the rear flank is likely accelerated a bit more eastward relative to the reference member, in which no secondary initiation occurs. This additional eastward motion leads to more mass reaching the region of initial downdrafts, accelerating the cold pool circulation. The slight eastward shift and enhanced cold pool circulation is also consistent with Hovmöller diagrams of the cold pool in ENS-03 and the reference simulation, because immediately after the secondary initiation, the cold pool in ENS-03 occupied a larger area (Figure 5.5). In addition, the argument is supported by the tracer evolution after 30-35 minutes. The statistical links between on the one hand w_{loc}, v_{cp} and on the other hand downdraft area and mass flux are confirmed by Table 5.1. The convergence patterns in the ensemble sensitivity analysis provides further support: slightly above the cold pool, a region of increased convergence (2-4 km above ground level, Figure 5.8) at the cold air boundary was found, in association with high values of w_{loc}. This region of increased convergence thereby increases the inflow of downdrafts below melting level, at 2-4 km (Figure 5.11), exactly the height at which the downdraft fluxes rapidly increase with decreasing height. The low-level circulation around the cold pool is therefore very likely increased by the secondary convective initiation.
Overall, this common mode of variability increases the vertical overturning in both upward and downward mass fluxes, by increasing the intensity of the convective cells. This in turn affects the downdraft strength and leads to precipitation differences. Moreover, the mode of variability probably induces some of the variability in strength of convective *overshooting tops* into the stratosphere, after about 60 minutes, and the strength of mean upper tropospheric divergence (see Table 5.1; and regarding upper tropospheric divergence, see also Groot and Tost [2022] and Chapter 3). Therefore, a common driver of squall line variability exists, of which w_{loc} was found as an early manifestation.
This w_{loc} is the earliest identified manifestation of the common mode of variability. It may be present before this manifestation, hidden in the gravity wave variability within the ensemble. The mode of variability is responsible for much of the variability in w_{loc} and lives on for the following 45-60 minutes. It covaries with the variables shown in Table 5.1 and explains part of the variability in them. Furthermore, it affects the circulation within the squall line, as revealed by the ensemble sensitivity analysis.

5.4.1.4 Approach of intrinsic limit? The tiny difference in initial state - of less than 2% in terms the shear layer depth between ENS-03 and the reference run - implies that the mode of variability is very sensitive to initial conditions. Given that the total variability in initial shear layer depth was 5%, it can be argued in line with Melhauser and Zhang [2012] (in particular based on the illustration in their Figure 18) that there can occasionally be an *intrinsic limit of predictability* on time scales of about an hour, at mesoscales. A pattern very closely matching such behaviour is exposed by the presented simulations and analysis (Section 5.3), after doing a *perfect error assumption* [see Selz, 2019].
The non-linear behaviour in the evolution from initial conditions to $t = 30$ minutes indicates the probable existence of an *intrinsic limit of predictability*. The 'random' realisation of gravity wave amplitude and phase, after about 30 minutes, leads to random excitation of the identified mode of variability: Figure 5.3 suggests a possibility that amplitude and phase of gravity waves could be directly responsible for w_{loc}.
This non-linearity, in the evolution between $t = 0$ and $t = 30$ minutes, directly implies that characteristics of the initial conditions cannot be monotonically linked with the conditions afterwards, including those during the second phase of convective initiation (see also Appendix E). These conditions afterwards also include the flow anomalies (or perturbations), associated with the squall line ensemble, as found in Section 5.3.3.2. Initial condition perturbations are non-linearly linked to much of the squall line variability that occurs after 30-85 minutes. Therefore, the illustration of Figure 18 in Melhauser and Zhang [2012] is applicable to the findings presented in this Chapter and it can argued that intrinsic sensitivity is a key implication.

5.4.1.5 Flow pattern anomalies within the squall line ensemble The flow perturbations in the squall line were very likely affected by w_{loc} and so by the common mode of variability that is suggested to exist. The pattern of flow perturbations builds up after about 40-45 minutes of simulation time. Its relation with w_{loc} peaked after 55-60 minutes. The anomalous flow pattern in the squall line, as shown in Figure 5.8, resembles to some extent that of an enhanced circulation of the *jump updraft*, downdraft and *overturning updraft* of Moncrieff [1992] (see Figure 1 in that work, for an explanation of these terms). Figure 5.8 suggests that the mode of variability, identified in this study, is partly explained by intensification of this 2D circulation after 45-80 minutes. If this is true, the corresponding downdraft and *overturning updraft* are likely comparatively shallow.
During the second hour of the simulations, the traces of the identified mode of variability seem to disappear gradually. The gradual dissipation of the earlier mode of variability was identified with the ensemble sensitivity analysis, between about 70 and 85 minutes, with a new structure of u_{avg} variability appearing. The

new structure in the variability is partially opposing the earlier circulation signal, in terms of zonal flow. In combination with the flattening error curve in Figure 5.12 during the second hour this might suggest a sign of saturation, in which (Δu) reaches about 4 m/s. That value is a significant fraction of the actual u, but only halfway on the way to saturation (roughly).
There is a possibility that the identified common mode of variability covaries with a sub-hourly time scale, imposed on the squall line by cyclic behaviour during its growth, as in McAnelly et al. [1997], Adams-Selin [2020a]. That is very speculative and additionally not supported by traces of any other variables that were analysed.
Next to the common mode of variability, other patterns can of course also affect the flow perturbations within the squall line ensemble and the resulting signals in retrieved diagnostics.

5.4.2 Discussion

5.4.2.1 Relevance in context of squall line research The squall lines in this study, which are initiated by a cold pool, get mature only later on in the 120 minute simulations. Furthermore, the simulations are restricted to a relatively small domain. Parts of the *mature* stage and the full *dissipation* stage of the system are excluded. Still, this study is able to illustrate that small errors in the initiation phase lead to a systematic variability within the idealised convective system. A different set-up (e.g. larger domain, different boundary conditions and an extended simulation time) could provide more insights into the development of ensemble spread during the mature and dissipation phases of the system. Nevertheless, this study identifies a highly relevant window for squall line error growth in the first 80 minutes of its development, in which systematic variability in the squall line-relative flow has fully developed and also decays.
The settings in the presented ensemble are very similar to those in Adams-Selin [2020a,b]. The main difference in the environmental conditions is that the ensemble, analysed in this Chapter, has a reduced depth of the shear layer: to about half of their environment. Furthermore, the domain and geometry was different: squall lines in this study behave as "infinite-length", nearly-2D squall lines (see also Chapter 3). There is also similarity to Adams-Selin [2020a,b] in the evolution - in the sense that a *discrete propagation event* on small length scales is diagnosed, or at least a new convective cell growing ahead of the squall lines presented here. In the ensemble presented in this work, the propagation event occurs a lot earlier: already after 30 minutes and just after the first phase of convective initiation. Furthermore the event occurs only a couple of km ahead of the squall line, as opposed to the clearer separation in Adams-Selin [2020a,b] and Fovell et al. [2006]. Even though one could wonder whether the ensemble in this chapter actually manifests as a *discrete propagation event*, or just growth ahead of the squall line, Figure 5.3 suggests that the secondary convective initiation starts as a discrete propagation event. Quite soon, this discrete propagation event is absorbed by the main squall line itself and is found to contribute substantially to its successive evolution.
Certainly, the discrete propagation event, detected in Fovell et al. [2006], could not happen as closely ahead of the squall line as in ENS-03 here, as typical model resolutions were lower at the time and small updrafts were often at the minimum size resolvable in their simulation. Results in this Chapter definitely demonstrate that distinct convective initiation, only about 3 km ahead of a squall line, can easily be resolved at 200 m resolution. With a resolution below 100 m, one could assume that events, resembling discrete propagation, could be simulated in LES when they happen at length scales of about 500-1500 m. This would require a higher output frequency, as in Adams-Selin [2020a,b].
A degree of similarity is also shared with Weyn and Durran [2017], even though these authors use warm bubbles to initiate convection and slightly different temperature, moisture and wind profiles, with deeper shear of varying magnitude. In spite of their analysis mostly carried out in spectral space, their error growth curves of mesoscale convective systems can be compared to the curves in this chapter (Figure 5.12). The main difference between simulations by Weyn and Durran [2017] and the squall line ensemble, presented here, is first of all that the simulations in this Chapter take place in a smaller domain, in a set-up of higher resolution and covering a shorter integration time. They integrate their simulations over six hours simulation time, which leads to error saturation ($> 75\%$) after 4.2-6.0 hours. In the simulations presented here, error saturation is not reached. Moreover, the occurrence of a bulging error growth curve, with stages of no error growth, is shared with their Figure 8. Despite, their bulges appear comparatively small in magnitude. For an assessment of error saturation, their study provides a much more suitable approach - the simulations here have not been integrated sufficiently far ahead and the metrics are not so suitable for that assessment. Error saturation is beyond the scope of this study, in which the focal point is the investigation of the chain and evolution of early convective dynamics within the squall line ensemble.
Even though Weyn and Durran [2017] approach squall line predictability from a different perspective, this Chapter provides additional evidence on how squall line predictability may be extended very slightly only (by on the order of an hour), when initial conditions are very accurately known: initial conditions are non-linearly linked to the second phase of convective initiation and the second phase of convective initiation is

highly sensitive to these initial conditions. On the other hand, the findings also suggest that some of the information on convective initiation can be stored as linear signals in the cold pool-relative circulation that live for time scales on the order of one hour, while feedback effects are probably of secondary importance. This finding once more confirms the known ideas of shorter and shorter saturation time scales at smaller and smaller scales [e.g. Lorenz, 1969a, Durran and Gingrich, 2014].
The ensemble investigated here starts with highly, but not fully, 2D initial conditions and is part of a wide spectrum from highly simplified squall line studies [see Houze, 2004, for references] to more recent simulations of real cases, coupled to the large scales [e.g. Melhauser and Zhang, 2012]. The initial conditions selected (Sections 5.2.1 and 3.2) are practically the same as those in Adams-Selin [2020a], apart from the depth of the shear layer. The high degree of two-dimensionality makes the variety of diagnostics, applied here, very affordable to deeply assess, which is particularly beneficial in error growth studies. It is not common that squall lines initiate in a time period as short as 10 minutes and along a straight line, as in our idealised setting. Even if not completely representative of many squall lines in the real atmosphere, *convergent rolls* (as occurring in for example the planetary boundary layer) often help to organise convection and occur along real squall lines. Insights into error growth, provided here, and into processes responsible for error growth are likely largely applicable along sections of real squall lines, especially those insights closely relating to findings of Melhauser and Zhang [2012]. The idealisation only emphasizes signals, which is of benefit to the analyses.

5.4.2.2 Tests of statistical signals The robustness of statistical results may appear somewhat questionable at the very first glance, even after statistical tests, since only two simulations are compared in Section 5.3.2 and given the ensemble size of just $n = 10$. Nonetheless, the very high correlations in Section 5.3.3.2 easily survive any significance tests, with a null hypothesis that correlations found are random, which means the robustness of the signal is verified. Fractional areas, over which the ensemble sensitivity analysis survives the significance testing in the squall line core region, implied confidence in robust flow anomalies. Statistical test outcomes strongly suggest that a larger ensemble would reveal the same signal as the 10 member ensemble, given the outcome of the statistical tests. As confirmed by the cold pool edge-relative and quasi-Eulerian error growth curves, the signal of the main mode of variability is demonstrated to be well established and well separable from noise and non-linear contributions. These non-linear components consist of the feedbacks, that do occur to a limited extent. The ensemble sensitivity analysis reveals the main mode of squall line variability, which is strongly related to the second phase of convective initiation, with high confidence.

5.4.2.3 Potential for future research directions The relations found in this study indicate that cold pool acceleration, after about 30 minutes of simulation time, is very likely explained by the main mode of variability and, hence, by variability in gravity wave propagation. As described in Section 2.3 (and in more detail documented in for example Houze [2004], Mapes [1993], Mapes and Houze [1995] and Adams-Selin [2020a,b]), localised heating, associated with deep convection, triggers gravity waves. Rapid changes in the heating profile also triggers gravity waves [Adams-Selin and Johnson, 2013, Adams-Selin, 2020a,b]. Therefore, it is reasonable to pose the hypothesis that variability in the heating profile may result in consequent gravity wave variability. Grant et al. [2018] have posed and investigated a similar hypothesis, for example. One could argue that the depth of heating profile, immediately before cold pool acceleration, can affect the vertical wavelength and propagation speed of gravity waves of a certain vertical wavenumber, in agreement with findings by Pandya and Durran [1996].
A heating profile depth, differing by about 1 km, would provide a variability in gravity wave propagation speed of about 8-10%. Consequentially, proportional variability in cold pool propagation may occur in a flow-relative framework. Resulting variability in heating profile, of about 8-10% for a 12 km deep troposphere, may explain an 8-10% difference in cold pool propagation speed, in a flow-relative framework. The gravity wave propagation velocity is inversely proportional to the wavenumber of the triggered wave, at a given $\frac{\partial \theta}{\partial z}$ [e.g. Grant et al., 2018]. If at the same time, a wave has a vertical wavenumber of $n = \frac{5}{2}$, over twice the depth of the troposphere - i.e. a vertical wavelength of about 10 km, it will propagate at about 17 m/s (given the imposed tropospheric bulk value of $\frac{\partial \theta}{\partial z}$). That wavelength is equal to wavenumber one, in the layer between the surface cold pool and the tropopause. Furthermore, it is close to the depth of the heating profile that may trigger the waves (which could be derived from Appendix B, Figure B3). Against easterly near-surface winds that are on the order of 12-14 m/s, these gravity waves would propagate eastward. The flow-relative propagation to this near-surface flow would be at low speeds of 3-4 m/s: the density current could surf on this wave. Furthermore, the 3-4 m/s estimate is close to the calculated cold pool propagation velocities, in this study. The cold pool edge propagation velocity varies by 1.7 m/s, between ENS-03 and the reference simulation, i.e. about 10% of 17 m/s propagation velocity of the mode of interest. This 10% relative variability is consistent with the rough estimate for heating profile variability. All in all, at the low-level

inflow rates of 12-14 m/s, the cold pool edge propagation might be a manifestation of a propagating $n = \frac{5}{2}$ gravity wave mode, near to the surface! Inspection of the precursor condensation rates after 25 minutes (directly before the gravity wave leads to secondary initiation) suggests a deviation in heating profile depth of at least 500 m, between ENS-03 and the reference simulation, probably close to 1 km. Furthermore, mean cloud top detections between the two deviate by 800 m, after 60-90 minutes of simulation time.
In other words, there are some suspicious patterns that could support the hypothesis, about the role of the $n = \frac{5}{2}$ gravity wave mode. The arguments to support the hypothesis are comparable to Grant et al. [2018], and references herein, and Stechmann and Majda [2009]. Whether or not the gravity wave propagation actually leads to differential cold pool acceleration, is beyond the scope of this study. It would require a detailed, minute by minute, analysis for the 20-30 minutes interval (with sub-minute output frequencies). Such an analysis would include a computation and analysis of additional quantities, such as the Scorer parameter.

5.5 Conclusion

This Chapter describes the variability within an ensemble of idealised squall line simulations, with nearly identical initial conditions. It demonstrates that some degree of linearity is maintained throughout the second half hour of the simulation, within the error pattern of the modelled squall line ensemble. In this specific stage, the squall line grows mature. A second phase of convective initiation, after ~ 30 minutes, has been identified as crucial for the evolution of the ensemble spread. A mode of variability has been identified, associated with this second phase of convective initiation. The mode is suggested to be induced by shifts in phase and amplitude of gravity waves triggered by the developing squall line itself, originating from the very small initial disturbances. It is first revealed by the upward motion, a few km ahead of the squall line, after 30 minutes. Leading to contrasts in secondary initiation of convection, the effect of this mode of variability on the squall line can be followed. These effects are identified as solid signals in upward tracer and mass transport, downward mass transport, cloud top height and variability in squall line circulation. The effect of the mode of variability is most clearly present after 55-60 minutes of simulation time. After almost an hour of existence, this mode of variability gradually disappears (70-85 minutes).
It is concluded that, in good agreement with Melhauser and Zhang [2012], Hanley et al. [2013], convective initiation sensitively depends on environmental conditions, in the presented ensemble of idealized simulations. The chain of interactions has been documented in much detail: following the crucial second phase of convective initiation, a cold pool acceleration is coupled to the intensity at which mass is moved by updrafts and downdrafts. On the other hand, once established (35-45 minutes), the cold pool velocity v_{cp} is maintained well throughout the next 30-45 minutes, as shown by Section 5.3.3.1. Variation in v_{cp} explains much of the subsequent variance in flow perpendicular to and relative to the cold pool (u_{avg}). Therefore, a substantial fraction of u_{avg} is explained by the mode of variability identified in this Chapter. It is exposed by Eulerian and feature-centred perspectives on error growth that both the cold pool propagation itself and non-linear feedback mechanisms play a substantial role in the idealised squall line ensemble spread, after 45-60 minutes.
Consequently, two stages of error growth are identified:

- A stage dominated by de-correlating gravity wave patterns, originating from the initial triggering of convection (between 20 and 30 minutes).
- A stage associated with the main mode of squall line variability, which to a substantial degree depends linearly on v_{cp} and the second phase of convective initiation (between 40 and 65 minutes).

Noteworthy, initial condition uncertainties within the ensemble lose their structure quickly, within 30 minutes. Less than 2% variation in initial top height of the shear layer, z_i, can result in convective intensities and overturned mass at opposite ends of an ensemble with 5% initial variation, in that z_i. Loss of error structure (e.g. top row, Table 5.1, see also Appendix E) is likely explained by non-linear developments, as a result of the triggered gravity waves (phase, amplitude, during the stage after 20-30 minutes). These differences in gravity waves are a precursor to the second phase of convective initiation. This combination of loss of the initial structure and subsequent second phase of convective initiation can lead to very different developments within the squall line ensemble, in the mature stage. The ensemble of squall line simulations can chaotically diverge into a wider envelope, during the stage in which gravity waves de-correlate flow perturbations. Information about earlier states is lost during this stage. Loss of uncertainty structure, within a narrow ensemble of squall line simulations, is in good agreement with the picture that Melhauser and Zhang [2012] draw for intrinsic and practical predictability, at the end of their study. Comparably to their findings, it can be concluded from this study that a very small subspace of initial conditions can provide the same ensemble spread as a much wider subspace: an intrinsic limit of predictability may be present.

6 Conclusions

6.1 Existence of predictability limits in convective systems

Chapter 5, on variability within a squall line ensemble and its error growth, has shown that small-scale (km-scale) errors and uncertainties in the gravity wave signal can have large impacts on the squall line-relative circulation at later times: these small-scale errors subsequently propagate to differences in the initiation of convective cells along the squall line and the errors grow further, towards larger length scales. The presence of intrinsic sensitivity is very probable within the ensemble, which implies a non-linear connection between initial ensemble errors and the resulting differences (in state) with the ensemble mean, later. Intrinsic sensitivity signifies that initial errors in the atmospheric state, as represented in a model simulation, continue to limit the forecast accuracy beyond a certain time horizon T, no matter how small the magnitude of these errors is. The probability density of the forecasted state after T can never be estimated more accurately, than that of forecasting the underlying background distribution. The accuracy is even limited, if these errors are reduced by several orders of magnitude, compared to nowadays reasonable values (from a practical point of view) [see Selz et al., 2022, Melhauser and Zhang, 2012, Lorenz, 1969a]. It is only possible to estimate the forecast distribution of an atmospheric state more accurately, before time T.
Whereas the structure in initial condition errors of the squall line de-correlates, during the stage before the second phase of initiation of convective cells (after 20-30 minutes; see also Appendix E), errors can grow mostly linearly, afterwards. Thereby, the errors sustain some degree of coherent structures, in a statistical sense, after this initiation of the new convective cells. Hence, small-scale initial condition errors (such as in local vertical velocity) can non-linearly lead to larger mesoscale errors, both in dynamics *and* precipitation. These errors may keep part of their structure, on a time scale of about an hour. Other covariants (e.g. cloud tops, updrafts, downdrafts) are also shown to cohere with the precipitation pattern and errors at larger mesoscale (order 100 km) dynamics. The precipitation rate and dynamics at this length scale itself has been emphasised in Chapters 3 and 4.
It is important to realise that intrinsic sensitivity does not just imply strong sensitivity on itself. It is also associated with ever decreasing time scales of error saturation (i.e. growth of errors to the background variability on that specific length scale), on smaller and smaller length scales. Therefore, if a mesoscale convective system's evolution can contain substantial errors, even with extremely detailed knowledge of conditions 30 minutes before a critical event, predictability limits of turbulence and other dynamics can (occasionally) be expected to even be substantially shorter [in line with Lorenz, 1969a]. Exactly this small scale dynamics, consisting of gravity waves and turbulence, is shown to be critical to the underlying dynamics of mesoscale convective systems, with rapid divergence in simulations of these convective systems as a consequence (Chapter 5, Groot and Tost [2023]).
Consequentially, mesoscale convective systems, such as squall lines, can likely even be exposed to limited predictability, at time scales less than an hour. Saturation of mesoscale errors may occasionally emerge at time scales of 0.5-2 hours, even while knowing prior conditions perfectly - likely on time scales substantially less than the 4-6 hours, found by Weyn and Durran [2017]. As mesoscale convection can be hazardous [Wilhelm et al., 2021, Antonescu et al., 2017, Clark et al., 2012, Doswell, 2003, and many others], the limited predictability, demonstrated in Chapter 5, can have consequences for early warning systems (such as warning systems for flooding): practical ensemble simulations of mesoscale convection events would be even more likely to de-correlate, on the time scale of an hour, than those in Chapter 5. The more rapid de-correlation is a result of the much larger initial conditions spread than in Chapter 5. The forecasting problem is likely to sustain for specific events, even if forecast errors would reduce by (several) orders of magnitude [Chapter 5, Groot and Tost, 2023, Melhauser and Zhang, 2012].

6.2 Ordering convective variability: precipitation rate as dependent variable

From the convective scale's perspective, precipitation-rate-dependent (conditional, Bayesian) variability is associated with, and revealed in, mesoscale dynamics. The precipitation variability is driven by even smaller scale convective storms and their precipitation maxima, which also contain a component of (seemingly) random variability [e.g. Craig and Cohen, 2006]. The variability in precipitation rate, or column integrated latent heating, feeds back onto larger mesoscale dynamics. Splitting-off a precipitation-dependent contribution of variability, from convective variability, is suggested to be a highly beneficial tool for better understanding of mesoscale convective variability, in particular in the dynamics (Chapters 3, 4 and 5). In case of the squall line ensemble, statistical coherence is found between variability in the precipitation rate and variability in various other indicators of the system's dynamics (e.g. downdrafts variability and upper tropospheric divergence; Section 5.3.3.3, Table 5.1). Nevertheless, given the findings of Chapter 4, it is important to question whether non-linearities, occurring as a result of convective organisation, may affect (and partially destroy) the linear association with variability in precipitation rate (Chapter 5) in realistic convective systems. Precipitation-

rate-dependent variability can explain a substantial portion of convective variability, which dominates the dynamical consequences in the idealised LES simulations (Chapters 3 and 5).
In Chapter 3, convective systems have been conceptualised as isolated point (i.e. supercell, regular multicell) or line sources of mass (i.e. squall lines) for the upper troposphere. Thereby, the convection induces net upward mass transport and net latent heating. Conceptually, "point", or 3D, sources can create outflow (diverging winds) in all directions, but a "line", or 2D, source only in one horizontal dimension. Intermediacies between a point and a line source can also exists, as convective cells tend to collect (aggregate), and non-idealised storm geometries occur. The analysis of Chapter 3 investigated the divergent upper tropospheric wind, induced by convective systems, with precipitation rate as dependent variable. The analysis has revealed that outflow dimensionality (2D versus 3D versus intermediate dimensionality) and convective aggregation (most likely through a change in outflow dimensionality) very likely play a key role in the precipitation-rate-dependent dynamical variability among the convective systems in LES simulations. Thereby, it is shown that the magnitude of divergent outflows is explained by convective organisation. The convective organisation can be conceptualised as resulting from the combined effect of storm dimensionality and convective aggregation (i.e. the tendency of convective systems to collect and together grow larger over time). The findings are consistent with Bretherton and Smolarkiewicz [1989], Nicholls et al. [1991] and Mapes [1993]. Here, the precipitation conditional (Bayesian) perspective is essential, especially to understand the convective variability at mesoscales, on the order of 100 km.
The precipitation-rate-dependent perspective has been very beneficial for the comparison of the divergent outflow feedback from deep convection, between two ensembles of ICON simulations, for an event on the 10^{th} and 11^{th} of June 2019 over Central Europe (Chapter 4). The perspective shows that an envelope of outflow variability (with substantial spread, when conditioned on precipitation rate) exists in ICON convection-permitting simulations, at 1 km grid spacing. However, a linear relationship with much smaller spread exists between precipitation rate and magnitude of divergent outflow for simulations with parameterised deep convection, at 13 km grid spacing.

6.3 The dependency of outflows from deep convection in convection-permitting ICON

Using the precipitation-rate-dependent (Bayesian) perspective on convective variability, the effect of convective aggregation on the relative magnitude of the divergent outflow has been investigated. An effect of convective aggregation on the associated upper tropospheric divergent winds is clearly present in ICON convection-permitting simulations: convective systems with larger areas are associated with a significantly lower divergence to precipitation ratio, based on a statistical analysis (Figure 4.11). Furthermore, a sub-linear fit confidently applies to the relation between precipitation rate and divergent outflows from deep convection.
On the other hand, the effect of dimensionality on the variable magnitude of the deep convective outflows is not detected easily, in ICON convection-permitting simulations. The impact of dimensionality, on the variability of these outflows in these ICON simulations, has been assessed in a multivariate way, using the precipitation rate as dependent variable and ellipse fitting to estimate degree of (geometric) linearity of a convective system. Some of the detected signals behave as expected, but many signals are weaker, or even neutral and insignificant. Nevertheless, the difficulty of detecting the signal is explainable, even in the potential presence of dimensionality impact on the deep convective outflows (Section 4.7).
Regardless of the many mixed signals, simulations with clear developments into a squall line-like structure revealed a reduction of the divergence to precipitation ratio, as the squall line-like structures developed. The magnitude of mass divergence is close to stable and the precipitation intensity generally increasing (Figure 4.9 and Table 4.2). This behaviour of the squall line-like system is consistent with the understanding of divergent outflows from deep convection, based on idealised LES simulations (Chapter 3). Therefore, the exact impact of dimensionality on the variability in the divergent outflows remains difficult to determine. Further research would be needed, to draw a definitive conclusion on this impact in convection-permitting ICON.

7 Implications, significance and recommendations

7.1 Precipitation-dependence as a tool to evaluate of convective variability

Summarising the benefit of the precipitation conditional (Bayesian) perspective for the understanding of convective variability, it improves insight and could be a benchmark in the assessment of convective variability. In this work, the perspective has been beneficial for the following dynamical and representativity assessments:

- Comparing ensemble members and assessing ensemble variability, as illustrated by squall line variability evolution in Chapter 5
- Comparing modelling approaches: LES, convection-permitting NWP and NWP with parameterised deep convection (Chapters 3, 4 and 5)
- It can shed light on interactions between deep convection and other processes in atmospheric dynamics (e.g. the way outflow divergence can vary)
- It can provide additional insight, when evaluating spread in a dynamic evolution. Thereby, it can assist in separating structured highly non-linear from weakly non-linear/near-linear evolution in ensemble spread for instance, as shown in Chapter 5
- Information on physical mechanisms that are represented in simulations may be extractable, e.g. on convective aggregation in LES and ICON (Chapters 3 and 4)

A limitation exists, when opposing signals might neutralise each other, which might have occurred in convection-permitting ICON (see Section 4.7.1). However, more careful experimental design and considerate selection of case studies may also allow for a reduction of such effects.
It is emphasised that other representation and representativity issues of smaller scale processes, parameterised in NWP, may be addressable with similar *conditional* strategies [in line with Stein et al., 2014, for example]. In spite of that, precipitation rate and net latent heating are near-optimal (dominant) conditioning variables for deep convection only. The big advantage is that net latent heating drives the dominant contribution of the feedback between deep convection and large-scale dynamics, in case of the convection.

7.2 Progress in understanding the magnitude of deep convective divergent outflows

All of the three main Chapters (Chapters 3, 4 and 5) provide key insights into the understanding of upper tropospheric divergent outflows from deep convection. An analysis of an idealised squall line ensemble in LES reveals that the deviations in strength of these divergent flows, in the upper troposphere, are directly related to deviations in precipitation rate and variability other dynamical processes (Figure 5.8 and Table 5.1). The following can be concluded on the magnitude of those divergent outflows [Nicholls et al., 1991], based on a box analysis [Groot and Tost, 2022, Groot et al., 2023]:

- A linear dependence on net latent heating (possibly within the appropriate geometric regime, thus probably conditionally on geometric constraints) is supported by idealised LES, convection-permitting and parameterising ICON and idealised linear gravity wave modelling. The dependence is also consistent with the weak temperature gradient approximation [Sobel et al., 2001], which represents an idealisation of atmospheric dynamics in the tropics.
- Idealised linearised gravity wave modelling [Bretherton and Smolarkiewicz, 1989, Nicholls et al., 1991] and idealised LES simulations suggest a strong dependence of divergent convective outflows on dimensionality (2D/3D/intermediate regimes) of convective systems. The dependence is weakly supported by convection-permitting ICON simulations and also by other recent analyses [Morrison, 2016a,b].
- Idealised LES and convection-permitting simulations suggest a dependence of such outflows on convective organisation and aggregation, likely as a consequence of the dimensionality effect (suggested by idealised LES).
- Convective momentum transport may directly enhance upper tropospheric divergence, although convection-permitting ICON and idealised LES simulations do not agree on this aspect.

The disagreement on the CMT dependence, among LES and ICON convection-permitting simulations, could likely be induced (at least partially) by the highly idealised wind shear profile in LES. However, other unknown aspects, such as experimental design, may also cause the apparent disagreement. The wind shear profile may also be accountable for the difficulty, encountered in the detection of dimensionality effects on divergent convective outflows in convection-permitting ICON. In the selected case, apparently separable 2D, 3D and intermediate regimes [Moncrieff, 1992, Nicholls et al., 1991, Trier et al., 1997, Groot and Tost, 2022, and Chapter 3] might be practically absent. The weak presence is plausible, as a consequence of much weaker low-level shear than in LES simulations (Section 4.7.1 and Chapter 3).
Hence, additional experiments, with different experimental design, should shed more light upon the apparent inconsistencies, as described in Section 4.7.1. It would be worthwhile to investigate the upper tropospheric divergent outflow from deep convection in an additional ensemble or a different case, in which a clear bimodal distribution of (quasi-2D) squall line developments and other convective cloud formations exists. That may strengthen the signals found in Chapter 4. In an ideally suited ensemble, ellipse fitting algorithms might be entirely circumvented.

7.3 Significance for 21^{st} century NWP

7.3.1 Predictability research

Potential vorticity inversion offers a handlebar to understand error growth at (very) large mesoscales to synoptic and planetary scales [Baumgart et al., 2019]. Conditioning on precipitation rate might arguably be of similar benefit, to the understanding of (small to larger mesoscale) convective uncertainty and variability. Future considerations of this conditional perspective could complement the PV inversion method, with possibly large benefit to the understanding of error growth. The role of precipitation has been known and identified by Zhang [2005], Zhang et al. [2007], amongst others. Splitting the convective variability, conditional on precipitation rate (in particular at mesoscales of order 100 km), off of other contributions will be of particular benefit and essential, when convection-permitting and convection parameterising simulations are compared in a specific case study.
The characterisation of the two types of variability that can be split-off differ fundamentally: the precipitation variability can always be reduced in theory, at least on short lead times (going to infinitely short). The bias produced by not generating variability through convective organisation can only be reduced by improving the representation of convective organisation and aggregation in simulations. Such a reduction may be achieved eventually, by abandoning or adjusting parameterisation of deep convection, or by continuing the quest for improved representation [Moncrieff, 2019]. Of course, many other biases than those induced by the deep convective parameterisation exist in NWP models. Chapter 4 suggests that a correct precipitation climatology is not the only improvement needed for better representation of the flow feedback from parameterised deep convection to the large-scale. Furthermore, results also suggest that increasing mean (convective) precipitation rates can destroy flow predictability.
Merging the potential vorticity perspective and a precipitation conditional perspective might lead to a breakthrough for error growth studies, when applied to explicit convection simulations. As a first step, the merging essentially requires an orientation study of how diabatic PV tendencies relate to the precipitation conditional perspective. Secondly, the merging also requires a study that would unify the precipitation conditional perspective with the important contribution of divergent wind modes, as identified in the PV perspective (Figure 1.3 in Chapter 1 [Baumgart et al., 2019]). The whole combined framework might then be usable for an even broader assessment of the evolution of error features, from kilometer scale to planetary scale.
In spite of the promising forethought, Selz et al. [2022] shows that, on average, the understanding of the divergent outflows will not help practical weather forecasting with NWP for the next years. A careful selection of a case study, in which a convective system is affecting ensemble variability *upscale*, makes the new perspective interesting for rare cases (such as forecast busts Rodwell et al. [2013]). In (at least some of) such rare cases, deep convection is very likely a key player for large ensemble variability in operational NWP simulations. Research evaluating a full upscale chain of interactions, would be the ultimate goal. Such an evaluation, in a way, combines the elements and approaches of Rodwell et al. [2013], Zhang et al. [2007], Baumgart et al. [2019], Selz et al. [2022] and Groot and Tost [2023] with the approach to an ensemble, as presented in this work [Groot et al., 2023, and Chapter 4]. In spite of this, large-scale errors can simultaneously affect the error evolution critically [Durran and Gingrich, 2014]. The scientific debate on the significance, or dominance, of upscale versus *up-amplitude error* growth has not been concluded yet [e.g. Zhang et al., 2019].

7.3.2 Stochasticity and convection-permitting NWP

Improved process representation, with explicitly resolved deep convection at high resolution, is the intuitive way forward for the next decades in NWP and climate modelling. Global convection-permitting simulations

at high resolution demonstrate promising potential in terms of representation, based on Chapter 4 [i.e. in line with for example Bauer et al., 2015, Satoh et al., 2019, Peters et al., 2019, Palmer, 2020]. High resolution convection-permitting simulations are in one way the next natural step towards the seamless approach in NWP, that is currently widely invested in [e.g. Hazeleger et al., 2010, Bauer et al., 2015, 2018] - in which weather and climate models are unified more and more. Furthermore, (global/large) error growth studies, based on convection-permitting simulations at grid spacings of 3-4 km, have also recently started to appear [Judt, 2020, Zhang et al., 2019, Judt, 2018]. Nevertheless, these works have so far mostly been looking at errors from the statistical and spectral point of view of Lorenz [1969a].

An alternative to global convection-permitting simulations is achieved with the concept of *superparameterisation*. Partially resolved sub-grid processes, occurring in a high resolution sub-model with restricted subdomain, are coupled with a parental global simulation: by embedding a high resolution convection-permitting or large eddy simulation in each column of a global circulation model [e.g. Grabowski and Smolarkiewicz, 1999, Grabowski, 2016]. *Superparameterisation* is well-established in climate research, but has not been particularly beneficial for numerical weather prediction methods, as a consequence of its limitations [see Grabowski, 2016, and references herein]. Therefore, NWP issues addressed in this work, like propagation of forecast uncertainty and ensemble spread, has not been within the scope of *superparameterisation* studies, as far as the author is aware of.

Even if the meteorological community would try to circumvent conditional representation and representativity issues, arising from any parameterisation, stochasticity has been introduced in the models with a concept, called SPPT: stochastic perturbation of parameterisation tendencies [Buizza et al., 1999, Leutbecher et al., 2017, Ollinaho et al., 2017, Palmer, 2017], which is important to the evolution of flow variability [Rodwell and Wernli, 2022]. If looking at the net latent-heating/precipitation rate-mass divergence space (Figure 4.9), this SPPT approach is equivalent to a manipulation of vertically integrated net latent heating. The manipulation is suggested to simultaneously modify the (out)flow from deep convection by a certain coherent proportionality (Chapter 4). Hence, small-scale flow perturbations are provided to the background flow, that correspond to the adjusted net latent heating in the column and parameterised tendencies in water species (including q_v) [Leutbecher et al., 2017, Ollinaho et al., 2017, Davini et al., 2017] (note that precipitation rate is not perturbed accordingly, at the surface boundary of the model, see [Leutbecher et al., 2017, Davini et al., 2017]!). But the additional stochasticity, that high resolution convection-permitting simulations may introduce, at a given precipitation intensity - by implicitly taking into account outflow variability, as a result of convective organisation and convective aggregation - is completely ignored [in line with Christensen, 2020, Rodwell and Wernli, 2022]. Constraints on the (conditional) outflow divergence distribution cannot be accounted for. Even if the updated concept of stochastic parameter perturbations (SPP) is used, parameterised variability is, in principle, only introduced along the slope in Figure 4.9b (still) [Ollinaho et al., 2017]. Therefore, correct stochasticity of flow perturbations probably requires convection-permitting simulations, or development of structural coherent stochastic physics representations.

Coherent stochasticity is more feasible, if fewer parameterisations are needed (and no deep convective parameterisation). Just a single parameterisation could create demand for a lot of research and tuning investments, to represent its physics fully stochastically [Craig and Cohen, 2006, Plant and Craig, 2008, Keane et al., 2014, Palmer, 2017]. In spite of that, a holistic approach to remaining sub-grid processes would be preferred [see also Palmer, 2019]. Coupled stochastic variability may lead to coherent representation of stochasticity of sub-grid processes. Imposing coupled stochastic variability for clouds, sub-grid turbulence and sub-grid topography and moving to convection-permitting global NWP simulations may be achievable, in the next one to two decades. That strategy needs to be invested in for improved NWP. Such coupled stochasticity may only be representable with the unified strategy, or not even this way. Machine learning could potentially provide an avenue for coherent stochasticity [Rasp et al., 2018].

Of course, the evolution towards convection-permitting global NWP will lead to a next process that is inaccurately represented. Currently, deep convection parameterisation is arguably the most notable process, likely even at mid-latitudes [see also Baumgart et al., 2019]. Once global simulations will move to a $\approx 1-3$ km grid spacing, the limitations shift to the parameterisation of turbulence and radiation [Palmer, 2019, Selz et al., 2022]. *Global LES* is beyond reach at the moment (at least in terms of research practices). However, Bryan et al. [2003], Bryan and Morrison [2012], Lebo and Morrison [2015] and a wide variety of work, beyond the scope of deep convection, have suggested that this is the next - very big - step of potential improvement, after implementing NWP with explicit convection [see Satoh et al., 2019, Grabowski, 2016]. That step towards global application of LES could easily take another couple of decades, while the current step is already demanding and takes time on a decadal scales [see also Bauer et al., 2015, Dudhia, 2014]. Operational high resolution convection-permitting LAM has started about two decades ago and it is still on the way for near-real-time global applications [Brown et al., 2022].

Appendix A: Vertical structure of the troposphere

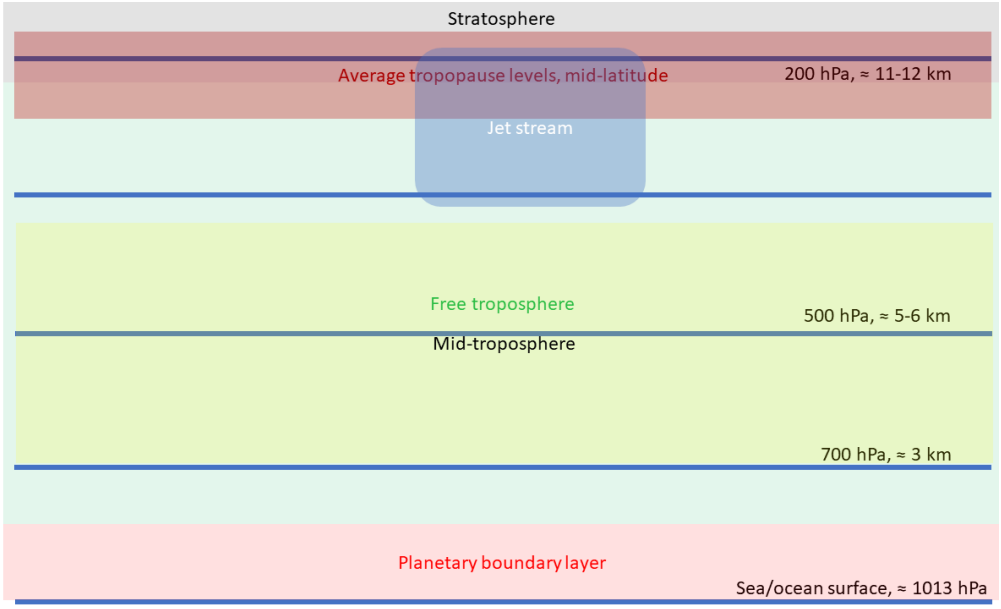

Figure A1: Layering of the lower atmosphere. From top to bottom, the troposphere is first found, consisting of the planetary boundary layer (red shading) and the free troposphere (green shading) on top of it. On top of the troposphere, the tropopause is found (brown shading), which marks the boundary to the stratosphere directly above (grey shading). The mid-troposphere is also highlighted by yellow shading, regions above which are referred to as upper troposphere (if within the troposphere), and below as lower troposphere respectively.

Figure A1 represents the structure of the troposphere. The troposphere itself is defined by the tropopause: by definition, the dynamical tropopause is located at the level where the potential vorticity equals 2 Potential Vorticity Units. The thermal tropopause is defined by the vertical derivative of the potential temperature or temperature, the latter of which usually changes sign at the tropopause: such a sign change of the vertical temperature derivative is called (temperature) *inversion*. Often, the tropopause is marked by a strong temperature inversion - the temperature (and potential temperature) suddenly increase strongly with height, which damps vertical motion (and cloud development) very strongly.
The height of the tropopause can vary from about 8 to about 18 km - typical values at mid-latitudes are in the range of 8-14 km. The lowermost layer of the troposphere is called the planetary boundary layer, or simply the boundary layer. It may be as shallow as a few percent of the total tropopause depth in terms of altitude, while more typical values are about 10% of the depth of the troposphere and it may reach about 30-40% of the vertical depth of the troposphere in a few cases. The part of the troposphere that does not belong to the boundary layer is called free troposphere.
Typically pressure levels are used to indicate certain vertical altitudes or their ranges - Mid-levels of the troposphere are usually located at about 700-400 hPa. The low levels of the troposphere are levels below about 700 hPa and the upper troposphere is the region between the tropopause and about 400 hPa, although in the tropics about 300 hPa may be more appropriate as upper bound and in the polar regions 500 or even 600 hPa may be more appropriate as upper bound. In the upper troposphere one may find a jet stream.

Appendix B: Precipitation accumulation and outflow levels in CM1 experiments

The Figures in this appendix provide supplementary panels and illustrations of the experimental simulations in Chapter 3. Figure B1 shows the spatial distribution of precipitation in the simulations with adjusted physics, with a mean precipitation accumulation as colour shading and isolines for individual experiments at a few accumulation thresholds.
Figure B2 shows an extended version of Figure 3.8 in the main text. It shows how (in)appropriate outflow integration masks at 7-14 km are for experiments with physics perturbations: for some −40% latent heating simulations (left column, lowest outflow levels) the divergent outflow is generally located at 6-11km altitude instead of 7-14 km.
Figure B3 shows how strongly the vertical advection of horizontal momentum (VAUV) was actually perturbed in the simulations where VAUV was perturbed with artificial source and sink terms (centre right). The corresponding effect on divergence (left) and condensation rate (left centre) is also shown. It can be seen that the intensity of the divergence maximum near the tropopause changes (with respect to the ensemble and

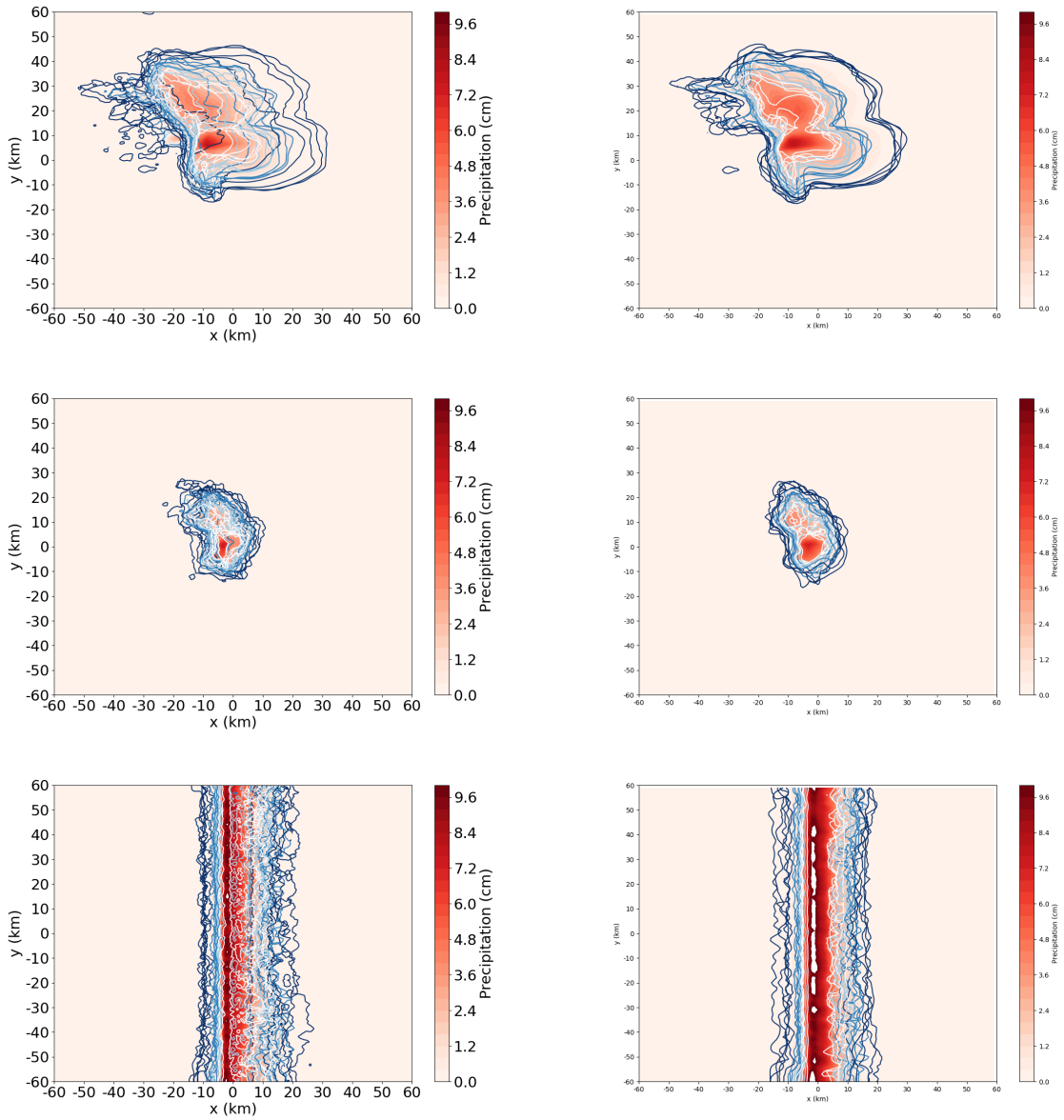

Figure B1: Continuation of Figure 3.5, but for (top) supercell, (middle) regular multicell and (bottom) infinite-length squall lines. On the left, the precipitation distribution is shown for experiments with adjusted latent heating constant and on the right for simulations with a different grid/resolution. Mean precipitation is indicated by the colour fill and isolines are shown at 1, 10, 20 and 30 mm accumulation.

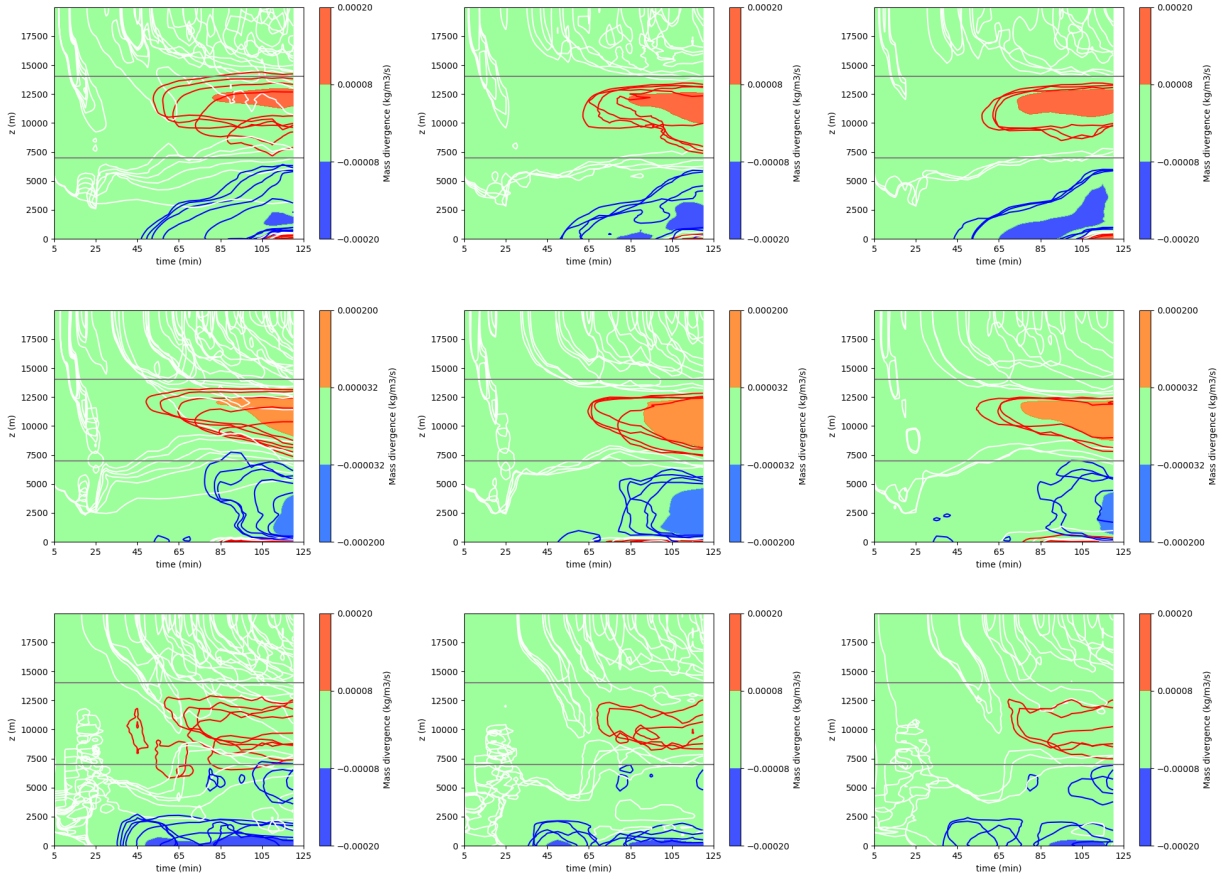

Figure B2: Divergence profiles as in Figure 4 of main text, with mean of the experiments as shading and spaghetti contours for individual experiments, at (blue) -5×10^{-5} kg m^{-3}s^{-1}, (white) 0 kg m^{-3}s^{-1} and (red) $+5 \times 10^{-5}$ kg m^{-3}s^{-1} (middle column shows $\pm 2 \times 10^{-5}$ kg m^{-3}s^{-1} instead). Top to bottom: supercell, regular multicell, infinite length squall line; left to right: latent heating perturbations (−40%, −20%, −10%, +10%, +20%), vertical advection of horizontal momentum (−100%, −50%, +50%) and near-surface potential temperature perturbations.

control simulations) mostly correspondingly with differences in condensation rate across all cases, which is in broad agreement with the results presented in Figure 3.9 (Chapter 3) and further justifies those conclusions. Proportional changes in outflow divergence and condensation rates are the main reason to split off a direct and an indirect effect of CMT on upper tropospheric outflow divergence: a direct effect would perturb the relation between net latent heating and divergence (shown in Figure 3.9) for a given type of convective organisation systematically. Systematic effects of CMT are not found in the structure of the dataset (not shown). An indirect effect of CMT perturbs the evolution of a convective system, and thereby condensation and precipitation rates and net latent heating. In the case of such an indirect effect, systematic differences in the net latent heating rates (together with convective organisation) are translated accordingly into a different magnitude of upper tropospheric divergent outflow - purely caused by changes in net latent heating. The presence of an indirect effect is consistent with Figure B3 and Figure 3.9 (among others).
Furthermore, there is a general tendency for reduced sharpness of the divergence maximum in the vertical and accordingly less strongly tropopause focused outflow in case of perturbed (physically unbalanced) CMT in a simulation.
Nevertheless, moving to the right plot, no CMT simulations diagnose 0 CMT (naturally) and the -50 and +50 % simulations deviate from the ensemble mean as expected. Note that another -20% simulation was additionally included in this dataset, as the Figure is based on and taken from the pre-study: Groot and Tost [2020].

Aside from the insight governed by the perturbations of convective momentum transport in CM1, Figure B3 also highlights the increased ensemble spread among the (infinite length) squall line simulations compared to the supercell and regular multicell simulations (black line and grey lines). Together with the deviating upper tropospheric divergence when normalised with net latent heating (Chapter 3) it was the motivation to do a refined investigation of the variability within this squall line ensemble: the curiosity has eventually

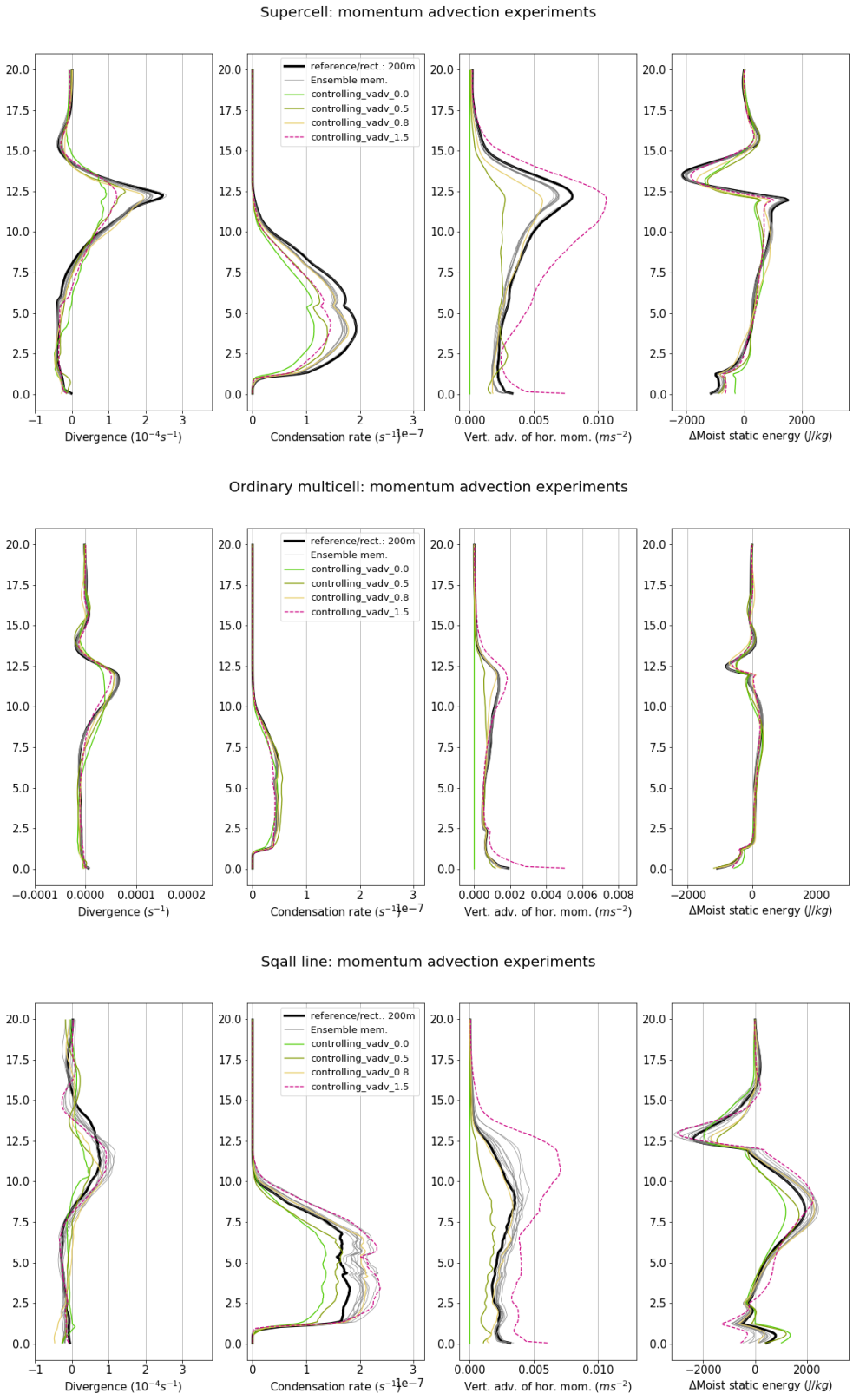

Figure B3: Taken from Groot and Tost [2020]. Profiles of (from left to right) divergence, condensation rate, moist static energy change and vertical advection of horizontal momentum over the first time interval of the analysis of Chapter 3 (0-75 or 0-90 minutes) for each ensemble and the corresponding perturbed CMT (VAUV-)experiments.

lead to Chapter 5.

Appendix C: Vertical profiles for some PAR simulations

C.1 Convective systems in PAR simulations

The synoptic configuration as displayed in Figure 4.1, but examined at more classically analysed levels in synoptic meteorology is provided in Figure C1.
Convective systems have been selected in the PAR simulations by looking at maxima in (both grid scale and convective) precipitation rate and divergence pattern. Hereto, both maxima in divergence at upper levels as well as low levels and the spread in those quantities have been inspected rigorously.
Persistent maxima in upper tropospheric divergence and precipitation rate move northward. They moved along the eastern side of the cold front, as described in Section 4.2. The Northeastern German system moved northeastward within the warm air mass and initiated further to the northeast (Figure 4.7d), in Central Germany. On the other hand, the system over the Alps (Figure 4.7c) initiates with surface-based convection just ahead of the front. It persists in the simulations while moving northward and becoming elevated, as the front moves closer from the southwest. The Central German system is the same system as the one over the Alps (just about 8 hours later, further downstream) and it is initiated by some weak convergence patterns at low levels over Switzerland, possibly related to cold near-surface air approaching from the west within the Alps region (see also Figure 4.2 in Chapter 4). The corresponding divergence-convergence dipole could be followed in vertical cross sections all the way northward - from Switzerland to Northern-Germany (not shown). However, once the convective system reaches Central and Northern Germany, the near-tropopause maximum (i.e. at 200-250 hPa) in divergence moves to the central and western flank of the precipitation system. On the other hand, the precipitation rate still maximises on the eastern side of the convective system (Figure C2). Over the Alps and Northeastern Germany, upper tropospheric divergence and precipitation maxima are co-located. This behaviour - good co-location in the latter case and deviations for the Central German system - was present among all ensemble members.
The relative motion of the upper tropospheric divergence zone compared to the precipitation maximum can be (and is thought to be) a consequence of the deep convection parameterisation: as only reduced vertical velocities are permitted by the hydrostatic assumption, the mesoscale convective system is not properly resolved. The relative location shift difference the precipitation maximum and the divergence maximum in the upper troposphere seems to resemble a system of slantwise convection with stratiform heavy precipitation, rather than a mesoscale convective system with heating (and resulting divergence at higher levels) constrained to a horizontally small, narrow region.

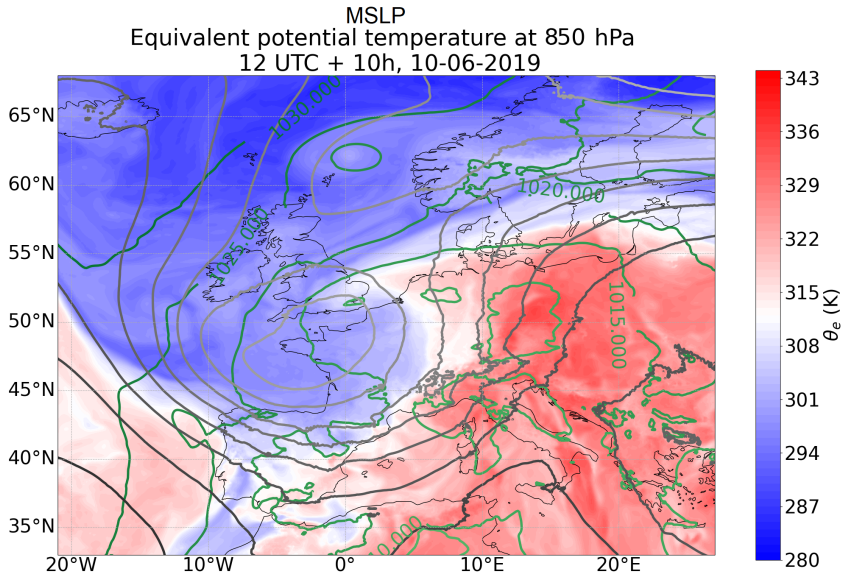

Figure C1: Mean sea level pressure (green isobars) and 850 hPa θ_e (colours), as well as 500 hPa height (grey lines) for the 10th of June 2019, 12 UTC + 10h (analogous to Figure 4.1 in the default PAR simulation, but for 850 hPa, sea level pressure and 500 hPa).

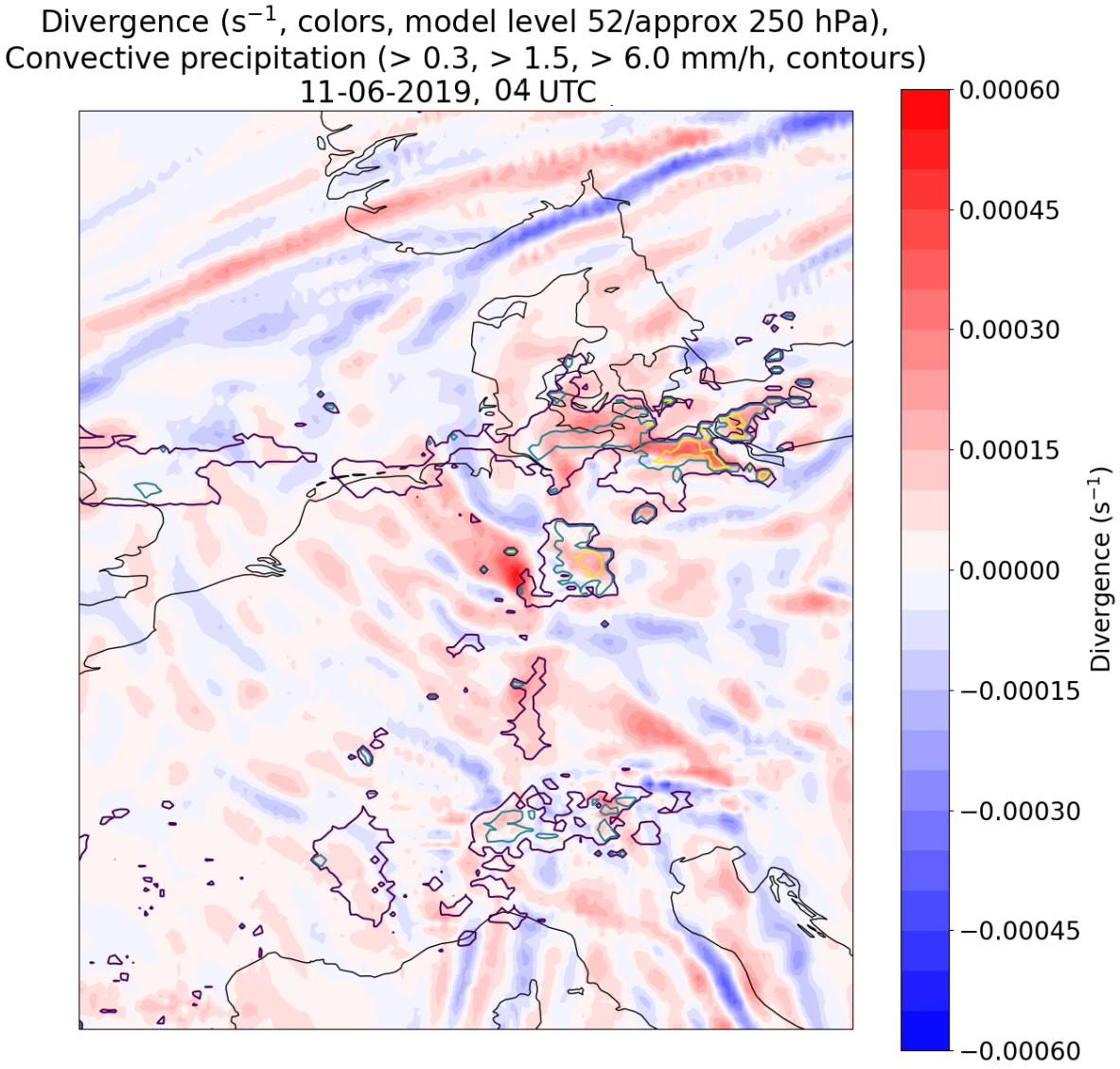

Figure C2: Divergence and convective precipitation in the reference simulation for +16 hours, 11^{th} of June 2019, 04 UTC. The Northeastern German system has a good co-location of convective precipitation maximum and divergence maximum, but in the Central German system to the west of it, the convective precipitation maximum occurs east of the divergence maximum. To the west of the western mesoscale convective system, precipitation occurs predominantly as grid scale precipitation in the simulations (no contours).

C.2 Divergence and condensation profiles

Figure C3 shows the vertical profiles obtained from PAR simulations in three regions of convective activity in the evening and night of 10-11^{th} of June 2019, based on the simulations presented in Chapter 4. Five quantities are shown for each system and 15 selected simulations. The profiles have been averaged over one hour. The first column shows that every simulation (for each of the systems, except one simulation of the Northeastern German system) reveals a typical profile of upper tropospheric outflow from deep convection, with a strong outflow peaking just below 200 hPa: not far below the tropopause. The one exception is a physically perturbed simulation with +20% latent heating constant, in which no condensation (and deposition) occurs either. The exception is caused by a location shift of the convective system in that particular simulation.

The profiles also show that the upper tropospheric outflow occurs upward of about 400-500 hPa, with some variation for simulations with physical perturbations, in particular in the Central German system (middle row). The upper boundary of outflow is also particularly sensitive to perturbations in the same system - varying between about 180 and 220 hPa and with strong variations in magnitude of the divergent outflow.

The condensation profiles in the second column reveal that strong excursions in the condensation rate are

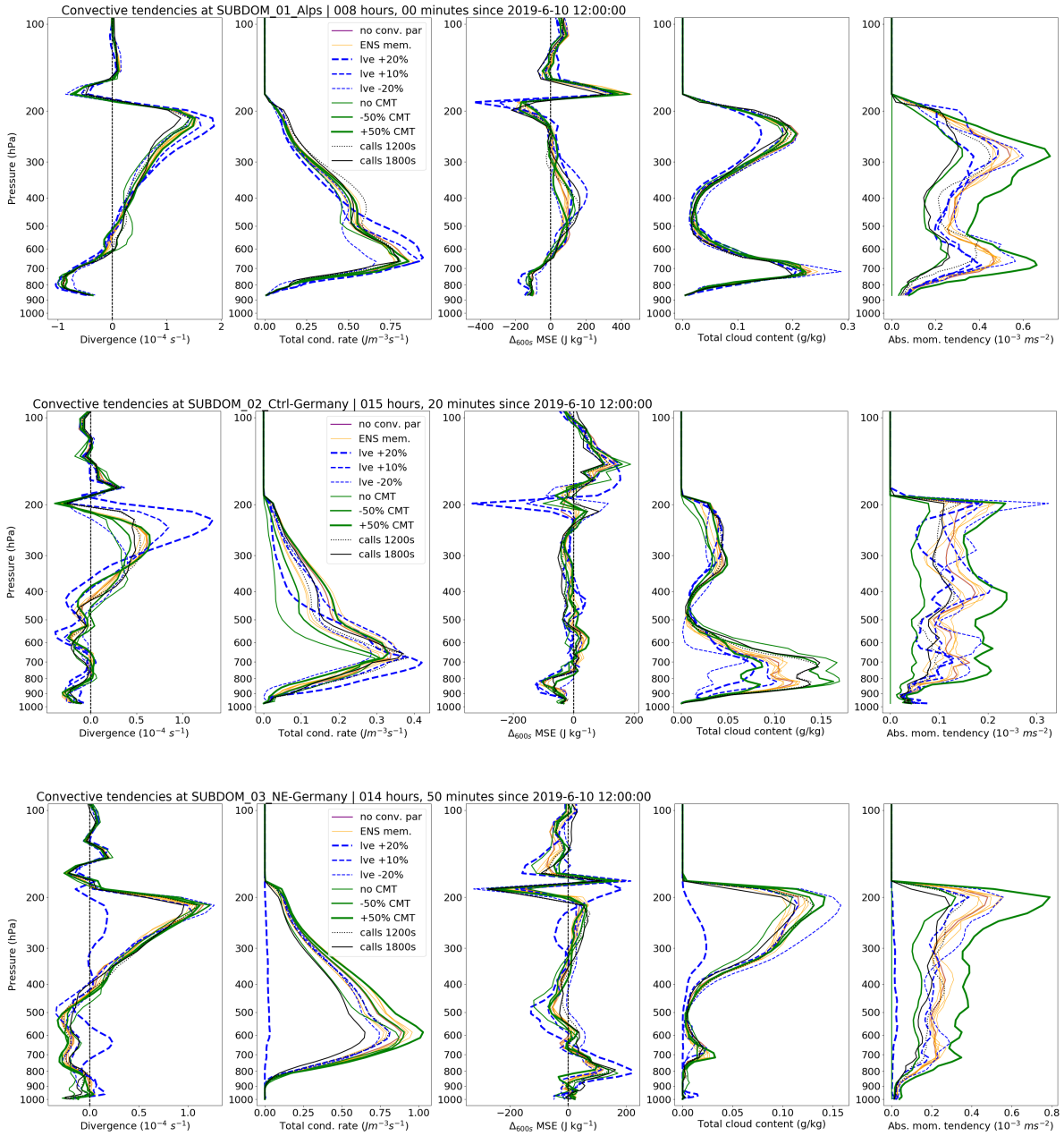

Figure C3: Profiles of (from left to right) divergence, condensation rate (including vapour deposition onto pre-existing hydro-meteors), moist static energy tendency, mean total cloud content and diagnosed CMT as a function of pressure for the three convective systems as analysed in PAR-simulations (including one ensemble member of the ensemble with explicit convection at the same resolution with otherwise the same configuration as the ensemble). Some simulations of the complete PAR-dataset have been omitted to improve readability of the panel.

related to correlated excursions in the divergence profiles: increased heating rates generally relate to increased upper troposhperic divergence. This is true for the convective systems in the first and second row - but not so obvious for the third row. When looking more closely, excursions away from the ensemble mean tend to be stronger in the condensation rate than in divergence, which can partially be offset by differences in evaporation tendency (reducing the net latent heat release) and top and bottom boundaries of the outflow. Generally, the impression of the vertical profiles of divergence and condensation (and deposition) rate is in close agreement with Figure 4.9 (where one system actually shows a small offset of the dominant linear relation between net latent heating and divergent outflow - the circled markers). However, evaporation and sublimation are not taken into account in the profiles shown in Figure C3 - as opposed to Figure 4.9 of Chapter 4. Therefore, the conclusions that can be drawn from the vertical profiles shown above are the same

as those based on Figure 4.9.

C.3 Moist static energy tendencies

The third column of Figure C3 shows mean *moist static energy* tendencies over each of the 10 minute intervals within the analysis window of one hour. Moist static energy is a measure to express the specific total energy contained in an air mass - which includes potential energy due to the vertical elevation of an air parcel, heat as a consequence of the temperature that a parcel has and the energy contained by water vapour that could be released upon lifting and condensation. The profiles all reveal a strong oscillation just above 200 hPa, at the tropopause. That spike may even lead to sign changes in the vertical maximum of the absolute tendencies in moist static energy at a given pressure level among the various simulations. Given the physics and ensemble perturbations utilised in the simulations, this near-tropopause behaviour is an indication of sensitivity. However, the ensemble members tend to have much smaller spread in the moist static energy profiles than the set of physical perturbations, which is likely because they all represent the convective system in this region (as indicated by condensation profiles). Nevertheless, among simulations in which the appearance and intensity of convective systems can be described with a bimodal distribution, similar sensitivity of moist static energy, air mass exchange and divergence as for the bottom row profiles may be particularly strong at and near the tropopause.

C.4 Cloud content

The cloud content in the fourth column of Figure C3 has been included as a direct representation of convective systems, which are expected to have cloud development mostly throughout the vertical column. Particularly strong cloud development can be expected at low levels (800 hPa; horizontal convergence) and high levels (200-300 hPa; anvils and horizontal divergence of system-relative winds), which is present accordingly in the profiles of Figure C3.

C.5 Convective momentum transport

Lastly, the vertical momentum tendency is shown for all simulations in the last, fifth, column of Figure C3. Imposed convective momentum transport perturbations are indeed represented in the diagnostics: removing CMT representation from simulations eliminates the momentum tendencies of CMT, while 50% reduction in the parameterisation indeed leads to decreases of about 50% magnitude in diagnosed CMT. On the other hand 50% increases lead to substantial increases, although it seems to have proportionalities to the ensemble mean that deviate somewhat from +50%. This is a result of indirect effects of CMT on convective systems, like changes in condensation and precipitation rate, as a result of application the physical perturbations (second column, condensation rates) amongst others. Nevertheless, there is a dominant direct impact of CMT-perturbations on diagnosed CMT.

C.6 Summary

Since variability in divergence is very well explained by changes in the precipitation rates (Figures 4.9 and C3), direct effects of CMT on upper tropospheric divergence are not robustly present in the analysed diagnostics. Nevertheless, both of these figures demonstrated slightly increased spread in the divergent outflows from deep convection in the PAR simulations for physically perturbed settings than for the background ensemble. Moreover, divergence maxima and convective precipitation maxima may not be co-located if deep convection is parameterised, which suggests that parameterised representation of deep convection partially sometimes better resembles slantwise (tilted) convection than dynamics of mesoscale convective dynamics.

Appendix D: Evolution of cold pool and convergence-divergence patterns at refined vertical resolution

In order to check appropriateness of the vertical grid length in the ensemble, a simulation with refined vertical grid length has been analysed to complement Section 5.3.3.1. In short, no sensitivity of cold pool dynamics to the vertical grid length has been identified. Nevertheless, the keys of the analysis are presented below [Groot and Tost, 2023].

It has been noted that cold pool propagation and evaporation processes may be sensitive to vertical resolution [e.g. Lebo and Morrison, 2015, Grant et al., 2018]: cold pool dynamics and convective dynamics might be affected substantially by small-scale processes (e.g. microphysics tendencies or turbulence), such that they may not be resolved properly with a vertical mesh of about 100 m.

In the analysis of squall line variability (Chapter 5), sub-optimal representation of shallow layer microphysics processes and cold pool dynamics as a consequence of an insufficiently fine vertical mesh would possibly induce very similar biases among all ensemble members, if biases are substantial. Having executed a simulation at 50 m vertical grid spacing with (presumably) improved cold pool representation, the equivalent of Figure 5.2 in Chapter 5 derived from a simulation with vertically refined grid spacing looks very similar to Figure 5.2. In terms of details, behaviour is intermediate between the control simulation and ENS-03 described in Chapter 5.

If one looks carefully at Figures 5.2 and D1, the three pictures with dynamical evolution differ only slightly and the top panel represents an intermediate between the two at the bottom of Figure D1. The cold pool is

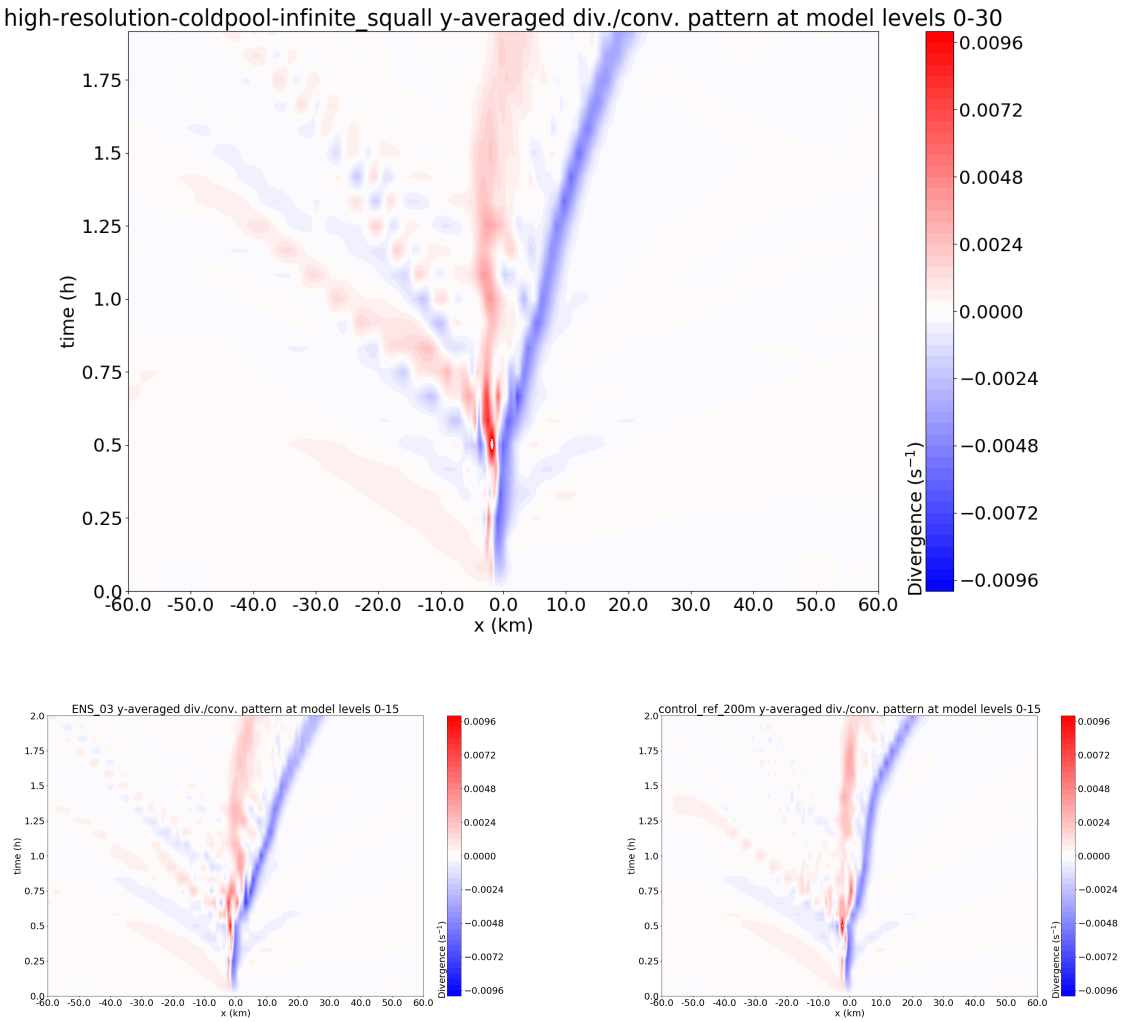

Figure D1: Top: Evolution of convergence and divergence zones (similar to Figure 5.2 in Chapter 5) for the reference simulation, but with a modified vertical grid spacing of 50 m. Bottom: same for reference simulation (left) and ensemble member 3 (right) in Chapter 5 (as in Figure 5.2, but without annotations).

propagating by more than 10 km in ENS-03 over the interval 30-90 minutes, whereas it propagates by less than 10 km in the reference simulation. This corresponds with velocities of 2.5 m/s (9 km/h) and 4.3 m/s (15 km/h). In the high-resolution simulation, the cold pool propagates at about 11-12 km and it initiates after 30 minutes, like in ENS-03 and the reference simulation. The way the cold pool propagation initiates resembles the other two simulations well: a strengthening of the convergence zone at x = 0 km, with subsequent double convergence branches after 35 minutes or so. The jump is comparatively very pronounced in ENS-03 (especially in the divergence, less so in the convergence), very subtle in the high-resolution simulation in especially the divergence (not in the convergence) and practically absent – rather a smooth evolution occurs – in the reference simulation.
Hence, the evolution of convergence zones in a simulation at refined vertical resolution suggest that cold pool dynamics is represented sufficiently well represented by the ensemble at 100 m vertical resolution coarser resolution. The difference in evolution between the ensemble and vertically refined simulation may arise in the last 20 or 30 minutes: a pronounced acceleration occurs in both ENS-03 and the reference, but a weaker acceleration in the simulation with refined vertical grid spacing. This is however not of interest, as any of the patterns that the Chapter 5 has focused on occur until about 80 or 90 minutes into the simulation. The evolution after this time window is beyond the scope of Chapter 5 and therefore, the accuracy of the representation of the cold pool dynamics is not relevant for Chapter 5 - non-linear effects left unconsidered there may take over in the last 30 minutes of the simulation.

Appendix E: Correlation structures in CM1 ensembles - temporal evolution

This appendix has appeared in Groot and Tost [2020], as part of the supplement.

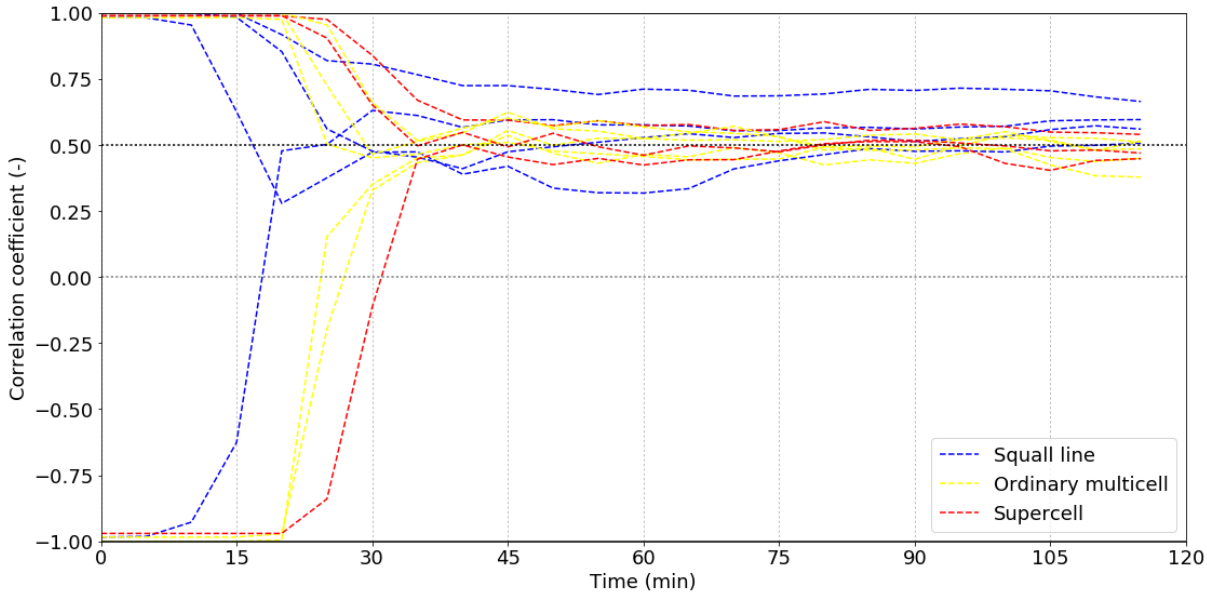

Figure E1: Correlations between zonal velocity deviation pairs from the reference simulation as function of time for the squall line (blue), regular multicell (yellow) and supercell (red) ensembles.

In Figure E1 the de-correlation between ensemble pairs of the three main ensembles in Chapter 3 (infinite length squall line, supercell and regular multicell ensembles) is depicted per case (analogously to and based on Hohenegger and Schär [2007]). The calculation of a zonal velocity deviation field is given in the equation below.

$$U_{deviation.x} = U_{reference} - U_{member.x}$$

Subsequently, members have been paired to calculate the correlation coefficient between their zonal velocity deviation fields $U_{deviation.x}$. As initial conditions or final conditions (after 0 and 120 minutes) were not stored properly in the output of a few simulations [Groot and Tost, 2020], some member pairs of the 10 member ensemble have been omitted. When this led to an odd number of ensemble members with complete output for a mode of convection, one member has been used twice. Initially, the errors behave nearly linearly (0-10 minutes; Figure E1), starting from nearly ± 1. Then there is a transition stage (10-35 minutes). After the transition stage, all pairs of zonal velocity deviation fields but two (both from the squall line case) seem to behave randomly, approaching the asymptotic value [Hohenegger and Schär, 2007]. After 70 minutes only one has not yet approached the random realization asymptote at 0.5 very closely.
The key point of this Figure is the transition stage in which de-correlations within each of the three ensembles occur: between $t = 10$ and $t = 30$ minutes for the infinite length squall lines discussed in Chapter 5.

List of Figures

List of Tables

Code and data availability

A readme file for the dataset of Chapters 3 and 5 and the amended namelist file of simulations in Chapters 3 and 5 are available at `https://tinyurl.com/groot-tost-22` [Groot, 2022] (last accessed: 10-01-2023) and `https://zenodo.org/record/7629669` [Groot, 2023] (last accessed: 16-02-2023), including code to download the output of the simulations of Chapters 3 and 5.

The full code (e.g. ellipse fitting, box analysis) and the output of simulations discussed in Chapter 4 are available in [Groot and Kuntze, 2023] and via `https://doi.org/10.5281/zenodo.7541631` (last accessed: 16-02-2023). Furthermore, the ellipse fitting datasets are also available there.

The individual records, displayed in Figure 3.9, are tabulated explicitly in a spreadsheet of the online supplement of Groot and Tost [2022].

The datasets can also be downloaded from the IRODS of the University of Mainz, using the code provided at the Zenodo webpages, or the readme files.

References

R.D. Adams-Selin. Impact of convectively generated low-frequency gravity waves on evolution of mesoscale convective systems. *Journal of the Atmospheric Sciences*, 77(10):3441 – 3460, 2020a. doi: 10.1175/JAS-D-19-0250.1. URL https://journals.ametsoc.org/view/journals/atsc/77/10/jasD190250.xml.

R.D. Adams-Selin. Sensitivity of mcs low-frequency gravity waves to microphysical variations. *Journal of the Atmospheric Sciences*, 77(10):3461 – 3477, 2020b. doi: 10.1175/JAS-D-19-0347.1. URL https://journals.ametsoc.org/view/journals/atsc/77/10/jasD190347.xml.

R.D. Adams-Selin and R.H. Johnson. Examination of gravity waves associated with the 13 march 2003 bow echo. *Monthly Weather Review*, 141(11):3735 – 3756, 2013. doi: 10.1175/MWR-D-12-00343.1. URL https://journals.ametsoc.org/view/journals/mwre/141/11/mwr-d-12-00343.1.xml.

D.A. Alfaro. Low-tropospheric shear in the structure of squall lines: Impacts on latent heating under layer-lifting ascent. *Journal of the Atmospheric Sciences*, 74(1):229 – 248, 2017. doi: 10.1175/JAS-D-16-0168.1. URL https://journals.ametsoc.org/view/journals/atsc/74/1/jas-d-16-0168.1.xml.

B. Antonescu, D.M. Schultz, A. Holzer, and P. Groenemeijer. Tornadoes in Europe: An underestimated threat. *Bulletin of the American Meteorological Society*, 98(4):713–728, 2017.

A. Arakawa. The cumulus parameterization problem: Past, present, and future. *Journal of Climate*, 17(13): 2493–2525, 2004.

R.L. Badlan, T.P. Lane, M.W. Moncrieff, and C. Jakob. Insights into convective momentum transport and its parametrization from idealized simulations of organized convection. *Quarterly Journal of the Royal Meteorological Society*, 143(708):2687–2702, 2017.

R.N. Bannister. A review of operational methods of variational and ensemble-variational data assimilation. *Quarterly Journal of the Royal Meteorological Society*, 143(703):607–633, 2017.

C. Barthlott, A. Zarboo, T. Matsunobu, and C. Keil. Importance of aerosols and shape of the cloud droplet size distribution for convective clouds and precipitation. *Atmospheric Chemistry and Physics*, 22(3):2153–2172, 2022a. doi: 10.5194/acp-22-2153-2022. URL https://acp.copernicus.org/articles/22/2153/2022/.

C. Barthlott, A. Zarboo, T. Matsunobu, and C. Keil. Impacts of combined microphysical and land-surface uncertainties on convective clouds and precipitation in different weather regimes. *Atmospheric Chemistry and Physics*, 22(16):10841–10860, 2022b. doi: 10.5194/acp-22-10841-2022. URL https://acp.copernicus.org/articles/22/10841/2022/.

P. Bauer, A. Thorpe, and G. Brunet. The quiet revolution of numerical weather prediction. *Nature*, 525 (7567):47–55, 2015.

P. Bauer, A. Brown, R. Buizza, and F. Rabier. ECMWF 2016-2025 strategy: moving towards seamless ensembles. In *EGU General Assembly Conference Abstracts*, page 19523, 2018.

M. Baumgart, P. Ghinassi, V. Wirth, T. Selz, G.C. Craig, and M. Riemer. Quantitative view on the processes governing the upscale error growth up to the planetary scale using a stochastic convection scheme. *Monthly Weather Review*, 147(5):1713–1731, May 2019. doi: 10.1175/mwr-d-18-0292.1. URL https://doi.org/10.1175/mwr-d-18-0292.1.

P. Bechtold, N. Semane, P. Lopez, J.P. Chaboureau, A. Beljaars, and N. Bormann. Representing equilibrium and nonequilibrium convection in large-scale models. *Journal of the Atmospheric Sciences*, 71(2):734–753, 2014.

C.N. Bednarczyk and B.C. Ancell. Ensemble sensitivity analysis applied to a southern plains convective event. *Monthly Weather Review*, 143(1):230 – 249, 2015. doi: 10.1175/MWR-D-13-00321.1. URL https://journals.ametsoc.org/view/journals/mwre/143/1/mwr-d-13-00321.1.xml.

L. Bierdel, T. Selz, and G.C. Craig. Theoretical aspects of upscale error growth through the mesoscales: an analytical model. *Quarterly Journal of the Royal Meteorological Society*, 143(709):3048–3059, October 2017. doi: 10.1002/qj.3160. URL https://doi.org/10.1002/qj.3160.

L. Bierdel, T. Selz, and G. C. Craig. Theoretical aspects of upscale error growth on the mesoscales: Idealized numerical simulations. *Quarterly Journal of the Royal Meteorological Society*, 144(712):682–694, April 2018. doi: 10.1002/qj.3236. URL https://doi.org/10.1002/qj.3236.

C.S. Bretherton and P.K. Smolarkiewicz. Gravity waves, compensating subsidence and detrainment around cumulus clouds. *Journal of Atmospheric Sciences*, 46(6):740 – 759, 1989. doi: 10.1175/1520-0469(1989)046⟨0740:GWCSAD⟩2.0.CO;2. URL https://journals.ametsoc.org/view/journals/atsc/46/6/1520-0469_1989_046_0740_gwcsad_2_0_co_2.xml.

A. Brown, P. Browne, S. English, F. Pappenberger, and F. Rabier. Recent and planned NWP developments at ECMWF. Technical report, Copernicus Meetings, 2022.

A.R. Brown. Large-eddy simulation and parametrization of the effects of shear on shallow cumulus convection. *Boundary-layer meteorology*, 91(1):65–80, 1999.

G.H. Bryan. Cloud Model 1. version 19.8/cm1r19.8, 2019. URL https://www2.mmm.ucar.edu/people/bryan/cm1/.

G.H. Bryan and H. Morrison. Sensitivity of a simulated squall line to horizontal resolution and parameterization of microphysics. *Monthly Weather Review*, 140(1):202 – 225, 2012. doi: 10.1175/MWR-D-11-00046.1. URL https://journals.ametsoc.org/view/journals/mwre/140/1/mwr-d-11-00046.1.xml.

G.H. Bryan, J.C. Wyngaard, and M.J. Fritsch. Resolution requirements for the simulation of deep moist convection. *Monthly Weather Review*, 131:2394–2416, 2003.

R. Buizza and M. Leutbecher. The forecast skill horizon. *Quarterly Journal of the Royal Meteorological Society*, 141(693):3366–3382, 2015.

R. Buizza, M. Miller, and T.N. Palmer. Stochastic representation of model uncertainties in the ecmwf ensemble prediction system. *Quarterly Journal of the Royal Meteorological Society*, 125(560):2887–2908, 1999.

H.M. Christensen. Constraining stochastic parametrisation schemes using high-resolution simulations. *Quarterly Journal of the Royal Meteorological Society*, 146(727):938–962, 2020.

A.J. Clark, S.J. Weiss, J.S. Kain, I.L. Jirak, M. Coniglio, C.J. Melick, C. Siewert, R.A. Sobash, P.T. Marsh, A.R. Dean, et al. An overview of the 2010 hazardous weather testbed experimental forecast program spring experiment. *Bulletin of the American Meteorological Society*, 93(1):55–74, 2012.

S.J. Clarke, S.L. Gray, and N.M. Roberts. Downstream influence of mesoscale convective systems. part 1: influence on forecast evolution. *Quarterly Journal of the Royal Meteorological Society*, 145(724):2933–2952, 2019a. doi: https://doi.org/10.1002/qj.3593. URL https://rmets.onlinelibrary.wiley.com/doi/abs/10.1002/qj.3593.

S.J. Clarke, S.L. Gray, and N.M. Roberts. Downstream influence of mesoscale convective systems. part 2: Influence on ensemble forecast skill and spread. *Quarterly Journal of the Royal Meteorological Society*, 145(724):2953–2972, 2019b. doi: https://doi.org/10.1002/qj.3613. URL https://rmets.onlinelibrary.wiley.com/doi/abs/10.1002/qj.3613.

B.G. Cohen and G.C. Craig. The response time of a convective cloud ensemble to a change in forcing. *Quarterly Journal of the Royal Meteorological Society*, 130(598):933–944, 2004.

M.C. Coniglio, D.J. Stensrud, and L.J. Wicker. Effects of upper-level shear on the structure and maintenance of strong quasi-linear mesoscale convective systems. *Journal of the Atmospheric Sciences*, 63(4):1231–1252, 2006. doi: 10.1175/jas3681.1.

G. C. Craig and T. Selz. Mesoscale dynamical regimes in the midlatitudes. *Geophysical Research Letters*, 45(1):410–417, 2018. doi: https://doi.org/10.1002/2017GL076174. URL https://agupubs.onlinelibrary.wiley.com/doi/abs/10.1002/2017GL076174.

G.C. Craig and B.G. Cohen. Fluctuations in an equilibrium convective ensemble. part i: Theoretical formulation. *Journal of the Atmospheric Sciences*, 63(8):1996 – 2004, 2006. doi: 10.1175/JAS3709.1. URL https://journals.ametsoc.org/view/journals/atsc/63/8/jas3709.1.xml.

B. Cushman-Roisin and J.M. Beckers. *Introduction to geophysical fluid dynamics: physical and numerical aspects*. Academic press, 2011.

P. Davini, J. von Hardenberg, S. Corti, H.M. Christensen, S. Juricke, A. Subramanian, P.A.G. Watson, A. Weisheimer, and T.N. Palmer. Climate sphinx: evaluating the impact of resolution and stochastic physics parameterisations in the ec-earth global climate model. *Geoscientific Model Development*, 10(3): 1383–1402, 2017.

J.W. Deardorff. Stratocumulus-capped mixed layers derived from a three-dimensional model. *Boundary-Layer Meteorology*, 18(4):495–527, 1980. doi: 10.1007/bf00119502.

V. Dixit, L. Nuijens, and K.C. Helfer. Counter-gradient momentum transport through subtropical shallow convection in ICON-LEM simulations. *Journal of Advances in Modeling Earth Systems*, 13(6):e2020MS002352, 2021. doi: https://doi.org/10.1029/2020MS002352. URL `https://agupubs.onlinelibrary.wiley.com/doi/abs/10.1029/2020MS002352`.

J.M. Done, G.C. Craig, S.L. Gray, P.A. Clark, and M.E.B. Gray. Mesoscale simulations of organized convection: Importance of convective equilibrium. *Quarterly Journal of the Royal Meteorological Society.*, 132 (616):737–756, 2006.

H.M. van den Dool. Searching for analogues, how long must we wait? *Tellus A*, 46(3):314–324, 1994.

C.A. Doswell. Societal impacts of severe thunderstorms and tornadoes: Lessons learned and implications for Europe. *Atmospheric Research*, 67:135–152, 2003.

J. Dudhia. A history of mesoscale model development. *Asia-Pacific Journal of Atmospheric Sciences*, 50(1): 121–131, 2014.

D.R. Durran and M. Gingrich. Atmospheric predictability: Why butterflies are not of practical importance. *Journal of the Atmospheric Sciences*, 71(7):2476 – 2488, 2014. doi: 10.1175/JAS-D-14-0007.1. URL `https://journals.ametsoc.org/view/journals/atsc/71/7/jas-d-14-0007.1.xml`.

L. Eisenstein, B. Schulz, G. A. Qadir, J. G. Pinto, and P. Knippertz. Objective identification of high-wind features within extratropical cyclones using a probabilistic random forest (RAMEFI). part i: Method and illustrative case studies. *Weather and Climate Dynamics Discussions*, 2022:1–39, 2022. doi: 10.5194/wcd-2022-29. URL `https://wcd.copernicus.org/preprints/wcd-2022-29/`.

G. Evensen. Data assimilation: the ensemble kalman filter. 2, 2009.

R.G. Fovell, G.L. Mullendore, and S.H. Kim. Discrete propagation in numerically simulated nocturnal squall lines. *Monthly Weather Review*, 134(12):3735 – 3752, 2006. doi: 10.1175/MWR3268.1. URL `https://journals.ametsoc.org/view/journals/mwre/134/12/mwr3268.1.xml`.

K.S. Gage and G.D. Nastrom. Theoretical interpretation of atmospheric wavenumber spectra of wind and temperature observed by commercial aircraft during gasp. *Journal of Atmospheric Sciences*, 43(7):729 – 740, 1986. doi: 10.1175/1520-0469(1986)043⟨0729:TIOAWS⟩2.0.CO;2. URL `https://journals.ametsoc.org/view/journals/atsc/43/7/1520-0469_1986_043_0729_tioaws_2_0_co_2.xml`.

G. George, S. Bony, A.K. Naumann, R. Vogel, and B. Stevens. An apparent abundance of shallow circulations in the trades. In *AGU Fall Meeting Abstracts*, volume 2021, pages A25C–1678, 2021.

G. George, B. Stevens, S. Bony, R. Vogel, and A.K. Naumann. The ubiquity of shallow circulations in the trades. Technical report, Copernicus Meetings, 2022.

M. Ghil and P. Malanotte-Rizzoli. Data assimilation in meteorology and oceanography. 33:141–266, 1991. ISSN 0065-2687. doi: https://doi.org/10.1016/S0065-2687(08)60442-2. URL `https://www.sciencedirect.com/science/article/pii/S0065268708604422`.

M.A. Giorgetta, R. Brokopf, T. Crueger, M. Esch, S. Fiedler, J. Helmert, C. Hohenegger, L. Kornblueh, M. Köhler, E. Manzini, et al. ICON-A, the atmosphere component of the ICON earth system model: I. model description. *Journal of Advances in Modeling Earth Systems*, 10(7):1613–1637, 2018.

W.W. Grabowski. Towards global large eddy simulation: Super-parameterization revisited. *Journal of the Meteorological Society of Japan. Ser. II*, 2016.

W.W. Grabowski and P.K. Smolarkiewicz. Crcp: A cloud resolving convection parameterization for modeling the tropical convecting atmosphere. *Physica D: Nonlinear Phenomena*, 133(1-4):171–178, 1999.

L.D. Grant, T.P. Lane, and S.C. van den Heever. The role of cold pools in tropical oceanic convective systems. *Journal of the atmopsheric sciences*, 75(8):2615–2634, 2018. doi: 10.1175/jas-d-17-0352.1.

L.D. Grant, M.W. Moncrieff, T.P. Lane, and S.C. van den Heever. Shear-parallel tropical convective systems: Importance of cold pools and wind shear. *Geophysical Research Letters*, 47(12):e2020GL087720, 2020.

E. Groot. Output data and namelist - readme file 'evolution of squall line variability and error growth in an ensemble of les' [dataset], 2022. URL `https://irods-web.zdv.uni-mainz.de/irods-rest/rest/fileContents/zdv/project/m2_jgu-w2w/\w2w-a1/EG_HT_2022_squall_line_var/README.txt?ticket=tfKfvC272uyo1WC`. Also available at https://doi.org/10.5281/zenodo.6619313 and https://tinyurl.com/groot-tost-22.

E. Groot. Dataset of "Divergent convective outflow in large eddy simulations ", 2023. URL `https://doi.org/10.5281/zenodo.7629669`.

E. Groot and P. Kuntze. Dataset of "Divergent convective outflow in ICON deep convection permitting and parameterised deep convection simulations", 2023. URL `https://doi.org/10.5281/zenodo.7541630`.

E. Groot and H. Tost. Analysis of variability in divergence and turn-over induced by three idealized convective systems with a 3d cloud resolving model. *Atmospheric Chemistry and Physics Discussions*, pages 1–23, 2020. doi: 10.5194/acp-2020-1142. URL `https://acp.copernicus.org/preprints/acp-2020-1142/`.

E. Groot and H. Tost. Divergent convective outflow in large eddy simulations. *Atmospheric Chemistry and Physics*, 2022. doi: 10.5194/egusphere-2022-1261. *In review as of December 2022. Note: citation includes its supplement.*

E. Groot and H. Tost. Evolution of squall line variability and error growth in an ensemble of large eddy simulations. *Atmospheric Physics and Chemistry, 2023. Note: Citation includes its supplement.*, 2023. doi: https://doi.org/10.5194/acp-23-565-2023. URL `https://doi.org/10.5194/acp-23-565-2023`.

E. Groot, P. Kuntze, A. Miltenberger, and H. Tost. Divergent convective outflow in icon deep convection permitting and parameterised deep convection simulations. *Unknown.*, 2023. doi: Unknown. URL `Unknown`. *Note: To be submitted (Nov. 2022). Citation includes its supplement.*

K. E. Hanley, D. J. Kirshbaum, N. M. Roberts, and G. Leoncini. Sensitivities of a squall line over Central Europe in a convective-scale ensemble. *Monthly Weather Review*, 141(1):112 – 133, 2013. doi: 10.1175/MWR-D-12-00013.1. URL `https://journals.ametsoc.org/view/journals/mwre/141/1/mwr-d-12-00013.1.xml`.

K.E. Hanley, R.S. Plant, T.H.M. Stein, R.J. Hogan, J.C. Nicol, H.W. Lean, C. Halliwell, and P.A. Clark. Mixing-length controls on high-resolution simulations of convective storms. *Quarterly Journal of the Royal Meteorological Society*, 141(686):272–284, 2015.

W. Hazeleger, C. Severijns, T. Semmler, S. Ştefănescu, S. Yang, X. Wang, K. Wyser, E. Dutra, J.M. Baldasano, R. Bintanja, P. Bougeault, R. Caballero, A.M.L. Ekman, J.H. Christensen, B. van den Hurk, P. Jimenez, C. Jones, P. Kållberg, T. Koenigk, R. McGrath, P. Miranda, T. van Noije, T. Palmer, J.A. Parodi, T. Schmith, F. Selten, T. Storelvmo, A. Sterl, H. Tapamo, M. Vancoppenolle, P. Viterbo, and U. Willén. EC-Earth: A seamless earth-system prediction approach in action. *Bulletin of the American Meteorological Society*, 91(10):1357 – 1364, 2010. doi: 10.1175/2010BAMS2877.1. URL `https://journals.ametsoc.org/view/journals/bams/91/10/2010bams2877_1.xml`.

C. Hohenegger and C. Schär. Predictability and error growth dynamics in cloud-resolving models. *Journal of the atmospheric sciences*, 64:4467–4478, Dec 2007.

B. J. Hoskins and G.-Y. Yang. The detailed dynamics of the hadley cell. part ii: December–february. *Journal of Climate*, 34(2):805 – 823, 2021. doi: 10.1175/JCLI-D-20-0504.1. URL `https://journals.ametsoc.org/view/journals/clim/34/2/JCLI-D-20-0504.1.xml`.

R.A. Houze. Mesoscale convective systems. *Reviews of Geophysics*, 42(4), 2004. doi: 10.1029/2004rg000150.

R.A. Houze. 100 years of research on mesoscale convective systems. *Meteorological Monographs*, 59:17.1 – 17.54, 2018. doi: 10.1175/AMSMONOGRAPHS-D-18-0001.1. URL `https://journals.ametsoc.org/view/journals/amsm/59/1/amsmonographs-d-18-0001.1.xml`.

F. Judt. Insights into atmospheric predictability through global convection-permitting model simulations. *Journal of the Atmospheric Sciences*, 75(5):1477 – 1497, 2018. doi: 10.1175/JAS-D-17-0343.1. URL `https://journals.ametsoc.org/view/journals/atsc/75/5/jas-d-17-0343.1.xml`.

F. Judt. Atmospheric predictability of the tropics, middle latitudes, and polar regions explored through global storm-resolving simulations. *Journal of the Atmospheric Sciences*, 77(1):257 – 276, 2020. doi: 10.1175/JAS-D-19-0116.1. URL https://journals.ametsoc.org/view/journals/atsc/77/1/jas-d-19-0116.1.xml.

R.J. Keane, G.C. Craig, C.Keil, and G. Zängl. The Plant–Craig stochastic convection scheme in ICON and its scale adaptivity. *Journal of the Atmospheric Sciences*, 71(9):3404 – 3415, 2014. doi: 10.1175/JAS-D-13-0331.1. URL https://journals.ametsoc.org/view/journals/atsc/71/9/jas-d-13-0331.1.xml.

T.P. Lane and M.J. Reeder. Convectively generated gravity waves and their effect on the cloud environment. *Journal of the Atmospheric Sciences*, 58(16):2427 – 2440, 2001. doi: 10.1175/1520-0469(2001)058⟨2427:CGGWAT⟩2.0.CO;2. URL https://journals.ametsoc.org/view/journals/atsc/58/16/1520-0469_2001_058_2427_cggwat_2.0.co_2.xml.

T.P. Lane and F. Zhang. Coupling between gravity waves and tropical convection at mesoscales. *Journal Of The Atmospheric Sciences*, Nov 2011. URL https://doi.org/10.1175/2011JAS3577.1.

W. Langhans, J. Schmidli, and C. Schär. Bulk convergence of cloud-resolving simulations of moist convection over complex terrain. *Journal of the Atmospheric Sciences*, 69(7):2207 – 2228, 2012. doi: 10.1175/JAS-D-11-0252.1. URL https://journals.ametsoc.org/view/journals/atsc/69/7/jas-d-11-0252.1.xml.

M.G. Lawrence and M. Salzmann. On interpreting studies of tracer transport by deep cumulus convection and its effects on atmospheric chemistry. *Atmospheric Chemistry and Physics*, 8(20):6037–6050, 2008.

Z. J. Lebo and H. Morrison. Effects of horizontal and vertical grid spacing on mixing in simulated squall lines and implications for convective strength and structure. *Monthly Weather Review*, 143(11):4355 – 4375, 2015. doi: 10.1175/MWR-D-15-0154.1. URL https://journals.ametsoc.org/view/journals/mwre/143/11/mwr-d-15-0154.1.xml.

M. Leutbecher, S.J. Lock, P. Ollinaho, S.T.K. Lang, G. Balsamo, P. Bechtold, M. Bonavita, H.M. Christensen, M. Diamantakis, E. Dutra, S. English, M. Fisher, R.M. Forbes, J. Goddard, T. Haiden, R.J. Hogan, S. Juricke, H. Lawrence, D. MacLeod, L. Magnusson, S. Malardel, S. Massart, I. Sandu, P.K. Smolarkiewicz, A. Subramanian, F. Vitart, N. Wedi, and A. Weisheimer. Stochastic representations of model uncertainties at ECMWF: state of the art and future vision. *Quarterly Journal of the Royal Meteorological Society*, 143(707):2315–2339, 2017. doi: https://doi.org/10.1002/qj.3094. URL https://rmets.onlinelibrary.wiley.com/doi/abs/10.1002/qj.3094.

E.N. Lorenz. Deterministic nonperiodic flow. *Journal of Atmospheric Sciences*, 20(2):130 – 141, 1963. doi: 10.1175/1520-0469(1963)020⟨0130:DNF⟩2.0.CO;2. URL https://journals.ametsoc.org/view/journals/atsc/20/2/1520-0469_1963_020_0130_dnf_2_0_co_2.xml.

E.N. Lorenz. The predictability of a flow which possesses many scales of motion. *Tellus*, 21(3):289–307, 1969a. doi: 10.3402/tellusa.v21i3.10086. URL https://doi.org/10.3402/tellusa.v21i3.10086.

E.N. Lorenz. Atmospheric predictability as revealed by naturally occurring analogues. *Journal of Atmospheric Sciences*, 26(4):636 – 646, 1969b. doi: 10.1175/1520-0469(1969)26⟨636:APARBN⟩2.0.CO;2. URL https://journals.ametsoc.org/view/journals/atsc/26/4/1520-0469_1969_26_636_aparbn_2_0_co_2.xml.

E.N. Lorenz. Three approaches to atmospheric predictability. *Bulletin of the American Meteorological Society*, 50(5):345–351, 1969c. URL https://eapsweb.mit.edu/sites/default/files/Three_approaches_1969.pdf.

E.N. Lorenz. Predictability: A problem partly solved, 1996. URL https://eapsweb.mit.edu/sites/default/files/Predicability_a_Problem_2006.pdf.

B.E. Mapes. Gregarious tropical convection. *Journal of Atmospheric Sciences*, 50(13):2026 – 2037, 1993. doi: 10.1175/1520-0469(1993)050⟨2026:GTC⟩2.0.CO;2. URL https://journals.ametsoc.org/view/journals/atsc/50/13/1520-0469_1993_050_2026_gtc_2_0_co_2.xml.

B.E. Mapes and R.A. Houze. Diabatic divergence profiles in Western Pacific mesoscale convective systems. *Journal of Atmospheric Sciences*, 52(10):1807 – 1828, 1995. doi: 10.1175/1520-0469(1995)052⟨1807:DDPIWP⟩2.0.CO;2. URL https://journals.ametsoc.org/view/journals/atsc/52/10/1520-0469_1995_052_1807_ddpiwp_2_0_co_2.xml.

P. Markowski and Y. Richardson. *Mesoscale Meteorology in Midlatitudes*. Wiley, 2010.

T. Matsunobu, C. Keil, and C. Barthlott. The impact of microphysical uncertainty conditional on initial and boundary condition uncertainty under varying synoptic control. *Weather and Climate Dynamics*, 3 (4):1273–1289, 2022. doi: 10.5194/wcd-3-1273-2022. URL https://wcd.copernicus.org/articles/3/1273/2022/.

R.L. McAnelly, J.E. Nachamkin, W.R. Cotton, and M.E. Nicholls. Upscale evolution of mcss: Doppler radar analysis and analytical investigation. *Monthly Weather Review*, 125(6):1083 – 1110, 1997. doi: 10.1175/1520-0493(1997)125⟨1083:UEOMDR⟩2.0.CO;2. URL https://journals.ametsoc.org/view/journals/mwre/125/6/1520-0493_1997_125_1083_ueomdr_2.0.co_2.xml.

C. Melhauser and F. Zhang. Practical and intrinsic predictability of severe and convective weather at the mesoscales. *Journal of the Atmospheric Sciences*, 69(11):3350–3371, 2012. doi: 10.1175/jas-d-11-0315.1.

T. Miyoshi, K. Kondo, and T. Imamura. The 10,240-member ensemble kalman filtering with an intermediate agcm. *Geophysical Research Letters*, 41(14):5264–5271, 2014. doi: https://doi.org/10.1002/2014GL060863. URL https://agupubs.onlinelibrary.wiley.com/doi/abs/10.1002/2014GL060863.

M.W. Moncrieff. The dynamical structure of two-dimensional steady convection in constant vertical shear. *Quarterly Journal of the Royal Meteorological Society*, 104(441):543–567, 1978.

M.W. Moncrieff. A theory of organized steady convection and its transport properties. *Quarterly Journal of the Royal Meteorological Society*, 107(451):29–50, 1981.

M.W. Moncrieff. Organized convective systems: Archetypal dynamical models, mass and momentum flux theory, and parametrization. *Quarterly Journal of the Royal Meteorological Society*, 118(507):819–850, 1992. doi: https://doi.org/10.1002/qj.49711850703. URL https://rmets.onlinelibrary.wiley.com/doi/abs/10.1002/qj.49711850703.

M.W. Moncrieff. Toward a dynamical foundation for organized convection parameterization in gcms. *Geophysical Research Letters*, 46(23):14103–14108, 2019.

M.W. Moncrieff and M.J. Miller. The dynamics and simulation of tropical cumulonimbus and squall lines. *Quarterly Journal of the Royal Meteorological Society*, 102(432):373–394, 1976.

H. Morrison. Impacts of updraft size and dimensionality on the perturbation pressure and vertical velocity in cumulus convection. part i: Simple, generalized analytic solutions. *Journal of the Atmospheric Sciences*, 73(4):1441 – 1454, 2016a. doi: 10.1175/JAS-D-15-0040.1. URL https://journals.ametsoc.org/view/journals/atsc/73/4/jas-d-15-0040.1.xml.

H. Morrison. Impacts of updraft size and dimensionality on the perturbation pressure and vertical velocity in cumulus convection. part ii: Comparison of theoretical and numerical solutions and fully dynamical simulations. *Journal of the Atmospheric Sciences*, 73(4):1455 – 1480, 2016b. doi: 10.1175/JAS-D-15-0041.1. URL https://journals.ametsoc.org/view/journals/atsc/73/4/jas-d-15-0041.1.xml.

H. Morrison, J. A. Curry, and V. I. Khvorostyanov. A new double-moment microphysics parameterization for application in cloud and climate models. part i: Description. *Journal of the Atmospheric Sciences*, 62 (6):1665 – 1677, 2005. doi: 10.1175/JAS3446.1. URL https://journals.ametsoc.org/view/journals/atsc/62/6/jas3446.1.xml.

H. Morrison, G. Thompson, and V. Tatarskii. Impact of cloud microphysics on the development of trailing stratiform precipitation in a simulated squall line: Comparison of one- and two-moment schemes. *Monthly Weather Review*, 137(3):991–1007, 2009. doi: 10.1175/2008mwr2556.1.

C. Muller, D. Yang, G. Craig, T. Cronin, B. Fildier, J.O. Haerter, C. Hohenegger, B. Mapes, D. Randall, S. Shamekh, and S.C. Sherwood. Spontaneous aggregation of convective storms. *Annual Review of Fluid Mechanics*, 54(1):133–157, 2022. doi: 10.1146/annurev-fluid-022421-011319. URL https://doi.org/10.1146/annurev-fluid-022421-011319.

E.L. Nascimento and K.K. Droegemeier. Dynamic adjustment in a numerically simulated mesoscale convective system: Impact of the velocity field. *Journal of the Atmospheric Sciences*, 63(9):2246 – 2268, 2006. doi: 10.1175/JAS3744.1. URL https://journals.ametsoc.org/view/journals/atsc/63/9/jas3744.1.xml.

M.E. Nicholls, R.A. Pielke, and W.R. Cotton. Thermally forced gravity waves in an atmosphere at rest. *Journal of Atmospheric Sciences*, 48(16):1869 – 1884, 1991. doi: 10.1175/1520-0469(1991)048⟨1869:TFGWIA⟩2.0.CO;2. URL https://journals.ametsoc.org/view/journals/atsc/48/16/1520-0469_1991_048_1869_tfgwia_2_0_co_2.xml.

P. Ollinaho, S.J. Lock, M. Leutbecher, P. Bechtold, A. Beljaars, A. Bozzo, R.M. Forbes, T. Haiden, R.J. Hogan, and I. Sandu. Towards process-level representation of model uncertainties: stochastically perturbed parametrizations in the ecmwf ensemble. *Quarterly Journal of the Royal Meteorological Society*, 143(702): 408–422, 2017.

T.N. Palmer. The primacy of doubt: Evolution of numerical weather prediction from determinism to probability. *Journal of Advances in Modeling Earth Systems*, 9(2):730–734, 2017. doi: https://doi.org/10.1002/2017MS000999. URL https://agupubs.onlinelibrary.wiley.com/doi/abs/10.1002/2017MS000999.

T.N. Palmer. Stochastic weather and climate models. *Nature Reviews Physics*, 1(7):463–471, 2019.

T.N. Palmer. A vision for numerical weather prediction in 2030. *arXiv preprint arXiv:2007.04830*, 2020.

R.E. Pandya and D.R. Durran. The influence of convectively generated thermal forcing on the mesoscale circulation around squall lines. *Journal of the Atmospheric Sciences*, 53(20):2924–2951, 1996. doi: 10.1175/1520-0469(1996)053⟨2924:TIOCGT⟩2.0.co;2.

R.E. Pandya, D.R. Durran, and C.S. Bretherton. Comments on "thermally forced gravity waves in an atmosphere at rest". *Journal of the atmospheric sciences*, 50(24):4097–4101, 1993. URL ftp://eos.atmos.washington.edu/pub/breth/papers/1993/pandya-etal.pdf.

K. Peters, C. Hohenegger, and D. Klocke. Different representation of mesoscale convective systems in convection-permitting and convection-parameterizing NWP models and its implications for large-scale forecast evolution. *Atmosphere*, 10(9):503, 2019.

R. S. Plant and G. C. Craig. A stochastic parameterization for deep convection based on equilibrium statistics. *Journal of the Atmospheric Sciences*, 65(1):87–105, 2008. doi: 10.1175/2007jas2263.1.

S.B. Pope. *Turbulent flows*. Cambridge university press, 2000.

F. Prill, D. Reinert, D. Rieger, G. Zängl, J. Schröter, J. Örstner, S. Werchner, M. Weimer, R. Ruhnke, and B. Vogel. ICON model tutorial 2019, 2019. URL 2019_version_of_2020_tutorial,_2020_version_available_at_https://www.dwd.de/DE/leistungen/nwv_icon_tutorial/pdf_einzelbaende/icon_tutorial2020.pdf.

F. Prill, D. Reinert, D. Rieger, and G. Zängl. ICON model tutorial 2020, 2020. URL Availableathttps://www.dwd.de/DE/leistungen/nwv_icon_tutorial/pdf_einzelbaende/icon_tutorial2020.pdf.

S. Rasp, M.S. Pritchard, and P. Gentine. Deep learning to represent subgrid processes in climate models. *Proceedings of the National Academy of Sciences*, 115(39):9684–9689, 2018. doi: 10.1073/pnas.1810286115. URL https://www.pnas.org/doi/abs/10.1073/pnas.1810286115.

M. J. Rodwell and H. Wernli. The cyclogenesis butterfly: Uncertainty growth and forecast reliability during extratropical cyclogenesis. *Weather and Climate Dynamics Discussions*, pages 1–32, 2022. doi: https://doi.org/10.5194/wcd-2022-6.

M.J. Rodwell, L. Magnusson, P. Bauer, P. Bechtold, M. Bonavita, Carla C., M. Diamantakis, P. Earnshaw, A. Garcia-Mendez, L. Isaksen, E. Källén, D. Klocke, P. Lopez, T. McNally, A. Persson, F. Prates, and N. Wedi. Characteristics of occasional poor medium-range weather forecasts for europe. *Bulletin of the American Meteorological Society*, 94(9):1393–1405, September 2013. doi: 10.1175/bams-d-12-00099.1. URL https://doi.org/10.1175/bams-d-12-00099.1.

R. Rotunno, J.B. Klemp, and M.L. Weisman. A theory for strong, long-lived squall lines. *Journal of the Atmospheric Sciences*, 45(3):463–485, 1988. doi: 10.1175/1520-0469(1988)045⟨0463:ATFSLL⟩2.0.co;2.

S.T. Salesky, M. Chamecki, and E. Bou-Zeid. On the nature of the transition between roll and cellular organization in the convective boundary layer. *Boundary-layer meteorology*, 163(1):41–68, 2017.

M. Satoh, B. Stevens, F. Judt, M. Khairoutdinov, S.J. Lin, W.M. Putman, and P. Düben. Global cloud-resolving models. *Current Climate Change Reports*, 5(3):172–184, 2019.

L. Schlemmer, P. Bechtold, I. Sandu, and M. Ahlgrimm. Uncertainties related to the representation of momentum transport in shallow convection. *Journal of Advances in Modeling Earth Systems*, 9(2):1269–1291, 2017. doi: https://doi.org/10.1002/2017MS000915. URL https://agupubs.onlinelibrary.wiley.com/doi/abs/10.1002/2017MS000915.

C. Schraff, H. Reich, A. Rhodin, A. Schomburg, K. Stephan, A. Periáñez, and R. Potthast. Kilometre-scale ensemble data assimilation for the COSMO model (KENDA). *Quarterly Journal of the Royal Meteorological Society*, 142(696):1453–1472, 2016.

B. Schulz and S. Lerch. Machine learning methods for postprocessing ensemble forecasts of wind gusts: A systematic comparison. *Monthly Weather Review*, 150(1):235 – 257, 2022. doi: 10.1175/MWR-D-21-0150.1. URL https://journals.ametsoc.org/view/journals/mwre/150/1/MWR-D-21-0150.1.xml.

C. Schumacher, R.A. Houze, and I. Kraucunas. The tropical dynamical response to latent heating estimates derived from the trmm precipitation radar. *Journal of the Atmospheric Sciences*, 61(12):1341 – 1358, 2004. doi: 10.1175/1520-0469(2004)061⟨1341:TTDRTL⟩2.0.CO;2. URL https://journals.ametsoc.org/view/journals/atsc/61/12/1520-0469_2004_061_1341_ttdrtl_2.0.co_2.xml.

A. Seifert. A revised cloud microphysical parameterization for COSMO-LME. *COSMO Newsletter*, 7:25–28, 2008.

A. Seifert and K.D. Beheng. A two-moment cloud microphysics parameterization for mixed-phase clouds. part 1: Model description. *Meteorology and atmospheric physics*, 92(1):45–66, 2006.

T. Selz. Estimating the intrinsic limit of predictability using a stochastic convection scheme. *Journal of the Atmospheric Sciences*, 76(3):757–765, 2019. doi: 10.1175/jas-d-17-0373.1.

T. Selz and G.C. Craig. Upscale error growth in a high-resolution simulation of a summertime weather event over europe. *Monthly Weather Review*, 143(3):813–827, March 2015a. doi: 10.1175/mwr-d-14-00140.1. URL https://doi.org/10.1175/mwr-d-14-00140.1.

T. Selz and G.C. Craig. Simulation of upscale error growth with a stochastic convection scheme. *Geophysical Research Letters*, 42(8):3056–3062, April 2015b. doi: 10.1002/2015gl063525. URL https://doi.org/10.1002/2015gl063525.

T. Selz, M. Riemer, and G.C. Craig. The transition from practical to intrinsic predictability of midlatitude weather. *Journal of the Atmospheric Sciences*, 79(8):2013–2030, 2022. doi: 10.1175/JAS-D-21-0271.1. URL https://journals.ametsocwe.org/view/journals/atsc/aop/JAS-D-21-0271.1/JAS-D-21-0271.1.xml.

W.C. Skamarock. Evaluating mesoscale NWP models using kinetic energy spectra. *Monthly Weather Review*, 132(12):3019–3032, 2004. doi: 10.1175/mwr2830.1.

A.H. Sobel, J. Nilsson, and L.M. Polvani. The weak temperature gradient approximation and balanced tropical moisture waves. *Journal of the Atmospheric Sciences*, 58(23):3650 – 3665, 2001. doi: 10.1175/1520-0469(2001)058⟨3650:TWTGAA⟩2.0.CO;2. URL https://journals.ametsoc.org/view/journals/atsc/58/23/1520-0469_2001_058_3650_twtgaa_2.0.co_2.xml.

S.N. Stechmann and A.J. Majda. Gravity waves in shear and implications for organized convection. *Journal of the Atmospheric Sciences*, Sep 2009. URL https://doi.org/10.1175/2009JAS2976.1.

S.N. Stechmann and J.D. Neelin. A stochastic model for the transition to strong convection. *Journal of the Atmospheric Sciences*, 68(12):2955 – 2970, 2011. doi: 10.1175/JAS-D-11-028.1. URL https://journals.ametsoc.org/view/journals/atsc/68/12/jas-d-11-028.1.xml.

T.H.M. Stein, R.J. Hogan, K.E. Hanley, J.C. Nicol, H.W. Lean, R.S. Plant, P.A. Clark, and C.E. Halliwell. The three-dimensional morphology of simulated and observed convective storms over Southern England. *Monthly Weather Review*, 142(9):3264–3283, 2014. doi: 10.1175/mwr-d-13-00372.1.

Y.Q. Sun and F. Zhang. Intrinsic versus practical limits of atmospheric predictability and the significance of the butterfly effect. *Journal of the Atmospheric Sciences*, 73(3):1419 – 1438, 2016. doi: 10.1175/JAS-D-15-0142.1. URL https://journals.ametsoc.org/view/journals/atsc/73/3/jas-d-15-0142.1.xml.

M. Tiedtke. A comprehensive mass flux scheme for cumulus parameterization in large-scale models. *Monthly weather review*, 117(8):1779–1800, 1989.

R.D. Torn and G.S. Romine. Sensitivity of Central Oklahoma convection forecasts to upstream potential vorticity anomalies during two strongly forced cases during MPEX. *Monthly Weather Review*, 143(10):4064 – 4087, 2015. doi: 10.1175/MWR-D-15-0085.1. URL https://journals.ametsoc.org/view/journals/mwre/143/10/mwr-d-15-0085.1.xml.

S.B. Trier, W.C. Skamarock, and M.A. LeMone. Structure and evolution of the 22 february 1993 TOGA COARE squall line: Organization mechanisms inferred from numerical simulation. *Journal of the Atmospheric Sciences*, 54(3):386 – 407, 1997. doi: 10.1175/1520-0469(1997)054⟨0386:SAEOTF⟩2.0.CO;2. URL https://journals.ametsoc.org/view/journals/atsc/54/3/1520-0469_1997_054_0386_saeotf_2.0.co_2.xml.

A. Varble, E.J. Zipser, A.M. Fridlind, P. Zhu, A.S. Ackerman, J.P. Chaboureau, S. Collis, J. Fan, A. Hill, and B. Shipway. Evaluation of cloud-resolving and limited area model intercomparison simulations using TWP-ICE observations: 1. deep convective updraft properties. *Journal of Geophysical Research: Atmospheres*, 119(24):13,891–13,918, 2014. doi: https://doi.org/10.1002/2013JD021371. URL https://agupubs.onlinelibrary.wiley.com/doi/abs/10.1002/2013JD021371.

A. Varble, H. Morrison, and E. Zipser. Effects of under-resolved convective dynamics on the evolution of a squall line. *Monthly Weather Review*, 148(1):289 – 311, 2020. doi: 10.1175/MWR-D-19-0187.1. URL https://journals.ametsoc.org/view/journals/mwre/148/1/mwr-d-19-0187.1.xml.

M.L. Weisman and J.B. Klemp. The dependence of numerically simulated convective storms on vertical wind shear and buoyancy. *Monthly Weather Review*, 110(6):504–520, June 1982. doi: 10.1175/1520-0493(1982)110⟨0504:TDONSC⟩2.0.co;2. URL https://doi.org/10.1175/1520-0493(1982)110<0504:tdonsc>2.0.co;2.

M.L. Weisman and R. Rotunno. "a theory for strong long-lived squall lines" revisited. *Journal of the Atmospheric Sciences*, 61(4):361–382, 2004. doi: 10.1175/1520-0469(2004)061⟨0361:ATFSLS⟩2.0.co;2.

M.L. Weisman, W.C. Skamarock, and J.B. Klemp. The resolution dependence of explicitly modeled convective systems. *Monthly Weather Review*, 125(4):527–548, 1997. doi: 10.1175/1520-0493(1997)125⟨0527:TRDOEM⟩2.0.co;2.

J.A. Weyn and D.R. Durran. The dependence of the predictability of mesoscale convective systems on the horizontal scale and amplitude of initial errors in idealized simulations. *Journal of the Atmospheric Sciences*, 74(7):2191 – 2210, 2017. doi: 10.1175/JAS-D-17-0006.1. URL https://journals.ametsoc.org/view/journals/atsc/74/7/jas-d-17-0006.1.xml.

J.A. Weyn, D.R. Durran, and R. Caruana. Can machines learn to predict weather? using deep learning to predict gridded 500-hpa geopotential height from historical weather data. *Journal of Advances in Modeling Earth Systems*, 11(8):2680–2693, 2019. doi: https://doi.org/10.1029/2019MS001705. URL https://agupubs.onlinelibrary.wiley.com/doi/abs/10.1029/2019MS001705.

J. Wilhelm, S. Mohr, H.J. Punge, B. Mühr, M. Schmidberger, J.E. Daniell, K.M. Bedka, and M. Kunz. Severe thunderstorms with large hail across Germany in June 2019. *Weather*, 76(7):228–237, 2021. doi: https://doi.org/10.1002/wea.3886. URL https://rmets.onlinelibrary.wiley.com/doi/abs/10.1002/wea.3886.

D. S. Wilks. "the stippling shows statistically significant grid points": How research results are routinely overstated and overinterpreted, and what to do about it. *Bulletin of the American Meteorological Society*, 97(12):2263–2273, 2016. doi: 10.1175/bams-d-15-00267.1.

G. Zängl, D. Reinert, P. Rípodas, and M. Baldauf. The ICON (ICOsahedral Non-hydrostatic) modelling framework of DWD and MPI-M: Description of the non-hydrostatic dynamical core. *Quarterly Journal of the Royal Meteorological Society*, 141(687):563–579, 2015.

F. Zhang. Dynamics and structure of mesoscale error covariance of a winter cyclone estimated through short-range ensemble forecasts. *Monthly Weather Review*, Oct 2005. URL https://doi.org/10.1175/MWR3009.1.

F. Zhang, N. Bei, R. Rotunno, C. Snyder, and C.C. Epifanio. Mesoscale predictability of moist baroclinic waves: Convection-permitting experiments and multistage error growth dynamics. *Journal of the Atmospheric Sciences*, 64(10):3579–3594, October 2007. doi: 10.1175/jas4028.1. URL https://doi.org/10.1175/jas4028.1.

F. Zhang, Y.Q. Sun, L. Magnusson, R. Buizza, S.J. Lin, J.H. Chen, and K. Emanuel. What is the predictability limit of midlatitude weather? *Journal of the Atmospheric Sciences*, 76(4):1077 – 1091, 2019. doi: 10.1175/JAS-D-18-0269.1. URL https://journals.ametsoc.org/view/journals/atsc/76/4/jas-d-18-0269.1.xml.

Samenvatting

De gevolgen van convectieve organisatie, aggregatie en convectieve impulstransport voor variabiliteit in de divergente uitstroom van diepe convectie boven in de troposfeer worden in kaart gebracht. Daarnaast wordt de variabiliteit en de voorspelbaarheid van deze uitstroom gerelateerd aan andere aspecten van de dynamica en variabiliteit van de convectieve systemen. Drie verschillende methodes om convectieve systemen te simuleren worden onderzocht, waarbij de conditionele relatie tussen de neerslagintensiteit (oftewel van netto vrijkomende latente warmte) en de bijbehorende divergente convectieve uitstroom blijkt te verschillen als gevolg van de verschillen in representatie van de convectie in de simulatie.

Het theoretisch begrip van de intensiteit van de convectieve uitstroom bovenin de troposfeer wordt eerst onderzocht, door een uitgebreide set van geïdealiseerde *Large Eddy Simulaties (LES, Grote Eddy of Draaikolk Simulaties)* uitgevoerd met het model CM1 te analyseren. De fysische en *ensemble*-experimenten laten zien dat convectieve organisatie en de netto vrijkomende latente warmte (die kan worden vertaald naar neerslagintensiteit) bepalen hoe sterk de uitstroom van de convectieve systemen is. De dimensionaliteit van de convectieve uitstroom (2D versus 3D, of een mix daarvan) lijkt daarin de envelop die de algehele uitstroomvariabiliteit begrenst te bepalen - een uitkomst die in principe consistent is met uitstroomberekeningen op basis van een gelineariseerd model voor zwaartekrachtsgolven (*gravity waves*) [o.a. Nicholls et al., 1991].

Met een analyse van de uitstroom van convectieve systemen in ICON-simulaties voor een weerssituatie worden geparametriseerde en expliciet opgeloste convectie in ICON vergeleken. Nagenoeg lineaire afhankelijkheid van vrijgekomen netto latente warmte wordt gevonden voor simulaties met geparametriseerde diepe convectie, maar structurele niet-lineaire afhankelijkheid wordt gevonden bij simulaties met expliciet opgeloste convectie en een roosterpuntafstand van 1 km. Convectieve organisatie en aggregatie zorgen voor een sublineaire toename van de uitstroomdivergentie met een toename van de vrijkomende netto latente warmte - dit wordt duidelijk uit het onzekerheidsinterval van de optimale machtsrelatie tussen de twee grootheden (met een exponent van 0.70 ± 0.16). Ook andere statistische patronen gevonden voor de dataset met simulaties van deze weerssituatie boven Centraal-Europa ondersteunen de rol van convectieve organisatie en aggregatie voor de sterkte van zulke uitstroom. Daarnaast worden ellipsen afgepast op de convectieve systemen in ICON-simulaties, waarvan de ratio tussen de twee aslengtes en andere karakteristieken worden gebruikt om te onderzoeken of ook een relatie met de divergente uitstroom van een convectief systeem bovenin de troposfeer kan worden gedetecteerd. Daaruit komen geen volledig coherente signalen; die tweeledige signalen zijn verklaarbaar op meerdere manieren. De ratio van intensiteit divergente uitstroom en netto vrijgekomen latente warmte correleert positief met het op dezelfde wijze genormaliseerde convectieve impulstransport, mogelijk wijzend op een oorzakelijke verband.

Op een *ensemble* van *LES*-simulaties met sterk georganiseerde buienlijnen (*squall lines*) wordt een analyse van verschilgroei toegepast, die ook kan worden geïnterpreteerd als foutengroei. Die analyse wordt ook gerelateerd aan de evolutie van de variabiliteit in andere grootheden, zoals grootheden die dynamica en neerslag beschrijven. Structurele decorrelatie in de variabiliteit tussen ensembleleden kan worden verbonden met zwaartekrachtsgolven, die veroorzaakt zijn tijdens de initiatie van de eerste convectieve cellen in de twee uur durende simulaties. Een tweede fase van convectieve initiatie wordt sterk beïnvloed door deze antecedente zwaartekrachtsgolven en creëert een nieuwe structuur in de ensemblespreiding, welke op een tijdsschaal van ongeveer een uur gehandhaafd blijft. Direct daarna accelereert een *cold pool*. De voortplantingssnelheid van de voorste begrenzing van deze *cold pool* blijft vrijwel constant over het interval van 45 tot 100 minuten simulatietijd. Samenhangende verstoringen in de stroming die tot stand komen direct na de tweede fase van convectieve initiatie blijven ook bestaan op een tijdsschaal van ongeveer een uur. Ze verdwijnen na ongeveer 80-100 minuten. Bij het bestuderen van de stroming in een frame ten opzichte van de begrenzing van de *cold pool* wordt duidelijk dat de foutengroei vanuit dit perspectief duidelijk kleiner is dan vanuit het Euleriaanse perspectief. Een aanzienlijk deel van de spreiding in de stroming kan direct worden uitgelegd door verschillen in propagatie van de rand van de *cold pool*. Veel van de spreiding binnen het ensemble na 45-80 minuten is sterk verbonden met de tweede fase van convectieve initiatie - bijvoorbeeld die in neerslagsom en in karakteristieken van de *downdrafts*.

Bij het kijken naar convectieve variabiliteit vanuit het conditionele oogpunt, wordt voorbijgegaan aan de subtiele eventualiteit van convectieve initiatie. Maar de benadering vanuit het perspectief van een gegeven hoeveelheid netto vrijgekomen latente warmte kan wel op haar eigen unieke manier licht schijnen op de representatie van (diep) convectieve variabiliteit in verschillende typen numerieke weermodellen. Zo laat dit werk zien dat er contrasten zijn tussen diepe convectie zoals beschreven in *LES* en zoals beschreven in parameterisaties - impliciete aannames van geparametriseerde diepe convectie worden op een nieuwe manier kenbaar gemaakt. De sterke koppeling tussen convectieve variabiliteit, dynamica, voorspelbaarheid en variabiliteit neerslagintensiteit (vrijgekomen latente warmte) op een korte tijdsschaal (enkele uren, hooguit een dag) wordt benadrukt. In representativiteitsstudies en voorspelbaarheidsstudies zou de hier gebruikte samenhangende conditionele benadering een helpende hand kunnen bieden.